Nonlinear two-dimensional Rayleigh-Bénard convection

Benjamin James Hepworth

Submitted in accordance with the requirements for the degree of Doctor of Philosophy

The University of Leeds

Department of Applied Mathematics

March 2014

The candidate confirms that the work submitted is his own and that appropriate credit has been given where reference has been made to the work of others.

"One must from time to time attempt things that are beyond one's capacity."

—Pierre Auguste Renoir

Acknowledgements

I would like to extend my gratitude to all those who have helped me complete this work, both academically and personally.

First I would like to thank my supervisors, Chris Jones and Steve Tobias, for their wisdom, guidance and most of all good humour, throughout the duration of my PhD study. Further recognition must be given to current and former members of the Astrophysical and Geophysical Fluid Dynamics research group in Leeds: specifically Rob, Tina, Nikolai, Laura and Julian, for supporting me and sharing in the day-to-day experience of completing my PhD, as well as being good friends outside of the university.

On a personal note I would like to thank my parents, Carolyn and Craig; sister, Hayley and grandparents John, Sheila and Raymond, for encouraging me throughout many years of education, despite not really understanding what I was doing. Thanks also to Matthew, for many a coffee and stroll, providing a welcome distraction from the toils of research. Finally, and most importantly, thank you to Sofia: you believed in me when I did not, and put up with me unwaveringly for the past three and a half years.

This research has been funded by a grant from STFC.

Abstract

Two dimensional Rayleigh-Bénard convection in a Boussinesq fluid is the simplest possible system that exhibits convective instability. Moreover it contains the same basic physics as occurring in many geophysical and astrophysical systems, such as the interiors of the Earth and the Sun. We study this ubiquitous system with and without the effect of rotation, for stress free boundary conditions. We review the linear stability theory of two dimensional Rayleigh-Bénard convection, deriving conditions on the dimensionless parameters of the system, under which we expect convection to occur. Building on this we solve the equations governing the dynamics of the nonlinear system using a pseudospectral numerical method. This is done for a range of different values of the Rayleigh, Prandtl and Taylor numbers. We analyse the results of these simulations using a variety of applied mathematical techniques. Paying particular attention to the manner in which the flow becomes unstable and looking at global properties of the system such as the heat transport, we concur with previous work conducted in this area. For a particular subset of parameters studied, we find that motion is always steady. Motivated by this we develop an asymptotic theory to describe these nonlinear, steady state solutions, in the limit of large Rayleigh number. This asymptotic theory provides analytical expressions for the governing hydrodynamical variables as well as predictions about the heat transport. With only a few terms we find excellent agreement with the results of our numerical simulations.

Contents

List of figures

List of tables

Chapter 1

Introduction

1.1 Motivation

Thermal convection is a phenomenon where heat energy is transported by the bulk movement of molecules within a fluid—a liquid or a gas. This cannot take place in a solid, since they do not support molecular flows.

In order for convection to occur, we require the density to be inversely related to the temperature, such that an increase in temperature leads to a decrease in density. Furthermore, it is necessary to have hot fluid lying beneath cold fluid. The onset of convection is governed by the *Rayleigh number*. As a fluid is warmed in one region, it will expand, becoming less dense than its surroundings and thus rise due to buoyancy. Concurrently, colder, heavier, fluid will sink in its place, due to being more dense than its surroundings. This is the basic physical process behind thermal convection. The induced motion can be a very efficient way in which heat can be transported and fluid can be mixed. It is a paradigm problem for the study of fluid instability, and an important setting for the investigation of turbulence. Indeed, the basic convection mechanism that we have described is very simple, yet this can lead to complex fluid behaviour, and captivating mathematical analysis.

Convection plays an important role in many geophysical and astrophysical systems,

such as: the Earth's core and atmosphere, inside the Sun and other stellar bodies, and in the cores and atmospheres of planets. All of these systems have areas that are hotter in one region than another, thus convection can be the preferred method in which heat energy is transported from one to another. Since convection plays such an elemental role within these systems, it is not only an interesting topic of study, but vital in order to describe the world and, indeed, the universe in which we live.

The simplest possible convective system, and the one that we study here, is Rayleigh-Bénard convection (see Bénard (1900), Bénard (1901) and Rayleigh (1916)). This contains the same basic physics as occurring in a natural geophysical or astrophysical system, yet is much more straightforward to study, owing to the simplified geometry and thermodynamic properties involved. It is important, however, to understand the way in which the work presented here fits into the wider theory of geophysical and astrophysical fluid dynamics.

1.1.1 Dynamo theory

Of particular interest is convection in the presence of an electrically conducting fluid, as in the core of the Earth, or the Sun. This can lead to the generation of magnetic fields, by a process known as dynamo action. It had been conjectured as early as the 16th century that the Earth possesses a magnetic field, with the first hypothesis of its origin put forward by Gilbert (1600). However it was not until centuries later that Larmor (1919) conceived of the idea that this magnetic field, and likewise that of the Sun, was maintained by dynamo action. Dynamo theory asserts that a body may possess a self-sustaining magnetic field, generated within an electrically conducting fluid. In geophysical and astrophysical systems, dynamos are often driven by the effects of convection and planetary rotation. The equations that are central to dynamo theory are the Navier-Stokes equations, governing the evolution of the fluid velocity, and Maxwell's equations of electromagnetism (see

Moffatt (1978)). We are interested only in the effects of thermal convection, so at no point in this work will we consider the effects of magnetic fields. For an overview of dynamo theory in a variety of geophysical and astrophysical settings, one should consult Dormy & Soward (2007).

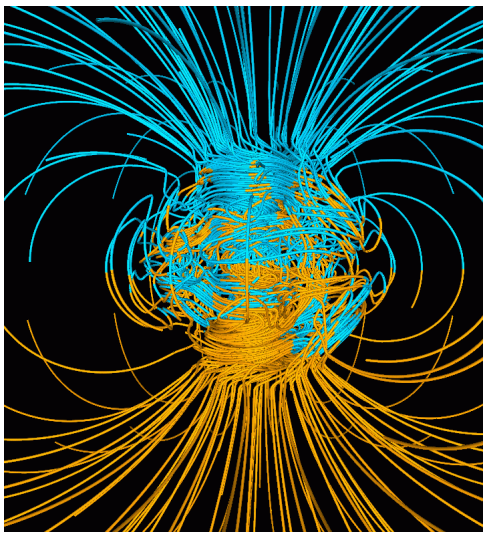

Figure 1.1: Radial component of the magnetic field taken from a simulation of the geodynamo. Image taken from Glatzmaier & Roberts (1995).

1.1.2 Convection in the Earth's core

The radius of the Earth is approximately 6371km. Its interior profile has been inferred from seismic observations and can be seen in Figure 1.2. At the centre of the Earth is a high density metallic core, surrounded by a rocky mantle. The core mantle boundary (CMB) that separates these regions is located approximately 3480km from the centre of the Earth. The core itself is divided into two parts: a solid iron inner core, and a liquid outer core. The liquid outer core is thought to be composed of molten iron, as well as lighter elements such as sulphur and oxygen (see Gubbins & Herrero-Bervera (2007)). The inner core boundary (ICB) that separates these regions is located approximately 1220km from the centre of the Earth. The presence of a solid inner core and a fluid outer core was first detected by Lehmann

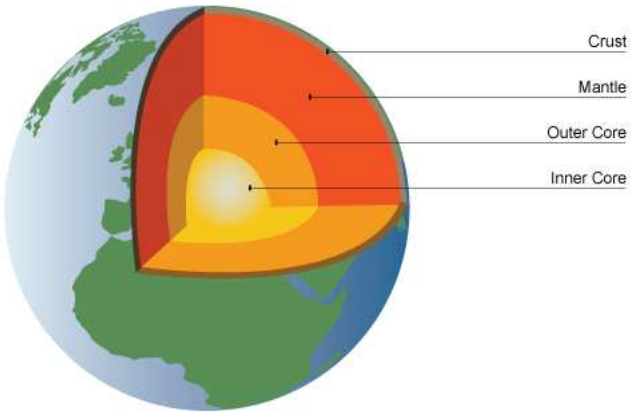

Figure 1.2: The internal structure of the Earth.

(1936). Following an earthquake, seismic waves are produced that travel through the Earth. Hence if there is an earthquake in one location, its presence will be detected elsewhere, as a byproduct of these seismic waves.

It is conjectured that the Earth's magnetic field is generated due to interactions between convective motions in the liquid outer core and the background effect of planetary rotation. For a review of the research into the theory of the geodynamo see Fearn (2007). A natural question is: how do we know that the inner core is convecting? Any electrically conducting fluid possesses an associated resistance that leads to the loss of electromagnetic energy as a current flows through it, due to conversion into heat. This is known as Ohmic dissipation. For a body such as the Earth, this would lead to a complete decay of the magnetic field within approximately 20,000 years (see Moffatt (1978)). This is obviously not the case, since it is known that the Earth has possessed its magnetic field for at least 3.5 billion years (see Jacobs (1987)). Hence something must be mixing the fluid within the outer core, and this is conjectured to be due to convective motions. Convection is believed to be driven due to a temperature difference between the inner and outer core. It should be noted however, that compositional, as well as thermal convection, could be occurring. This is conjectured to be due to lighter elements, being released from the inner core and rising due to buoyancy. A review of thermal

and compositional convection in the Earth's core is given by Jones (2007).

The features that define convection in the Earth's core are its spherical geometry and the fact that it is rotating about its axis. Analytically, convection in spherical geometry is difficult to study, especially because of problems arising due to the presence of the inner core. Matters can be simplified by considering full sphere geometry (see Roberts (1968), Soward (1977) and Jones *et al.* (2000)). However it has been shown by Hollerbach & Jones (1993a)/Hollerbach & Jones (1993b) that this leads to a discrepancy in the magnetic field that is generated, so spherical shell geometry is preferred. Analytic work is possible (see Busse & Cuong (1977)), especially in the limit of rapid rotation, although numerical simulations are the preferred method of study (see Zhang (1992), Dormy (1997), Tilgner & Busse (1997), Christensen (2002) and Dormy *et al.* (2004)). The rapid rotation of the Earth has a profound effect on the appearance of the convection and can be explained by the Taylor- Proudman theorem. This asserts that motion is uniform in the same direction of the axis of rotation (see Taylor (1917), Taylor (1922) and Proudman (1916)). This leads to so-called *Taylor columns*, an example of which can be witnessed in Figure 1.3. In order to take advantage of this behaviour, convection can be studied under what is known as the *quasi-geostrophic approximation*, as considered by Gillet & Jones (2006). They study the system in cylindrical geometry, independent of the vertical coordinate, since this is the flow structure that is predicted by the Taylor-Proudman theorem. This is valid outside an imaginary region that is known as the tangent cylinder: the cylinder with radius coinciding with that of the Earth's inner core.

1.1.3 Convection in the Sun

The radius of the Sun is approximately 695,500km and its interior is separated into four regions that are distinct in terms of the physical processes occurring, as can be seen in Figure 1.4. The interior profile of the Sun is known from Helioseismology

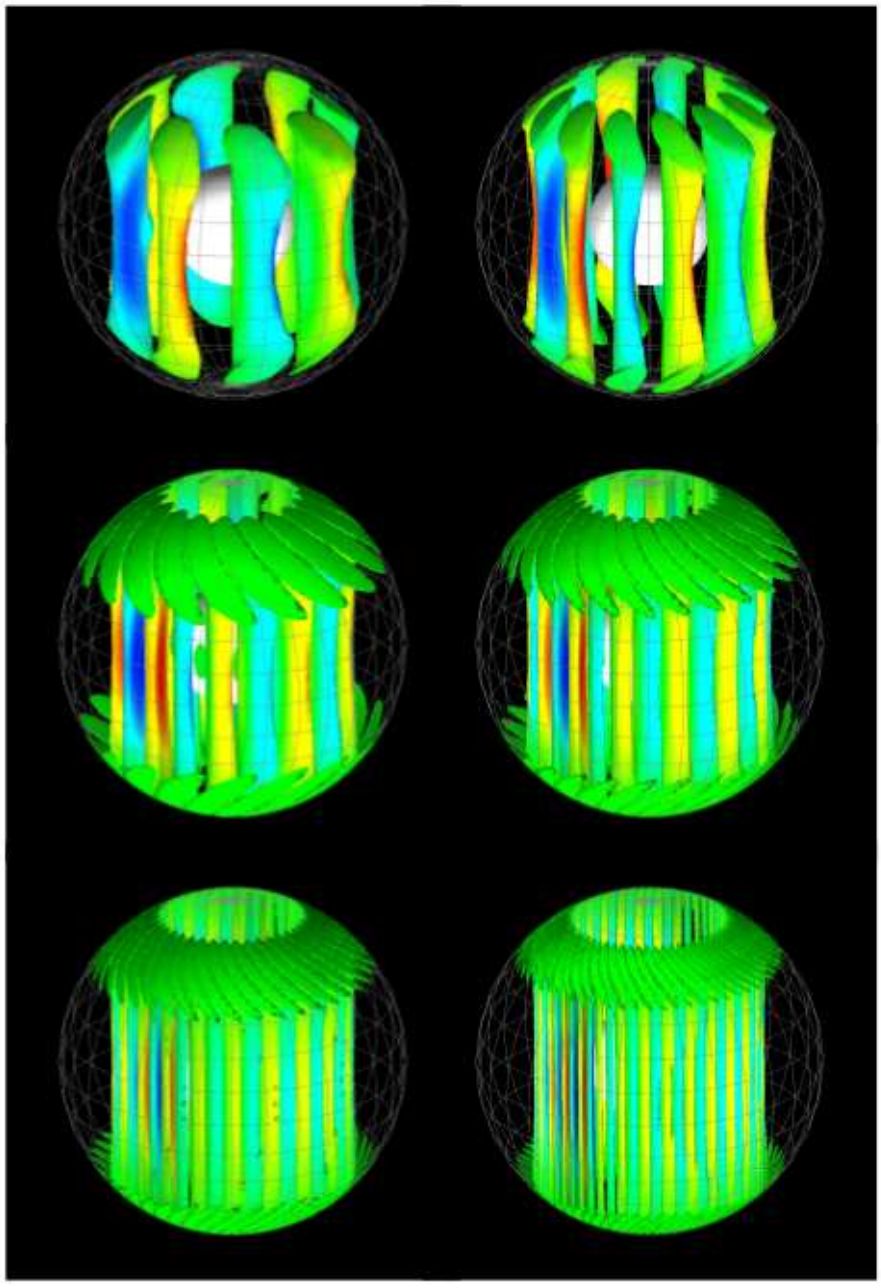

Figure 1.3: Contours of the axial vorticity, coloured according to the temperature, from numerical simulations of rotating, spherical shell convection, for Taylor number increasing from 10^7 to 10^{12} (left to right, top to bottom). Image taken from Dormy (1997).

(see Christensen-Dalsgaard (1988)). Like the Earth, seismic waves are present inside the Sun that cause it to oscillate. Based on the travel times of these waves, it is possible to infer the interior profile of the Sun. At the very centre of the Sun is the core, with a radius of approximately 25% that of the solar radius. Here, hydrogen nuclei collide and form helium, in a process known as nuclear fusion. As a byproduct of this process, an enormous amount of energy is released. Outside of the core this energy is transported by radiation, in what is known as the radiative zone. This extends from the edge of the core to approximately 70% of the solar radius. The final 30%, extending to the very surface of the Sun is where convection takes place,

known as the convective zone. Between the radiative zone and the convective zone is an extremely thin layer know as the tachocline, and it is conjectured that this could be the location in which the Sun's magnetic field is generated (see Hughes *et al.* (2007)). Fluid motions in the convective zone rapidly carry heat from the boundary of the radiative zone to the solar surface. Fluid expands and cools as it rises, and these convective motions are visible at the solar surface in the form of *granules* and *supergranules*. These are the signature of convection cells on the solar surface and are approximately 1000km and 35,000km in diameter respectively. Furthermore, these flow features hold important consequences for the transport of magnetic flux from the tachocline to the solar surface (see Tobias *et al.* (2001)).

Unlike in the case of the Earth, the Sun's rotation does not dominate the dynamics of the system, meaning that we do not expect the tall thin columnar flow structures that are present in the Earth. Whilst some work has been conducted in spherical shell geometry (see Gilman (1977), Gilman (1978a) and Gilman (1978b)), there is a general preference for simplified planar geometry. Because there is no vertical constraint on the flow, and since the radius of the Sun far exceeds that of the Earth, convection is often studied in a three-dimensional plane that is tangential to the surface of a sphere. The local effect of rotation is taken into consideration through the governing equations and these models attempt to recreate the solar surface features that we have already described (see Brummell *et al.* (1996) and Brummell

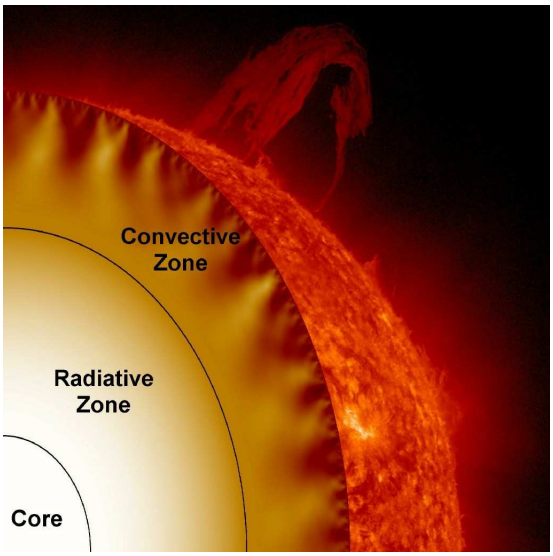

Figure 1.4: The internal structure of the Sun. Image taken from NASA.

et al. (1998)). An example of a numerically simulated patch of solar surface can be seen in Figure 1.5.

1.2 Rayleigh-Bénard convection

Rayleigh-Bénard convection is the original and definitive convective fluid system. Its geometry is very simple; that of a fluid layer, and the basic state is also very simple; the lower boundary is maintained at a higher temperature than the upper boundary, and the fluid is at rest. Yet this basic system provides such a bounty of fascinating fluid behaviour and interesting mathematical analysis that it is studied more intensely today than in its inception over a century ago. Moreover, the basic dynamics are encapsulated within the much more complex geophysical and astrophysical systems that we have described.

Rayleigh-Bénard convection owes its title to the pioneering scientists who first studied it experimentally and analytically. The original experiments on a layer of fluid heated from below were conducted by Bénard (1900) (see also Bénard (1901)).

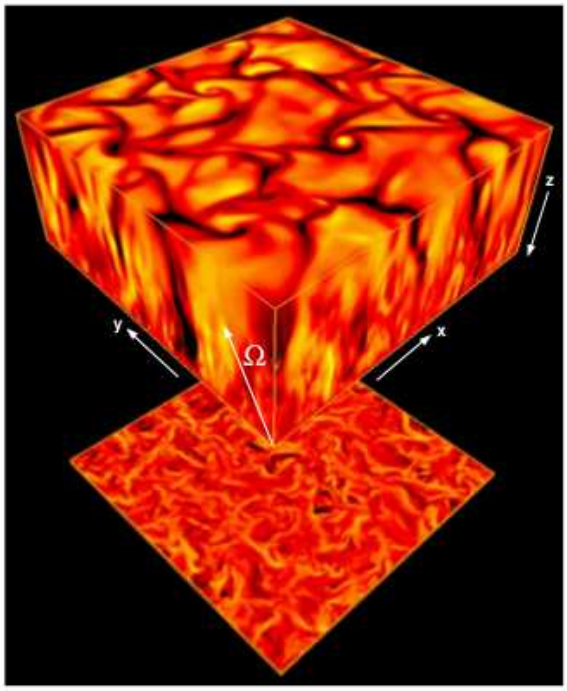

Figure 1.5: Vertical velocity from a three-dimensional compressible convection simulation, with dark shades representing downflows and light shades representing upflows. Image taken from Brummell *et al.* (1996).

A photograph from one of these experiments can be seen in Figure 1.6. Subsequently Rayleigh (1916) performed a mathematical analysis of the very same system in order to try and qualitatively reproduce the results of Bénard (1900). This work provided the stimulus for countless other studies of convection in the past century; analytical, numerical and experimental. As techniques and technology have improved, so has the insight gained into this ubiquitous fluid instability. We shall now outline the evolution of Rayleigh-Bénard convection since its original study by Bénard (1900), highlighting some of the seminal investigations into its dynamics.

1.2.1 Theory

Much analytical work has been conducted on the dynamics of Rayleigh-Bénard convection, in many different capacities, straddling the very breadth of applied

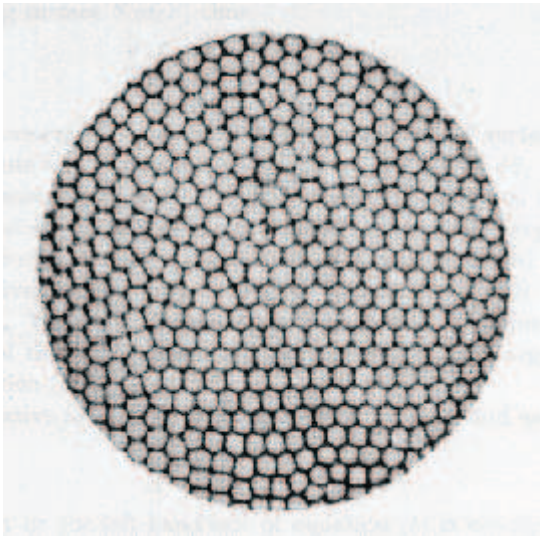

Figure 1.6: A definitive photograph taken by Bénard (1900), from one of his pioneering convection experiments, showing the pattern within a fluid layer heated from below.

mathematics. The theory outlined by Rayleigh (1916) in order to explain the observations of Bénard (1900) was for the idealised case of two free boundaries, whereas the original experiment had a rigid lower boundary and a free upper boundary. This linear stability theory predicted the value of the Rayleigh number at which convection would onset, for a given horizontal wavenumber. Further work was conducted, building upon the work of Rayleigh (1916), by Jeffreys (1926), Jeffreys (1928) and Pellow & Southwell (1940), who derived results for general boundary conditions. An astounding treatise comprising all this work was collated and presented in an altogether clearer manner by Chandrasekhar (1961). This is the primary text on the linear theory of Rayleigh-Bénard convection that is still consulted today. It encompasses all aspects of plane layer convection and includes a number of other physical effects, such as rotation, magnetic field and the composite effect of both.

The linear theory of Rayleigh-Bénard convection gives the critical value of the Rayleigh number at which convection onsets. Since the analysis is conducted in terms of normal modes, this theory predicts either exponential growth or decay, and

gives no further insight into the dynamics after the system has become unstable. Building on these foundations that were laid in the first half of the 20th century, focus then turned to the introduction of nonlinearity within the system. Malkus & Veronis (1958) conducted a nonlinear analysis of the stability of the system to finite amplitude perturbations. This allowed them to determine under what circumstances the system reaches a thermal equilibrium. Furthermore they were able to make predictions about the ratio of the convective to conductive heat flux transported through the layer: the Nusselt number. This is an important output parameter of nonlinear convection studies, and facilitates comparison with experimental data. This work was modified to include the effect of rotation by Veronis (1959).

An incredible body of analytical work encompassing all aspects of Rayleigh-Bénard convection was conducted, and—a portion of it—is summarised by, Busse (1978). Boundless are his contributions to this area of research; his work exploring both rotating and non-rotating convection, with and without magnetic fields. Moreover, he made vital contributions to both the existing linear theory of Rayleigh-Bénard convection, as well as exploring new avenues in the nonlinear regime: both analytically and numerically. For a range of boundary conditions, under varying theoretical assumptions, he analysed the stability of the system, discovering a range of new instability mechanisms.

Building on the nonlinear, finite amplitude instability of Rayleigh-Bénard convection, Lorenz (1963) derived his celebrated system of equations, attempting to model weather in the atmosphere. The Lorenz equations are the manifestation of a three mode truncation of the equations governing two dimensional convection, when expanded in a double Fourier series. Lorenz (1963) showed that these deterministic equations give rise to chaotic solutions for differing values of the initial conditions and governing parameters. Furthermore this provided a significant catalyst for the area of research now termed Chaos theory, and has since been applied to problems from a wide spectrum of subjects. These include geometry, biology, chemistry, engineering, computer science, information theory and a whole range of others. For

a detailed study of the Lorenz system, one should consult Sparrow (1982). Related to the work of Lorenz (1963), within the realm of nonlinear dynamics, Rayleigh-Bénard convection is one of the canonical systems in which complex spatio-temporal patterns are formed. The Swift-Hohenberg equation (see Swift & Hohenberg (1977)) was originally derived from the equations governing Rayleigh-Bénard convection, but is now widely used to study pattern formation in its generality. For an overview of pattern forming systems, including ones arising in Rayleigh-Bénard convection, one should consult Hoyle (2006).

The final analytical area in which Rayleigh-Bénard is studied, that we wish to mention, is related to the general theory of the existence and uniqueness of the Navier-Stokes equations. Using variational methods and energy arguments, a common aim is to try and derive rigorous upper bounds on the Nusselt number. This is a relevant quantity in Rayleigh-Bénard convection, and as we have seen, has direct applications to convection in geophysical and astrophysical bodies, such as the Earth. Developed by Malkus (1954b) in order to try and explain the findings from his physical experiments, work is constantly evolving, developing new bounds (see Doering & Constantin (1996), Kerswell (2000), Doering *et al.* (2006) and Whitehead & Doering (2011)). Although guided by numerical and physical experimental data, this work is entirely analytical, considering different global energy balances within the governing equations.

1.2.2 Experiments

Whilst analytical theory is very well-adept at providing insight into the linear, or weakly nonlinear, instability of the system, in nature many convective systems are highly supercritical. As such, it is relevant to study Rayleigh-Bénard convection for large thermal driving, as measured by the Rayleigh number, and experiments provide a means for doing this. Analytical theory is not confined to a particular geometry, since the choice is arbitrary, however experiments are ultimately three-dimensional.

After the initial experiments on Rayleigh-Bénard convection conducted by Bénard (1900)/Bénard (1901), and the subsequent development in theory by Rayleigh (1916) there were several attempts to not only repeat these experiments, but confirm that the theory was correct. Schmidt & Milverton (1935) undertook this, and although the nonlinear system they modelled experimentally differed from the linear theory of Rayleigh (1916) in terms of the heat transport, the actual point of onset of instability was confirmed. Malkus (1954a) corroborated these findings, establishing a comprehensive suite of numerical results for Rayleigh numbers up to 10^{10}. He made predictions about the Nusselt number scaling and the nature of the convective turbulence. Furthermore, as we have already mentioned, this was supplemented with an analytical theory to explain these observations (see Malkus (1954b)). In conjunction with this, Kraichnan (1962) developed a theory in order to explain the results of many of the experiments that had taken place. He attempted to derive different laws for the heat transport in the turbulent convective system, as a function of the Rayleigh number and Prandtl number. Rossby (1969) extended the experimental techniques of others in order to incorporate the effect of rotation within the system. Furthermore, he was able to capture detailed photographs of some of the flows that were observed, one of which can be seen in Figure 1.7.

It should be noted that a lot of these early experiments into Rayleigh-Bénard convection were conducted in very shallow layers of fluid. Since convection is an inherently vertical process, in order to visualise the types of flow structures one might expect, and really probe the dynamics of the system, experiments in much deeper layers are necessary. With improvements in experimental techniques, and technological advances, this was made possible towards the end of the 20th century. In a layer nearly ten times as deep Castaing *et al.* (1989) studied Rayleigh-Bénard convection at higher Rayleigh numbers than Malkus (1954a), observing consistent scaling of the heat transport with the Rayleigh number. Furthermore, Zocchi *et al.* (1990) analysed the dominant flow structures occurring in their convection experiments in some detail. These included boundary layer waves, thermal plumes

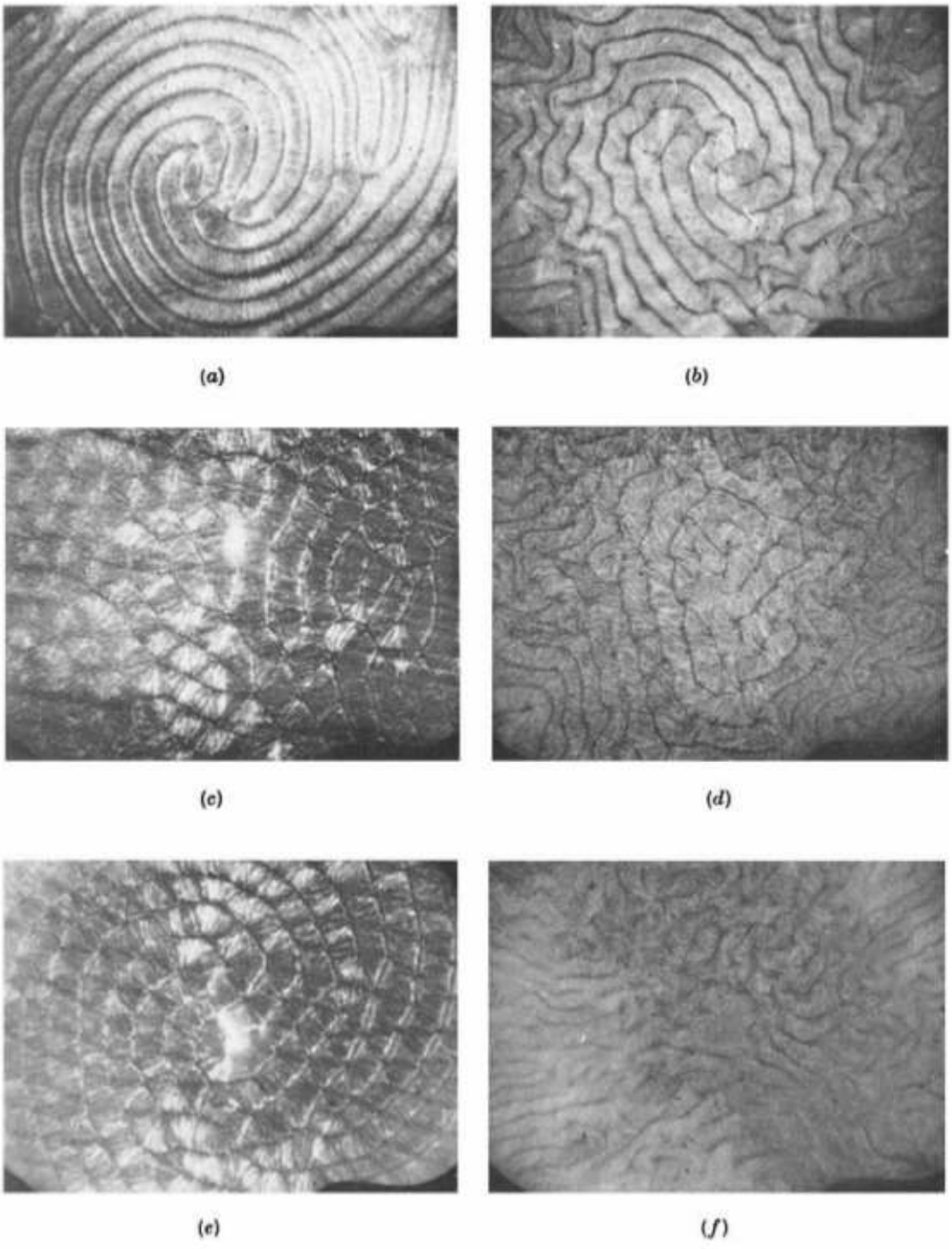

Figure 1.7: Vertical view of convection for different values of the Rayleigh number and Taylor number. Image taken from Rossby (1969).

and swirling spirals of fluid motion. The work was extended to include the effects of rotation by Liu & Ecke (1997). Their study was much more comprehensive than, for example, that of Rossby (1969), reaching much higher Rayleigh and Taylor numbers, in a much deeper layer.

The most current experiments on Rayleigh-Bénard convection are almost exclusively performed in order to develop scaling laws governing the Nusselt number and the Reynolds number. Furthermore, with theoretical predictions of such quantities being readily available, as we have discussed, there are many competing hypotheses. Grossman & Lohse (2000) developed a theory in order to try and corroborate all the different experimental results. They postulate that there exist different regimes, where the Nusselt number scales differently, according to the values of the Rayleigh number and the Prandtl number. Moreover, since the majority of the convective systems that are found in nature are influenced by rotation, advances in technology mean that nearly all modern experiments on Rayleigh-Bénard convection incorporate this. Notable examples include the work of King *et al.* (2009), King *et al.* (2012) and Liu & Ecke (2009).

1.2.3 Numerical simulations

Straddling the boundary between linear and weakly nonlinear theory and experiments are numerical simulations. Furthermore, they can be applied to a range of geometries and scenarios not easily realisable in physical experiments.

Building on his own weakly nonlinear theory Veronis (1966) devised a numerical algorithm in order to extend his predictions about two-dimensional Rayleigh-Bénard convection deeper into the nonlinear regime. The maximum Rayleigh number that he was able to reach was orders of magnitudes below the physical experiments of that time. He observed only steady state behaviour in this limited Rayleigh number regime. This differs from experiments in the fact that they are inherently turbulent. He was able, however, to observe how the initial convective instability saturated, in

a nonlinear manner. Furthermore his predictions for the Nusselt number were in line with physical experiments. Veronis (1968) extended this work to incorporate the effect of rotation into the system, using a largely similar numerical method. Despite noticing some similarities with the experimental work of Rossby (1969), it was pointed out that a lot of the differences were due to the fact that two-dimensional geometry is somewhat restrictive.

Moore & Weiss (1973) extended the work of Veronis (1966), studying non-rotating, two-dimensional Rayleigh-Bénard convection for a much more comprehensive range of Rayleigh and Prandtl numbers. Despite using different numerical methods, the results from these two studies agreed at coinciding parameter values. Moore & Weiss (1973) observed nonlinear, time-dependent instability, specifically motion that was periodic in time. This behaviour was identical to that noticed by Krishnamurti (1970a)/Krishnamurti (1970b) in convection experiments. Furthermore, they were able to give a simple physical explanation of this instability and relate it to the theoretical work of Welander (1967). They observed a Nusselt number scaling that corroborated both the theory of Kraichnan (1962) and the experimental results of Malkus (1954a). This work stood as a prime reference on two-dimensional Rayleigh-Bénard convection for the remainder of the 20th century, due to the detail in which it was studied for such a range of parameters.

The subsequent evolution of numerical simulations into two-dimensional Rayleigh-Bénard convection was largely governed by the progress made in computing hardware. The numerical methods developed in the mid-20th century were limited by the numerical resolution that was able to be implemented on a given computer architecture, the actual mathematics that they were conceived from did not change. With the rapid development of fast, efficient computing resources in the late 20th century, numerical algorithms were able to progress too. Notably DeLuca *et al.* (1990) performed high Rayleigh number simulations of non-rotating convection, observing new scalings of the Nusselt number, in what was termed the hard turbulence regime. These scalings had been predicted on theoretical grounds, and

in physical experiments previously (see Zocchi *et al.* (1990)). With this success, by the time the authors came to apply their numerical method to that of rotating convection, advances in technology had developed so rapidly that they were able to implement a three-dimensional study (see Julien *et al.* (1996b)/Julien *et al.* (1996a)). Despite this, Vincent & Yuen (1999)/Vincent & Yuen (2000) used similar numerical techniques to achieve what are the highest—that we are aware of—Rayleigh number numerical simulations of nonlinear two-dimensional Rayleigh-Bénard convection to-date. They observed a whole regime of different behaviour that had not been predicted on theoretical grounds. The behaviour was so turbulent that existing theories relying on large scale energy balances were not valid, since the flow had begun to develop on a much shorter length scale.

It is with the exponential growth in the advancement of modern computing technology that three-dimensional Rayleigh-Bénard convection has become a more favourable problem to simulate numerically, and for that matter, theoretically. It is not the case that everything is known about the two-dimensional system; there is still a wealth of insight to be gleaned. Something we shall endeavour to do here.

1.3 Thesis outline

It remains to outline the structure of the work that this thesis comprises. In Chapter 2 we present the governing hydrodynamic equations and rearrange them into various useful forms that we shall use later in this work. Furthermore some important consequences of these equations shall be noted. In Chapter 3 we review the linear stability theory of Chandrasekhar (1961), which is included for completeness. In Chapter 4 we develop an algorithm in order to perform numerical simulations of the nonlinear equations, so that we can further probe the dynamics of the system. In Chapter 5 we present the findings of our numerical results for both rotating and non-rotating Rayleigh-Bénard convection, drawing comparisons with all the literature that we have mentioned. In Chapter 6 we present an asymptotic theory designed to

address a particular phenomenon that we observe in the numerical results of Chapter 5. In Chapter 7 we summarise all our findings, relating them to the work of the wider geophysical and astrophysical research community. Furthermore, we indicate potential areas of development that could be undertaken to extend our insight into the dynamics of two-dimensional Rayleigh-Bénard convection.

Chapter 2

The equations governing rotating convection

The equations governing rotating Rayleigh-Bénard convection have been derived in significant detail by Chandrasekhar (1961), therefore we shall not repeat this here. We shall, however, explain their origins, which lie in the conservation of mass, momentum and energy. We shall present the equations in the most general of circumstances, before specifying the exact problem that we wish to study mathematically. For the specific basic state that we consider, equations will be derived governing perturbations to this state. This involves expressing the equations in dimensionless form, introducing several important parameters that govern the dynamics of the system. We shall manipulate these equations into several useful forms that will play a part within the analysis of subsequent chapters. Furthermore, some important results stemming from the governing hydrodynamic equations shall be presented, such as the Taylor-Proudman theorem.

2.1 Mathematical statement

2.1.1 Continuity equation

For a fixed volume V, the total mass within the volume is given by the integral of the density $\rho \equiv \rho(\mathbf{x}, t)$, which itself may be a function of both position and time

$$\int_V \rho \, \mathrm{d}V \tag{2.1}$$

where $\mathrm{d}V = \mathrm{d}x \, \mathrm{d}y \, \mathrm{d}z$ is a volume element. The only way the mass within V can change in time is via fluid flowing in and out across its surface S. If $\mathrm{d}S$ is a surface element of S, with associated outward-pointing, unit normal vector $\hat{\mathbf{n}}$, then the rate of change of mass—in time—is given by

$$\frac{\mathrm{d}}{\mathrm{d}t} \int_V \rho \mathrm{d}V = - \int_S \rho \mathbf{U} \cdot \hat{\mathbf{n}} \mathrm{d}S, \tag{2.2}$$

where $\mathbf{U} \equiv \mathbf{U}(\mathbf{x}, t)$ is the fluid velocity. Since the volume V is fixed in space, and does not depend on time, we may differentiate inside the integral. Furthermore, using the divergence theorem, we may turn the surface integral on the right-hand side into a volume integral, giving

$$\int_V \left(\frac{\partial \rho}{\partial t} + \nabla \cdot (\rho \mathbf{U}) \right) \mathrm{d}V = 0. \tag{2.3}$$

Since this must hold for any arbitrary volume V, we must have that

$$\frac{\partial \rho}{\partial t} + \nabla \cdot (\rho \mathbf{U}) = 0. \tag{2.4}$$

This is the general expression for the continuity of mass. For a fluid with constant density, this reduces to

$$\nabla \cdot \mathbf{U} = 0, \tag{2.5}$$

stating that the fluid velocity is solenoidal, or *incompressible*.

2.1.2 Momentum equation

The *Navier-Stokes equations* are a mathematical expression of Newton's Second law of motion, in the context of fluid dynamics. They state that the product of the density and fluid acceleration are equal to the net force per unit volume on a fluid parcel as it moves within a flow. Derived by Chandrasekhar (1961), the momentum equation is given by

$$\rho\frac{\partial \mathbf{U}}{\partial t} + \rho(\mathbf{U}\cdot\nabla)\mathbf{U} = \mathbf{f} + \nabla\cdot\boldsymbol{\sigma}, \tag{2.6}$$

where ρ and $\mathbf{U}$ are the fluid density and velocity respectively that we have already introduced. Here $\mathbf{f}$ is the macroscopic, or body, forcing that is exerted on a particular fluid parcel and $\boldsymbol{\sigma}$ accounts for microscopic stresses internal to the fluid. Written in tensor notation, we have

$$\rho\frac{\partial U_i}{\partial t} + \rho U_j\frac{\partial U_i}{\partial x_j} = f_i + \frac{\partial \sigma_{ij}}{\partial x_j}, \tag{2.7}$$

for $i = 1, 2, 3$, where the stress tensor σ_{ij} represents the i'th component of stress, on a given surface element, that has unit normal pointing in the j-direction. For all the work considered here, we shall assume that the fluid is *Newtonian*, in that the viscous stress is proportional to the rate of strain of the fluid. Mathematically this is written

$$\sigma_{ij} = -P\delta_{ij} + \mu\left(\frac{\partial U_i}{\partial x_j} + \frac{\partial U_j}{\partial x_i} - \frac{2}{3}\frac{\partial U_k}{\partial x_k}\delta_{ij}\right). \tag{2.8}$$

The term containing P is isotropic (its magnitude is independent of direction) and the remaining terms are anisotropic, representing the microscopic effects of viscous forces acting on a fluid parcel. Here μ is the dynamic viscosity, and in general does not have to be constant, although for our purposes we shall assume that it is.

In the absence of any body forcing other than that of gravity-induced buoyancy—causing less dense fluid to rise and denser fluid to sink—the form of our external force term is thus

$$f_i = \rho g_i, \tag{2.9}$$

where $\mathbf{g}$ is the gravity vector. Inserting equations (2.8) and (2.9) into equation (2.7) gives, in vector notation

$$\rho\frac{\partial \mathbf{U}}{\partial t} + \rho(\mathbf{U}\cdot\nabla)\mathbf{U} = -\nabla P + \rho\mathbf{g} + \mu\left(\nabla^2\mathbf{U} + \frac{1}{3}\nabla\left(\nabla\cdot\mathbf{U}\right)\right). \tag{2.10}$$

2.1.3 Temperature equation

The first law of thermodynamics states that energy is conserved; it may be converted from one form to another, e.g. work to heat, but not created or destroyed. For a detailed derivation see Chandrasekhar (1961), who presents the equations of heat conduction as

$$\rho\frac{\partial}{\partial t}(c_v T) + \rho(\mathbf{U}\cdot\nabla)(c_v T) = \nabla\cdot(k\nabla T) - P(\nabla\cdot\mathbf{U}) + \Phi \tag{2.11}$$

where ρ, $\mathbf{U}$, and P are the already-introduced fluid density, velocity and pressure. Here T is the temperature, c_v the specific heat at constant volume—the amount of heat energy required to increase the temperature of a fixed fluid parcel by a given amount—and k is the thermal conductivity. We shall assume that both of these quantities are constant throughout the fluid. Φ represents the heating from the microscopic effect of viscous dissipation and is written in terms of the fluid velocity (see Chandrasekhar (1961))

$$\Phi = \frac{\mu}{2}\left(\frac{\partial U_i}{\partial x_j} + \frac{\partial U_j}{\partial x_i}\right)^2 - \frac{2}{3}\mu\left(\frac{\partial U_k}{\partial x_k}\right)^2. \tag{2.12}$$

2.2 The Boussinesq approximation

In order to simplify the equations that we have just presented, we use an important result due to Boussinesq (1903) (see Spiegel & Veronis (1960), Chandrasekhar (1961)). The *Boussinesq approximation* comprises the following assumptions: firstly, it assumes that the depth of the fluid layer is small relative to the hydrostatic scale heights of pressure, temperature and density. Thus it can be considered that the

Boussinesq approximation assumes that the domain we are studying is, in this sense, shallow. Secondly, it assumes that density fluctuations are thermal in origin, rather than being driven by the pressure. Analogous to the anelastic liquid approximation (see Gough (1969)), the Boussinesq approximation assumes that the flow speed is much less than the speed of sound; here considered infinite. With this result, we proceed by assuming that the density is constant in all terms except the buoyancy force term in the momentum equation. We must retain a fluctuating density here in order to account for hot fluid rising due to thermal expansion and sinking due to gravity. We shall denote the constant density by ρ_0. Setting $\rho = \rho_0$ in equation (2.4) gives

$$\nabla \cdot \mathbf{U} = 0, \tag{2.13}$$

hence the fluid is incompressible. This has implications within the other hydrodynamic equations. The momentum equation reads

$$\frac{\partial \mathbf{U}}{\partial t} + (\mathbf{U} \cdot \nabla)\mathbf{U} = -\frac{1}{\rho_0}\nabla P + \frac{\rho}{\rho_0}\mathbf{g} + \nu \nabla^2 \mathbf{U}, \tag{2.14}$$

where $\nu = \frac{\mu}{\rho_0}$ is the *kinematic viscosity*, a constant.

As well as the assumption of incompressibility, within the temperature equation we assume that the effects of viscous dissipation, included via the Φ term, are negligible compared to the conduction of heat (see Chandrasekhar (1961)). Thus the temperature equation reads

$$\frac{\partial T}{\partial t} + (\mathbf{U} \cdot \nabla)T = \kappa \nabla^2 T, \tag{2.15}$$

where $\kappa = \frac{k}{\rho_0 c_v}$ is the coefficient of thermal diffusivity.

Finally, in order to make our equation set closed, we must have an *equation of state* that links the density of the fluid with the temperature. For our purposes this can be written (see Chandrasekhar (1961))

$$\rho = \rho_0 \left(1 - \alpha \left(T - T_0\right)\right), \tag{2.16}$$

where α is the coefficient of thermal expansion and T_0 is the constant temperature at which $\rho = \rho_0$.

2.3 Rotation

Consider a vector $\mathbf{a} = (a_x, a_y, a_z)$ in a Cartesian reference frame, rotating with constant angular velocity $\mathbf{\Omega}$ relative to a fixed, inertial reference frame. We may write $\mathbf{a}$ in the form

$$\mathbf{a} = a_x\hat{\mathbf{x}} + a_y\hat{\mathbf{y}} + a_z\hat{\mathbf{z}}, \tag{2.17}$$

where $\hat{\mathbf{x}}, \hat{\mathbf{y}}$, and $\hat{\mathbf{z}}$ are fixed unit vectors in the rotating frame. The rate of change of $\mathbf{a}$ within this rotating frame is given by

$$\left(\frac{\mathrm{D}\mathbf{a}}{\mathrm{D}t}\right)_R = \frac{\mathrm{D}a_x}{\mathrm{D}t}\hat{\mathbf{x}} + \frac{\mathrm{D}a_y}{\mathrm{D}t}\hat{\mathbf{y}} + \frac{\mathrm{D}a_z}{\mathrm{D}t}\hat{\mathbf{z}}, \tag{2.18}$$

since in the rotating frame, the unit vectors are fixed in length and position. In the inertial frame, the unit vectors $\hat{\mathbf{x}}, \hat{\mathbf{y}}$, and $\hat{\mathbf{z}}$ are not fixed, hence the rate of change of $\mathbf{a}$, in the inertial frame, is given by

$$\left(\frac{\mathrm{D}\mathbf{a}}{\mathrm{D}t}\right)_I = \frac{\mathrm{D}a_x}{\mathrm{D}t}\hat{\mathbf{x}} + \frac{\mathrm{D}a_y}{\mathrm{D}t}\hat{\mathbf{y}} + \frac{\mathrm{D}a_z}{\mathrm{D}t}\hat{\mathbf{z}} \tag{2.19}$$

$$+ a_x\frac{\mathrm{D}\hat{\mathbf{x}}}{\mathrm{D}t} + a_y\frac{\mathrm{D}\hat{\mathbf{y}}}{\mathrm{D}t} + a_z\frac{\mathrm{D}\hat{\mathbf{z}}}{\mathrm{D}t}, \tag{2.20}$$

$$= \left(\frac{\mathrm{D}\mathbf{a}}{\mathrm{D}t}\right)_R + a_x\mathbf{\Omega}\times\hat{\mathbf{x}} + a_y\mathbf{\Omega}\times\hat{\mathbf{y}} + a_z\mathbf{\Omega}\times\hat{\mathbf{z}}, \tag{2.21}$$

$$= \left(\frac{\mathrm{D}\mathbf{a}}{\mathrm{D}t}\right)_R + \mathbf{\Omega}\times\mathbf{a}, \tag{2.22}$$

where we have used the fact that the rate of change of the unit vectors in time, as observed in the inertial frame, is equal to the cross product of the unit vector and the rotation vector (see Acheson (1990)). Now, let the vector $\mathbf{x}$ describe the position of a fluid particle. Applying (2.22) to $\mathbf{x}$ gives

$$\left(\frac{\mathrm{D}\mathbf{x}}{\mathrm{D}t}\right)_I = \left(\frac{\mathrm{D}\mathbf{x}}{\mathrm{D}t}\right)_R + \mathbf{\Omega}\times\mathbf{x}. \tag{2.23}$$

The rate of change of position of a fluid particle is its fluid velocity, hence we have

$$\mathbf{U}_I = \mathbf{U}_R + \mathbf{\Omega}\times\mathbf{x}. \tag{2.24}$$

That is, the fluid velocity in the inertial frame is equal to the fluid velocity in the rotating frame, plus the velocity gained from the solid body rotation $\mathbf{\Omega}\times\mathbf{x}$. In

the Navier Stokes equations, on the left hand side, we have the rate of change of velocity, in an inertial frame. We need to work out what this is in a rotating frame. Applying (2.22) to $\mathbf{U}_I$ gives

$$\left(\frac{\mathrm{D}\mathbf{U}_I}{\mathrm{D}t}\right)_I = \left(\frac{\mathrm{D}\mathbf{U}_I}{\mathrm{D}t}\right)_R + \boldsymbol{\Omega} \times \mathbf{U}_I. \tag{2.25}$$

Using equation (2.24), this gives

$$\left(\frac{\mathrm{D}\mathbf{U}_I}{\mathrm{D}t}\right)_I = \left(\frac{\mathrm{D}}{\mathrm{D}t}(\mathbf{U}_R + \boldsymbol{\Omega} \times \mathbf{x})\right)_R + \boldsymbol{\Omega} \times (\mathbf{U}_R + \boldsymbol{\Omega} \times \mathbf{x}), \tag{2.26}$$

$$= \left(\frac{\mathrm{D}\mathbf{U}_R}{\mathrm{D}t}\right)_R + \boldsymbol{\Omega} \times \left(\frac{\mathrm{D}\mathbf{x}}{\mathrm{D}t}\right)_R + \boldsymbol{\Omega} \times \mathbf{U}_R + \boldsymbol{\Omega} \times (\boldsymbol{\Omega} \times \mathbf{x}). \tag{2.27}$$

Now, the second term on the right-hand side may be re-written making use of equation (2.24), to give

$$\left(\frac{\mathrm{D}\mathbf{U}_I}{\mathrm{D}t}\right)_I = \left(\frac{\mathrm{D}\mathbf{U}_R}{\mathrm{D}t}\right)_R + 2\boldsymbol{\Omega} \times \mathbf{U}_R + \boldsymbol{\Omega} \times (\boldsymbol{\Omega} \times \mathbf{x}), \tag{2.28}$$

$$= \left(\frac{\mathrm{D}\mathbf{U}_R}{\mathrm{D}t}\right)_R + 2\boldsymbol{\Omega} \times \mathbf{U}_R - \frac{1}{2}\nabla\left(|\boldsymbol{\Omega} \times \mathbf{x}|^2\right), \tag{2.29}$$

where we have re-written the final term in a more useful form. Hence the rate of change of velocity in the inertial frame is equal to the rate of change of the velocity in the rotating frame, plus the effects of two other terms on the right hand side. The first term is known as the *Coriolis acceleration*. It is oriented perpendicular to both the direction of rotation and fluid velocity in the rotating frame, and is proportional to the magnitude of the velocity in the rotating frame. Hence for a clockwise rotation vector, a fluid particle moving in a straight line in the rotating frame will appear to be deflected to the left, when viewed in the inertial frame. The second term is known as the *centrifugal force*. It is oriented away from the axis of rotation and is proportional to the distance of a fluid particle from the axis of rotation. Hence a fluid particle circling the axis of rotation in the rotating frame will be pushed outwards, when viewed in the inertial frame.

Re-writing the momentum equation with these additional terms, and dropping the subscript $_R$, we have

$$\frac{\partial \mathbf{U}}{\partial t} + (\mathbf{U} \cdot \nabla)\mathbf{U} = -\frac{1}{\rho_0}\nabla P_{\text{total}} + \frac{\rho}{\rho_0}\mathbf{g} - 2\boldsymbol{\Omega} \times \mathbf{U} + \nu\nabla^2\mathbf{U}, \tag{2.30}$$

where we have absorbed the centrifugal force into the pressure gradient term, hence the pressure can be thought of as a modified pressure, given by

$$P_{\text{total}} \equiv P - \frac{\rho_0}{2}|\boldsymbol{\Omega} \times \mathbf{x}|^2. \tag{2.31}$$

Note that the effects of rotation do not alter the Boussinesq approximation, and so its validity is still justified. Furthermore, the other hydrodynamic equations remain unaltered under these conditions.

2.4 Mathematical formulation

We consider a two-dimensional layer of fluid with depth d and horizontal extent L. The lower boundary is maintained at a higher temperature than the upper boundary, providing a temperature difference—the driving force of convection—of ΔT across the layer. The side walls, located at $x = 0$ and $x = L$, are thermally insulating. Gravity is taken to act in the negative z direction ($\mathbf{g} = -g\hat{\mathbf{z}}$), whilst the axis of rotation is aligned with the z axis ($\boldsymbol{\Omega} = \Omega\hat{\mathbf{z}}$). This geometry can be seen in Figure 2.1. In our two-dimensional setup, we only allow quantities to be functions of x, z and t: the horizontal and vertical coordinates respectively. Whilst we do not allow any quantities to be a function of y, we do permit flows in the y-direction. This is necessary since we have aligned the rotation axis with the z-axis and so the term $2\boldsymbol{\Omega} \times \mathbf{U}$ in equation (2.30) will have a component in the y-direction, thus driving a flow in that direction.

2.4.1 Boundary conditions

To accompany the governing hydrodynamic equations, we must enforce a set of boundary conditions on the fluid velocity and temperature at the upper and lower surfaces. Convection is driven via an imposed temperature difference, ΔT, across

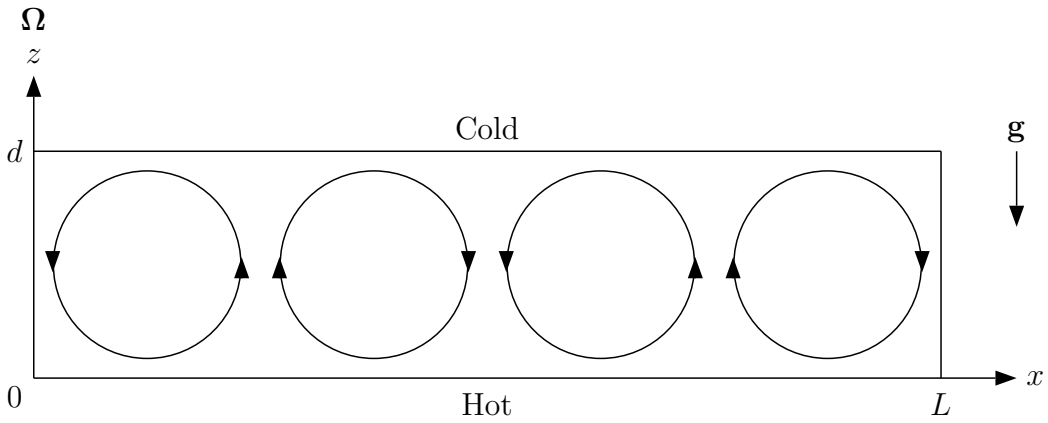

Figure 2.1: Physical setup of the problem: schematic of a convective layer.

the fluid layer. The temperature satisfies the following boundary conditions

$$T = T_0 + \Delta T \quad \text{at} \quad z = 0, \tag{2.32}$$

$$T = T_0 \quad \text{at} \quad z = d. \tag{2.33}$$

The boundary conditions on the fluid velocity depend on the nature of the bounding surface, and so we distinguish between *stress free* and *no slip* boundary conditions. In either case, no fluid may cross perpendicular to the boundary, so we have the following impermeability condition condition

$$\mathbf{U} \cdot \hat{\mathbf{n}} = W = 0 \quad \text{on any horizontal boundary.} \tag{2.34}$$

Throughout this work we shall utilise the same boundary condition at both bounding surfaces, i.e. both stress free, or both no slip.

Stress free

The stress free, or free slip, boundary condition is so named because it requires that the tangential stress must vanish at the boundary. This allows the fluid travelling in a direction tangential to the boundary, to move freely along it. From equation (2.8), equating the tangential components of the stress tensor, σ_{ij}, to zero, gives us

the following

$$\sigma_{xz} = \mu\left(\frac{\partial U}{\partial z} + \frac{\partial W}{\partial x}\right) = 0, \tag{2.35}$$

$$\sigma_{yz} = \mu\left(\frac{\partial V}{\partial z} + \frac{\partial W}{\partial y}\right) = 0. \tag{2.36}$$

Since $W = 0$ on either boundary, for any x, there is no change in W as we go along the boundary in the x direction. Hence the derivative of W with respect to x vanishes, and we have the boundary conditions

$$\frac{\partial U}{\partial z} = 0, \tag{2.37}$$

$$\frac{\partial V}{\partial z} = 0. \tag{2.38}$$

Now, if we differentiate the continuity equation with respect to z, and apply the above boundary condition, we have

$$\frac{\partial}{\partial z}\nabla \cdot \mathbf{U} = \frac{\partial^2 U}{\partial x \partial z} + \frac{\partial^2 V}{\partial y \partial z} + \frac{\partial^2 W}{\partial z^2} = 0 \Rightarrow \frac{\partial^2 W}{\partial z^2} = 0. \tag{2.39}$$

The z component of the vorticity is given by

$$\zeta = \frac{\partial V}{\partial x} - \frac{\partial U}{\partial y} = \frac{\partial V}{\partial x}. \tag{2.40}$$

If we differentiate this with respect to z we have

$$\frac{\partial \zeta}{\partial z} = \frac{\partial^2 V}{\partial x \partial z}, \tag{2.41}$$

hence, by the above boundary condition on V, we have

$$\frac{\partial \zeta}{\partial z} = 0. \tag{2.42}$$

No slip

The no slip boundary condition is so named because it requires that fluid not be allowed to pass along the boundary, meaning that all components of the velocity must vanish

$$\mathbf{U} = (U, V, W) = 0. \tag{2.43}$$

Since $\mathbf{U} = 0$ on either boundary, for any x, there is no change in $\mathbf{U}$ as we go along the boundary in the x direction. Hence the derivative of $\mathbf{U}$ with respect to x vanishes. The continuity equation gives

$$\nabla \cdot \mathbf{U} = \frac{\partial U}{\partial x} + \frac{\partial V}{\partial y} + \frac{\partial W}{\partial z} = 0 \;\Rightarrow\; \frac{\partial W}{\partial z} = 0. \tag{2.44}$$

The z component of the vorticity is given by equation (2.40). Since $V = 0$ everywhere on the boundary, its derivative with respect to x must also vanish, giving us a boundary condition on the normal component of the vorticity

$$\zeta = 0. \tag{2.45}$$

2.4.2 Basic state

Motivated by the mathematical description of the problem we must construct a solution that satisfies the governing hydrodynamic equations, known as a *basic state*. We then perturb this basic state and study its stability to such perturbations. It is conventional to assume that the basic state is steady—does not depend on time—and that the fluid is at rest—no fluid velocity. Furthermore we assume that the temperature is a function of the vertical coordinate only. We shall denote the basic state variables with a subscript B. With no fluid velocity we have $\mathbf{U_B} = \mathbf{0}$ and so the continuity equation is trivially satisfied. The x and y components of the momentum equation tell us that the basic state pressure is a function of z only. The z component of the momentum equation and the temperature equation yield, respectively

$$\frac{\mathrm{d}P_B}{\mathrm{d}z} = -g\rho_B, \tag{2.46}$$

$$\frac{\mathrm{d}^2 T_B}{\mathrm{d}z^2} = 0. \tag{2.47}$$

The first equation is an expression of hydrostatic equilibrium: the balance of pressure gradients and gravity. The temperature equation admits a solution of the form

$$T_B \equiv T_B(z) = C_1 z + C_0, \tag{2.48}$$

where the constants C_0 and C_1 are determined by application of the boundary conditions (2.32) and (2.33). Applying these boundary conditions gives the expression for the basic state temperature as

$$T_B(z) = T_0 + \Delta T \left(1 - \frac{z}{d}\right). \tag{2.49}$$

Knowing the basic state temperature profile allows us to solve for the basic state pressure. Using the equation of state (2.16) within the equation of hydrostatic equilibrium (2.46) gives

$$\frac{\mathrm{d}P_B}{\mathrm{d}z} = -g\rho_0 \left(1 - \alpha \left(T - T_0\right)\right), \tag{2.50}$$

$$= -g\rho_0 \left(1 - \alpha\Delta T \left(1 - \frac{z}{d}\right)\right). \tag{2.51}$$

Solving this equation for the basic state pressure gives

$$P_B = P_0 - g\rho_0 z \left(1 - \alpha\Delta T \left(1 - \frac{z}{2d}\right)\right), \tag{2.52}$$

where P_0 is the constant value at $z = 0$.

2.4.3 Perturbation equations

We now take our basic state solutions and apply a perturbation to them. We shall denote perturbation quantities in lower case, such that

$$\mathbf{U} \equiv \mathbf{U_B} + \mathbf{u}, \quad T \equiv T_B + \theta, \quad P \equiv P_B + p.$$

Note that since $\mathbf{U_B} = \mathbf{0}$, this means $\mathbf{u}$ satisfies the boundary conditions that we derived in Section 2.4.1. However, since the basic state temperature already satisfies the required boundary conditions, the temperature perturbation must vanish on both boundaries. That is

$$\theta = 0 \quad \text{at} \quad z = 0 \text{ and } z = d. \tag{2.53}$$

The continuity, momentum and temperature equations then read

$$\nabla \cdot \mathbf{u} = 0, \tag{2.54}$$

$$\frac{\partial \mathbf{u}}{\partial t} + (\mathbf{u} \cdot \nabla)\mathbf{u} = -\frac{1}{\rho_0}\nabla p + g\alpha\theta\hat{\mathbf{z}} - 2\boldsymbol{\Omega} \times \mathbf{u} + \nu\nabla^2\mathbf{u}, \tag{2.55}$$

$$\frac{\partial \theta}{\partial t} + (\mathbf{u} \cdot \nabla)\theta = \frac{\Delta T}{d}w + \kappa\nabla^2\theta, \tag{2.56}$$

where we have used equation (2.46) to cancel the basic state terms in the momentum equation that are in hydrostatic equilibrium.

2.4.4 Dimensionless equations

When studying problems such as convection in geophysical and astrophysical bodies, it is extremely difficult to create an experiment that exactly models the physical conditions within the centre of the Earth, for example: the length scales and temperatures required are far too large. We could however make a drastically scaled-down experiment, or perform numerical simulations, but how would we know that they truly represent processes occurring in the Earth? This leads us to the concept of *dynamic similarity*. For different values of the parameters within the governing equations (e.g. layer depth, temperature difference, kinematic viscosity) we would expect different resultant flows. Crucially, it is the dimensionless groupings of these different parameters that give rise to different flows. In expressing the governing equations in dimensionless form, we are able to classify the type of flow based on certain dimensionless parameters. This means that although two different experiments may have different parameter values, we are able to compare them like-for-like, based on the value of these dimensionless parameter couplings.

In order to express the governing equations in dimensionless form, we must choose certain values with which to scale the different quantities. A natural length scale of the problem is the layer depth, d. For the unit of time, we shall choose the thermal diffusive time, $\frac{d^2}{\kappa}$. This is the characteristic amount of time that it takes for a thermal anomaly to diffuse, over the length scale d. The unit of temperature is

chosen based on the temperature difference across the layer, ΔT. Re-written with these scalings, our variables are

$$\mathbf{x} = d\widetilde{\mathbf{x}}, \quad t = \frac{d^2}{\kappa}\widetilde{t}, \quad \mathbf{u} = \frac{\kappa}{d}\widetilde{\mathbf{u}}, \quad \theta = \Delta T\widetilde{\theta}, \quad p = \frac{\rho_0\kappa^2}{d^2}\widetilde{p}, \tag{2.57}$$

where all $\widetilde{}$ variables are dimensionless. Note that with the chosen length scaling we have $\nabla = \frac{1}{d}\widetilde{\nabla}$. Furthermore, this means the boundaries are located at $z = 0$ and $z = 1$ in dimensionless coordinates. Proceeding with these scalings in equations (2.54), (2.55) and (2.56), the continuity, momentum and temperature equations read, respectively, in dimensionless form

$$\nabla \cdot \mathbf{u} = 0, \tag{2.58}$$

$$\frac{\partial \mathbf{u}}{\partial t} + (\mathbf{u}\cdot\nabla)\mathbf{u} = -\nabla p + RaPr\theta\hat{\mathbf{z}} - Ta^{\frac{1}{2}}Pr\hat{\mathbf{z}}\times\mathbf{u} + Pr\nabla^2\mathbf{u}, \tag{2.59}$$

$$\frac{\partial \theta}{\partial t} + (\mathbf{u}\cdot\nabla)\theta = w + \nabla^2\theta, \tag{2.60}$$

where we have dropped the $\widetilde{}$ notation and from now on, all variables are to be presumed dimensionless, unless otherwise stated. The dimensionless parameters are the Rayleigh number Ra, the Prandtl number Pr and the Taylor number Ta, which is related to the Ekman number Ek as shown. These are defined as

$$Ra = \frac{g\alpha\Delta T d^3}{\kappa\nu}, \quad Pr = \frac{\nu}{\kappa}, \quad Ta = \left(\frac{2\Omega d^2}{\nu}\right)^2 = Ek^{-2}. \tag{2.61}$$

The *Rayleigh number* is a measure of convective driving of the system. It is a ratio of buoyancy forces that promote convection—causing hotter, lighter fluid to rise—and diffusive forces that negate this, causing both heat and motion to dissipate. Increasing the Rayleigh number increases the convective driving of the system. The *Prandtl number* is the ratio of the kinematic viscosity to the thermal diffusivity. For Prandtl number greater (less) than unity, momentum will diffuse faster (slower) than heat. The *Taylor number* expresses the ratio of the rotation and viscous diffusion time scales. Increasing the Taylor number increases the rotational effects on the system. We now need only keep track of these three dimensionless parameters and varying these will allow us to explore all possible flow regimes. Some examples of

realisable values of these parameters are given in the table below. Note that there is differing opinion as to the value that diffusivities take inside the Earth's core, since they can be estimated on molecular or turbulent grounds, giving rise to different estimates of the dimensionless parameters.

	Ra	Pr	Ta
Earth's core (molecular)	10^{30}	1	10^{30}
Earth's core (turbulent)	10^{23}	1	10^{18}

Table 2.1: Estimates for the Rayleigh, Prandtl and Taylor number in the Earth's core, taken from Jones (2007).

2.4.5 Vorticity-streamfunction formulation

Though we have already derived the governing hydrodynamic equations (cf. equations (2.58), (2.59) and (2.60)), it shall be seen later (particularly in Chapter 4) that it is convenient to express them in a different form, using the vorticity and a streamfunction as the governing hydrodynamic variables, along with the temperature. Beginning with the momentum equation, as written in equation (2.59), we may re-write the $(\mathbf{u}\cdot\nabla)\mathbf{u}$ term using vector identity (A.1), giving the following

$$\frac{\partial \mathbf{u}}{\partial t} + \nabla\left(\frac{1}{2}|\mathbf{u}|^2\right) + \boldsymbol{\omega}\times\mathbf{u} = -\nabla p + RaPr\theta\hat{\mathbf{z}} - Ta^{\frac{1}{2}}Pr\hat{\mathbf{z}}\times\mathbf{u} + Pr\nabla^2\mathbf{u}, \quad (2.62)$$

where we have introduced the fluid vorticity $\boldsymbol{\omega} = \nabla\times\mathbf{u}$. Taking the curl of the above equation renders all gradient terms zero, leaving us with

$$\frac{\partial \boldsymbol{\omega}}{\partial t} + \nabla\times(\boldsymbol{\omega}\times\mathbf{u}) = -RaPr\frac{\partial\theta}{\partial x}\hat{\mathbf{y}} - Ta^{\frac{1}{2}}Pr\nabla\times(\hat{\mathbf{z}}\times\mathbf{u}) + Pr\nabla^2\boldsymbol{\omega}. \quad (2.63)$$

Using vector identity (A.2), along with $\boldsymbol{\omega} = \nabla\times\mathbf{u}$ and the fact that $\nabla\cdot\mathbf{u} = 0$, allows us to re-write the terms $\nabla\times(\boldsymbol{\omega}\times\mathbf{u})$ and $\nabla\times(\hat{\mathbf{z}}\times\mathbf{u})$ as follows

$$\frac{\partial \boldsymbol{\omega}}{\partial t} + (\mathbf{u}\cdot\nabla)\boldsymbol{\omega} - (\boldsymbol{\omega}\cdot\nabla)\mathbf{u} = -RaPr\frac{\partial\theta}{\partial x}\hat{\mathbf{y}} + Ta^{\frac{1}{2}}Pr(\hat{\mathbf{z}}\cdot\nabla)\mathbf{u} + Pr\nabla^2\boldsymbol{\omega}. \quad (2.64)$$

Taking the y-component of this equation we have

$$\frac{\partial \omega}{\partial t} + (\mathbf{u} \cdot \nabla)\omega = -RaPr\frac{\partial \theta}{\partial x} + Ta^{\frac{1}{2}}Pr\frac{\partial v}{\partial z} + Pr\nabla^2\omega, \tag{2.65}$$

where v and ω are the y-components of the velocity and vorticity respectively. Since we are considering two-dimensional flows, dependent only on x and z, then via the incompressibility condition we may introduce a streamfunction that satisfies the following

$$u = -\frac{\partial \psi}{\partial z}, \quad w = \frac{\partial \psi}{\partial x}. \tag{2.66}$$

Working now with the streamfunction renders explicitly solving the continuity equation irrelevant, since any flow described by such a streamfunction is automatically incompressible as $\frac{\partial v}{\partial y}$ is also zero. Furthermore, we have that

$$\omega = -\nabla^2\psi. \tag{2.67}$$

Hence writing the above equation in these variables we have

$$\frac{\partial \omega}{\partial t} + \frac{\partial \psi}{\partial x}\frac{\partial \omega}{\partial z} - \frac{\partial \psi}{\partial z}\frac{\partial \omega}{\partial x} = -RaPr\frac{\partial \theta}{\partial x} + Ta^{\frac{1}{2}}Pr\frac{\partial v}{\partial z} + Pr\nabla^2\omega, \tag{2.68}$$

or, be letting J denote the Jacobian determinant on the left-hand side, we have

$$\frac{\partial \omega}{\partial t} + J(\psi, \omega) = -RaPr\frac{\partial \theta}{\partial x} + Ta^{\frac{1}{2}}Pr\frac{\partial v}{\partial z} + Pr\nabla^2\omega. \tag{2.69}$$

Since this equation contains a term involving the y-component of the velocity, v, we require an evolution equation for this quantity. Taking the y-component of equation (2.59) will provide us with such an equation. Written in vorticity-streamfunction variables, this gives us

$$\frac{\partial v}{\partial t} + J(\psi, v) = Ta^{\frac{1}{2}}Pr\frac{\partial \psi}{\partial z} + Pr\nabla^2 v. \tag{2.70}$$

In a similar manner, we may write the heat equation in the form

$$\frac{\partial \theta}{\partial t} + J(\psi, \theta) = \frac{\partial \psi}{\partial x} + \nabla^2\theta. \tag{2.71}$$

It remains to specify the boundary conditions in terms of the vorticity-streamfunction variables. From the impermeability condition we have $w = 0$ on

$z = 0$ and $z = 1$. In terms of the streamfunction we have $w = \frac{\partial \psi}{\partial x}$, but requiring this to vanish at $z = 0$ and $z = 1$ is equivalent to ψ being equal to a constant. In order to conserve the horizontal flux through the layer, we have

$$\int_0^1 u \mathrm{d}z = -\int_0^1 \frac{\partial \psi}{\partial z} \mathrm{d}z = -\left[\psi\right]_0^1 = 0 \tag{2.72}$$

and hence the constant value of the streamfunction must be the same on both boundaries (which we may arbitrarily set to zero). If our bounding surfaces are stress free then we require that $\frac{\partial u}{\partial z}$ and $\frac{\partial v}{\partial z}$ both vanish on both bounding surfaces. Written in terms of the vorticity and using the fact that ψ is constant, allows us to specify that the vorticity should vanish on $z = 0$ and $z = 1$. The temperature boundary conditions remain unchanged in the vorticity-streamfunction formulation, hence we require

$$\omega = \psi = \theta = \frac{\partial v}{\partial z} = 0 \text{ at } z = 0 \text{ and } z = 1. \tag{2.73}$$

If our bounding surfaces are no-slip then we require that all components of the velocity vanish on both boundaries and so we have two boundary conditions on the streamfunction but none on the vorticity. In this case we require

$$\psi = \frac{\partial \psi}{\partial z} = \theta = v = 0 \text{ at } z = 0 \text{ and } z = 1. \tag{2.74}$$

2.5 Properties of rotating fluids

2.5.1 Rossby number

We have already introduced the Taylor number, accounting for the rotational driving of the system, although this does not determine whether the system is dominated by the rotation. Since the momentum equation is nonlinear in the velocity, it is feasible that for high enough Rayleigh number, such a strong flow is driven that the inertial term balances—or dominates—the rotation term. It is for this reason that we introduce the *Rossby number*, a further dimensionless number that is the

ratio of inertial forces to the Coriolis forces. Once again we use d as the length scale of the problem but this time scale the velocity with a general velocity scale U_*. Therefore the inertial and Coriolis forces respectively scale as $(\mathbf{u}\cdot\nabla)\mathbf{u} \sim {U_*}^2/d$ and $\boldsymbol{\Omega}\times\mathbf{u} \sim \Omega U_*$, hence their ratio, the Rossby number, is given by

$$Ro = \frac{U_*}{d\Omega}. \tag{2.75}$$

The Rossby number can be thought of as the ratio of the convective turnover time, $\frac{U_*}{d}$, to the rotation time, $\frac{1}{\Omega}$. For $Ro \ll 1$ the Coriolis force is much greater than inertial forces and so we expect that the flow will be dominated by the effects of rotation. For $Ro \gg 1$, since the Coriolis force is weaker than inertial forces, we expect that the flow will not 'feel' the effects of rotation and thus behave like a non-rotating flow. For Ro close to one, since the relative magnitudes of the Coriolis force and inertial forces are comparable, it is unclear from the outset whether the resulting flow will be rotationally influenced or not.

2.5.2 The Taylor-Proudman theorem

Within the study of rapidly rotating fluids, there is a significant theory, owing to Proudman (1916) and Taylor (1917)/Taylor (1922). We suppose that we are in a situation with a slow—relative to rotation—steady, velocity, in a fluid with negligible viscosity. That is, large Taylor number, low Rossby number. To leading order the momentum equation gives

$$Ta^{\frac{1}{2}}Pr\,\hat{\mathbf{z}}\times\mathbf{u} = -\nabla p. \tag{2.76}$$

This balance between the Coriolis force and the pressure gradient is known as *geostrophic balance*. We have neglected viscosity, so this is an idealised situation, not entirely mirrored within a natural setting. Since viscous diffusion acts on small length scales, for example within very thin boundary layers, it is possible for the bulk of a fluid to be held in geostrophic balance, with a departure from this state in the boundary layer. The resulting flow is known as a geostrophic wind and is oriented parallel to isobars: lines of constant pressure.

Taking the curl of the above equation renders the right hand side zero, and we are left with

$$Ta^{\frac{1}{2}}Pr\nabla \times (\hat{\mathbf{z}} \times \mathbf{u}) = 0, \tag{2.77}$$

Using vector identity (A.2), the fact that $\hat{\mathbf{z}}$ is a constant vector, and owing to the incompressibility of $\mathbf{u}$ we may transform this, to give

$$Ta^{\frac{1}{2}}Pr(\hat{\mathbf{z}} \cdot \nabla)\mathbf{u} = 0, \tag{2.78}$$

which may be written

$$\frac{\partial \mathbf{u}}{\partial z} = 0. \tag{2.79}$$

This final statement expresses, mathematically, the Taylor-Proudman theorem: that the fluid velocity be independent of z, the vertical coordinate that is aligned with the rotation vector. Hence any steady, large Taylor number, low Rossby number flow, is essentially two-dimensional. Within a three-dimensional domain, the resulting flow is composed of so-called Taylor columns; rotating columns of fluid, uniform in vertical extent. They can be visualised in physical experiments, and are an important feature of numerical geodynamo models. Within the Earth's outer core, the Rossby number is small, $Ro \sim 3 \times 10^{-6}$ (see e.g. Jones (2007)), therefore fluid velocity is small compared with rotation, and viscosity is negligible except on small length scales. It is expected that the convection pattern in the outer core is composed of Taylor columns, present everywhere except inside the tangent cylinder (Rotvig & Jones (2002)).

2.5.3 The Ekman Layer

No-slip boundary conditions require that all three components of velocity vanish on any given surface. The transition from non-zero velocity within the interior, to zero velocity on the boundary, occurs within a very thin region know as a boundary layer. In rotating flows, the thickness of this boundary layer is $\mathcal{O}(Ek^{\frac{1}{2}})$ (see Greenspan (1968)). Within the derivation of the Taylor-Proudman theorem, we said that in

nature it was generally valid in regions away from the boundary layer. Within the boundary layer, viscosity is not negligible, and so we must include it in the necessary mathematical balance. In dimensionless terms, the balance within the boundary layer is given by

$$Ek^{-1}Pr(\hat{\mathbf{z}} \times \mathbf{u}) = -\nabla p + Pr\nabla^2\mathbf{u}, \tag{2.80}$$

where we have written the Ekman number in place of the Taylor number. Taking the curl and double curl of this equation, and using vector identities (A.2) and (A.3) respectively gives

$$-Ek^{-1}\frac{\partial \mathbf{u}}{\partial z} = \nabla^2\boldsymbol{\omega}, \tag{2.81}$$

$$Ek^{-1}\frac{\partial \boldsymbol{\omega}}{\partial z} = \nabla^4\mathbf{u}. \tag{2.82}$$

We stated that viscous diffusion only acts on small length scales. In this case the small length scale is the distance over which the velocity changes from its interior value, to zero on the boundary. This distance is measured along the vertical coordinate, and hence derivatives in the z direction will be much larger than horizontal derivatives. Taking this into account, the z components of the above equations are

$$-Ek^{-1}\frac{\partial W}{\partial z} = \frac{\partial^2 Z}{\partial z^2}, \tag{2.83}$$

$$Ek^{-1}\frac{\partial Z}{\partial z} = \frac{\partial^4 W}{\partial z^4}, \tag{2.84}$$

where W and Z are the vertical components of velocity and vorticity respectively. We may combine the above two equations, to gain a single equation for W, or Z

$$\frac{\partial W}{\partial z} = -Ek^2\frac{\partial^5 W}{\partial z^5}, \tag{2.85}$$

$$\frac{\partial Z}{\partial z} = -Ek^2\frac{\partial^5 Z}{\partial z^5}. \tag{2.86}$$

Both W and Z satisfy the same differential equation. We may integrate once, giving

$$W = W_{\text{int}} - Ek^2\frac{\partial^4 W}{\partial z^4}, \tag{2.87}$$

$$Z = Z_{\text{int}} - Ek^2\frac{\partial^4 Z}{\partial z^4}, \tag{2.88}$$

where the constants of integration W_{int} and Z_{int} refer to the interior vertical velocity and interior vertical vorticity respectively. Since W and Z satisfy the same differential equation, for now we will work with just one variable, say, W. The homogeneous part of the solution satisfies

$$\frac{\partial^4 W}{\partial z^4} = -\frac{1}{Ek^2} W, \tag{2.89}$$

and so we propose a solution proportional to $e^{\lambda z}$, giving $\lambda = \frac{\pm(1\pm i)}{\sqrt{2Ek}}$. Considering the boundary at $z = 0$, the two roots with $\Re(\lambda) > 0$ are not permissible, since they represent solutions that grow as we move from the boundary layer to the interior, so we discard them. The remaining roots give the following solutions

$$W = W_{\text{int}} + W_1 \exp\left(\frac{-1+i}{\sqrt{2Ek}} z\right) + W_2 \exp\left(\frac{-1-i}{\sqrt{2Ek}} z\right), \tag{2.90}$$

$$Z = Z_{\text{int}} + Z_1 \exp\left(\frac{-1+i}{\sqrt{2Ek}} z\right) + Z_2 \exp\left(\frac{-1-i}{\sqrt{2Ek}} z\right). \tag{2.91}$$

Our solutions for W and Z must satisfy equation (2.83). Enforcing this and equating coefficients of like terms allows us to work out expressions for the coefficients in the vorticity expression, in terms of the coefficients in the velocity expression. Hence our solutions read

$$W = W_{\text{int}} + W_1 \exp\left(\frac{-1+i}{\sqrt{2Ek}} z\right) + W_2 \exp\left(\frac{-1-i}{\sqrt{2Ek}} z\right), \tag{2.92}$$

$$Z = Z_{\text{int}} + \frac{(1+i)}{\sqrt{2Ek}} W_1 \exp\left(\frac{-1+i}{\sqrt{2Ek}} z\right) + \frac{(1-i)}{\sqrt{2Ek}} W_2 \exp\left(\frac{-1-i}{\sqrt{2Ek}} z\right). \tag{2.93}$$

We now wish to express the complex exponentials in the expressions above, in terms of sines and cosines, doing so gives

$$W = W_{\text{int}} + \exp\left(\frac{-z}{\sqrt{2Ek}}\right)\left(A\cos\left(\frac{z}{\sqrt{2Ek}}\right) + B\sin\left(\frac{z}{\sqrt{2Ek}}\right)\right), \tag{2.94}$$

$$Z = Z_{\text{int}} + \exp\left(\frac{-z}{\sqrt{2Ek}}\right)\left(\frac{A+B}{\sqrt{2Ek}}\cos\left(\frac{z}{\sqrt{2Ek}}\right) + \frac{B-A}{\sqrt{2Ek}}\sin\left(\frac{z}{\sqrt{2Ek}}\right)\right), \tag{2.95}$$

where $A = W_1 + W_2$ and $B = (W_1 - W_2)i$.

We must now apply the boundary conditions on W and Z, which are given by

$$W = \frac{\partial W}{\partial z} = Z = 0 \text{ at } z = 0. \tag{2.96}$$

The first two boundary conditions tell us that $A = B = -W_{\text{int}}$ and so our solutions for W and Z read

$$W = W_{\text{int}} \left(1 - \exp\left(\frac{-z}{\sqrt{2Ek}}\right)\left(\cos\left(\frac{z}{\sqrt{2Ek}}\right) + \sin\left(\frac{z}{\sqrt{2Ek}}\right)\right)\right), \tag{2.97}$$

$$Z = Z_{\text{int}} - \sqrt{\frac{2}{Ek}} W_{\text{int}} \exp\left(\frac{-z}{\sqrt{2Ek}}\right) \cos\left(\frac{z}{\sqrt{2Ek}}\right). \tag{2.98}$$

It is now apparent why we referred to the constants of integration as the interior velocity and vorticity. Looking at the above expressions, as we move away from the boundary layer (z increasing) the exponential terms decay and we are left with interior values. Furthermore, they satisfy our original postulate, that the boundary layer thickness is $O(Ek^{\frac{1}{2}})$. Applying the final boundary condition gives the following

$$W_{\text{int}} = \sqrt{\frac{Ek}{2}} Z_{\text{int}}, \tag{2.99}$$

which is consistent with Greenspan (1968). Furthermore, this shows that the interior velocity is proportional to the interior vorticity. For cyclonic interior vorticity ($Z_{\text{int}} > 0$) this gives $W_{\text{int}} > 0$ and so motion is directed into the interior: this is known as *Ekman pumping*. For anticyclonic interior vorticity ($Z_{\text{int}} < 0$) this gives $W_{\text{int}} < 0$ and so motion is directed into the boundary layer: this is known as *Ekman suction*.

It is these effects that intrinsically render the case of no-slip boundary conditions more complex than the case of stress-free boundary conditions. In particular, when performing numerical simulations—something we shall address in Chapters 4 and 5—the added complexity of the Ekman layer can be problematic. For this reason, subsequent analysis shall be devoted only to the case of stress-free boundary conditions.

2.6 Summary

In this chapter we presented the equations governing two-dimensional nonlinear Rayleigh-Bénard convection and expressed them in dimensionless form. This lead

to the introduction of three dimensionless parameters: the Rayleigh, Prandtl and Taylor numbers.

The governing equations were presented in two different ways: the 'traditional' formulation expressed the equations in terms of the three components of fluid velocity $\mathbf{u} = (u, v, w)$ and temperature T, with boundary conditions on these quantities, as well as the z component of the vorticity ζ. The vorticity-streamfunction formulation expressed the equations in terms of the y component of the vorticity ω, the streamfunction ψ, the y component of the velocity v and the temperature T, with boundary conditions on these quantities.

It is important for the reader to distinguish between these formulations—particularly since we have defined two vorticity quantities—since both will be used independently in the subsequent analysis. The traditional formulation shall be used primarily in Chapter 3 and the vorticity-streamfunction formulation in the remaining chapters.

Chapter 3

Linear theory

In Chapter 2 we derived a set of equations governing perturbations to the hydrodynamic variables, about a steady, stationary basic state. The basic state temperature had a purely conducting profile, dependent on the vertical coordinate only. Upon deriving these perturbation equations we made no assumptions about the form or, furthermore, the magnitude of these perturbations. In this chapter we proceed by assuming that these are small, in the sense that the nonlinear product of any two perturbation quantities is negligible, hence we are able to linearise the equations. We then perform a stability analysis of the system by looking at the disturbances in terms of normal modes. We calculate the critical wavenumber and Rayleigh number at which convection will onset, for given values of the Taylor number and Prandtl number. Furthermore, we establish bounds on the governing parameters, allowing us to discern when the system is unstable. We shall just present the important results here. For a detailed review of the linear stability of Rayleigh-Bénard convection one should consult Veronis (1959), Chandrasekhar (1961) or Drazin & Reid (1981).

3.1 Linearisation

We begin by recalling the equations we derived in Chapter 2, governing the evolution of the fluid velocity $\mathbf{u}$ and temperature T. These are the continuity, momentum and temperature equations given by equations (2.58), (2.59), and (2.60) respectively. As we have already said, we shall be studying the stability of small perturbations and so we linearise these equations. This involves ignoring the nonlinear advective terms on the left-hand sides of equations (2.59) and (2.60). Thus we have

$$\nabla \cdot \mathbf{u} = 0, \tag{3.1}$$

$$\frac{\partial \mathbf{u}}{\partial t} = -\nabla p + RaPr\theta\hat{\mathbf{z}} - Ta^{\frac{1}{2}}Pr\hat{\mathbf{z}} \times \mathbf{u} + Pr\nabla^2\mathbf{u}, \tag{3.2}$$

$$\frac{\partial \theta}{\partial t} = w + \nabla^2\theta, \tag{3.3}$$

where we recall that w is the z-component of the fluid velocity. In order to eliminate the pressure term we begin by taking the curl and double curl of equation (3.2), and using vector identities (A.2) and (A.3) to transform them into the following form

$$\frac{\partial \boldsymbol{\omega}}{\partial t} = RaPr\left(\nabla \times \theta\hat{\mathbf{z}}\right) + Ta^{\frac{1}{2}}Pr\frac{\partial \mathbf{u}}{\partial z} + Pr\nabla^2\boldsymbol{\omega}, \tag{3.4}$$

$$\frac{\partial}{\partial t}\nabla^2\mathbf{u} = RaPr\frac{\partial^2\theta}{\partial x^2}\hat{\mathbf{z}} - Ta^{\frac{1}{2}}Pr\frac{\partial \boldsymbol{\omega}}{\partial z} + Pr\nabla^4\mathbf{u}, \tag{3.5}$$

where we recall that the vorticity is given by $\boldsymbol{\omega} = \nabla \times \mathbf{u}$. We now take the z-components of these equations, along with the temperature equation, as the equations upon which we shall conduct our linear stability analysis. They are given by

$$\frac{\partial \zeta}{\partial t} = Ta^{\frac{1}{2}}Pr\frac{\partial w}{\partial z} + Pr\nabla^2\zeta, \tag{3.6}$$

$$\frac{\partial}{\partial t}\nabla^2 w = RaPr\frac{\partial^2\theta}{\partial x^2} - Ta^{\frac{1}{2}}Pr\frac{\partial \zeta}{\partial z} + Pr\nabla^4 w, \tag{3.7}$$

$$\frac{\partial \theta}{\partial t} = w + \nabla^2\theta, \tag{3.8}$$

where we recall that ζ is the z-component of the vorticity given by equation (2.40) that itself is a function of u and v—hence we do not require evolution equations for u and v.

3.2 Normal mode analysis

We now postulate normal mode solutions of the form

$$w(x,z,t) = \Re\Big\{W(z)e^{iax+\sigma t}\Big\}, \tag{3.9}$$

$$\zeta(x,z,t) = \Re\Big\{Z(z)e^{iax+\sigma t}\Big\}, \tag{3.10}$$

$$\theta(x,z,t) = \Re\Big\{\Theta(z)e^{iax+\sigma t}\Big\}. \tag{3.11}$$

In the above expansions, the functions $W(z)$, $Z(z)$ and $\Theta(z)$ could be complex. a is the wave number of a particular normal mode and σ is the complex eigenvalue that shall determine the stability of the system. It is actually the real part of the eigenvalue that determines the stability of the system. Note that for $\Re(\sigma) < 0$, as time evolves the solutions will decay exponentially, and hence the system is stable. For $\Re(\sigma) > 0$, as time evolves the solutions will grow exponentially, and hence the system is unstable. The case $\Re(\sigma) = 0$ characterises the point at which the system is neither stable nor unstable, often termed marginally stable. σ can be thought of as a bifurcation parameter, and since the stability of the system changes at $\sigma = 0$, this is the corresponding bifurcation point. Hence there are two different classes of instability that may occur: instability due to a purely real eigenvalue going through zero—a direct, or ordinary bifurcation textemdash and instability due to the real part of a complex conjugate pair of eigenvalues going through zero—a Hopf bifurcation. The former is often termed a stationary instability and the latter is often termed overstability, or an oscillatory instability.

With expansions of such a functional dependence on x, z and t we have the following

$$\frac{\partial}{\partial t} = \sigma, \quad \frac{\partial}{\partial x} = ia, \quad \frac{\partial}{\partial z} = D, \quad \nabla^2 = D^2 - a^2, \tag{3.12}$$

where D is an operator representing differentiation with respect to z. Note that the stress-free boundary conditions in terms of these variables are as follows

$$W = D^2W = DZ = \Theta = 0 \quad \text{at} \quad z = 0 \quad \text{and} \quad z = 1. \tag{3.13}$$

Inserting our expansions (3.9), (3.10) and (3.11) into equations (3.6), (3.7) and (3.8) respectively give

$$\sigma Z = Ta^{\frac{1}{2}} PrDW + Pr\left(D^2 - a^2\right) Z, \tag{3.14}$$

$$\sigma\left(D^2 - a^2\right) W = -a^2 RaPr\Theta - Ta^{\frac{1}{2}} PrDZ + Pr\left(D^2 - a^2\right)^2 W, \tag{3.15}$$

$$\sigma\Theta = W + \left(D^2 - a^2\right)\Theta. \tag{3.16}$$

Rearranging the above equations so that like terms are together gives

$$\left(D^2 - a^2 - \frac{\sigma}{Pr}\right) Z = -Ta^{\frac{1}{2}} DW, \tag{3.17}$$

$$\left(D^2 - a^2\right)\left(D^2 - a^2 - \frac{\sigma}{Pr}\right) W = a^2 Ra\Theta + Ta^{\frac{1}{2}} DZ, \tag{3.18}$$

$$\left(D^2 - a^2 - \sigma\right)\Theta = -W. \tag{3.19}$$

If we evaluate equation (3.18) on the boundaries then since $\Theta = DZ = 0$ at $z = 0$ and $z = 1$ then the right-hand side vanishes. Furthermore, on the left-hand side, since $W = D^2 W = 0$ at $z = 0$ and $z = 1$, this tell us that $D^4 W = 0$ is also required on the boundaries. Furthermore, it can be seen that any even-powered derivative of W, with respect to z, will vanish on the boundaries. The solution that satisfies these boundary conditions is given by $W = W_0 \sin n\pi z$. Looking at equation (3.17) tells us that the solution for Z must be of an opposite parity to W, hence we have $Z \sim \cos n\pi z$, whilst equation (3.19) tell us that the solution for Θ must be of the same parity as W, hence we have $\Theta \sim \sin n\pi z$ also.

We seek to form an equation governing just one of the variables, hence we need to apply the operators $\left(D^2 - a^2 - \frac{\sigma}{Pr}\right)$ and $\left(D^2 - a^2 - \sigma\right)$ to equation (3.18), yielding

$$\begin{aligned}
&\left(D^2 - a^2\right)\left(D^2 - a^2 - \frac{\sigma}{Pr}\right)^2 \left(D^2 - a^2 - \sigma\right) W \\
=&a^2 Ra\left(D^2 - a^2 - \frac{\sigma}{Pr}\right)\left(D^2 - a^2 - \sigma\right)\Theta \\
+&Ta^{\frac{1}{2}} D\left(D^2 - a^2 - \sigma\right)\left(D^2 - a^2 - \frac{\sigma}{Pr}\right) Z
\end{aligned} \tag{3.20}$$

We can now eliminate Z and Θ by using equations (3.17) and (3.19) to give an

equation entirely in terms of W

$$\left(D^2 - a^2\right)\left(D^2 - a^2 - \frac{\sigma}{Pr}\right)^2\left(D^2 - a^2 - \sigma\right)W$$
$$+a^2 Ra\left(D^2 - a^2 - \frac{\sigma}{Pr}\right)W + TaD^2\left(D^2 - a^2 - \sigma\right)W = 0. \tag{3.21}$$

Since we have justified that $W \sim \sin n\pi z$ this has the consequence that $D^2 \sim -n^2\pi^2$. Using this within equation (3.21) gives

$$\left(n^2\pi^2 + a^2\right)\left(n^2\pi^2 + a^2 + \frac{\sigma}{Pr}\right)^2\left(n^2\pi^2 + a^2 + \sigma\right)$$
$$-a^2 Ra\left(n^2\pi^2 + a^2 + \frac{\sigma}{Pr}\right) + n^2\pi^2 Ta\left(n^2\pi^2 + a^2 + \sigma\right) = 0. \tag{3.22}$$

Equation (3.22) is a dispersion relation that allows us to determine the eigenvalue σ, as given by Drazin & Reid (1981). For reasons that shall become evident, at this point we shall make a distinction between the analysis of the rotating and non-rotating systems, beginning with the non-rotating one since it is conceptually simpler.

3.3 No rotation

Before analysing the dispersion relation given by equation (3.22) we shall present a general result due to Chandrasekhar (1961) and Drazin & Reid (1981). The principle of exchange of stabilities allows us to infer from the governing equations some specific details about the eigenvalue σ.

3.3.1 The principle of exchange of stabilities

Setting $Ta = 0$ in equations (3.18) and (3.19) gives the following

$$\left(D^2 - a^2\right)\left(D^2 - a^2 - \frac{\sigma}{Pr}\right)W = a^2 Ra\Theta, \tag{3.23}$$
$$\left(D^2 - a^2 - \sigma\right)\Theta = -W, \tag{3.24}$$

where we have in fact disregarded the equation for Z, since it is identically zero in the non-rotating system.

We begin by multiplying equation (3.24) with the complex conjugate of Θ, denoted Θ^* and integrating across the fluid layer, from $z = 0$ to $z = 1$.

$$\int_0^1 \left(\Theta^* D^2\Theta - (a^2+\sigma)|\Theta|^2\right) \mathrm{d}z = -\int_0^1 \Theta^* W \mathrm{d}z. \tag{3.25}$$

Taking the first term on the right-hand side and integrating by parts, noting that Θ^* satisfies the same boundary conditions as Θ tell us

$$\int_0^1 \left(|D\Theta|^2 + (a^2+\sigma)|\Theta|^2\right) \mathrm{d}z = \int_0^1 \Theta^* W \mathrm{d}z. \tag{3.26}$$

We may write this in the form

$$I_1 + \sigma I_2 = \int_0^1 \Theta^* W \mathrm{d}z, \tag{3.27}$$

where the integrals I_1 and I_2 can be identified by inspection. Their precise form is of no particular interest, the crucial thing is that since the integrands in I_1 and I_2 are real and strictly positive, the integrals themselves will yield real and strictly positive values. Now, turning our attention to equation (3.23), we multiply this by W^*, the complex conjugate of W, to give

$$\int_0^1 W^* \left(D^4 W - \left(2a^2 + \frac{\sigma}{Pr}\right) D^2 W + \left(a^4 + \frac{a^2\sigma}{Pr}\right) W\right) \mathrm{d}z = a^2 Ra \int_0^1 W^* \Theta \mathrm{d}z. \tag{3.28}$$

Now if we integrate the first term on the left-hand side by parts twice, and the second term by parts once, using the fact that W^* satisfies the same boundary conditions as W, then we have

$$\int_0^1 \left(|D^2 W|^2 + \left(2a^2 + \frac{\sigma}{Pr}\right)|DW|^2 + \left(a^4 + \frac{a^2\sigma}{Pr}\right)|W|^2\right) \mathrm{d}z = a^2 Ra \int_0^1 W^* \Theta \mathrm{d}z. \tag{3.29}$$

Similarly we may write this in the form

$$I_3 + \sigma I_4 = a^2 Ra \int_0^1 W^* \Theta \mathrm{d}z, \tag{3.30}$$

where the integrals I_3 and I_4 can once again be identified by inspection. Again, the precise form of I_3 and I_4 is of no particular interest, yet congruously to I_1 and I_2, since the integrands are real and strictly positive, the integrals I_3 and I_4 themselves will yield real and strictly positive values. It is noteworthy that the integrals within the right-hand sides of equations (3.27) and (3.30) are the complex conjugate of one another. Furthermore, denoting the real and imaginary parts of the complex eigenvalue σ by σ_r and σ_i respectively, we have

$$a^2 Ra \left(I_1 + (\sigma_r + i\sigma_i) I_2\right) = \left(I_3 + (\sigma_r + i\sigma_i) I_4\right)^* . \tag{3.31}$$

For this equation to be satisfied, we must equate its real and imaginary parts, giving

$$a^2 Ra \left(I_1 + \sigma_r I_2\right) - \left(I_3 + \sigma_r I_4\right) = 0, \tag{3.32}$$

$$\sigma_i \left(a^2 Ra I_2 + I_4\right) = 0. \tag{3.33}$$

Since I_2, I_4, a and Ra are all themselves positive, the only way in which the latter equation can be satisfied is if σ_i is itself zero. This means that σ is purely real and that for non-rotating convection, linear theory predicts that convection cannot set in via a Hopf bifurcation. Furthermore, the onset of instability will occur when the now real eigenvalue σ is equal to zero.

3.3.2 Growth rates

Setting $Ta = 0$ in the dispersion relation given by equation (3.22) gives

$$\left(n^2\pi^2 + a^2\right)\left(n^2\pi^2 + a^2 + \frac{\sigma}{Pr}\right)\left(n^2\pi^2 + a^2 + \sigma\right) - a^2 Ra \left(n^2\pi^2 + a^2 + \frac{\sigma}{Pr}\right) = 0, \tag{3.34}$$

where we have taken out a factor of $\left(n^2\pi^2 + a^2 + \frac{\sigma}{Pr}\right)$. Here we have lost a power of σ and effectively reduced the order of the system. This stems from the fact that the vorticity is identically zero within the non-rotating system. Rearranging this equation and equating like powers of σ gives

$$\sigma^2 + \left(n^2\pi^2 + a^2\right)(Pr + 1)\,\sigma + Pr \frac{\left(\left(n^2\pi^2 + a^2\right)^3 - a^2 Ra\right)}{\left(n^2\pi^2 + a^2\right)} = 0. \tag{3.35}$$

Clearly, in order to have a root $\sigma = 0$ we require

$$Ra = \frac{(n^2\pi^2 + a^2)^3}{a^2}. \tag{3.36}$$

For stability, by the Routh-Hurwitz criterion, we require that all coefficients of σ in equation (3.35) are positive. The coefficients of σ^2 and σ are both positive., but for the constant coefficient to be positive we require that Ra is less than the marginal value given by equation (3.36). Therefore to determine the critical Rayleigh number—the value at which the onset of convection will occur—we must minimise this expression over both n and a. Clearly $n = 1$ is the minimal non-trivial value of n, giving

$$Ra = \frac{(\pi^2 + a^2)^3}{a^2}. \tag{3.37}$$

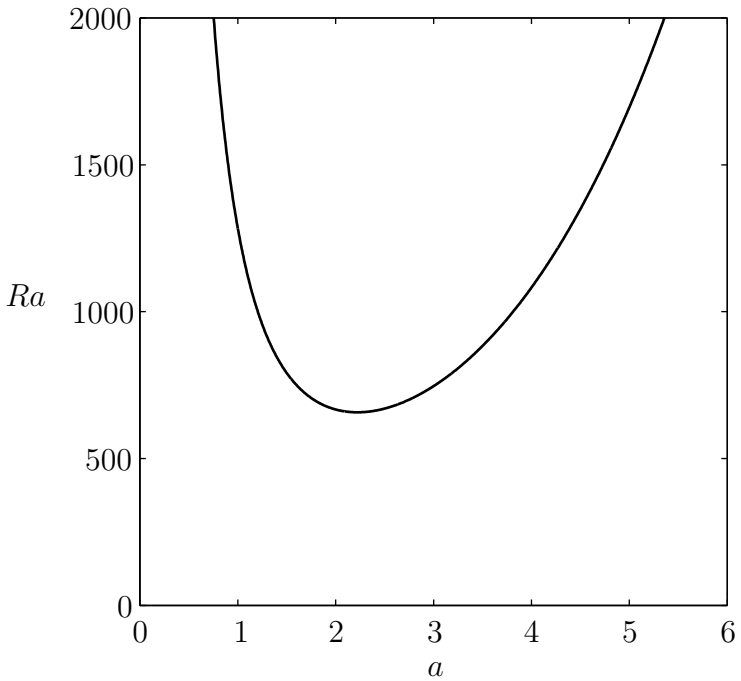

Figure 3.1: Plot of the Rayleigh number versus wave number for non-rotating convection, from equation (3.37).

In order to minimise with respect to a, it is a simple matter of differentiating Ra

with respect to a and equating the resultant derivative to zero. This gives

$$a_c = \frac{\pi}{\sqrt{2}} \simeq 2.221, \tag{3.38}$$

$$Ra_c = Ra(a_c) = \frac{27\pi^4}{4} \simeq 657.511. \tag{3.39}$$

The roots for general σ can be found by applying the quadratic formula to the dispersion relation (3.35), giving, for $n = 1$

$$\sigma = \frac{(\pi^2 + a^2)(Pr + 1)}{2}\left[-1 \pm \left(1 + \frac{4Pr\left(\frac{Ra}{Ra_c} - 1\right)}{(Pr+1)^2}\right)^{\frac{1}{2}}\right]. \tag{3.40}$$

Note that the onset of instability was not governed by the value of the Prandtl number, yet the precise rate at which solutions will grow or decay does have Prandtl number dependence.

3.4 Rotation

For non-zero Taylor number there does not exist a theory analogous to the principle of exchange of stabilities, whereby we were able to determine that the eigenvalue governing the stability of the non-rotating system was purely real. For rotating convection we have to assume that in general the eigenvalues are complex.

3.4.1 Growth rates

We return to the dispersion relation for σ, given by equation (3.22). For the non-rotating system, instability set in according to the lowest non-trivial value of n. Since in the limit as $Ta \to 0$ the rotating system converges to the non-rotating system, it is clear that we must have $n = 1$ here also. Enforcing this and rearranging equation (3.22), equating like powers of σ gives

$$\sigma^3 + c_2\sigma^2 + c_1\sigma + c_0 = 0, \tag{3.41}$$

where the coefficients c_0, c_1 and c_2 are given by

$$c_2 = \left(\pi^2 + a^2\right)(1 + 2Pr), \tag{3.42}$$

$$c_1 = Pr\left(\left(\pi^2 + a^2\right)^2 (2 + Pr) + \frac{\pi^2 TaPr - a^2 Ra}{(\pi^2 + a^2)}\right), \tag{3.43}$$

$$c_0 = Pr^2\left(\left(\pi^2 + a^2\right)^3 + \pi^2 Ta - a^2 Ra\right). \tag{3.44}$$

Guided by Chandrasekhar (1961), an important combination of the coefficients in equation (3.41), notably $c_1c_2 - c_0$, is given by the Routh-Hurwitz stability criterion. Evaluating this based on the values given by equations (3.42), (3.43) and (3.44) gives

$$c_1c_2 - c_0 = a^2 Pr(1 + Pr)\left(\frac{2\,(1 + Pr)}{a^2}\left(\left(\pi^2 + a^2\right)^3 + \frac{\pi^2 TaPr^2}{(1 + Pr)^2}\right) - Ra\right). \tag{3.45}$$

Clearly $c_2 > 0$ always holds, since its constituent components are all themselves greater than zero. In general c_0 and c_1 are not greater than zero, as they are affected by the values of the other parameters. Congruously $c_1c_2 - c_0$ is not always greater than zero due to the effect of the Rayleigh number.

To begin, we shall consider $Ra = 0$. In this case c_0, c_1, c_2 and $c_1c_2 - c_0$ will all be greater than zero. Since $c_0 > 0$ this means that there is at least one stable—negative—real root. We shall denote this by $\sigma_0 < 0$. Thus equation (3.41) can be factorised as follows

$$(\sigma - \sigma_0)(\sigma^2 + 2d_1\sigma + d_0) = 0, \tag{3.46}$$

with the solutions for the other roots being given by

$$\sigma = -d_1 \pm \sqrt{d_1^2 - d_0}. \tag{3.47}$$

Expanding equation (3.46) gives

$$\sigma^3 + (2d_1 - \sigma_0)\sigma^2 + (d_0 - 2d_1\sigma_0)\sigma - \sigma_0 d_0 = 0. \tag{3.48}$$

Upon comparison with the dispersion relation given by equation (3.41) we see that the coefficients in the two equations are related in the following manner

$$(2d_1 - \sigma_0) = c_2, \quad (d_0 - 2d_1\sigma_0) = c_1, \quad -\sigma_0 d_0 = c_0. \tag{3.49}$$

Hence we have expressions for d_0 and d_1. These are given by

$$d_0 = -\frac{c_0}{\sigma_0}, \quad d_1 = \frac{c_1 c_2 - c_0}{2(c_1 + \sigma_0^2)}. \tag{3.50}$$

This means that both d_0 and d_1 are positive and hence the solutions given by equation (3.47) both have negative real parts. This is known as absolute stability, since all three roots have negative real parts.

Now, as Ra is increased from zero, the values of c_0 and $c_1 c_2 - c_0$ will decrease. If c_0 becomes zero then by equation (3.49) this means that one of σ_0 and d_0 has become zero. σ_0 is a real root and with $d_0 = 0$ in equation (3.47) this also gives a real—zero—root. Hence if $c_0 = 0$ we will have a stationary instability .

If $c_1 c_2 - c_0$ becomes zero then by equation (3.50) this means that d_1 has become zero. Equation (3.47) then gives the roots as $\sigma = \pm\sqrt{-d_0}$. Furthermore, $c_1 c_2$ and c_0 must have the same sign, in order to satisfy $c_1 c_2 - c_0 = 0$. Since c_2 is always positive this means that if c_0 is positive (negative), then c_1 is positive (negative). If c_0 is negative then that means it has already gone through zero, i.e. a stationary instability has set in. Hence for c_0 positive, c_1 is positive. With $d_1 = 0$, equation (3.49) gives $c_1 = d_0$, hence d_0 is positive also. By equation (3.47) this means that we have a complex conjugate pair of roots with zero real part. Hence if $c_1 c_2 - c_0 = 0$ then we will have an oscillatory instability. This behaviour is in exact accordance with Chandrasekhar (1961) and Kloosterziel & Carnevale (2003).

3.4.2 Stationary instability

For a stationary instability, we must have $c_0 = 0$, giving

$$Ra^{(s)} = \frac{(\pi^2 + a^2)^3 + \pi^2 Ta}{a^2}, \tag{3.51}$$

which must be minimised over a and Ta in order to find the critical Rayleigh number. Note that if $Ta = 0$ then this expression reduces to that of the non-rotating case. Hence we would expect that as the Taylor number increases, the critical Rayleigh

number at which convection will onset will also increase. For a given value of Ta, minimising over a will give the critical Rayleigh number for that particular Taylor number. We achieve this by differentiating equation (3.51) with respect to a and equating the resultant derivative to zero. This gives

$$2a^6 + 3\pi^2 a^4 = \pi^6 + \pi^2 Ta. \tag{3.52}$$

We must solve this equation for a, for a given Ta in order to find the critical wave number. In general this is difficult to achieve analytically, so we do it numerically, with the results being given in Table 3.1 (cf. Chandrasekhar (1961)), along with the corresponding critical Rayleigh numbers. We can however say something in the

Ta	$a_c^{(s)}$	$Ra_c^{(s)}$
10^4	5.698	5.377×10^3
10^5	8.626	2.131×10^4
10^6	12.86	9.222×10^4
10^7	19.02	4.147×10^5
10^8	28.02	1.897×10^6

Table 3.1: Critical wave number and Rayleigh number, for a given Taylor number, for stationary rotating convection.

asymptotic limit $Ta \to \infty$. The dominant balance in this case will be between the sextic term on the left-hand side and the term involving the Taylor number on the right-hand side

$$2a^6 \sim \pi^2 Ta. \tag{3.53}$$

We can solve this to get an asymptotic solution for the wave number a. Furthermore, using this value within the expression for the Rayleigh number, given by equation (3.51), we can get an asymptotic solution for $Ra^{(s)}$ also. Hence as $Ta \to \infty$, we have

$$a_c^{(s)} \sim \left(\frac{\pi^2}{2}\right)^{\frac{1}{6}} Ta^{\frac{1}{6}}, \tag{3.54}$$

$$Ra_c^{(s)} \sim 3\left(\frac{\pi^2}{2}\right)^{\frac{2}{3}} Ta^{\frac{2}{3}}. \tag{3.55}$$

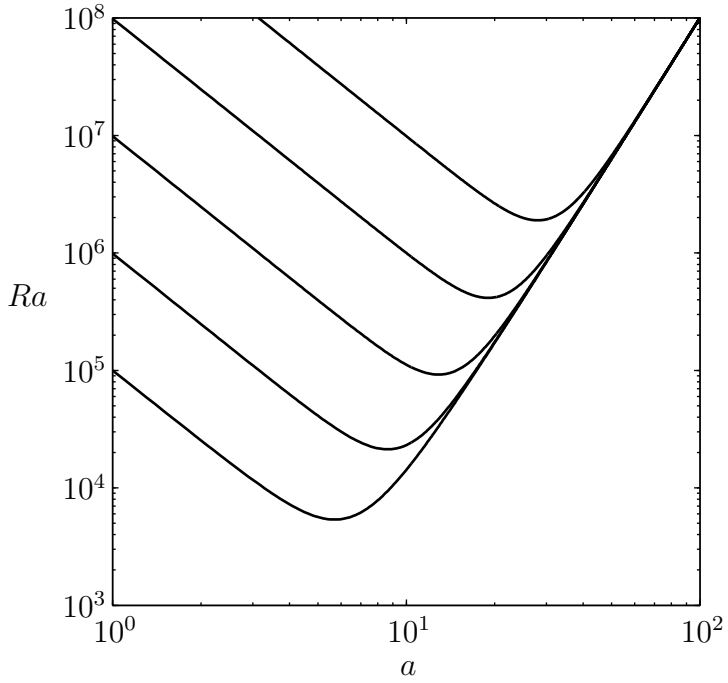

Figure 3.2: Plot of the Rayleigh number versus wave number for stationary rotating convection, from equation (3.51). The curves, in order of increasing Rayleigh number, correspond to $Ta = 10^4$, 10^5, 10^6, 10^7 and 10^8 respectively.

The Taylor-Proudman theorem told us that in the limit as $Ta \to \infty$, the flow would be comprised of columns of fluid aligned with the rotation axis. Since the critical wavenumber increases as the rotation rate increases, this means that the critical wavelength decreases. Hence the significance of the asymptotic wavenumber relation is that at onset, convection shall take the form of tall thin columns.

3.4.3 Oscillatory instability

For an oscillatory instability, we must have $c_1 c_2 - c_0 = 0$, giving

$$Ra^{(o)} = \frac{2\left(1+Pr\right)}{a^2}\left(\left(\pi^2+a^2\right)^3 + \frac{\pi^2 Ta Pr^2}{\left(1+Pr\right)^2}\right). \tag{3.56}$$

Once again, in order to find the critical Rayleigh number, we must minimise this expression over a for a given Ta and Pr. Doing this gives

$$2a^6 + 3\pi^2 a^4 = \pi^6 + \frac{\pi^2 Ta Pr^2}{(1+Pr)^2}. \tag{3.57}$$

We solve this numerically for a and the critical values, along with the corresponding values of the critical Rayleigh number can be found in Table 3.2 (cf. Chandrasekhar (1961)). Again we can say something in the asymptotic limit $Ta \to \infty$. The

Ta	$a_c^{(o)}$	$Ra_c^{(o)}$
10^4	2.542	1.761×10^3
10^5	3.583	3.404×10^3
10^6	5.501	1.063×10^4
10^7	8.340	4.164×10^4
10^8	12.45	1.794×10^5

Table 3.2: Critical wave number and Rayleigh number, for a given Taylor number at $Pr = 0.1$, for oscillatory rotating convection.

dominant balance in this case will be between the sextic term on the left-hand side and the term involving the Taylor number on the right-hand side

$$2a^6 \sim \frac{\pi^2 Ta Pr^2}{(1+Pr)^2}. \tag{3.58}$$

We can solve this to get an asymptotic solution for the wave number a. Furthermore, using this value within the expression for the Rayleigh number, given by equation (3.56), we can get an asymptotic solution for $Ra^{(o)}$ also. Hence as $Ta \to \infty$, we have

$$a_c^{(o)} \sim \left(\frac{\pi^2 Pr^2}{2\,(1+Pr)^2}\right)^{\frac{1}{6}} Ta^{\frac{1}{6}}, \tag{3.59}$$

$$Ra_c^{(o)} \sim 6\,(1+Pr)\left(\frac{\pi^2 Pr^2}{2\,(1+Pr)^2}\right)^{\frac{2}{3}} Ta^{\frac{2}{3}}, \tag{3.60}$$

which is the same asymptotic scaling as in the case of a stationary instability.

Since $c_1 c_2 - c_0 = 0$ means that $d_1 = 0$, and furthermore that $c_1 = d_0$ is necessarily positive when we have an oscillatory instability, this means that by equation (3.43)

we have

$$Pr\left(\left(\pi^2+a^2\right)^2(2+Pr)+\frac{\pi^2 TaPr-a^2Ra}{(\pi^2+a^2)}\right)\geq 0. \tag{3.61}$$

Using the expression for the Rayleigh number from equation (3.56) and rearranging gives us a constraint on the Taylor number and the Prandtl number, namely

$$(1-Pr)\,Ta \geq \frac{\left(\pi^2+a^2\right)^3}{\pi^2}(1+Pr)\,. \tag{3.62}$$

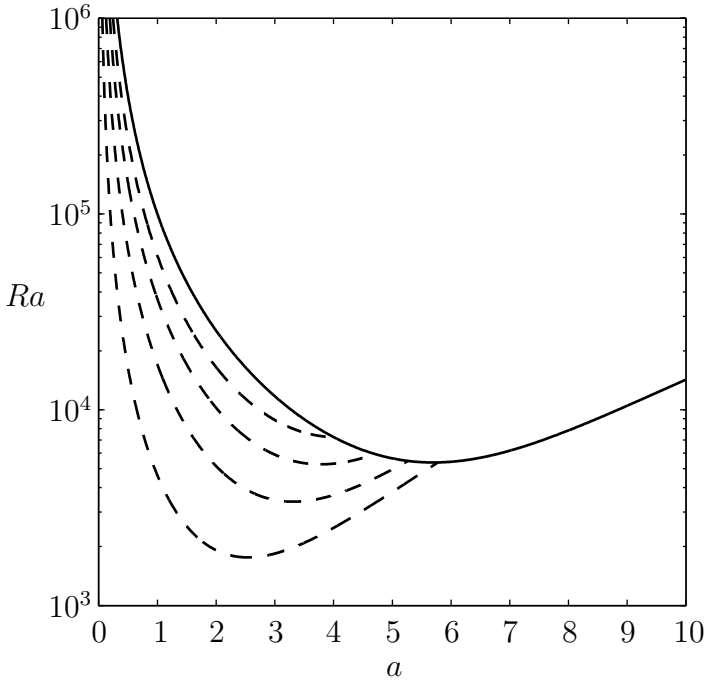

Figure 3.3: Plot of the Rayleigh number versus wave number for rotating convection at $Ta = 10^4$. The solid curve is for stationary convection and the dashed curves are for oscillatory convection at the following values of the Prandtl number, in order of increasing Rayleigh number: $Pr = 0.1$, 0.3, 0.5 and 0.7 respectively.

Equation (3.62) gives a necessary but not sufficient requirement that must be satisfied in order that convection onset in an oscillatory manner. By looking at this we can see that for $Pr > 1$ oscillatory convection is not possible, since we must have $Ta > 0$. Using equations (3.51) and (3.56) we may write the following

$$Ra^{(o)} = Ra^{(s)} + \frac{(1+2Pr)}{a^2}\left(\left(\pi^2+a^2\right)^3 - \pi^2 Ta\left(\frac{1-Pr}{1+Pr}\right)\right). \tag{3.63}$$

Hence for $Pr > 1$ we have $Ra^{(o)} > Ra^{(s)}$ so we can deduce that $Ra_c^{(o)} > Ra_c^{(s)}$ and convection will therefore set in first as stationary convection; indeed we have just shown that in this case oscillatory convection is not even possible. Further to this we may derive a tighter upper bound on the value of the Prandtl number that will permit oscillatory convection. Equation (3.62) reduces to an equality only at the point of bifurcation—the point at which either one of stationary or oscillatory convection could onset. Taking this to be so, and using the resulting expression for the Taylor number within the sextic for a, given by equation (3.57), gives

$$(2 - 3Pr^2)a^6 + 3\pi^2(1 - 2Pr^2)a^4 - 3\pi^4 Pr^2 a^2 - \pi^6 = 0, \tag{3.64}$$

hence as $\mathrm{Pr} \to \sqrt{\frac{2}{3}}$, one root $a \to \infty$, thus providing an upper bound on the Prandtl number for which convection can set in via an oscillatory instability. The value of Ta when the left and right-hand sides of equation (3.62) are equal, that depends on the Prandtl number and the wave number, acts as dividing line between the stationary and oscillatory regimes.

For $Pr < 1$ we have $Ra^{(s)} > Ra^{(o)}$ (see Figure 3.3), yet this does not guarantee that $Ra_c^{(s)} > Ra_c^{(o)}$, hence we cannot say which type of convection will dominate. It is possible to determine, numerically, another dividing line which will separate this intermediate region, where convection could be of either form, and a region whereby convection will always be oscillatory. Following Chandrasekhar (1961) and Veronis (1959) this will occur when $Ra_c^{(s)} = Ra_c^{(o)}$ at wave numbers $a_c^{(s)}$ and $a_c^{(o)}$—that in general will not be equal—respectively for given values of the Taylor number and the Prandtl number. As $Ta \to \infty$ we derived the following asymptotic dependence of the Rayleigh number with the Taylor number

$$Ra_c^{(s)} \sim 3\left(\frac{\pi^2}{2}\right)^{\frac{2}{3}} Ta^{\frac{2}{3}}, \tag{3.65}$$

$$Ra_c^{(o)} \sim 6\,(1 + Pr)\left(\frac{\pi^2 Pr^2}{2\,(1 + Pr)^2}\right)^{\frac{2}{3}} Ta^{\frac{2}{3}}. \tag{3.66}$$

The point at which these become equal as $Ta \to \infty$ is the root of the equation

$$\frac{2Pr^{\frac{4}{3}}}{(1 + Pr)^{\frac{1}{3}}} = 1, \tag{3.67}$$

given by

$$Pr_c = 0.6766. \tag{3.68}$$

Due to the similar functional form of equations (3.51) and (3.56) we can deduce that for $Pr > Pr_c$, $Ra_c^{(s)} < Ra_c^{(o)}$ so convection will always be stationary. For $Pr < Pr_c$, provided there exists an Ta that gives $Ra_c^{(o)} < Ra_c^{(s)}$, we will have oscillatory convection. We are able to determine these stability boundaries numerically and plot them in a regime diagram in (Ta, Pr) space in Figure 3.4.

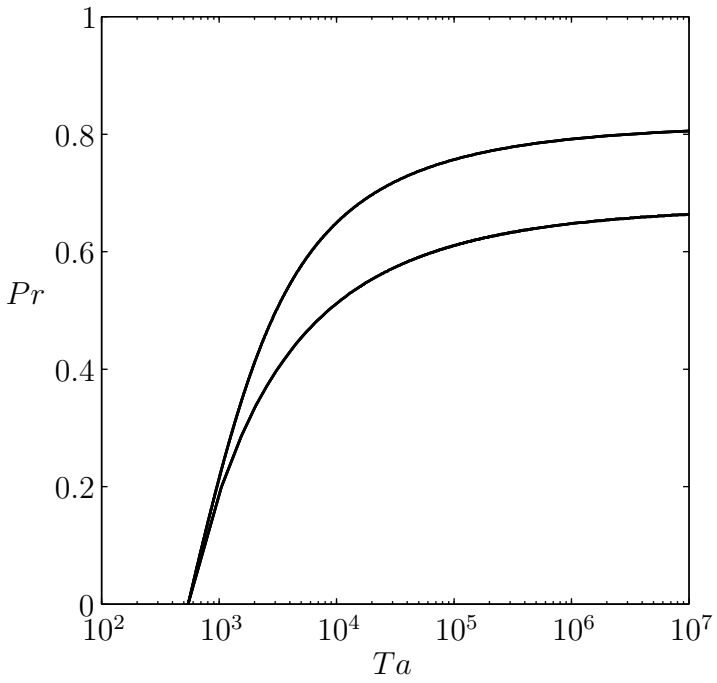

Figure 3.4: Stability boundaries in (Ta, Pr) space for rotating convection. In the top region, stationary convection is the only possibility and in the bottom region, oscillatory convection is the only possibility. In the middle region, stationary convection is preferred at onset, although oscillatory convection is possible.

3.5 Eigenfunction solution

We shall now produce two-dimensional plots of the hydrodynamic variables in (x, z) space. For the sake of brevity, since the non-rotating plots are very similar, we

present plots for the rotating system. Furthermore, we shall just do this for one particular parameter set. As we have shown, the discernible difference in increasing the rotation rate is to increase the critical wave number. Physically this means that solutions will oscillate more in the horizontal direction, as the rotation rate is increased.

We stated that the solution for the vertical velocity was $W \sim \sin n\pi z$, with the mode $n = 1$ facilitating the lowest Rayleigh number. It was necessary for Θ to be of the same parity as W and Z to be of opposite parity. Using equations (3.17), (3.18) and (3.19), the solutions for W, Θ and Z are given by

$$W = W_0 \sin \pi z, \tag{3.69}$$

$$\Theta = \frac{W_0}{(a^2 + \pi^2)} \sin \pi z, \tag{3.70}$$

$$Z = \frac{\pi T a^{\frac{1}{2}} W_0}{(\pi^2 + a^2)} \cos \pi z, \tag{3.71}$$

where W_0 is a constant determining the amplitude of the perturbations. Using the original form of our normal mode expansions given by equations (3.9), (3.10) and (3.11), we have

$$w = \left(a^2 + \pi^2\right) \cos ax \sin \pi z, \tag{3.72}$$

$$\theta = \cos ax \sin \pi z, \tag{3.73}$$

$$\zeta = \pi T a^{\frac{1}{2}} \cos ax \cos \pi z, \tag{3.74}$$

where we have —arbitrarily—chosen $W_0 = a^2 + \pi^2$. In Figure 3.5 we plot these quantities for stationary convection at $Ta = 10^4$, in a box whose length is determined by the critical wave number. It can be seen that the flow is composed of rising and sinking columns of fluid, that are driven by the buoyancy. These are known as convection cells. For a larger Taylor number, in a box of the same length, the linear eigenfunctions would be composed of more cells in the horizontal.

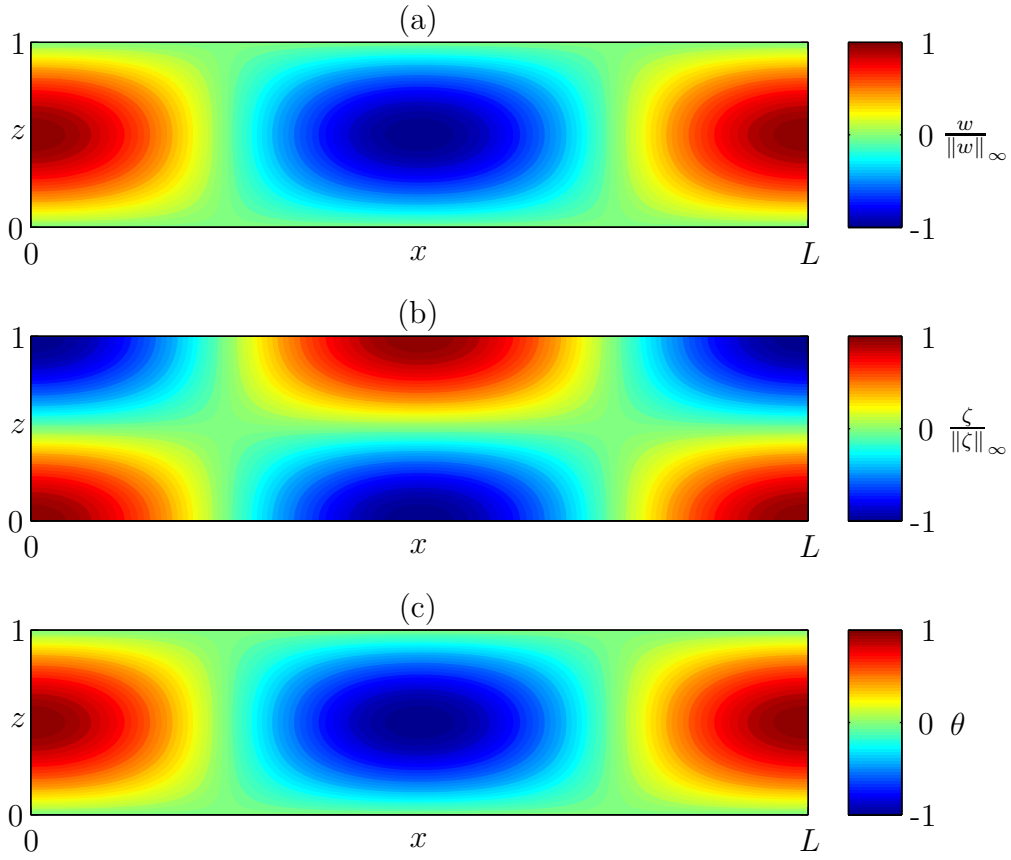

Figure 3.5: Plots of (a) the normalised vertical velocity ($\|w\|_\infty = 42.3$), (b) the normalised vertical vorticity ($\|\zeta\|_\infty = 314$) and (c) the temperature perturbation, for $Ta = 10^4, Pr = 1, R = Ra_c^{(s)}$, where $L = 1.10$.

3.6 Summary

In this chapter we reviewed the linear stability of the system to normal mode disturbances, guided by Chandrasekhar (1961), Veronis (1959) and Drazin & Reid (1981). We derived conditions upon the governing dimensionless parameters: the Rayleigh number, Ra; the Prandtl number, Pr and the Taylor number, Ta as well as the particular wave number of a disturbance, a, that determined when instability would manifest. This gave us the critical value of the Rayleigh number, for a particular wave number, at which convection could occur. This was done for the

case of no rotation, as well as the rotating system. Furthermore, we distinguished between the type of instability at the onset of convection—stationary or oscillatory. We computed stability conditions to determine the type of instability at the onset of convection that were dependent on the value of the Taylor number and the Prandtl number.

Chapter 4

Nonlinear numerical method

In Chapter 3 we studied the linear theory of rotating convection, revealing information about the onset of instability in terms of normal modes. Since we really wish to chart the nonlinear evolution of these instabilities as they progress in time, we must solve the governing hydrodynamic equations numerically. Thus the primary concern of this chapter is with the derivation of a suitable numerical procedure. Using a Fourier-Chebyshev pseudospectral method allows us to transform the continuous system of PDEs into a discrete system of matrix-vector problems that can be efficiently solved using a computer. Spectral methods are widely used in the area of fluid dynamics and—as well as convection—have been used to solve, numerically, problems that include: shear flow, magnetohydrodynamic and inertial instabilities. We shall begin by reviewing the class of numerical methods we are to use, followed by an in-depth application to the specific problem we are looking at.

4.1 Mathematical formulation

4.1.1 Overview

To solve the time-dependent, hydrodynamic equations we employ a Fourier-Chebyshev, pseudospectral method, of which the constituent components outlined in this chapter can be found within Canuto *et al.* (1988), Trefethen (2000), Boyd (2001), Peyret (2002), Canuto *et al.* (2006) and Glatzmaier (2013). Since their inception in the 1960s spectral methods have become one of the primary ways of solving partial differential equations. Spectral methods were developed concurrently with the Fast Fourier Transform algorithm of Cooley & Tukey (1965)—an algorithm apparently known to Carl Friedrich Gauss in 1805 but published posthumously (see Gauss (1866))—and have grown in popularity since. This is due to the subsequent development of both computing hardware, and computing resources: in particular fast, efficient algorithms such as FFTW (Frigo & Johnson (2005), Frigo & Johnson (2012)) for numerically computing Fast Fourier Transforms. In rectangular domains, spectral methods are especially powerful, achieving high levels of accuracy for relatively low computational effort. Fourier-Chebyshev pseudospectral methods have been used successfully in previous nonlinear two-dimensional convection studies (see e.g. DeLuca *et al.* (1990)) and are also favoured in three-dimensional studies (see e.g. Cox & Matthews (1997) and Schmitz & Tilgner (2009)).

When applying spectral methods to time-dependent, partial differential equations, the underlying principle is to write the dependent variables as a sum of known spatially-varying basis functions and unknown time-dependent coefficients. We then need only work with the coefficients, solving such that they satisfy the equations and boundary conditions. We discretise the computational domain with a grid of coordinates and are able to interchange between the physical values of the dependent variables (evaluated at the grid points) and their spectral representations, by suitable spectral transformations. In particular, the Fast Fourier Transform (see Cooley &

Tukey (1965)) and the Chebyshev transform, which is itself a manifestation of the real-valued Fast Fourier Transform. Knowing the physical values of a dependent variable and its spectral coefficients are equivalent, and one can be inferred from the other.

Spectral methods are *global* in the sense that each basis function is defined on the whole computational domain. Hence information at any point within the domain is inherently linked to every other point within the domain. For this reason, we require that the dependent variables are sufficiently smooth, i.e. they do not develop sharp discontinuities (shocks). This is in contrast to local methods, such as finite difference methods, where dependent variables are only non-zero over a defined subdomain. In principle, the series expansions of our dependent variables contain an infinite number of terms, though in practice they are truncated at some finite integer value, N, known as the *numerical resolution*. Increasing N improves the accuracy of our solution, although requires more computational effort, owing to the greater number of terms in the expansion. Therefore it will be seen that the resolution plays a pivotal role in our solving of the governing equations: we wish to solve the equations as accurately as possible, in a realistic amount of time. Spectral methods demonstrate *exponential convergence*, whereby the error due to truncation scales like $O(e^{-N})$.

Since we have the power to choose the basis functions that comprise our spectral expansions, differentiation is computed easily and we are able to derive spectral analogues of the differential operators occurring in the governing partial equations, and how these affect the spectral coefficients. The precise term *pseudospectral* owes to the way in which nonlinear terms within the equations are handled. For two dependent variables expressed as finite sums, multiplying these together requires the use of convolution. This is a computationally expensive process so we choose to perform all multiplication on the physical grid. Multiplication is performed in a pointwise manner, evaluating the product of two dependent variables at each grid point. We then calculate the spectral representation of the resulting nonlinear product using the requisite spectral transformations. In the whole procedure

outlined in this chapter, it is the evaluation of nonlinear terms that requires most computational time per cycle.

4.1.2 The equations

A detailed derivation of the governing equations in the so-called vorticity-streamfunction formulation has already been given in Chapter 2, though we will re-state the equations to be solved numerically here, for ease of reference. Collecting time derivatives and diffusive terms on the left-hand side and all other terms on the right-hand side, we have

$$\frac{\partial \omega}{\partial t} - Pr\nabla^2\omega = -RaPr\frac{\partial \theta}{\partial x} + Ta^{\frac{1}{2}}Pr\frac{\partial v}{\partial z} - J(\psi,\omega) \equiv f, \tag{4.1}$$

$$\frac{\partial \theta}{\partial t} - \nabla^2\theta = \frac{\partial \psi}{\partial x} - J(\psi,\theta) \equiv g, \tag{4.2}$$

$$\frac{\partial v}{\partial t} - Pr\nabla^2 v = Ta^{\frac{1}{2}}Pr\frac{\partial \psi}{\partial z} - J(\psi,v) \equiv h, \tag{4.3}$$

$$\nabla^2\psi = -\omega \tag{4.4}$$

where we have denoted by f, g and h, the right-hand sides of equations (4.1), (4.2) and (4.3) respectively. It is in this specific form that we shall numerically solve the equations, supplemented with the following stress-free boundary conditions

$$\psi = \omega = \theta = \frac{\partial v}{\partial z} = 0 \quad \text{at} \quad z = 0 \text{ and } z = 1. \tag{4.5}$$

4.1.3 Coordinate transformation

Our dimensionless set of governing hydrodynamic equations are posed on the interval given by $(x, z) \in [0, L] \times [0, 1]$, where $L = 2\pi/a$ and a is a wavenumber that acts to define the *aspect ratio* of our domain. The Fourier-Chebyshev pseudospectral method which we are to use, requires equations that are posed on the interval $[0, 2\pi] \times [-1, 1]$. Hence it is necessary to employ the following coordinate transformation, in order to map our equations from the actual domain

into a computational domain, given by the following

$$(X, Z) = (ax, 2z - 1) \in [0, 2\pi] \times [-1, 1]. \tag{4.6}$$

[Note that we have introduced Z above to denote the rescaled vertical coordinate within the computational domain. In Chapter 3 this was used to denote the vertical velocity eigenfunction. Whilst this quantity shall not arise in the following analysis, it is prudent to comment on this redefinition, to avoid any confusion.] With such a scaling, this obviously has implications when taking derivatives, hence

$$\nabla = (\partial_x, \partial_z) = (a\partial_X, 2\partial_Z) \Rightarrow \nabla^2 = a^2\partial_{XX} + 4\partial_{ZZ}. \tag{4.7}$$

4.2 Fourier series

4.2.1 Series expansion

We have already seen that the equations governing rotating convection admit instabilities in the form of normal modes: sinusoidal disturbances to the basic conducting state. Following on from this we expand our hydrodynamic variables in a truncated Fourier series in the horizontal coordinate x. This has the implication that everything is periodic in the x-direction. With this we posit

$$\omega(X, Z, t) = \sum_{m=0}^{N_x-1} \hat{\omega}_m(Z, t)e^{imX} + \text{c.c.}, \tag{4.8}$$

$$\theta(X, Z, t) = \sum_{m=0}^{N_x-1} \hat{\theta}_m(Z, t)e^{imX} + \text{c.c.}, \tag{4.9}$$

$$\psi(X, Z, t) = \sum_{m=0}^{N_x-1} \hat{\psi}_m(Z, t)e^{imX} + \text{c.c.}, \tag{4.10}$$

$$v(X, Z, t) = \sum_{m=0}^{N_x-1} \hat{v}_m(Z, t)e^{imX} + \text{c.c.}, \tag{4.11}$$

where we have used c.c. to denote the complex conjugate. Here we must recall that $X = ax$, so whilst in the computational domain quantities are periodic with

period 2π, in the actual domain, they are periodic with period $2\pi/a$. Here N_x is our *numerical resolution* in the x direction; we have N_x different terms within our spectral expansion. We refer to the distinct m as wave numbers, wave modes, or harmonics, since a particular m gives a particular sine or cosine.

We now sample all our variables on an evenly spaced, periodic grid, with grid values given by

$$X_k = \frac{2\pi k}{N_x} \quad \text{for} \quad k = 0, 1, \ldots, N_x - 1. \tag{4.12}$$

Considering the vorticity for purposes of example only, since all other quantities are treated likewise, this gives

$$\omega_k(Z,t) \equiv \omega(X_k, Z, t) = \sum_{m=0}^{N_x-1} \hat{\omega}_m(Z,t) e^{\frac{2\pi imk}{N_x}}. \tag{4.13}$$

We may now infer the spectral coefficients from the above expansion by taking the discrete Fourier transform (see Frigo & Johnson (2012), §4.8.2), given by

$$\hat{\omega}_m(Z,t) = \frac{1}{N_x} \sum_{k=0}^{N_x-1} \omega_k(Z,t) e^{-\frac{2\pi imk}{N_x}}. \tag{4.14}$$

4.2.2 Differentiation

Looking at the form of expansions (4.8)–(4.11) it is clear that if we wish to differentiate with respect to x, this amounts to multiplying the expansion through by a factor of iam, i.e.

$$\partial_x \omega(X, Z, t) = \sum_{m=0}^{N_x-1} iam\hat{\omega}_m(Z,t) e^{imX}.$$

Using this fact, and substituting these series expansions into the governing equations gives

$$\partial_t \hat{\omega}_m - Pr\left(4\partial_{ZZ} - a^2m^2\right)\hat{\omega}_m = \hat{f}_m, \tag{4.15}$$

$$\partial_t \hat{\theta}_m - \left(4\partial_{ZZ} - a^2m^2\right)\hat{\theta}_m = \hat{g}_m, \tag{4.16}$$

$$\partial_t \hat{v}_m - Pr\left(4\partial_{ZZ} - a^2m^2\right)\hat{v}_m = \hat{h}_m, \tag{4.17}$$

$$(4\partial_{ZZ} - a^2m^2)\hat{\psi}_m = -\hat{\omega}_m. \tag{4.18}$$

We have cancelled all exponential terms and dropped the summation signs for convenience, yet it is key to remember that the above set of equations must be solved for $m = 0, 1, \ldots, N_x - 1$, along with the boundary conditions given by equation (4.5). In our series expansion this amounts to satisfying

$$\hat{\omega}_m(\pm 1, t) = \hat{\theta}_m(\pm 1, t) = \hat{\psi}_m(\pm 1, t) = \partial_Z \hat{v}_m(\pm 1, t) = 0. \tag{4.19}$$

Note also, that $\hat{f}_m$, $\hat{g}_m$ and $\hat{h}_m$ are the Fourier coefficients of the right hand sides of equations (4.1), (4.2) and (4.3) that have been computed in a point-wise manner, on the physical grid, as described in the introduction to this chapter.

4.2.3 Aliasing

As a cautionary note, we must be aware that *aliasing* errors could be present due to the pseudospectral nature of our numerical method. Aliasing occurs when periodic functions are sampled on a finite grid, causing modes with different wave numbers to become indistinguishable. For example, consider the functions $\sin x$ and $\sin 5x$ when sampled five times at equispaced points in the interval $[0, 2\pi]$. Despite the fact that $\sin 5x$ oscillates much more rapidly than $\sin x$, when sampled on the grid we have chosen, both functions attain the exact same values. Furthermore, both functions will have the same spectral coefficients.

When computing Fourier transforms of—quadratic—nonlinear products, it is conceivable that the interaction between two Fourier wave modes in our spectrum could generate a wave mode that lies outside this spectrum. Such a wave mode would then be *aliased* to a lower wave mode in our spectrum, that is still below the cut-off provided by the numerical resolution. This would give the—false —appearance of a more vigorously oscillating mode. There are several methods used to quell this spurious behaviour, most notably Orszag's 2/3 rule (see Orszag (1971)). This involves equating to zero the coefficients of the highest third of modes, immediately before performing a Fourier transformation from spectral to grid space. This method

works since the quadratic interaction of any two wave modes within the spectrum is aliased to a wave mode that is filtered out (see Boyd (2001)).

4.3 Chebyshev series

4.3.1 Properties

Convection is driven by buoyancy, so the bulk of the motion is dominated by processes occurring in the vertical direction. Coupled with the boundary conditions on the top and bottom boundaries, we expect that there will be thin boundary layer regions where the temperature perturbation drops from its core value to zero on the boundary. For this reason we must ensure that our spectral expansions are structured such that they capture this sharp transitional behaviour, hence we choose to expand our vertical dependence as a sum of Chebyshev polynomials, rather than Fourier modes. Chebyshev polynomials possess the desirable property of rapid convergence, as well as oscillating more rapidly as you approach the boundaries of the computational domain; key in order to capture the boundary layer behaviour.

The Chebyshev polynomials of the first kind are defined, with $Z \in [-1, 1]$, according to the following recurrence relation

$$T_0(Z) = 1, \tag{4.20}$$

$$T_1(Z) = Z, \tag{4.21}$$

$$T_n(Z) = 2ZT_{n-1}(Z) - T_{n-2}(Z) \quad \text{for} \quad n \geq 2. \tag{4.22}$$

Concurrently they may be defined trigonometrically as follows

$$T_n(Z) = \cos\left(n \arccos(Z)\right) \quad \text{for} \quad n = 0, 1, \ldots \tag{4.23}$$

For further properties of Chebyshev polynomials, in the framework of pseudospectral methods, one should consult Boyd (2001).

4.3.2 Series expansion

Thus we expand our variables as follows

$$\hat{\omega}_m(Z,t) = \sum_{l=0}^{N_z+1} \hat{\omega}_{lm}(t) T_l(Z), \tag{4.24}$$

$$\hat{\theta}_m(Z,t) = \sum_{l=0}^{N_z+1} \hat{\theta}_{lm}(t) T_l(Z), \tag{4.25}$$

$$\hat{\psi}_m(Z,t) = \sum_{l=0}^{N_z+1} \hat{\psi}_{lm}(t) T_l(Z), \tag{4.26}$$

$$\hat{v}_m(Z,t) = \sum_{l=0}^{N_z+1} \hat{v}_{lm}(t) T_l(Z). \tag{4.27}$$

Here N_z represents the *numerical resolution* of our spectral expansions in the z-direction, though note that they actually comprise $N_z + 2$ Chebyshev polynomials, rather than N_z. Once again we evaluate our expansions on a grid of points; the N_z Chebyshev-Gauss-Lobatto points, defined by

$$Z_j = \cos \frac{(2j+1)\pi}{2N_z} \quad \text{for} \quad j = 0, 1, \ldots, N_z - 1. \tag{4.28}$$

The Gauss-Lobatto points are actually the zeros of the Chebyshev polynomials themselves and so possess the desirable property of clustering near the boundaries, allowing us to resolve the boundary layer structures. It should be noted, however, that the above set of N_z points do not include the boundary points at $Z = \pm 1$, therefore we require two supplementary equations, in order to impose the boundary conditions. This is the reason why our series expansions above contain $N_z + 2$, rather than N_z, terms; so that we have enough terms in order to satisfy the boundary conditions. For demonstrative purposes, sampling the vorticity on the Gauss-Lobatto grid gives

$$\hat{\omega}_{mj}(t) \equiv \hat{\omega}_m(Z_j, t) = \sum_{l=0}^{N_z+1} \hat{\omega}_{lm}(t) T_l(Z_j). \tag{4.29}$$

Once again we may infer the spectral coefficients by taking a suitable transform: a discrete cosine transform (see Frigo & Johnson (2012), §4.8.3), which is a real, even,

discrete Fourier transform

$$\hat{\omega}_{lm}(t) = 2 \sum_{j=0}^{N_z+1} \hat{\omega}_{mj}(t) T_l(Z_j). \tag{4.30}$$

4.3.3 Differentiation

Unlike the Fourier expansions used in the x direction, where differentiation just involved multiplying through by some factor, Chebyshev expansions do not permit such simplicity. Considering the vorticity, since the same principle applies for the other hydrodynamic variables, we write

$$\frac{\partial^p}{\partial Z^p} \hat{\omega}_m(Z,t) = \sum_{l=0}^{N_z+1} \hat{\omega}_{lm}^{(p)}(t) T_l(Z). \tag{4.31}$$

That is, we have expanded the p-th partial derivative of $\hat{\omega}_m(Z,t)$ with respect to Z in a Chebyshev series of its own. For example, suppose that for a particular m

$$\hat{\omega}_m(Z,t) = Z^2 + 2Z + 1. \tag{4.32}$$

From equation (4.22) we know that $T_0 = 1,\ T_1 = Z,\ T_2 = 2Z^2 - 1$, so the Chebyshev expansion of (4.32) has the following coefficients

$$\left\{ \hat{\omega}_{0m} = \frac{3}{2}, \quad \hat{\omega}_{1m} = 2, \quad \hat{\omega}_{2m} = \frac{1}{2}, \quad \hat{\omega}_{lm} = 0 \quad \text{for} \quad l \geq 3 \right\}. \tag{4.33}$$

Explicitly differentiating equation (4.32), twice with respect to Z, gives

$$\partial_{ZZ} \hat{\omega}_m(Z,t) = 2, \tag{4.34}$$

yielding the following set of second derivative coefficients

$$\left\{ \hat{\omega}_{0m}^{(2)} = 2, \quad \hat{\omega}_{lm}^{(2)} = 0 \quad \text{for} \quad l \geq 1 \right\}. \tag{4.35}$$

We insert our spectral expansions, given by equations (4.24)–(4.27), into equations (4.16)–(4.18), giving

$$\partial_t \hat{\omega}_{lm} - Pr\left(4\hat{\omega}^{(2)}_{lm} - a^2 m^2 \hat{\omega}_{lm}\right) = \hat{f}_{lm}, \tag{4.36}$$

$$\partial_t \hat{\theta}_{lm} - \left(4\hat{\theta}^{(2)}_{lm} - a^2 m^2 \hat{\theta}_{lm}\right) = \hat{g}_{lm}, \tag{4.37}$$

$$\partial_t \hat{v}_{lm} - \left(4\hat{v}^{(2)}_{lm} - a^2 m^2 \hat{v}_{lm}\right) = \hat{h}_{lm}, \tag{4.38}$$

$$\left(4\hat{\psi}^{(2)}_{lm} - a^2 m^2 \hat{\psi}_{lm}\right) = -\hat{\omega}_{lm}. \tag{4.39}$$

Note that we have cancelled all the $T_l(z_j)$ terms and once again dropped the summation signs for convenience, remembering that this set of equations must be solved for $l = 0, 1, \ldots, N_z + 1$, $m = 0, 1, \ldots, N_x - 1$. Finally, in terms of our series expansions, the boundary conditions read

$$\sum_{l=0}^{N_z+1} (\pm 1)^l \hat{\omega}_{lm}(t) = \sum_{l=0}^{N_z+1} (\pm 1)^l \hat{\theta}_{lm}(t) = \sum_{l=0}^{N_z+1} (\pm 1)^l \hat{\psi}_{lm}(t) = \sum_{l=0}^{N_z+1} (\pm 1)^l \hat{v}^{(1)}_{lm}(t) = 0, \tag{4.40}$$

For a more complicated expression, containing many more terms, analytically carrying out an explicit differentiation would be a very costly procedure. For this reason we seek to determine the second derivative coefficients via recursion, in terms of the known spectral coefficients. In general, the p-th derivative coefficients are to be determined, in descending order, using the following recurrence relation due to Boyd (2001)

$$c_{l-1}\hat{\omega}^{(p)}_{(l-1)m} = \hat{\omega}^{(p)}_{(l+1)m} + 2l\hat{\omega}^{(p-1)}_{lm} \quad \text{for} \quad l = 1, 2, \ldots, N_z + 2 - p, \quad p \geq 1 \tag{4.41}$$

with the starting condition(s) $\hat{\omega}^{(p)}_{lm} = 0 \quad \text{for} \quad l \geq N_z + 2 - p$, where we have

$$c_l = \begin{cases} 2 & \text{for} \quad l = 0, \\ 1 & \text{for} \quad l > 0. \end{cases} \tag{4.42}$$

Using the recurrence relation above, it is possible to express the p-th derivative coefficients in terms of the original spectral coefficients via

$$\hat{\omega}^{(p)}_{lm} = \sum_{k=0}^{N_z+1} C^{(p)}_{lk} \hat{\omega}_{km}, \tag{4.43}$$

for $l = 0, 1, \ldots, N_z + 1$, $m = 0, 1, \ldots, N_x$. This allows us to write the second derivative coefficients in hydrodynamic equations above, in terms of the original spectral coefficients. Furthermore, this allows us to write the final boundary condition in equation (4.40) as

$$\sum_{l=0}^{N_z+1} \left(\sum_{k=0}^{N_z+1} (\pm 1)^k C_{kl}^{(1)} \right) \hat{v}_{lm} = 0. \tag{4.44}$$

4.4 System recombination

4.4.1 Derivation

Rather than using equation (4.43) to express the second derivative coefficients in terms of the original spectral coefficients in equations (4.36)–(4.39) we follow the guidance of Peyret (2002). Consider the recurrence relation in equation (4.41) above, written with $p = 1$ and $p = 2$. This gives, respectively

$$c_{l-1}\hat{\omega}_{(l-1)m}^{(1)} = e_{l+2}\hat{\omega}_{(l+1)m}^{(1)} + 2l\hat{\omega}_{lm} \quad \text{for} \quad l = 1, 2, \ldots, N_z + 1, \tag{4.45}$$

$$c_{l-1}\hat{\omega}_{(l-1)m}^{(2)} = e_{l+3}\hat{\omega}_{(l+1)m}^{(2)} + 2l\hat{\omega}_{lm}^{(1)} \quad \text{for} \quad l = 1, 2, \ldots, N_z + 1, \tag{4.46}$$

with

$$e_l = \begin{cases} 1 & \text{for} \quad l \leq N_z + 1, \\ 0 & \text{for} \quad l > N_z + 1. \end{cases} \tag{4.47}$$

In the above equations, note that we have $\hat{\omega}_{lm}^{(0)} \equiv \hat{\omega}_{lm}$, the original series coefficients. Substituting $l - 1$ and $l + 1$, for l, in the $p = 2$ equation, respectively gives

$$c_{l-2}\hat{\omega}_{(l-2)m}^{(2)} = e_{k+2}\hat{\omega}_{lm}^{(2)} + 2(l-1)\hat{\omega}_{(l-1)m}^{(1)} \qquad \text{for} \quad l = 2, 3, \ldots, N_z + 2, \tag{4.48}$$

$$c_l\hat{\omega}_{lm}^{(2)} = e_{l+4}\hat{\omega}_{(l+2)m}^{(2)} + 2(l+1)\hat{\omega}_{(l+1)m}^{(1)} \qquad \text{for} \quad l = 0, 1, \ldots, N_z. \tag{4.49}$$

We are then able to rearrange the above equations, collecting terms of the same order derivative, giving

$$\Rightarrow \hat{\omega}^{(1)}_{(l-1)m} = \frac{c_{l-2}\hat{\omega}^{(2)}_{(l-2)m} - e_{k+2}\hat{\omega}^{(2)}_{lm}}{2(l-1)} \qquad \text{for} \quad l = 2, 3, \ldots, N_z + 2, \tag{4.50}$$

$$\Rightarrow \hat{\omega}^{(1)}_{(l+1)m} = \frac{c_l\hat{\omega}^{(2)}_{lm} - e_{l+4}\hat{\omega}^{(2)}_{(l+2)m}}{2(l+1)} \qquad \text{for} \quad l = 0, 1, \ldots, N_z. \tag{4.51}$$

We can now use these expressions within equation (4.45), in order to eliminate the $l-1$ and $l+1$ terms

$$\frac{c_{l-1}(c_{l-2}\hat{\omega}^{(2)}_{(l-2)m} - e_{l+2}\hat{\omega}^{(2)}_{lm})}{2(l-1)} = \frac{e_{l+2}(c_l\hat{\omega}^{(2)}_{lm} - e_{l+4}\hat{\omega}^{(2)}_{(l+2)m})}{2(l+1)} + 2l\hat{\omega}_{lm} \tag{4.52}$$

$$\text{for} \quad l = 2, 3, \ldots, N_z + 1$$

Due to the range of l values, we may disregard c_{l-1} and c_l, since they will always be equal to one and furthermore, we notice that $e_{l+2}e_{l+4} \equiv e_{l+4}$. Finally, rearranging gives

$$\frac{c_{l-2}\hat{\omega}^{(2)}_{(l-2)m}}{4l(l-1)} - \frac{e_{l+2}\hat{\omega}^{(2)}_{lm}}{4l(l-1)} - \frac{e_{l+2}\hat{\omega}^{(2)}_{lm}}{4l(l+1)} + \frac{e_{l+4}\hat{\omega}^{(2)}_{(l+2)m}}{4l(l+1)} = \hat{\omega}_{lm} \quad \text{for} \quad l = 2, 3, \ldots, N_z + 1. \tag{4.53}$$

We can write the above in the following form

$$P_l\hat{\omega}^{(2)}_{(l-2)m} + Q_l\hat{\omega}^{(2)}_{lm} + R_l\hat{\omega}^{(2)}_{(l+2)m} = \hat{\omega}_{lm} \quad \text{for} \quad l = 2, 3, \ldots, N_z + 1, \tag{4.54}$$

where

$$P_l = \frac{c_{l-2}}{4l(l-1)},\ Q_l = -\frac{e_{l+2}}{2(l^2-1)},\ R_l = \frac{e_{l+4}}{4l(l+1)} \quad \text{for} \quad l = 2, 3, \ldots, N_z + 1, \tag{4.55}$$

with c_l and e_l defined as in equations (4.42) and (4.47).

Hence if we consider the combination given by equation (4.54), we are able to eliminate all $\hat{\omega}^{(2)}_{lm}$ terms in favour of $\hat{\omega}_{lm}$ terms. In doing this, we notice that the system can be decoupled into odd and even components, since terms at order l are only affected by terms at order $l-2$ and $l+2$. To solve for the spectral coefficients we are going to pose the equations as a matrix-vector problem, thus in order to

calculate the coefficients we will have to invert a matrix. Furthermore this must be done for each variable, at every time step. Due to the aforementioned coupling, these matrices will possess a banded structure. This is the very reason for restructuring the equations in the way we have; banded matrices can be inverted in a more efficient manner than full matrices.

4.4.2 Example

For $N_z = 4$ we have a series with 6 spectral coefficients. Using the recurrence relation from equation (4.41) we have, for $p = 1$

$$\hat{\omega}_{5m}^{(1)} = 0 \tag{4.56}$$

$$c_4\hat{\omega}_{4m}^{(1)} = \hat{\omega}_{6m}^{(1)} + 10\hat{\omega}_{5m} \quad \Rightarrow \quad \hat{\omega}_{4m}^{(1)} = 10\hat{\omega}_{5m}, \tag{4.57}$$

$$c_3\hat{\omega}_{3m}^{(1)} = \hat{\omega}_{5m}^{(1)} + 8\hat{\omega}_{4m} \quad \Rightarrow \quad \hat{\omega}_{3m}^{(1)} = 8\hat{\omega}_{4m}, \tag{4.58}$$

$$c_2\hat{\omega}_{2m}^{(1)} = \hat{\omega}_{4m}^{(1)} + 6\hat{\omega}_{3m} \quad \Rightarrow \quad \hat{\omega}_{2m}^{(1)} = 10\hat{\omega}_{5m} + 6\hat{\omega}_{3m}, \tag{4.59}$$

$$c_1\hat{\omega}_{1m}^{(1)} = \hat{\omega}_{3m}^{(1)} + 4\hat{\omega}_{2m} \quad \Rightarrow \quad \hat{\omega}_{1m}^{(1)} = 8\hat{\omega}_{4m} + 4\hat{\omega}_{2m}, \tag{4.60}$$

$$c_0\hat{\omega}_{0m}^{(1)} = \hat{\omega}_{2m}^{(1)} + 2\hat{\omega}_{1m} \quad \Rightarrow \quad \hat{\omega}_{0m}^{(1)} = 5\hat{\omega}_{5m} + 3\hat{\omega}_{3m} + \hat{\omega}_{1m}. \tag{4.61}$$

Applying the recurrence relation once more, with $p = 2$, and using the computed values at $p = 1$, we are able to write the second derivative coefficients in terms of the original series coefficients

$$\hat{\omega}_{5m}^{(2)} = 0 \tag{4.62}$$

$$\hat{\omega}_{4m}^{(2)} = 0 \tag{4.63}$$

$$c_3\hat{\omega}_{3m}^{(2)} = \hat{\omega}_{5m}^{(2)} + 8\hat{\omega}_{4m}^{(1)} \quad \Rightarrow \quad \hat{\omega}_{3m}^{(2)} = 80\hat{\omega}_{5m}, \tag{4.64}$$

$$c_2\hat{\omega}_{2m}^{(2)} = \hat{\omega}_{4m}^{(2)} + 6\hat{\omega}_{3m}^{(1)} \quad \Rightarrow \quad \hat{\omega}_{2m}^{(2)} = 48\hat{\omega}_{4m}, \tag{4.65}$$

$$c_1\hat{\omega}_{1m}^{(2)} = \hat{\omega}_{3m}^{(2)} + 4\hat{\omega}_{2m}^{(1)} \quad \Rightarrow \quad \hat{\omega}_{1m}^{(2)} = 120\hat{\omega}_{5m} + 24\hat{\omega}_{3m}, \tag{4.66}$$

$$c_0\hat{\omega}_{0m}^{(2)} = \hat{\omega}_{2m}^{(2)} + 2\hat{\omega}_{1m}^{(1)} \quad \Rightarrow \quad \hat{\omega}_{0m}^{(2)} = 32\hat{\omega}_{4m} + 4\hat{\omega}_{2m}. \tag{4.67}$$

Thus, we may write this as

$$\begin{bmatrix} \hat{\omega}_{0m}^{(2)} \\ \hat{\omega}_{1m}^{(2)} \\ \hat{\omega}_{2m}^{(2)} \\ \hat{\omega}_{3m}^{(2)} \\ \hat{\omega}_{4m}^{(2)} \\ \hat{\omega}_{5m}^{(2)} \end{bmatrix} = \begin{bmatrix} 0 & 0 & 4 & 0 & 32 & 0 \\ 0 & 0 & 0 & 24 & 0 & 120 \\ 0 & 0 & 0 & 0 & 48 & 0 \\ 0 & 0 & 0 & 0 & 0 & 80 \\ 0 & 0 & 0 & 0 & 0 & 0 \\ 0 & 0 & 0 & 0 & 0 & 0 \end{bmatrix} \begin{bmatrix} \hat{\omega}_{0m} \\ \hat{\omega}_{1m} \\ \hat{\omega}_{2m} \\ \hat{\omega}_{3m} \\ \hat{\omega}_{4m} \\ \hat{\omega}_{5m} \end{bmatrix}. \tag{4.68}$$

It is apparent from looking at the above matrix that it possesses an upper-triangular structure: entries on and above the main diagonal only. Using the recombination technique we have

$$P_2 = \frac{c_0}{8} = \frac{1}{4}, \quad Q_2 = -\frac{e_4}{6} = -\frac{1}{6}, \quad R_2 = \frac{e_6}{24} = 0, \tag{4.69}$$

$$P_3 = \frac{c_1}{24} = \frac{1}{24}, \quad Q_3 = -\frac{e_5}{16} = -\frac{1}{16}, \quad R_3 = \frac{e_7}{48} = 0, \tag{4.70}$$

$$P_4 = \frac{c_2}{48} = \frac{1}{48}, \quad Q_4 = -\frac{e_6}{30} = 0, \quad R_4 = \frac{e_8}{80} = 0, \tag{4.71}$$

$$P_5 = \frac{c_3}{80} = \frac{1}{80}, \quad Q_5 = -\frac{e_7}{48} = 0, \quad R_5 = \frac{e_9}{120} = 0. \tag{4.72}$$

Thus, we may write this as

$$\begin{bmatrix} 0 & 0 & 0 & 0 & 0 & 0 \\ 0 & 0 & 0 & 0 & 0 & 0 \\ \frac{1}{4} & 0 & -\frac{1}{6} & 0 & 0 & 0 \\ 0 & \frac{1}{24} & 0 & -\frac{1}{16} & 0 & 0 \\ 0 & 0 & \frac{1}{48} & 0 & 0 & 0 \\ 0 & 0 & 0 & \frac{1}{80} & 0 & 0 \end{bmatrix} \begin{bmatrix} \hat{\omega}_{0m}^{(2)} \\ \hat{\omega}_{1m}^{(2)} \\ \hat{\omega}_{2m}^{(2)} \\ \hat{\omega}_{3m}^{(2)} \\ \hat{\omega}_{4m}^{(2)} \\ \hat{\omega}_{5m}^{(2)} \end{bmatrix} = \begin{bmatrix} \hat{\omega}_{0m} \\ \hat{\omega}_{1m} \\ \hat{\omega}_{2m} \\ \hat{\omega}_{3m} \\ \hat{\omega}_{4m} \\ \hat{\omega}_{5m} \end{bmatrix}. \tag{4.73}$$

Here it is possible to see the banded structure of the matrix: entries only on the main diagonal and the second sub-diagonal. For a larger value of N_z there would also be entries on the second super-diagonal.

4.4.3 Application

Following this derivation, we now consider the proposed linear combination above, applied to the governing equations. Using the recombination given by equation (4.54) within equations (4.36)–(4.39) gives

$$\begin{aligned} &\partial_t \left(P_l \hat{\omega}_{(l-2)m} + Q_l \hat{\omega}_{lm} + R_l \hat{\omega}_{(l+2)m} \right) \\ &-Pr \left(4\hat{\omega}_{lm} - a^2 m^2 \left(P_l \hat{\omega}_{(l-2)m} + Q_l \hat{\omega}_{lm} + R_l \hat{\omega}_{(l+2)m} \right) \right) \\ &= \quad P_l \hat{f}_{(l-2)m} + Q_l \hat{f}_{lm} + R_l \hat{f}_{(l+2)m}, \end{aligned} \tag{4.74}$$

$$\begin{aligned} &\partial_t \left(P_l \hat{\theta}_{(l-2)m} + Q_l \hat{\theta}_{lm} + R_l \hat{\theta}_{(l+2)m} \right) \\ &- \left(4\hat{\theta}_{lm} - a^2 m^2 \left(P_l \hat{\theta}_{(l-2)m} + Q_l \hat{\theta}_{lm} + R_l \hat{\theta}_{(l+2)m} \right) \right) \\ &= \quad P_l \hat{g}_{(l-2)m} + Q_l \hat{g}_{lm} + R_l \hat{g}_{(l+2)m}, \end{aligned} \tag{4.75}$$

$$\begin{aligned} &\partial_t \left(P_l \hat{v}_{(l-2)m} + Q_l \hat{v}_{lm} + R_l \hat{v}_{(l+2)m} \right) \\ &-Pr \left(4\hat{v}_{lm} - a^2 m^2 \left(P_l \hat{v}_{(l-2)m} + Q_l \hat{v}_{lm} + R_l \hat{v}_{(l+2)m} \right) \right) \\ &= \quad P_l \hat{h}_{(l-2)m} + Q_l \hat{h}_{lm} + R_l \hat{h}_{(l+2)m}, \end{aligned} \tag{4.76}$$

$$\begin{aligned} &4\hat{\psi}_{lm} - a^2 m^2 \left(P_l \hat{\psi}_{(l-2)m} + Q_l \hat{\psi}_{lm} + R_l \hat{\psi}_{(l+2)m} \right) \\ &= - \left(P_l \hat{\omega}_{(l-2)m} + Q_l \hat{\omega}_{lm} + R_l \hat{\omega}_{(l+2)m} \right). \end{aligned} \tag{4.77}$$

4.5 System solution

4.5.1 Time stepping

To discretise in time, we use a hybrid, implicit-explicit, predictor-corrector time stepping scheme. Within the predictor step, the diffusive terms on the left hand side are treated implicitly using the Crank-Nicolson scheme, which allows the use of

a larger timestep than if we used an explicit scheme. Unfortunately we cannot treat the nonlinear terms implicitly, so instead we use the second order Adams-Bashforth scheme for all the terms on the right hand side. Such a scheme can be depicted, with τ taking the value $1/2$, by

$$\frac{\hat{u}_P^{n+1} - \hat{u}^n}{\Delta t} - \nabla^2(\tau\hat{u}_P^{n+1} + (1-\tau)\hat{u}^n) = \frac{1}{2}(3\mathcal{N}^n - \mathcal{N}^{n-1}), \tag{4.78}$$

where $\hat{u}_P^{n+1}$ is to represent the predicted value of one of our state variables and $\mathcal{N}$ is to represent the nonlinear terms. It should be noted, however, that we can increase τ in order to make the scheme more implicit. Although this sacrifices accuracy, Hollerbach (2000) notes that it acts to enhance numerical stability and for some of the more computationally demanding runs, this can be implemented. For the corrector step, we use the predicted value $\hat{u}_P^{n+1}$ to calculate the nonlinear terms at the $n+1$ time level and then use both these, and the nonlinear terms at the n level, in a trapezoidal rule, to get a corrected $\hat{u}^{n+1}$ at the $n+1$ level, i.e.

$$\frac{\hat{u}_C^{n+1} - \hat{u}^n}{\Delta t} - \nabla^2(\tau\hat{u}_C^{n+1} + (1-\tau)\hat{u}^n) = \frac{1}{2}(\mathcal{N}_P^{n+1} + \mathcal{N}^n). \tag{4.79}$$

We then look at the relative size of the solutions $\hat{u}_P^{n+1}$ and $\hat{u}_C^{n+1}$ and only take $\hat{u}^{n+1} = \hat{u}_P^{n+1}$ if the following is satisfied

$$\frac{|\hat{u}_P - \hat{u}_C|_\infty}{|\hat{u}_C|_\infty} \leq \sigma_e, \tag{4.80}$$

where σ_e is a specified error tolerance. If the above cannot be satisfied, the original values are reset, we halve the timestep Δt and begin again by calculating $\hat{u}_P^{n+1}$. This process is continued until the constraint (4.80) is satisfied and then we take $\hat{u}^{n+1} = \hat{u}_P^{n+1}$ and proceed to the next timestep.

Proceeding with $\tau = 1/2$ in equations (4.74)–(4.77) we have, gathering all terms at

the same timestep together

$$\left(P_l+\frac{\Delta tPr}{2}P_l'\right)\hat{\omega}^{n+1}_{(l-2)m}+\left(Q_l+\frac{\Delta tPr}{2}Q_l'\right)\hat{\omega}^{n+1}_{lm}+\left(R_l+\frac{\Delta tPr}{2}R_l'\right)\hat{\omega}^{n+1}_{(l+2)m}$$
$$=\left(P_l-\frac{\Delta tPr}{2}P_l'\right)\hat{\omega}^{n}_{(l-2)m}+\left(Q_l-\frac{\Delta tPr}{2}Q_l'\right)\hat{\omega}^{n}_{lm}+\left(R_l-\frac{\Delta tPr}{2}R_l'\right)\hat{\omega}^{n}_{(l+2)m}$$
$$+\frac{3\Delta t}{2}\left(P_l\hat{f}^{n}_{(l-2)m}+Q_l\hat{f}^{n}_{lm}+R_l\hat{f}^{n}_{(l+2)m}\right)-\frac{\Delta t}{2}\left(P_l\hat{f}^{n-1}_{(l-2)m}+Q_l\hat{f}^{n-1}_{lm}+R_l\hat{f}^{n-1}_{(l+2)m}\right), \tag{4.81}$$

$$\left(P_l+\frac{\Delta t}{2}P_l'\right)\hat{\theta}^{n+1}_{(l-2)m}+\left(Q_l+\frac{\Delta t}{2}Q_l'\right)\hat{\theta}^{n+1}_{lm}+\left(R_l+\frac{\Delta t}{2}R_l'\right)\hat{\theta}^{n+1}_{(l+2)m}$$
$$=\left(P_l-\frac{\Delta t}{2}P_l'\right)\hat{\theta}^{n}_{(l-2)m}+\left(Q_l-\frac{\Delta t}{2}Q_l'\right)\hat{\theta}^{n}_{lm}+\left(R_l-\frac{\Delta t}{2}R_l'\right)\hat{\theta}^{n}_{(l+2)m}$$
$$+\frac{3\Delta t}{2}\left(P_l\hat{g}^{n}_{(l-2)m}+Q_l\hat{g}^{n}_{lm}+R_l\hat{g}^{n}_{(l+2)m}\right)-\frac{\Delta t}{2}\left(P_l\hat{g}^{n-1}_{(l-2)m}+Q_l\hat{g}^{n-1}_{lm}+R_l\hat{g}^{n-1}_{(l+2)m}\right), \tag{4.82}$$

$$\left(P_l+\frac{\Delta tPr}{2}P_l'\right)\hat{v}^{n+1}_{(l-2)m}+\left(Q_l+\frac{\Delta tPr}{2}Q_l'\right)\hat{v}^{n+1}_{lm}+\left(R_l+\frac{\Delta tPr}{2}R_l'\right)\hat{v}^{n+1}_{(l+2)m}$$
$$=\left(P_l-\frac{\Delta tPr}{2}P_l'\right)\hat{v}^{n}_{(l-2)m}+\left(Q_l-\frac{\Delta tPr}{2}Q_l'\right)\hat{v}^{n}_{lm}+\left(R_l-\frac{\Delta tPr}{2}R_l'\right)\hat{v}^{n}_{(l+2)m}$$
$$+\frac{3\Delta t}{2}\left(P_l\hat{h}^{n}_{(l-2)m}+Q_l\hat{h}^{n}_{lm}+R_l\hat{h}^{n}_{(l+2)m}\right)-\frac{\Delta t}{2}\left(P_l\hat{h}^{n-1}_{(l-2)m}+Q_l\hat{h}^{n-1}_{lm}+R_l\hat{h}^{n-1}_{(l+2)m}\right). \tag{4.83}$$

Finally, the streamfunction at the advanced time $n+1$ is calculated from the vorticity at $n+1$ via

$$P_l'\hat{\psi}^{(n+1)}_{(l-2)m}+Q_l'\hat{\psi}^{(n+1)}_{lm}+R_l'\hat{\psi}^{(n+1)}_{(l+2)m}=P_l\hat{\omega}^{(n)}_{(l-2)m}+Q_l\hat{\omega}^{(n)}_{lm}+R_l\hat{\omega}^{(n)}_{(l+2)m}, \tag{4.84}$$

where we have introduced the following throughout

$$P_l'=a^2m^2P_l,\quad Q_l'=a^2m^2Q_l-4,\quad R_l'=a^2m^2R_l. \tag{4.85}$$

We must remember that the above equations need to be solved for $l=2,3,\ldots,N_z+1$ and $m=0,1,\ldots,N_x-1$.

4.5.2 Matrix-vector formation

We wish to combine the discrete expressions given in equations (4.81)–(4.84) with their relevant boundary conditions, and express them in terms of matrix multiplications. We have $N_z + 2$ spectral coefficients to be determined per hydrodynamic variable, N_z equations coupling the spectral coefficients from inserting our expansions in the governing equations, plus a further two equations from the boundary conditions, thus we have $N_z + 2$ equations in total, for $N_z + 2$ unknowns, so the system is closed. Thus we pose the following matrix-vector multiplications

$$\mathcal{L}_1\hat{\boldsymbol{\omega}}_m^{n+1} = \mathcal{R}_1\hat{\boldsymbol{\omega}}_m^{n} + \frac{\Delta t}{2}\mathcal{P}\left(3\hat{\mathbf{f}}_m^{n} - \hat{\mathbf{f}}_m^{n-1}\right), \tag{4.86}$$

$$\mathcal{L}_2\hat{\boldsymbol{\theta}}_m^{n+1} = \mathcal{R}_2\hat{\boldsymbol{\theta}}_m^{n} + \frac{\Delta t}{2}\mathcal{P}\left(3\hat{\mathbf{g}}_m^{n} - \hat{\mathbf{g}}_m^{n-1}\right), \tag{4.87}$$

$$\mathcal{L}_3\hat{\mathbf{v}}_m^{n+1} = \mathcal{R}_3\hat{\mathbf{v}}_m^{n} + \frac{\Delta t}{2}\mathcal{P}\left(3\hat{\mathbf{h}}_m^{n} - \hat{\mathbf{h}}_m^{n-1}\right), \tag{4.88}$$

$$\mathcal{D}\hat{\boldsymbol{\psi}}_m^{n+1} = \mathcal{P}\hat{\boldsymbol{\omega}}_m^{n+1}. \tag{4.89}$$

The matrices above all have very similar components, differing only in the boundary conditions and the coefficients of $P_l, Q_l, R_l, P_l', Q_l', R_l'$. Generally, they are of the form

$$\{\mathcal{L}_i, \mathcal{R}_i, \mathcal{D}, \mathcal{P}\} = \begin{cases} \alpha_l & \text{for} \quad k = 0, \quad l = 0, 1, \ldots, N_z + 1, \\ \beta_l & \text{for} \quad k = 1, \quad l = 0, 1, \ldots, N_z + 1, \\ \gamma P_k + \delta P_k' & \text{for} \quad k = 2, 3, \ldots, N_z + 1, \quad l = k - 2, \\ \gamma Q_k + \delta Q_k' & \text{for} \quad k = 2, 3, \ldots, N_z + 1, \quad l = k, \\ \gamma R_k + \delta R_k' & \text{for} \quad k = 2, 3, \ldots, N_z + 1, \quad l = k + 2, \end{cases} \tag{4.90}$$

for $i = 1, 2, 3$. The coefficients take the following values in the following matrices

$$\mathcal{L}_1 \ : \ \alpha_l = 1, \quad \beta_l = (-1)^l, \quad \gamma = 1, \quad \delta = \frac{\Delta t Pr}{2}, \tag{4.91}$$

$$\mathcal{R}_1 \ : \ \alpha_l = \beta_l = 0, \quad \gamma = 1, \quad \delta = -\frac{\Delta t Pr}{2}, \tag{4.92}$$

$$\mathcal{L}_2 \ : \ \alpha_l = 1, \quad \beta_l = (-1)^l, \quad \gamma = 1, \quad \delta = \frac{\Delta t}{2}, \tag{4.93}$$

$$\mathcal{R}_2 \ : \ \alpha_l = \beta_l = 0, \quad \gamma = 1, \quad \delta = -\frac{\Delta t}{2}, \tag{4.94}$$

$$\mathcal{L}_3 \ : \ \alpha_l = \sum_{j=0}^{N_z+1} C_{jl}^{(1)}, \quad \beta_l = \sum_{j=0}^{N_z+1} (-1)^j C_{jl}^{(1)}, \quad \gamma = 1, \quad \delta = \frac{\Delta t Pr}{2}, \tag{4.95}$$

$$\mathcal{R}_3 \ : \ \alpha_l = \beta_l = 0, \quad \gamma = 1, \quad \delta = -\frac{\Delta t Pr}{2}, \tag{4.96}$$

$$\mathcal{D} \ : \ \alpha_l = 1, \quad \beta_l = (-1)^l, \quad \gamma = 0, \quad \delta = 1, \tag{4.97}$$

$$\mathcal{P} \ : \ \alpha_l = \beta_l = 0, \quad \gamma = 1, \quad \delta = 0, \tag{4.98}$$

for $l = 0, 1, \ldots, N_z + 1$. Within expression (4.90) we take k to be the matrix row index, l to be the matrix column index and recall that this set of matrix-vector equations must be solved for $m = 0, 1, \ldots, N_x - 1$. As can be seen above, the top two rows of the matrix (corresponding to $k = 0$ and $k = 1$) enforce the relevant boundary conditions and the remaining N_z rows are where we solve the equations. All matrix multiplication within the numerical code is performed using the basic linear algebra subroutines (BLAS) within LAPACK (see e.g. Anderson *et al.* (1999)).

The matrix $\mathcal{D}$ defined above, considered with $N_z = 4$, has entries

$$\mathcal{D} = \begin{bmatrix} \alpha_0 & \alpha_1 & \alpha_2 & \alpha_3 & \alpha_4 & \alpha_5 \\ \beta_0 & \beta_1 & \beta_2 & \beta_3 & \beta_4 & \beta_5 \\ P_2' & 0 & Q_2' & 0 & R_2' & 0 \\ 0 & P_3' & 0 & Q_3' & 0 & R_3' \\ 0 & 0 & P_4' & 0 & Q_4' & 0 \\ 0 & 0 & 0 & P_5' & 0 & Q_5' \end{bmatrix}. \tag{4.99}$$

The banded structure of this matrix is now readily apparent. For larger N_z the matrix size—but not structure—will change; we will only ever have entries in the top two rows, on the main diagonal, and on the second sub- and super-diagonals.

Our problem is now reduced to one of efficiently solving the set of matrix-vector products above, for each wavenumber m. This amounts to inverting the matrices appearing on the left hand sides of the above equations. To do this without taking into account any specific properties of the matrices involved, for an $(N_z+2)\times(N_z+2)$ matrix would incur a cost proportional to N_z^3 operations, which must be done N_x

times, once for each wavenumber. In the general case where we are dealing with matrices of size $(N_z+2)\times(N_z+2)$, the actual number of filled matrix entries is given by $5N_z+2$ and the number of zeros is given by $N_z^2-N_z+2$. For large matrices, the number of zero entries will greatly dominate the number of non-zero entries and to invert such a matrix without taking into account this property, would be extremely inefficient from a computational standpoint. The first step to solving this problem efficiently is to split the problem into two sub problems of half the original size, by considering odd and evenly indexed entries separately (see Peyret (2002)). This then gives us two quasi-tridiagonal matrices; entries on the main diagonal and on the first sub and super-diagonals, plus a row containing the boundary conditions. So long as the boundary conditions are the same at each bounding surface—both Dirichlet, or both Neumann—it can be seen from the expressions above that the following is true

$$\alpha_l+\beta_l=\begin{cases}2\alpha_l & \text{for } l \text{ even},\\ 0 & \text{for } l \text{ odd},\end{cases} \tag{4.100}$$

$$\alpha_l-\beta_l=\begin{cases}0 & \text{for } l \text{ even},\\ 2\alpha_l & \text{for } l \text{ odd},\end{cases} \tag{4.101}$$

thus when we split the system into odd and even components, we are able to decouple the boundary conditions also, by taking the required combination above. Hence, using $\mathcal{D}$ as an example, with $N_z=4$, after splitting, we have the following matrices

$$\mathcal{D}_{\text{even}}=\begin{bmatrix}2\alpha_0 & 2\alpha_2 & 2\alpha_4\\ P_2' & Q_2' & R_2'\\ 0 & p_4' & Q_4'\end{bmatrix}, \tag{4.102}$$

$$\mathcal{D}_{\text{odd}}=\begin{bmatrix}2\alpha_1 & 1\alpha_3 & 2\alpha_5\\ P_3' & Q_3' & R_3'\\ 0 & p_5' & Q_5'\end{bmatrix}. \tag{4.103}$$

The total number of filled matrix entries has obviously remained the same, since we have not thrown away any information, yet the number of zeros has decreased to

$1/4N_z^2 - 3/2N_z$. Again, without utilising the specific properties of these matrices, to invert them would still be inefficient, with a computational cost of the order N_z^3 operations per wavenumber, per timestep. Without the row containing the boundary conditions, these matrices would have a purely tridiagonal structure; in our case they are quasi-tridiagonal. Tridiagonal matrices can be solved at an operational cost proportional to N_z, so we seek an algorithm which can handle quasi-tridiagonal matrices in a like manner.

4.5.3 Quasi-tridiagonal matrix solution algorithm

The efficient solution to the quasi-tridiagonal matrices presented can be computed recursively, due to an algorithm presented by Peyret (2002). For demonstrative purposes, since the same technique can be applied to the other equations, we shall study the Helmholtz equation, used to determine the streamfunction. Consistent with the notation of Peyret (2002) the system may be written as follows, for either the even or odd components of the governing equations

$$p_i w_{i-1} + q_i w_i + r_i w_{i+1} = f_i, \quad \text{for} \quad i = 1, \ldots, \frac{N_z}{2} - 1 \tag{4.104}$$

$$p_{\frac{N_z}{2}} w_{\frac{N_z}{2}-1} + q_{\frac{N_z}{2}} w_{\frac{N_z}{2}} = f_{\frac{N_z}{2}}, \tag{4.105}$$

$$c_0 w_0 + c_1 w_1 + \ldots + c_{\frac{N_z}{2}} w_{\frac{N_z}{2}} = 0, \tag{4.106}$$

where p, q, r and f, are to represent the matrix entries given by equation (4.90). Here w_i is the spectral coefficient of any one of our hydrodynamic variables, for a particular wave number, at the advanced time step: $\hat{\omega}_{im}^{n+1}$, $\hat{\theta}_{im}^{n+1}$, $\hat{\psi}_{im}^{n+1}$, $\hat{v}_{im}^{n+1}$, for $i = 0, \ldots, \frac{N_z}{2}$ and $c_i = \alpha_i + \beta_i$ for $i = 0, \ldots, \frac{N_z}{2}$. The solution is written as

$$w_{i+1} = X_i w_i + Y_i, \quad \text{for} \quad i = 0, \ldots, \frac{N_z}{2} - 1. \tag{4.107}$$

The coefficients X_i and Y_i are also determined recursively. Inserting our postulate (4.107) into equation (4.104) gives

$$p_i w_{i-1} + q_i w_i + r_i \left(X_i w_i + Y_i\right) = f_i, \quad \text{for} \quad i = 1, \ldots, \frac{N_z}{2} - 1, \tag{4.108}$$

which allows us to rearrange for

$$w_i = -\frac{p_i}{(q_i + r_i X_i)} w_{i-1} + \frac{f_i - r_i Y_i}{(q_i + r_i X_i)} \quad \text{for} \quad i = 1, \ldots, \frac{N_z}{2} - 1. \tag{4.109}$$

Writing equation (4.107) with $i \equiv i - 1$ gives

$$w_i = X_{i-1} w_{i-1} + Y_{i-1}, \quad \text{for} \quad i = 1, \ldots, \frac{N_z}{2}, \tag{4.110}$$

and upon comparison with equation (4.109), allows us to identify the following

$$X_{i-1} = -\frac{p_i}{(q_i + r_i X_i)}, \quad Y_{i-1} = \frac{f_i - r_i Y_i}{(q_i + r_i X_i)} \quad \text{for} \quad i = 1, \ldots, \frac{N_z}{2} - 1. \tag{4.111}$$

We must first calculate $X_{\frac{N_z}{2}-1}$ and $Y_{\frac{N_z}{2}-1}$ in order to initiate the recurrence. Writing equation (4.107) with $i = \frac{N_z}{2} - 1$ gives

$$w_{\frac{N_z}{2}} = X_{\frac{N_z}{2}-1} w_{\frac{N_z}{2}-1} + Y_{\frac{N_z}{2}-1}. \tag{4.112}$$

Furthermore, rearranging equation (4.105) gives

$$w_{\frac{N_z}{2}} = -\frac{p_{\frac{N_z}{2}}}{q_{\frac{N_z}{2}}} w_{\frac{N_z}{2}-1} + \frac{f_{\frac{N_z}{2}}}{q_{\frac{N_z}{2}}}, \tag{4.113}$$

and upon comparing the previous two equations we have

$$X_{\frac{N_z}{2}-1} = -\frac{p_{\frac{N_z}{2}}}{q_{\frac{N_z}{2}}}, \quad Y_{\frac{N_z}{2}-1} = \frac{f_{\frac{N_z}{2}}}{q_{\frac{N_z}{2}}}. \tag{4.114}$$

Now that we are able to calculate X_i and Y_i for $i = 0, \ldots, \frac{N_z}{2} - 1$, we may calculate w_i provided we know the initial value w_0. In order to calculate this we write

$$w_i = \theta_i w_0 + \lambda_i, \quad \text{for} \quad i = 0, \ldots, \frac{N_z}{2}. \tag{4.115}$$

With $i = 0$ we may immediately identify

$$\theta_0 = 1, \quad \lambda_0 = 0. \tag{4.116}$$

Writing equation (4.115) with $i \equiv i - 1$ gives

$$w_{i-1} = \theta_{i-1} w_0 + \lambda_{i-1}, \quad \text{for} \quad i = 1, \ldots, \frac{N_z}{2} + 1. \tag{4.117}$$

Inserting this expression into equation (4.110) yields

$$w_i = X_{i-1}\left(\theta_{i-1}w_0 + \lambda_{i-1}\right) + Y_{i-1}, \quad \text{for} \quad i = 1, \ldots, \frac{N_z}{2}, \tag{4.118}$$

and upon comparison with equation (4.115) allows us to identify

$$\theta_i = X_{i-1}\theta_{i-1}, \quad \lambda_i = X_{i-1}\lambda_{i-1} + Y_{i-1}, \quad \text{for} \quad i = 1, \ldots, \frac{N_z}{2}. \tag{4.119}$$

Finally, substituting expression (4.115) into equation (4.106) gives

$$w_0 = \frac{g - \Lambda}{\Theta}, \tag{4.120}$$

where

$$\Theta = \sum_{i=0}^{\frac{N_z}{2}} c_i\theta_i, \tag{4.121}$$

$$\Lambda = \sum_{i=0}^{\frac{N_z}{2}} c_i\lambda_i. \tag{4.122}$$

Thus we are now able to calculate all the w_i and hence our solution is known. Using this algorithm for the odd and even components of each variable will give us a complete numerical solution to the hydrodynamic equations.

4.6 Testing

In order to confirm that the numerical method we have outlined in this chapter solves the governing equations correctly and does indeed model the convective process that it should, we have used the results of Moore & Weiss (1973) as a benchmark case. They present results for a range of different Rayleigh and Prandtl numbers, and give explicit values of output parameters such as the Nusselt number. Furthermore, they include plots of the vorticity, streamfunction and temperature, against which we have compared our results. We were able to reproduce the results of Moore & Weiss (1973) for several chosen test cases. For low Rayleigh numbers, we agreed exactly with their Nusselt number values, yet noted some divergence for higher Rayleigh numbers. This

can be attributed to the fact that our calculations were performed using a spectral method with a much higher spatial resolution than the finite difference method used by Moore & Weiss (1973). As we noted at the beginning of this chapter, spectral methods offer the advantage of superior accuracy over methods such as finite differences, hence the difference is likely to be caused by under-resolution on their part.

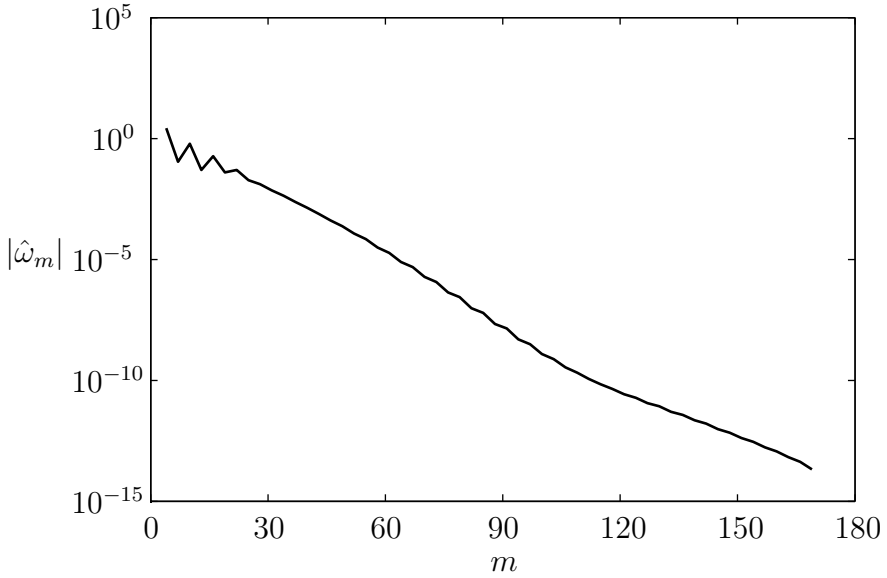

Figure 4.1: Example vorticity power spectrum for a well-resolved numerical simulation.

In order to check that our solutions were adequately resolved, we looked at the power spectrum of the spectral coefficients, versus the wavenumber. For a well-resolved simulation, this power spectrum should decay with increasing wavenumber. An example of this can be seen in Figure 4.1, where we show an example of the power spectra of the vorticity for a well-resolved run. Here the power in the lowest mode is at least a factor of 10^{10} greater than in the highest—a sufficient decay. In fact, even a decay of 10^5 in the power spectrum is sufficient for a run to be classified as well-resolved. All the simulations we performed exhibited at least such a decay in their power spectrum.

In order to confirm the reliability of our results we performed simulations at the same

input parameter values, for several different—increasing—resolutions. A numerical simulation is considered to be well-resolved and reliable at a given resolution if, when performed at a higher resolution, the results concur. A way to compare results at different resolutions is by looking at a time series of, for example, the kinetic energy, E_U. An example of this can be seen in Figure 4.2. After integrating for long enough that any initial, transient behaviour has ceased, both simulations approach the same average kinetic energy value. For all the test cases we performed, after performing numerical simulations at a given resolution, we doubled this resolution in order to confirm that we achieved the same results.

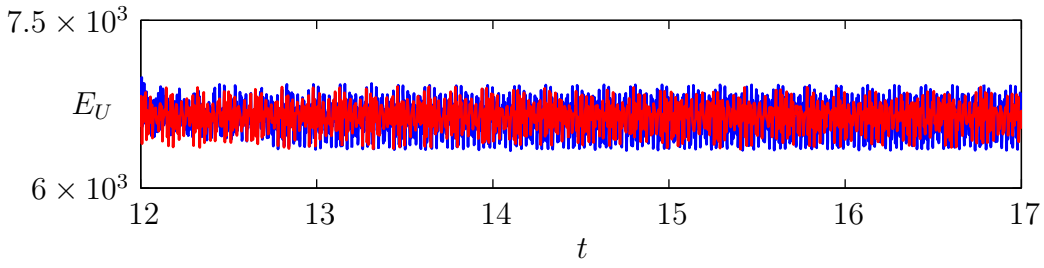

Figure 4.2: Time series of kinetic energy for two well-resolved simulations at the same parameter values. The numerical resolution for each run is given by $[N_x \times N_z] = [256 \times 96]$ (blue) and $[512 \times 69]$ (red).

Owing to all these tests, we proceed in the confidence that our numerical method is indeed correct. Furthermore, we are able to implement these tests for any simulations we perform, in order to confirm the reliability of the results generated.

4.7 Summary

In this chapter we presented a numerical method that will allow us to numerically solve the equations governing nonlinear two-dimensional Rayleigh-Bénard convection. We were primarily guided by Boyd (2001) and Peyret (2002) in the development of the Fourier-Chebyshev pseudospectral method that we

chose to utilise. Such methods are common in fluid dynamics, in particular in two-dimensional convection studies (see DeLuca *et al.* (1990)). This method is formulated in such a way that it can be efficiently solved using computer software such as FFTW (see Frigo & Johnson (2005)) for performing fast Fourier transforms, and LAPACK (see Anderson *et al.* (1999)) for performing matrix inversions. We benchmarked our results against those of Moore & Weiss (1973) and performed various checks to further confirm the reliability of our results.

Chapter 5

Nonlinear results

To begin we shall derive some useful quantities that will allow us to characterise the type of solutions that we see. Then we shall review the literature of nonlinear two-dimensional Rayleigh-Bénard convection, in order to establish the void in which our study sits. Despite being a previously well-studied problem, advances in computing technology have meant that three, instead of two-dimensional convection is now generally favoured.

For the nonlinear, non-rotating system, we shall study the properties of the flow at different Prandtl numbers—something that is often overlooked, with many studies focusing on only one value of Pr (e.g. DeLuca *et al.* (1990)). Where we find unsteady solutions, a detailed bifurcation analysis will be carried out, in order to map the route to chaos. This will not be performed for the rotating system, since in principle the behaviour is expected to be similar. We will still highlight the nature of the stability of solutions, just not the precise parameter values at which they occur, instead concentrating on the effect of rotation on different properties of the flow, such as the Nusselt number and Reynolds number scaling.

5.1 Energy balances

The governing equations are integrated using the numerical timestepping code outlined in Chapter 4 until a statistically steady state is reached. That is, the solutions no longer change in time; are periodic; or, in the case of chaotic solutions, can be averaged over a suitable period of time. In order to determine when a steady state is reached and, furthermore, to classify results at different values of the input parameters, we require some measure of the intensity of the flow. We would like to classify both the thermal and kinematic properties of our results and in order to do this, we will introduce several well-known output parameters. Although these have been stated numerous times (see e.g. Siggia (1994) and Grossman & Lohse (2000)) they are rarely derived from first principles, and it proves an insightful task to do so.

5.1.1 Nusselt number

The Nusselt number characterises the effectiveness of thermal convection, expressed as the ratio of the convective plus conductive heat flux, to the conductive heat flux in the absence of convection. The latter is given, in dimensionless units, by

$$\frac{1}{L}\int_0^L -\frac{\partial T_B}{\partial z}\mathrm{d}x = 1. \tag{5.1}$$

Therefore a Nusselt number of one corresponds to pure conduction and $Nu > 1$ characterises the effectiveness of thermal convection, at transporting heat.

To derive an expression for the Nusselt number we begin by considering the dimensionless heat equation, governing the evolution of the total temperature $T = T_B + \theta$

$$\frac{\partial T}{\partial t} + (\mathbf{u}\cdot\nabla)T = \nabla^2 T. \tag{5.2}$$

We then integrate this over the partial domain $A' = [0, L] \times [0, z']$, where $z' \leq 1$

$$\int_{A'} \left\{ \frac{\partial T}{\partial t} + (\mathbf{u}\cdot\nabla)T \right\} \mathrm{d}A' = \int_{A'} \nabla^2 T \; dA'. \tag{5.3}$$

We wish to calculate the Nusselt number after the system has settled down to a steady, or statistically steady state. The first term will vanish identically in the former case, and in the latter, we may perform a time average over a suitable period such that the first term vanishes. Hence we have

$$\int_{A'} (\mathbf{u} \cdot \nabla) T \mathrm{d}A' = \int_{A'} \nabla^2 T \; dA'. \tag{5.4}$$

Making use of the vector identities (A.4), (A.5) and using the fact that $\nabla \cdot \mathbf{u} = 0$, we may transform the above equation into a more usable form

$$\int_{A'} \nabla \cdot (\mathbf{u} T) \mathrm{d}A' = \int_{A'} \nabla \cdot (\nabla T) \; dA'. \tag{5.5}$$

The above is now in a suitable form so as to apply the two-dimensional divergence theorem (Green's theorem), which states the following

$$\int_{A'} \nabla \cdot \mathbf{F} \; \mathrm{d}A' = \oint_{c'} \mathbf{F} \cdot \hat{\mathbf{n}} \; \mathrm{d}s, \tag{5.6}$$

where c' is the curve enclosing the surface A', to be traversed in an anti-clockwise manner, with outward-pointing unit normal $\hat{\mathbf{n}}$. Applying the two-dimensional divergence theorem to our equation yields

$$\oint_{c'} \mathbf{u} T \cdot \hat{\mathbf{n}} \; \mathrm{d}s = \oint_{c'} \nabla T \cdot \hat{\mathbf{n}} \; \mathrm{d}s. \tag{5.7}$$

Evaluating these line integrals gives

$$\begin{aligned} &\int_0^L -wT|_{z=0} \, \mathrm{d}x + \int_0^{z'} uT|_{x=L} \, \mathrm{d}z + \int_0^L wT|_{z=z'} \, \mathrm{d}x + \int_0^{z'} -uT|_{x=0} \, \mathrm{d}z \\ &= \int_0^L -\frac{\partial T}{\partial z}\bigg|_{z=0} \mathrm{d}x + \int_0^{z'} +\frac{\partial T}{\partial x}\bigg|_{x=L} \mathrm{d}z + \int_0^L \frac{\partial T}{\partial z}\bigg|_{z=z'} \mathrm{d}x + \int_0^{z'} -\frac{\partial T}{\partial x}\bigg|_{x=0} \mathrm{d}z. \end{aligned} \tag{5.8}$$

The first term on the left-hand side vanishes due to the boundary conditions on the normal component of the velocity $w(z = 0) = 0$. Furthermore, since all physical quantities are periodic in the x direction, this allows us the cancel both the second and fourth terms on the left and right-hand sides of the above, and after rearranging, leaving us with

$$\int_0^L -\frac{\partial T}{\partial z}\bigg|_{z=0} \mathrm{d}x = \int_0^L \left\{ -\frac{\partial T}{\partial z} + wT \right\}\bigg|_{z=z'} \mathrm{d}x. \tag{5.9}$$

If we divide the right hand side by L, to get the flux per unit length then we have an expression for the Nusselt number, in accordance with Siggia (1994) and Grossman & Lohse (2000)

$$Nu \equiv \frac{1}{L}\int_0^L \left\{ -\frac{\partial T}{\partial z} + wT \right\}\Big|_{z=z'} \mathrm{d}x. \tag{5.10}$$

The first and second terms in equation (5.10) are the conductive and convective heat fluxes respectively. Computationally, equation (5.9) allows us to calculate the Nusselt number by evaluating the heat flux at the lower boundary, and thus we have

$$Nu \equiv \frac{1}{L}\int_0^L -\frac{\partial T}{\partial z}\Big|_{z=0} \mathrm{d}x. \tag{5.11}$$

Next we consider the thermal energy dissipation, formed by multiplying the heat equation by T, integrating over the whole domain $A = [0, L] \times [0, 1]$, and dividing by the area $A = L \times 1 = L$

$$\frac{1}{L}\int_A \left\{ T\frac{\partial T}{\partial t} + T(\mathbf{u}\cdot\nabla)T \right\} \mathrm{d}A = \frac{1}{A}\int_A T\nabla^2 T \, \mathrm{d}A. \tag{5.12}$$

We may transform this using vector identities (A.4) and (A.5) into the following form

$$\frac{1}{L}\int_A \left\{ \frac{1}{2}\frac{\partial}{\partial t}(T^2) + \frac{1}{2}\nabla\cdot(\mathbf{u}T^2) \right\} \mathrm{d}A = \frac{1}{L}\int_A \{\nabla\cdot(T\nabla T) - \nabla T\cdot\nabla T\} \, \mathrm{d}A. \tag{5.13}$$

Again, we are presuming that the system has settled down to a steady state, and if not, a suitable time average can be performed, thus meaning that the first term vanishes. If we apply the two-dimensional divergence theorem to the second term on the left-hand side we have

$$\frac{1}{2L}\int_A \nabla\cdot(\mathbf{u}T^2)\mathrm{d}A = \frac{1}{2L}\oint_c \mathbf{u}T^2\cdot\hat{\mathbf{n}}\mathrm{d}s, \tag{5.14}$$

$$= \frac{1}{2L}\left\{ \int_0^L -wT^2\big|_{z=0}\,\mathrm{d}x + \int_0^1 uT^2\big|_{x=L}\,\mathrm{d}z \right.$$

$$\left. + \int_0^L wT^2\big|_{z=1}\,\mathrm{d}x + \int_0^1 -uT^2\big|_{x=0}\,\mathrm{d}z \right\}. \tag{5.15}$$

The first and third terms vanish since $w(z=0) = w(z=1) = 0$ and the second and fourth terms cancel each other out due to periodicity, hence this term contributes

nothing to the integral. If we apply the two-dimensional divergence theorem to the first term on the right-hand side of equation (5.13) we have

$$\frac{1}{L}\int_A \nabla\cdot(T\nabla T)\mathrm{d}A = \frac{1}{L}\oint_c T\nabla T\cdot\hat{\mathbf{n}}\mathrm{d}s, \tag{5.16}$$

$$= \frac{1}{L}\left\{\int_0^L -T\frac{\partial T}{\partial z}\bigg|_{z=0}\mathrm{d}x + \int_0^1 T\frac{\partial T}{\partial x}\bigg|_{x=L}\mathrm{d}z + \int_0^L T\frac{\partial T}{\partial z}\bigg|_{z=1}\mathrm{d}x + \int_0^1 -T\frac{\partial T}{\partial x}\bigg|_{x=0}\mathrm{d}z\right\}. \tag{5.17}$$

The third term vanishes since in dimensionless units, arbitrarily choosing $T_0 = 0$—which we are free to do—gives $T(z=1)=0$ and, again, the second and fourth terms cancel each other out, due to periodicity. We are left with

$$\frac{1}{L}\int_0^L -T\frac{\partial T}{\partial z}\bigg|_{z=0}\mathrm{d}x, \tag{5.18}$$

which, using the fact that in dimensionless units $T(z=0)=1$, gives us the Nusselt number

$$\frac{1}{L}\int_0^L -\frac{\partial T}{\partial z}\bigg|_{z=0}\mathrm{d}x = Nu. \tag{5.19}$$

Therefore, going back to equation (5.13) and rearranging, we have

$$Nu = \frac{1}{A}\int_A \nabla T\cdot\nabla T\mathrm{d}A = \epsilon_T, \tag{5.20}$$

where we have denoted by ϵ_T the globally averaged thermal dissipation rate. Furthermore

$$Nu = \frac{1}{L}\int_0^L \left\{-\frac{\partial T}{\partial z} + wT\right\}\bigg|_{z=z'}\mathrm{d}x = \frac{1}{A}\int_A \nabla T\cdot\nabla T\mathrm{d}A, \tag{5.21}$$

again, in accordance with Siggia (1994).

5.1.2 Kinetic energy dissipation

We begin with the dimensionless Navier-Stokes equations, written in the form below

$$\frac{\partial\mathbf{u}}{\partial t} + (\mathbf{u}\cdot\nabla)\mathbf{u} = -\nabla P + RaPrT\hat{\mathbf{z}} - Ta^{\frac{1}{2}}Pr(\hat{\mathbf{z}}\times\mathbf{u}) + Pr\nabla^2\mathbf{u}, \tag{5.22}$$

that is, we haven't cancelled out the basic state terms that are in hydrostatic balance, instead combining them all into the pressure term so that we may work with the total temperature T. Using vector identity (A.1) and combining the resultant gradient term with the pressure term gives

$$\frac{\partial \mathbf{u}}{\partial t} - \mathbf{u} \times \boldsymbol{\omega} = -\nabla P + RaPrT\hat{\mathbf{z}} - Ta^{\frac{1}{2}}Pr(\hat{\mathbf{z}} \times \mathbf{u}) + Pr\nabla^2\mathbf{u}. \tag{5.23}$$

We define the globally averaged kinetic energy as

$$E_U = \frac{1}{A}\int_A \frac{1}{2}|\mathbf{u}|^2 \mathrm{d}A, \tag{5.24}$$

where $|\mathbf{u}|^2 = \mathbf{u} \cdot \mathbf{u}$. We now take the scalar product of equation (5.23) with $\mathbf{u}$ and integrate over the whole domain $A = [0, L] \times [0, 1]$. Since $\mathbf{u}$ is perpendicular to both $\mathbf{u} \times \boldsymbol{\omega}$ and $\hat{\mathbf{z}} \times \mathbf{u}$, the terms involving the scalar products of these quantities will not contribute anything to the integral, hence we have

$$\frac{\partial E_U}{\partial t} \equiv \frac{1}{L}\int_A \frac{1}{2}\frac{\partial}{\partial t}|\mathbf{u}|^2 \mathrm{d}A = \frac{1}{L}\int_A \left\{-\mathbf{u} \cdot \nabla P + RaPrT\mathbf{u} \cdot \hat{\mathbf{z}} + Pr\mathbf{u} \cdot \nabla^2\mathbf{u}\right\} \mathrm{d}A = 0. \tag{5.25}$$

The left-hand side is the time derivative of the globally averaged kinetic energy, E_U, of the flow. Again, we presume that we are in a situation such that the system has settled down to a (statistically) steady state, and in this case, the time derivative of the kinetic energy will vanish, given a suitable average. Dealing with the pressure term first, we may rewrite it using vector identity (A.4), along with the fact that $\nabla \cdot \mathbf{u} = 0$, and then apply the two-dimensional divergence theorem

$$-\frac{1}{L}\int_A \nabla \cdot (\mathbf{u}P)\mathrm{d}A = -\frac{1}{L}\oint_c \mathbf{u}P \cdot \hat{\mathbf{n}}\mathrm{d}s, \tag{5.26}$$

$$= -\frac{1}{L}\left\{\int_0^L -wP|_{z=0}\,\mathrm{d}x + \int_0^1 uP|_{x=L}\,\mathrm{d}z + \int_0^L wP|_{z=1}\,\mathrm{d}x + \int_0^1 -uP|_{x=0}\,\mathrm{d}z\right\}. \tag{5.27}$$

The first and third terms vanish since $w(z = 0) = w(z = 1) = 0$ and the second and fourth terms cancel due to periodicity in the x direction. Hence the pressure term does not contribute to the surface average. Next we shall consider the buoyancy

term in equation (5.25)

$$\frac{1}{L}\int_A RaPrT\mathbf{u}\cdot\hat{\mathbf{z}}\mathrm{d}A = \frac{RaPr}{L}\int_0^1\int_0^L wT\mathrm{d}x\mathrm{d}z. \tag{5.28}$$

From the Nusselt number calculation, we have

$$Nu = \frac{1}{L}\int_0^L \left\{-\frac{\partial T}{\partial z} + wT\right\}\Big|_{z=z'}\mathrm{d}x, \tag{5.29}$$

and by rearranging, we have

$$\frac{1}{L}\int_0^L wT|_{z=z'}\,\mathrm{d}x = Nu + \frac{1}{L}\int_0^L \frac{\partial T}{\partial z}\Big|_{z=z'}\mathrm{d}x. \tag{5.30}$$

Having made the substitution $z = z'$, if we now to integrate over the variable z', for $0 \leq z' \leq 1$, we will obtain the integral over the whole domain A. Furthermore, reversing the order of integration on the right-hand side gives

$$\frac{1}{L}\int_0^1\int_0^L wT|_{z=z'}\,\mathrm{d}x\mathrm{d}z' = \int_0^1 Nu\mathrm{d}z' + \frac{1}{L}\int_0^L\int_0^1 \frac{\partial T}{\partial z}\Big|_{z=z'}\mathrm{d}z'\mathrm{d}x, \tag{5.31}$$

$$= \left[Nuz' + \frac{1}{L}\int_0^L T\mathrm{d}x\right]_0^1. \tag{5.32}$$

Using the fact that $T(z'=0)=1$ and $T(z'=1)=0$, for $0 \leq z' \leq 1$, we have

$$\frac{1}{L}\int_0^1\int_0^L wT|_{z=z'}\,\mathrm{d}x\mathrm{d}z' = Nu - \frac{1}{L}\int_0^L \mathrm{d}x = Nu - 1, \tag{5.33}$$

and therefore

$$\frac{RaPr}{L}\int_0^1\int_0^L wT\mathrm{d}x\mathrm{d}z = RaPr(Nu-1) \tag{5.34}$$

Finally we consider the third term on the right-hand side of equation (5.25). Using index notation we may write

$$\mathbf{u}\cdot\nabla^2\mathbf{u} = u_i\frac{\partial^2 u_i}{\partial x_j^2} = \frac{\partial}{\partial x_j}\left(u_i\frac{\partial u_i}{\partial x_j}\right) - \frac{\partial u_i}{\partial x_j}\frac{\partial u_i}{\partial x_j}, \tag{5.35}$$

and hence we have

$$\frac{Pr}{L}\int_0^1\int_0^L \mathbf{u}\cdot\nabla^2\mathbf{u}\,\mathrm{d}x\mathrm{d}z = \frac{Pr}{L}\int_0^1\int_0^L \left\{\frac{\partial}{\partial x_j}\left(u_i\frac{\partial u_i}{\partial x_j}\right) - \frac{\partial u_i}{\partial x_j}\frac{\partial u_i}{\partial x_j}\right\}\mathrm{d}x\mathrm{d}z. \tag{5.36}$$

Using the two-dimensional divergence theorem on the first term on the right-hand side gives

$$\frac{Pr}{L}\int_0^1\int_0^L \frac{\partial}{\partial x_j}\left(u_i\frac{\partial u_i}{\partial x_j}\right)\mathrm{d}x\mathrm{d}z = \frac{Pr}{L}\oint_c u_i\frac{\partial u_i}{\partial x_j}\hat{n}_j\mathrm{d}s, \tag{5.37}$$

where n_j is the j-th component of the unit normal vector $\hat{\mathbf{n}}$. Evaluating this line integral around our convection cell gives

$$\begin{aligned}\frac{Pr}{L}\oint_c u_i\frac{\partial u_i}{\partial x_j}\hat{n}_j \mathrm{d}s = \frac{Pr}{L}\Bigg\{ &-\int_0^L \left(u\frac{\partial u}{\partial z}+v\frac{\partial v}{\partial z}+w\frac{\partial w}{\partial z}\right)\Bigg|_{z=0}\mathrm{d}x \\ &+\int_0^1 \left(u\frac{\partial u}{\partial x}+v\frac{\partial v}{\partial x}+w\frac{\partial w}{\partial x}\right)\Bigg|_{x=L}\mathrm{d}z \\ &+\int_0^L \left(u\frac{\partial u}{\partial z}+v\frac{\partial v}{\partial z}+w\frac{\partial w}{\partial z}\right)\Bigg|_{z=1}\mathrm{d}x \\ &-\int_0^1 \left(u\frac{\partial u}{\partial x}+v\frac{\partial v}{\partial x}+w\frac{\partial w}{\partial x}\right)\Bigg|_{x=0}\mathrm{d}z\Bigg\}. \end{aligned} \tag{5.38}$$

Since $\frac{\partial u}{\partial z}=\frac{\partial v}{\partial z}=w=0$ at $z=0$ and $z=1$ the first and third integrals vanish, and due to periodicity the second and fourth integrals cancel. Hence we have

$$\frac{Pr}{L}\int_0^1\int_0^L \mathbf{u}\cdot\nabla^2\mathbf{u}\,\mathrm{d}x\mathrm{d}z = -\frac{Pr}{L}\int_0^1\int_0^L \frac{\partial u_i}{\partial x_j}\frac{\partial u_i}{\partial x_j}\mathrm{d}x\mathrm{d}z = -Pr\epsilon_U, \tag{5.39}$$

where we have denoted by ϵ_U the globally averaged kinetic energy dissipation rate, as defined by Siggia (1994) and Grossman & Lohse (2000). Therefore, the only two non-zero contributions to equation (5.25) are given by equations (5.34) and (5.39). Equating these tells us

$$\epsilon_U = Ra(Nu-1), \tag{5.40}$$

hence the dissipation of kinetic energy is balanced by the energy due to the convective driving of the flow.

5.1.3 Reynolds number

The Reynolds number, characterising the ratio of inertial to viscous forces is given by

$$Re = \frac{UL}{\nu} \tag{5.41}$$

where U is a typical velocity and L is a typical length. In our dimensionless equations we have scaled length with the layer depth d and time on a thermal diffusive time, proportional to κ/d^2. Hence we have

$$U = \frac{\kappa}{d}\tilde{U} \tag{5.42}$$

Furthermore, we introduced the Prandtl number, which implies $\nu = \kappa Pr$ and so we have

$$Re = \frac{\tilde{U}}{Pr}, \tag{5.43}$$

where we calculate $\tilde{U}$ from the kinetic energy, E_U, defined via equation (5.24).

5.1.4 Enstrophy

Similar to the kinetic energy, the enstrophy characterises the energy of the flow, due to its vorticity. It is calculated, per unit volume, via the square of the vorticity, integrated over the whole domain

$$\mathcal{E} = \frac{1}{2}\int_0^1 \int_0^L |\boldsymbol{\omega}|^2 \mathrm{d}x\mathrm{d}z. \tag{5.44}$$

The enstrophy accounts for the dissipation of kinetic energy due to vortex motions; it is an important quantity in the study of turbulence (see Batchelor (1967)).

5.2 No rotation

As we saw in Chapter 3, the critical Rayleigh number required for the onset of convection as we alter the rotation rate is different. Therefore when comparing numerical data at different values of the Taylor number, rather than working with the Rayleigh number directly, we will introduce the ratio of criticality, defined as

$$R = \frac{Ra}{Ra_c}. \tag{5.45}$$

Furthermore, this will facilitate transparent comparison of how unstable the system is to convective motions, for different Taylor numbers.

5.2.1 $Pr = 1$

In two dimensions it has been noted that convection is remarkably steady for $Pr \leq 1$, despite flows reaching Reynolds numbers of the order of 10^4: far above the required

value to drive instability in, for example, pipe flow. Indeed Veronis (1966) and Curry *et al.* (1984) observed no oscillatory solutions in the range of Rayleigh numbers they studied and DeLuca *et al.* (1990) and Vincent & Yuen (1999) obtained steady solutions up to $Ra = 10^8$. The largest Rayleigh number reached here is of the order of 10^7 and at this Rayleigh number, as suspected, the flow is still steady. Due to the constraints placed on time and resources, with the numerical algorithm devised in Chapter 4, it was not practical to attempt to achieve a higher Rayleigh number here. In many ways it is just as interesting attempting to understand precisely why solutions are so persistently stable (something that shall be addressed in Chapter 6). The highest Rayleigh numbers reached in two-dimensional convection—that we are aware of—are by Vincent & Yuen (2000): up to $Ra = 10^{14}$. In this paper they describe the characteristics of the different regimes that are encountered as the Rayleigh number is increased. These can be seen schematically in Figure 5.1.

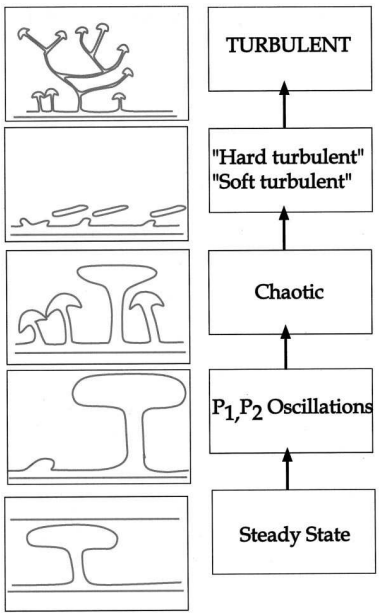

Figure 5.1: Schematic drawing showing the development in the style of plumes ranging from steady-state plumes for low Rayleigh number $O(10^5)$ to the turbulent regime where branching of plumes takes place at global Ra greater than 10^{10}. Taken from Vincent & Yuen (2000).

For $Pr = 1$ the highest Rayleigh number that we were able to achieve was $R \leq 10^5$, or $Ra \leq 6.57 \times 10^7$. Hence by Figure 5.1 we are still within what Vincent & Yuen (2000) describe as the steady-state regime. It is possible to enter the other regimes by varying the values of the Prandtl number and the Taylor number, as shall be seen in subsequent sections. Now however, we shall seek to outline the behaviour of the steady-state regime and classify its defining characteristics.

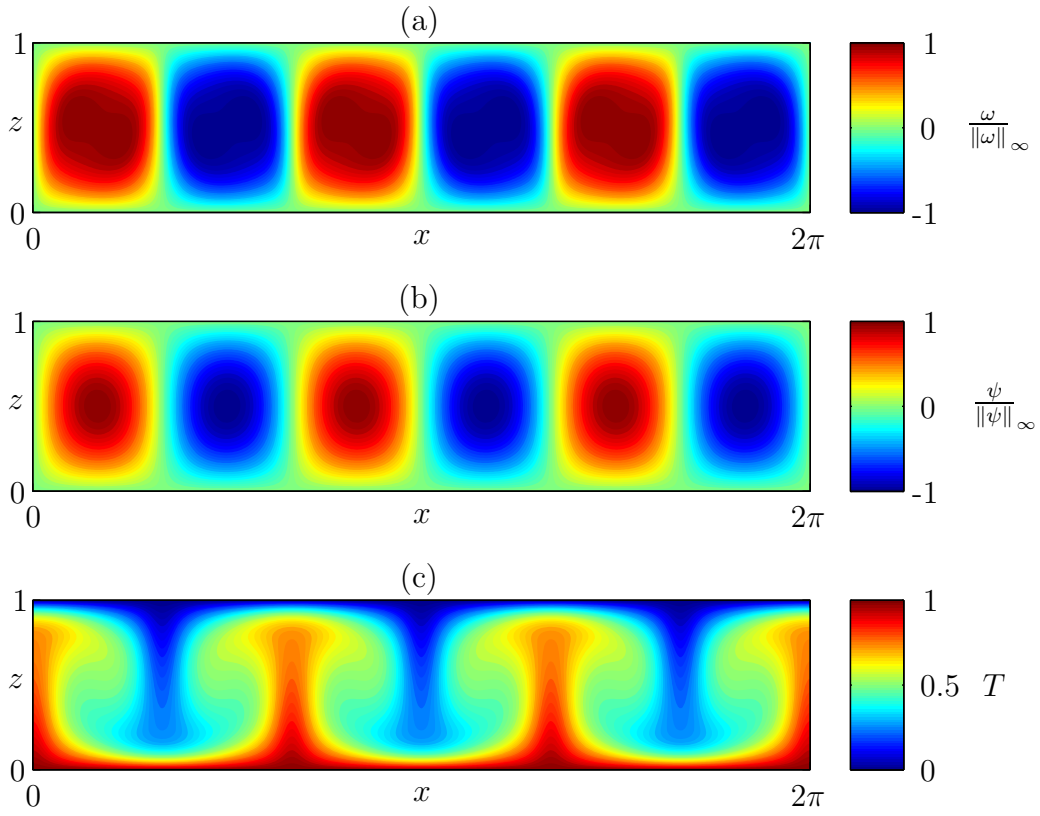

Figure 5.2: Contour plots of (a) the normalised vorticity ($\|\omega\|_\infty = 222$), (b) the normalised streamfunction ($\|\psi\|_\infty = 14$) and (c) the total temperature, for $Ta = 0$, $Pr = 1$, $R = 10$, with resolution $[512 \times 96]$: exhibition of a steady-state, six-cell solution.

For a long time it was thought that the specific horizontal form of the convection pattern was optimal in the sense that it maximised the convective heat transport (see Malkus (1954b)), however in a steady state the convection pattern is not uniquely determined solely by the governing parameters, but also the initial conditions, as

reported by Ogura (1971). Indeed we have witnessed convection patterns that give rise to a convective heat transport that is not optimal. Hence for the same parameter values, there could be a range of different valid convection patterns, dependent on the initial conditions used. This is an inherent manifestation of the fact that we are dealing with nonlinear equations.

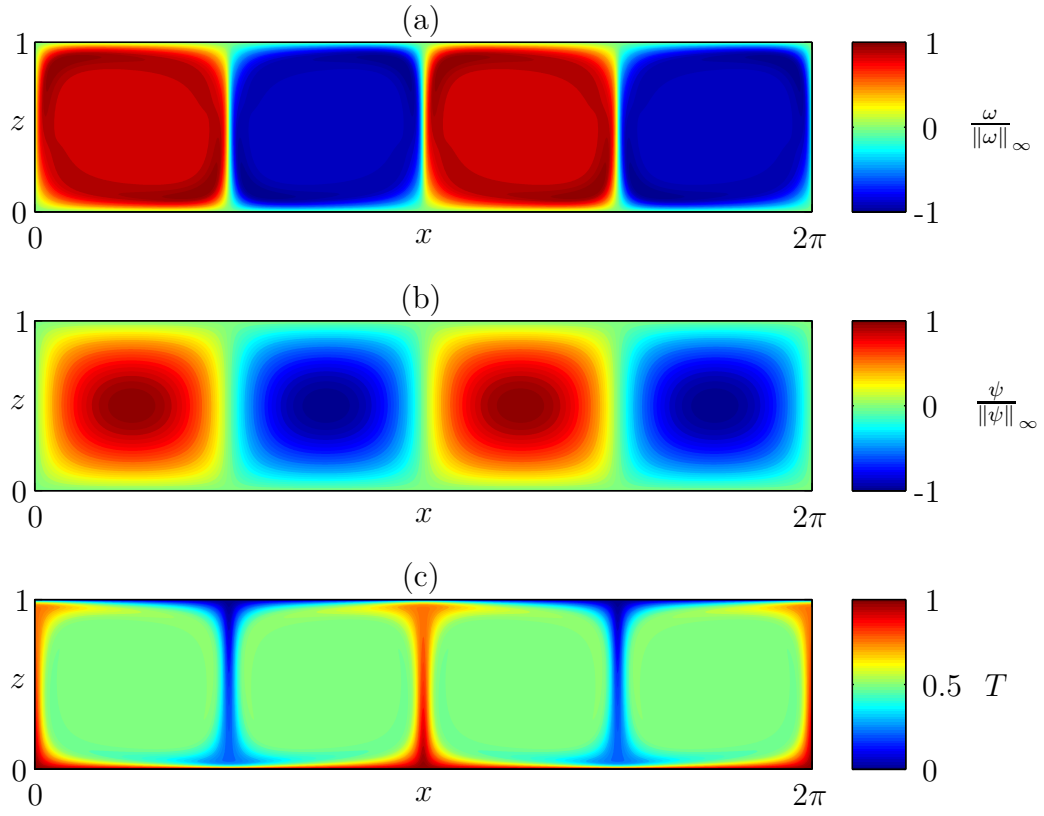

Figure 5.3: Contour plots of (a) the normalised vorticity ($\|\omega\|_\infty = 2824$), (b) the normalised streamfunction ($\|\psi\|_\infty = 255$) and (c) the total temperature, for $Ta = 0$, $Pr = 1$, $R = 500$, with resolution $[1024 \times 128]$: exhibition of a steady-state, four-cell solution.

We started our numerical simulations from a set of infinitesimal random initial conditions. This way the system was not influenced by a predetermined length scale: perturbations grew with whichever horizontal wave number was preferential. We maintained a fixed box length of $L = 2\pi$. For low Ra it is found that the dominant wave number is three, hence we see a six-cell convection pattern, as can be

seen in Figure 5.2. As the Rayleigh number is increased it seems that the preferential wave number decreases, first to two (see Figure 5.3) and finally one (see Figure 5.4). This is in contrast to the linear theory of Chapter 2 which predicts that the most unstable—linear—wave number should increase with increasing Rayleigh number. All of these plots are characterised by rising and sinking convective plumes, and thermal boundary layer regions located close to the top and bottom boundaries; the temperature dropping from its value within the core of the convection cell, to one on the bottom boundary and zero on the top boundary.

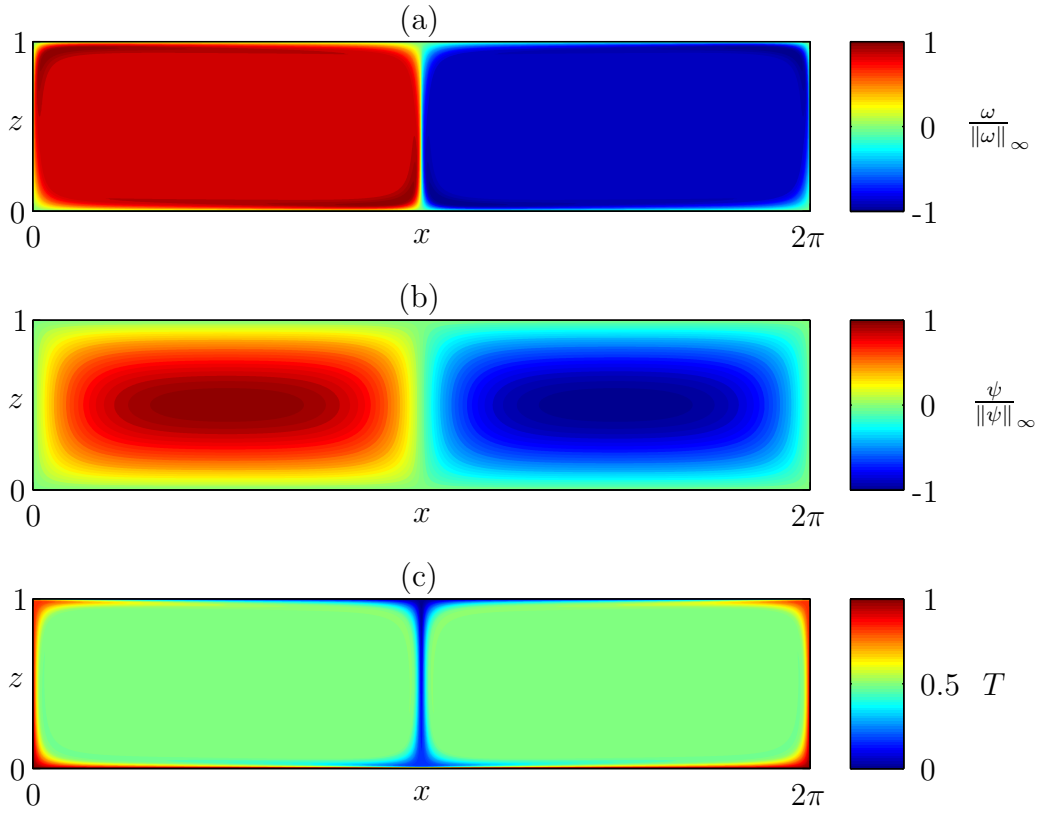

Figure 5.4: Contour plots of (a) the normalised vorticity ($\|\omega\|_\infty = 18253$), (b) the normalised streamfunction ($\|\psi\|_\infty = 1944$) and (c) the total temperature, for $Ta = 0$, $Pr = 1$, $R = 10000$, with resolution $[1024 \times 128]$: exhibition of a steady-state, two-cell solution.

As the Rayleigh number increases, it can be seen by looking at the evolution between Figures (5.2), (5.3) and (5.4), that the thickness of the convective plumes and also

the thermal boundary layers, decreases. The dynamics of the entire system are controlled via this boundary layer behaviour. It is revealing to look at plots of the horizontally-averaged temperature profile versus the vertical coordinate, as the Rayleigh number is altered, to see how the boundary layer thickness decreases as Ra is increased. This is shown in Figure 5.5. Looking at the mean temperature profile, we see that as the Rayleigh number is increased the temperature becomes isothermal in the bulk of the layer, taking the value $T = \frac{1}{2}$, and sharply changes within the boundary layer to attain its boundary value.

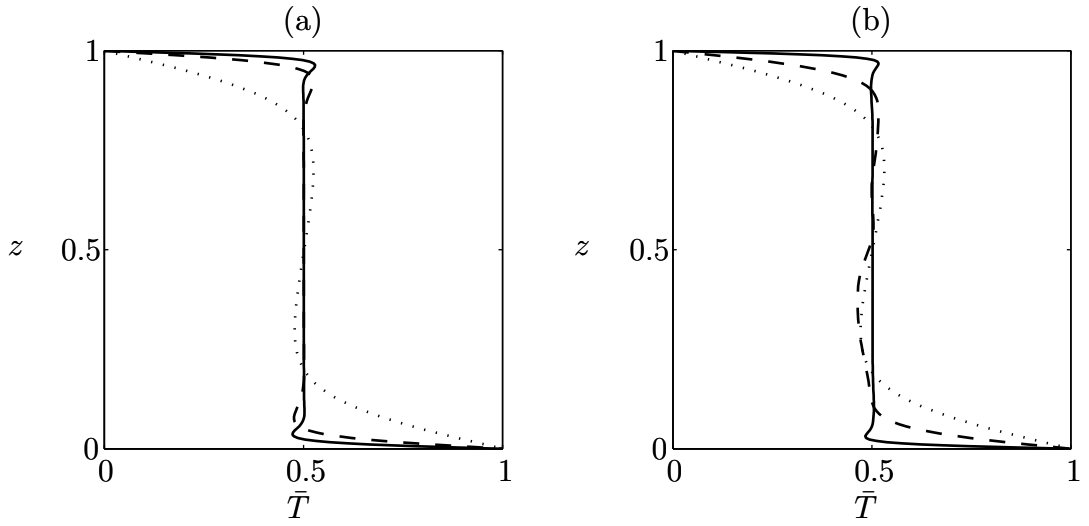

Figure 5.5: Mean temperature profile as a function of z for $R = 10$ (dotted line), $R = 500$ (dashed line) and $R = 10000$ (solid line), for (a) $Pr = 1$ and (b) $Pr = 10$.

We noted that as the Rayleigh number was increased, the number of cells in the horizontal decreased. Figure 5.6 shows the progression in terms of the dominant wave number as a function of Rayleigh number. It can be seen that the system does indeed progress to the largest permissible length scale as the Rayleigh number is increased. This is not to say that for a given Rayleigh number, patterns with a different horizontal wave are not possible. Moreover, it is the case that the basin of attraction of a solution with dominant wavenumber m_d is greater than that of a solution with another wavenumber (see Strogatz (2000)). This means that as time evolves the system will tend to the solution with wavenumber m_d. As we said, in

general $m_d \to 1$ as $Ra \to \infty$, however this is not a definite rule. For example in Figure 5.6, for $Ra \simeq 1.3 \times 10^5$, $Pr = 10$, there is a solution with $m_d = 3$ despite the fact that solutions at much lower values of Ra have already made the transition from $m_d = 3$ to $m_d = 2$. This behaviour is typical of a nonlinear system. In a box of length 2π, the smallest permissible wave number is $m = 1$. In a wider box, it is to be expected that the dominant wave number will tend to the smallest permissible allowed.

Note that in all the steady state contour plots viewed here, the solutions possess the following rotational symmetry

$$\omega(x, z, t) = \omega\left(\pi - x, 1 - z, t\right), \tag{5.46}$$

$$\psi(x, z, t) = \psi\left(\pi - x, 1 - z, t\right), \tag{5.47}$$

$$T(x, z, t) = 1 - T\left(\pi - x, 1 - z, t\right). \tag{5.48}$$

That is to say, if $\Big\{\omega(x, z, t), \psi(x, z, t), T(x, z, t)\Big\}$ is a solution of the system of equations given by

$$\frac{\partial \omega}{\partial t} + \frac{\partial \psi}{\partial x}\frac{\partial \omega}{\partial z} - \frac{\partial \psi}{\partial z}\frac{\partial \omega}{\partial x} = -RaPr\frac{\partial T}{\partial x} + Pr\nabla^2\omega, \tag{5.49}$$

$$\frac{\partial T}{\partial t} + \frac{\partial \psi}{\partial x}\frac{\partial T}{\partial z} - \frac{\partial \psi}{\partial z}\frac{\partial T}{\partial x} = \nabla^2 T, \tag{5.50}$$

$$\nabla^2\psi = -\omega, \tag{5.51}$$

and the boundary conditions $\omega = \psi = 0,\ T = 1$ at $z = 0$ and $\omega = \psi = T = 0$ at $z = 0$, then $\Big\{\omega = \tilde{\omega}(\pi - x, 1 - z, t), \psi = \tilde{\psi}(\pi - x, 1 - z, t), T = 1 - \tilde{T}(\pi - x, 1 - z, t)\Big\}$ is also a solution. This can be seen by putting such a solution into the governing equations and noting that

$$\frac{\partial}{\partial t}\Big\{\omega, \psi, T\Big\} = \frac{\partial}{\partial t}\Big\{\tilde{\omega}, \tilde{\psi}, -\tilde{T}\Big\}, \tag{5.52}$$

$$\frac{\partial}{\partial x}\Big\{\omega, \psi, T\Big\} = \frac{\partial}{\partial x}\Big\{-\tilde{\omega}, -\tilde{\psi}, \tilde{T}\Big\}, \tag{5.53}$$

$$\frac{\partial}{\partial z}\Big\{\omega, \psi, T\Big\} = \frac{\partial}{\partial z}\Big\{-\tilde{\omega}, -\tilde{\psi}, \tilde{T}\Big\}, \tag{5.54}$$

$$\nabla^2\Big\{\omega, \psi, T\Big\} = \nabla^2\Big\{\tilde{\omega}, \tilde{\psi}, -\tilde{T}\Big\}. \tag{5.55}$$

Furthermore, in Figure 5.5(a) it can be seen that the horizontally averaged temperature satisfies the symmetry condition

$$\bar{T}(z) = 1 - \bar{T}(1 - z). \tag{5.56}$$

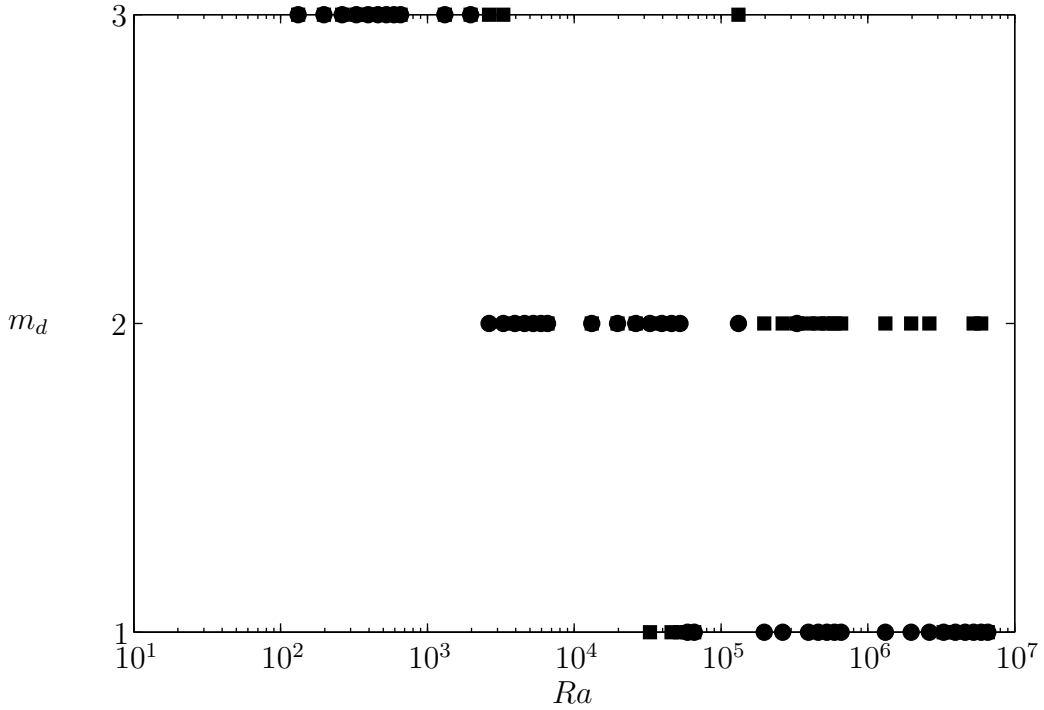

Figure 5.6: Dominant horizontal wave number m_d, versus Rayleigh number, with $Pr = 1$ (circles) and $Pr = 10$ (squares).

5.2.2 Route to chaos for $Pr = 10$

As we have already stated, often only one Prandtl number is studied—the general preference being for $Pr = 1$. We have chosen to study $Pr = 10$ also, to allow for comparison between the two cases. It is found that for $R < 49.50$, the system always settles down to a steady state. The preferential horizontal wave number is three, giving rise to a six cell pattern that is identical in form to the case for $Pr = 1$, hence we do not show it here. The progression of the dominant horizontal wave number versus Rayleigh number can be seen in Figure 5.6. As Ra increases, even for $Pr = 10$, the system always seems to prefer the largest scale allowable in the box. Furthermore, even though there is a distinction for lower Ra, as it is increased, the

mean temperature profile mimics that for $Pr = 1$. Note that the mean temperature profiles shown in Figure 5.5 are calculated at a particular moment in time, hence for a time-dependent solution, they are not symmetric about the line $z = \frac{1}{2}$.

At $R = 49.50$ the steady state undergoes a Hopf bifurcation leading to the creation of a periodic orbit that is of infinitesimal amplitude and only exists for a small window of Rayleigh number space. The periodic orbit corresponds to a fluid parcel moving in a loop around the interior of the convection cell. This initial bifurcation preserves the symmetry given by equation (5.56). Hence the fluid parcel moving from the bottom left corner to the top right corner of the convection cell is equivalent to it moving from the top right corner back to the bottom left corner, in order to complete the loop.

At $R = 49.80$ the system undergoes a period-doubling bifurcation. This secondary bifurcation breaks the symmetry given by equation (5.56). Hence the fluid parcel moving from the bottom left corner to the top right corner of the convection cell is no longer equivalent to it moving from the top right corner to the bottom left corner of the convection cell. The fluid parcel must complete one whole loop, taking twice the amount of time as the original oscillation, thus the name period doubling bifurcation. In Figure 5.7 we have plotted the temperature field at various points in time for one of these period doubled oscillatory solutions. It is clear that physically the periodic orbit amounts to a lateral motion of the upward and downward convective plumes; the plumes swaying from side to side. This feature was also noticed by Moore & Weiss (1973) and Lennie *et al.* (1988), in their numerical studies of convection, and Krishnamurti (1970a)/Krishnamurti (1970b) in physical convection experiments. A detailed explanation of this instability shall be put forward in the following section. A very revealing way to portray the nonlinear dynamics of the system is to plot trajectories in a three-dimensional energy, or phase space. The Nusselt number, kinetic energy and enstrophy are all time-dependent output parameters of our numerical simulations. Therefore plotting them against one another can tell us about the time dependent behaviour of the system. For example, if the system

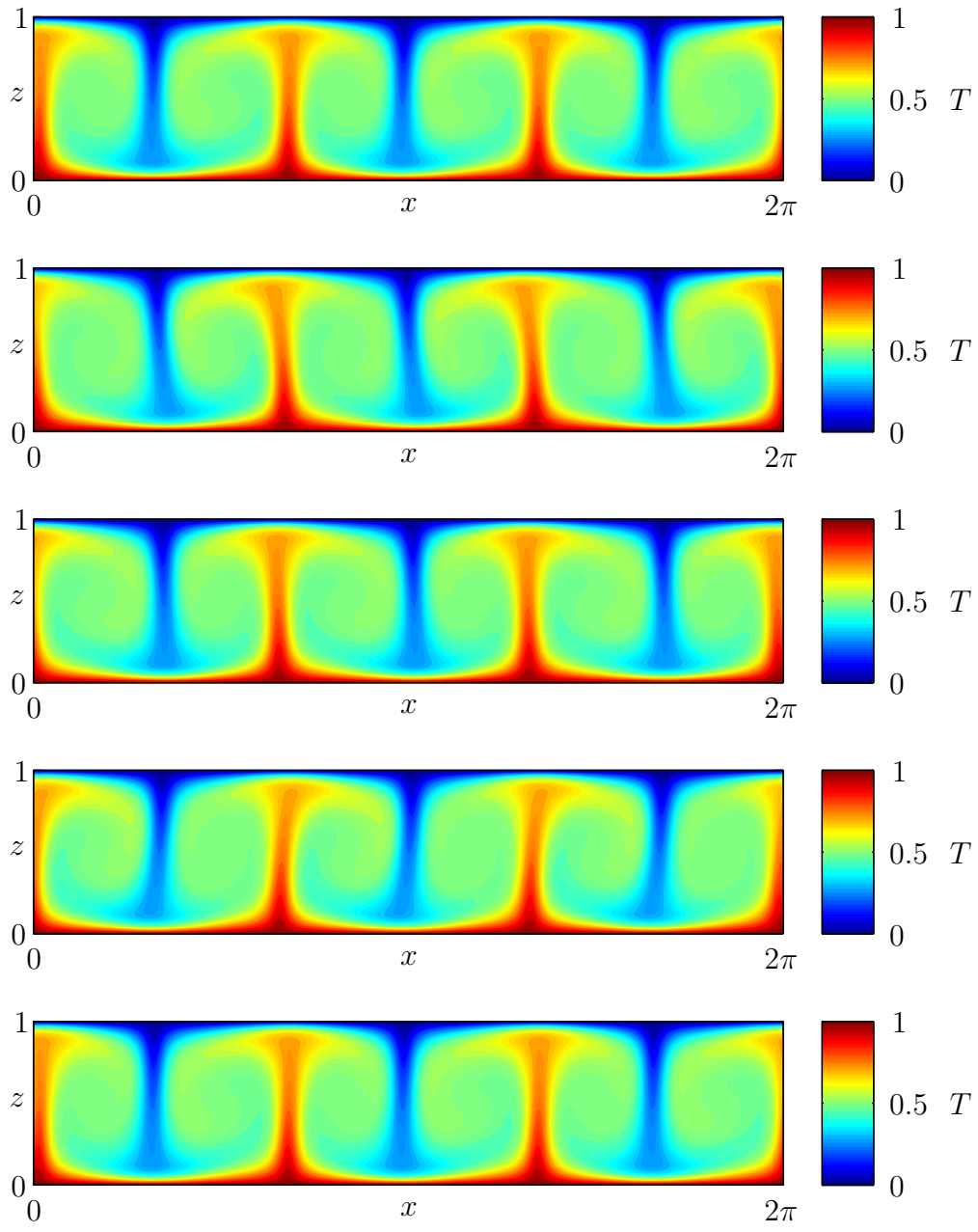

Figure 5.7: Contour plots of the total temperature at subsequent moments in time, for $Ta = 0$, $Pr = 10$, $R = 52$, with resolution $[512 \times 96]$: exhibition of a period-two, oscillatory, six-cell solution. The dimensionless time period of the oscillation is $\simeq 0.04$.

settles down to a steady state after a period of transient growth, these parameters will attain a constant value for all subsequent time. In phase space this corresponds to the trajectory converging to a fixed point. If the behaviour of these parameters is periodic in time, then within the three-dimensional $(E_U, Nu, \mathcal{E})$ phase space any trajectory starting at a particular point will return to that point after one time period, forming a closed loop known as a periodic orbit. Likewise, the parameters could be periodic with more than one period. For example if we had a period-two point then the phase space trajectory would perform two loops before returning to its initial point. For a chaotic system any trajectory in phase space will not tend to, or diverge from, any set point, instead following a random path for all time.

In the plots that will follow, although we shall plot trajectories in the three-dimensional space described above, for display purposes we shall project this into the (E_U, Nu) plane. A further thing do is construct a Poincaré section through the trajectory (see Guckenheimer & Holmes (1997) or Strogatz (2000)). This amounts to taking a slice through the trajectory at a constant value of one of the parameters, here the enstrophy. Hence for a period-m orbit, there should be $2m$ distinct clusters of points. The period-two point mentioned above can be seen in Figure 5.8, where we can clearly see that there are four clusters in the Poincaré section, corresponding to two loops and hence four crossings of the plane enstrophy=constant.

As the Rayleigh number is increased, the period-two orbit grows in amplitude until $R = 55$, when it becomes unstable. The amplitude has reached a critical value whereby the trajectory is no longer able to return to the same point in phase space after completing two loops. Instead it winds around the surface of a torus in a helical manner, only returning to the same point in phase space after completing one toroidal loop. In the terminology of dynamical systems, this is known as a *two-torus* and can be visualised in Figure 5.9. The Poincaré section consists of two rings of points, which displays the path of the trajectory around the torus more clearly. As the Rayleigh number is increased further, the amplitude of the orbit around the torus also increases.

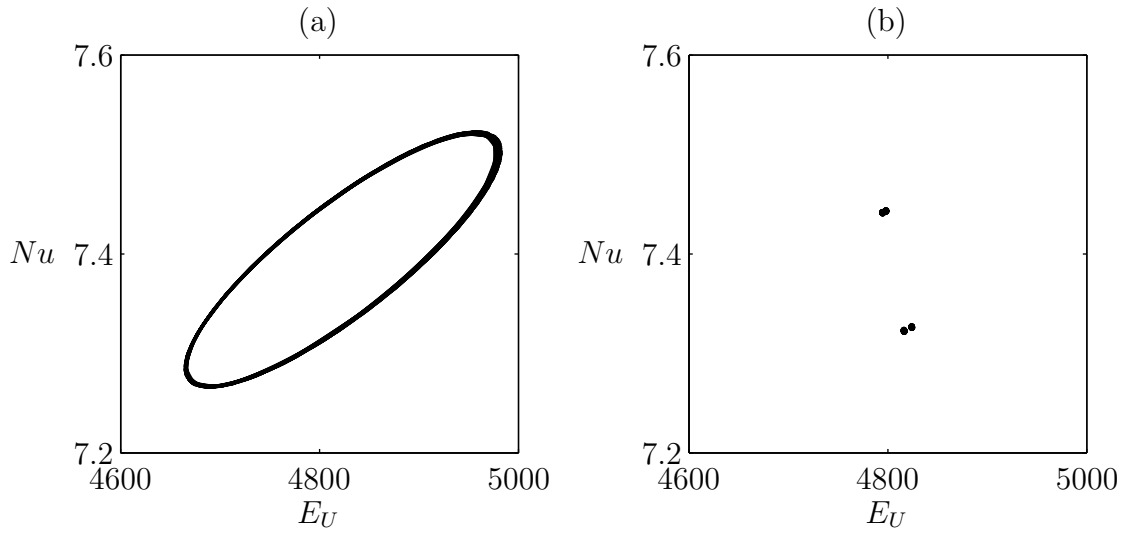

Figure 5.8: (a) two-dimensional projection of $(E_U, Nu, \mathcal{E})$ trajectory onto (E_U, Nu) plane with $1.06 \times 10^5 \leq \mathcal{E} \leq 1.13 \times 10^5$ and (b) corresponding Poincaré section at $\mathcal{E} = 1.09 \times 10^5$, for $R = 52$, $Pr = 10$: exhibition of a period-two orbit.

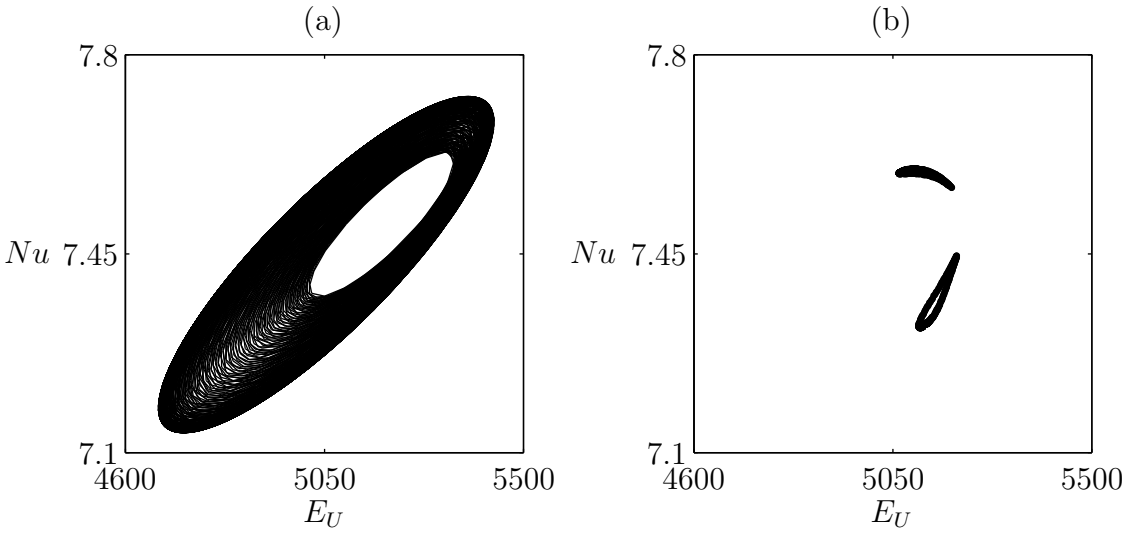

Figure 5.9: (a) two-dimensional projection of $(E_U, Nu, \mathcal{E})$ trajectory onto (E_U, Nu) plane with $1.07 \times 10^5 \leq \mathcal{E} \leq 1.25 \times 10^5$ and (b) corresponding Poincaré section at $\mathcal{E} = 1.17 \times 10^5$, for $R = 55$, $Pr = 10$: exhibition of a two-torus.

At $R = 56$ the system undergoes a further bifurcation, with the introduction of another period of oscillation. This causes the trajectory on the two-torus to become unstable, no longer able to return to the same point in phase space after completing one toroidal loop. Instead the trajectory evolves along the strange attractor shown in Figure 5.10. The structure of the attractor somewhat resembles that of the two-torus, since the trajectory has a 'memory' of its existence. Whilst the trajectory on the attractor is seemingly chaotic, it is nonetheless always confined to its surface. The remnant structure of the two-torus still wields enough influence over the trajectory as to keep its motion in phase space bounded. We are confident that this behaviour is independent of the particular initial conditions chosen, since we have integrated for long enough that all transient behaviour has ceased.

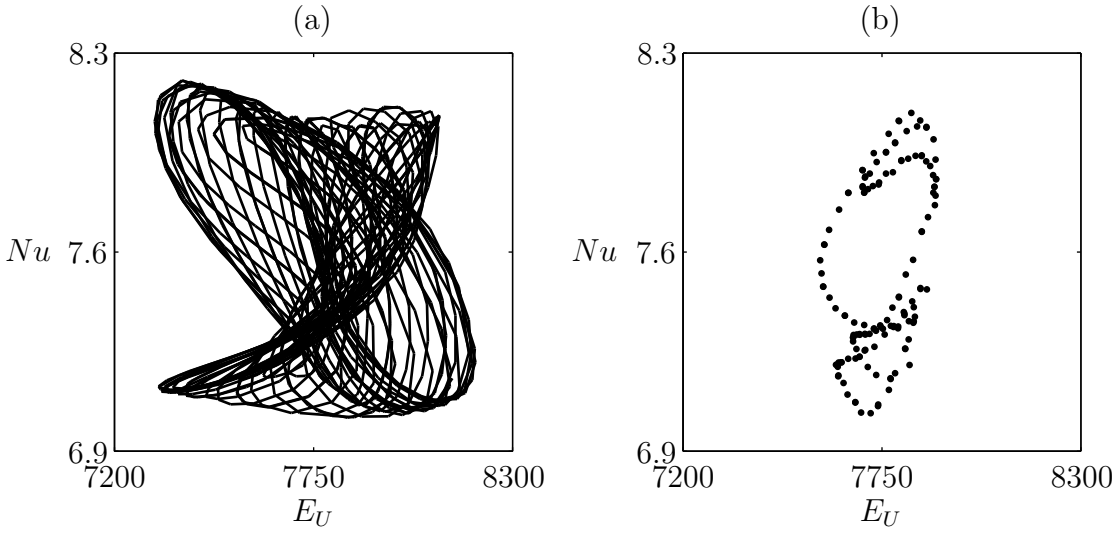

Figure 5.10: (a) two-dimensional projection of $(E_U, Nu, \mathcal{E})$ trajectory onto (E_U, Nu) plane with $1.34 \times 10^5 \leq \mathcal{E} \leq 1.57 \times 10^5$ and (b) corresponding Poincaré section at $\mathcal{E} = 1.46 \times 10^5$, for $R = 68$, $Pr = 10$: exhibition of quasi-periodicity.

This type of behaviour is known as *quasi-periodicity*. The trajectory continues to evolve in such a manner, as the Rayleigh number is increased, until $R = 71$, when the strange attractor finally loses stability. At this point the amplitude of the orbit has become so large that it has broken free from the attractor, unable to return

to a point on its surface. The trajectory now has no preferred path and wanders randomly around phase space, as can be seen in Figure 5.11. This behaviour is known as *chaos*. There is no way to predict, based on the location of the trajectory in phase space at a particular moment in time, how it will evolve for subsequent time. An example flow pattern for $R > 71$ can be seen in Figure 5.12. Notice that the coherent cell-like structure has been lost and the spontaneous break up of the convective plumes is now visible. This fits in with the schematic picture of chaos from Vincent & Yuen (2000).

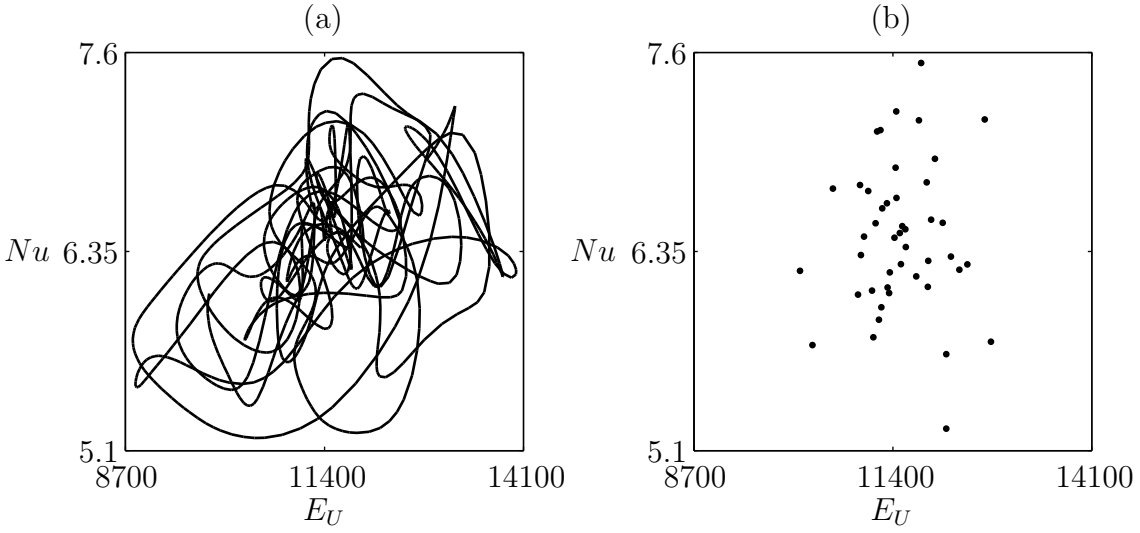

Figure 5.11: (a) two-dimensional projection of $(E_U, Nu, \mathcal{E})$ trajectory onto (E_U, Nu) plane with $1.31 \times 10^5 \leq \mathcal{E} \leq 2.11 \times 10^5$ and (b) corresponding Poincaré section at $\mathcal{E} = 1.77 \times 10^5$, for $R = 100$, $Pr = 10$: exhibition of chaos.

This transition to chaos that we have described is similar to one put forward by Newhouse *et al.* (1978) known as the *Ruelle-Takens-Newhouse route to chaos*. The additional frequency introduced into the system that causes the two-torus to go unstable is enough to set about an unavoidable transition to chaotic behaviour. This is in contrast to the period-doubling route to chaos, where successive period doubling bifurcations eventually saturate the system with innumerable different frequencies, resulting in chaotic behaviour. Indeed Curry (1978) noticed a similar

phase transition to the one we described here. That is, an initial Hopf bifurcation, followed by successive period doubling bifurcations that lead to motion on a torus, that in turn give way to a strange attractor. Curry (1978) did not use numerical simulations, instead studying a 14 mode truncated system of ordinary differential equations, similar to the Lorenz equations.

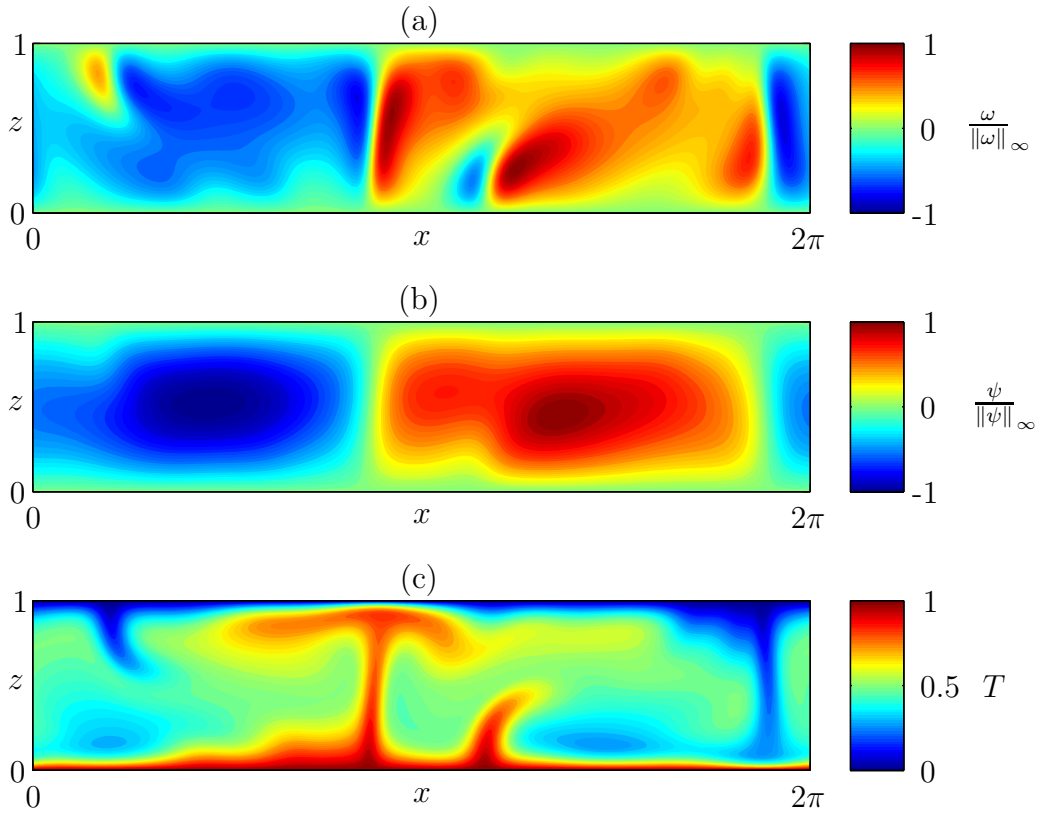

Figure 5.12: Contour plots of (a) the normalised vorticity ($\|\omega\|_\infty = 1252$), (b) the normalised streamfunction ($\|\psi\|_\infty = 89$) and (c) the total temperature, for $Ta = 0$, $Pr = 10$, $R = 100$, with resolution $[256 \times 96]$: exhibition of a chaotic solution.

For $R > 71$ the behaviour of the system is incredibly unpredictable. Despite the emergence of chaotic solutions, as we have mentioned, it seems that the system can spontaneously relapse into stable and periodic states. This was discovered entirely unintentionally, and it seems that these solutions are rather difficult to track numerically, with solutions rapidly switching between steady and unsteady branches in phase space. An example of such a scenario can be viewed in Figure 5.13, where

the trajectory in phase space forms a closed trefoil knot. Indeed, there is no saying how high the Rayleigh number would have to be, or even if such a Rayleigh number exists, where a consistent sort of behaviour is reached. This intermittent behaviour is consistent with another competing theory that explains the route to chaos, known as the *Pomeau-Manneville scenario* (Pomeau & Manneville (1980)). In this scenario the system is characterised by bursts of chaotic behaviour out of quasi-periodic states, themselves remnants of unstable periodic orbits. As the driving is increased, the system is pushed so far away from the unstable periodic orbit that chaos ensues. It is entirely plausible that this is the scenario in which we find ourselves, as opposed to a Ruelle-Takens-Newhouse type situation.

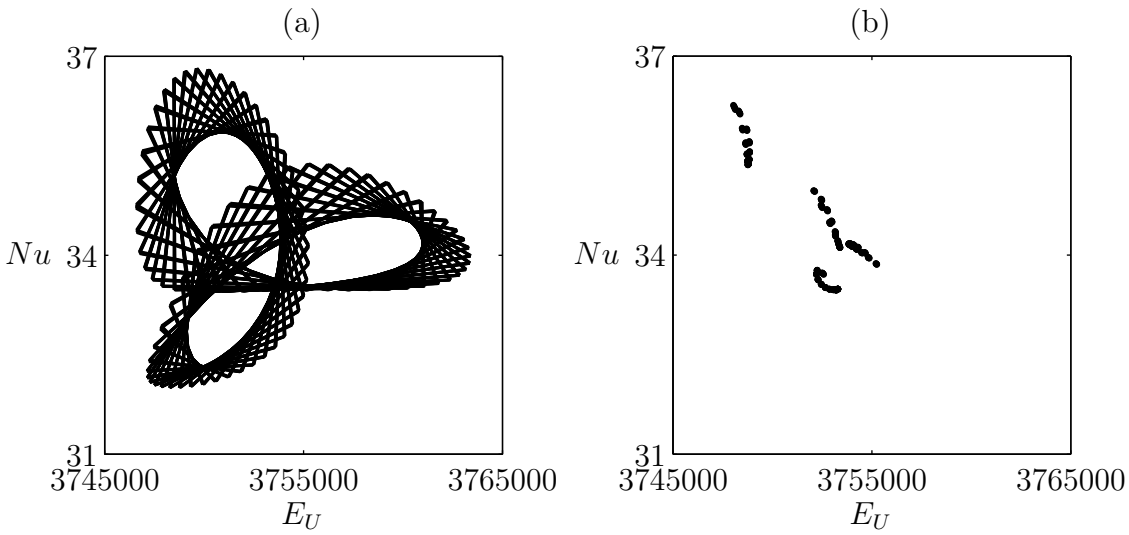

Figure 5.13: (a) two-dimensional projection of $(E_U, Nu, \mathcal{E})$ trajectory onto (E_U, Nu) plane with $7.40 \times 10^7 \leq \mathcal{E} \leq 7.78 \times 10^7$ and (b) corresponding Poincaré section at $\mathcal{E} = 7.60 \times 10^7$, for $R = 7000$, $Pr = 10$: exhibition of spontaneous order.

5.2.3 Physical instability mechanism

The oscillatory behaviour that we observed in the numerical simulations is caused due to a warm blob of fluid being released from the lower, warm boundary layer, and

the time it takes for the fluid blob to travel around the convective cell, returning to the same point, corresponds to the period of oscillation. By symmetry, the emission of a warm blob from the lower boundary layer necessitates the emission of a cold blob from the upper boundary layer. Welander (1967) conducted a simplified study of the motion described above by considering convection within a closed loop of fluid (later known as the Welander loop). The temperature gradient required to drive convection is imposed by having a positive heat flux at a point on the bottom of the loop and a negative heat flux at a point on the top of the loop. The model variables are the temperature within the loop and the flow speed along the loop, with the stability being governed by two dimensionless parameters that are akin to the Rayleigh number and Prandtl number. It is found that for the correct parameters, such a system supports oscillatory solutions, with warm and cold blobs traversing the fluid loop.

It is crucial to note that this behaviour was only observed for $Pr > 1$, where momentum diffusivity dominates thermal diffusivity. Hence, as the hot blob traverses the convection cell it does not shed sufficient heat so as to be absorbed into the ambient fluid and so it maintains its identity. Once it has completed one full cycle, the blob is again refreshed by the warm lower boundary layer, ready to complete another orbit of the cell. This means that the warm fluid blob rushes quickly past the cold upper boundary layer, and slowly past the warm lower boundary layer. Although the nature of the instability is thermal in origin, this asymmetry in the time spent near each boundary layer means that there must be a coupling with the momentum equation. At $Pr > 1$ the vorticity in the rising plume is balanced by the horizontal gradient of the temperature, so any warm thermal anomaly also induces a positive vortex anomaly. This build-up of vorticity in the rising plume induces a horizontal flow that is oriented in opposite directions above and below the vortex anomaly, causing the rising plume to be locally sheared. This accounts for the waving of the plumes that we saw. By symmetry an identical process occurs in the cold sinking plume, with a negative vortex anomaly.

For $Pr \leq 1$, thermal diffusivity is equal to, or dominates, momentum diffusivity. Hence any warm fluid blob emitted from the lower boundary layer sheds a sufficient amount of heat that its identity does not persist as it traverses the cell.

5.2.4 Nusselt number scaling

Convection is studied since it plays a part in many interesting and important geophysical and astrophysical settings. It is therefore of interest to simulate what happens at parameter values realistic to these environments—for example, convection at a Rayleigh number comparable to that of the Earth's core. These parameter values are often extreme and thus out of reach of even the most sophisticated numerical codes, using the greatest computer resources available. A common aim in the research community, therefore, is to derive scaling laws. The hope is that behaviour observed at lower parameter values may be extrapolated to these computationally out-of-reach regimes, in order to say something about the behaviour there.

For non-rotating convection, the key input parameters are the Rayleigh number and the Prandtl number, and the key output parameters are, most importantly, the Nusselt number and also the Reynolds number. We wish for expressions such as $Nu \equiv Nu(Ra, Pr)$, or more specifically, $Nu \sim Ra^{\alpha} Pr^{\beta}$, with the exponent α being particularly sought-after. Using arguments from *mixing length theory* the value of $\alpha = \frac{1}{3}$ was derived (see Kraichnan (1962) for a detailed discussion). It is assumed that in the interior of the fluid both the temperature and velocity vary over the same length scale, known as the mixing length scale. This is the characteristic length scale over which a buoyant parcel of fluid at a characteristic temperature is accelerated by a characteristic velocity, before its thermal energy is dissipated. At the top and bottom boundaries of the domain it is assumed that there exist thermal boundary layers of thickness δ, where most of the drop in temperature occurs, with all the heat being transported by conduction. Hence the ratio of the conductive heat flux

across the boundary layer, to the conductive heat flux across the whole layer, or, the Nusselt number, is given by

$$Nu \approx \frac{\frac{\kappa \Delta T}{2\delta}}{\frac{\kappa \Delta T}{d}} = \frac{d}{2\delta}. \tag{5.57}$$

It is assumed that the boundary layer Rayleigh number is close to its critical value—similar to that of linear stability theory—hence we have

$$\frac{g\alpha \Delta T \delta^3}{2\kappa\nu} \approx 10^3. \tag{5.58}$$

We may now eliminate δ between these two expressions to give

$$Nu \approx 0.04 Ra^{\frac{1}{3}}. \tag{5.59}$$

For a long time this exponent was favoured in both numerical (see Veronis (1966) and Moore & Weiss (1973)) and physical experiments (see Malkus (1954a)). The internal velocity and temperature are obtained by balancing the inertial and buoyancy terms in the momentum equation. In dimensional variables we have

$$(\mathbf{u} \cdot \nabla)\mathbf{u} \simeq g\alpha\theta\hat{\mathbf{z}}. \tag{5.60}$$

The mixing length scale is given by the depth of the convective layer, d, and $\frac{d}{U_*}$ is a typical turnover time, where U_* is a typical velocity. Denoting a typical temperature by T_*, we have

$$\frac{U_*^2}{d} \simeq g\alpha T_*. \tag{5.61}$$

The convective heat flux, H_*, is the amount of thermal energy carried over the mixing length, by the fluid velocity. It is given by

$$H_* \simeq U_* T_*, \tag{5.62}$$

hence we are able to determine the typical velocity and temperature

$$U_* = (g\alpha H_* d)^{\frac{1}{3}}, \quad T_* = \left(\frac{H_*^2}{g\alpha d}\right)^{\frac{1}{3}}. \tag{5.63}$$

Note that this result was also derived by Deardorff (1970), giving rise to the terminology *Deardorff velocity* and *Deardorff temperature*.

With advances in physical experimental techniques, higher Rayleigh numbers were able to be reached. This led to a subsequent favour for $\alpha = \frac{2}{7}$, as observed by Castaing *et al.* (1989). As computational resources improved too, this scaling relationship was also observed in numerical simulations by DeLuca *et al.* (1990) (see also Kerr (1996)), and led to the notion of a *hard turbulence regime*, where one observes such behaviour. For an overview encompassing all such early theory, one can consult Shraiman & Siggia (1990), or Siggia (1994) for a more in-depth discussion. As computational resources were improved further still Vincent & Yuen (2000) were able to observe the $\alpha = \frac{1}{2}$ dependence in their extremely high Rayleigh number simulations. Further to this Whitehead & Doering (2011) derived a rigorous upper bound of $\alpha = \frac{5}{12}$ which would seem to refute all previous arguments, as well as the results of Vincent & Yuen (2000). Within all these competing scaling theories, there is a fundamental question of exactly what role—if any—the horizontal aspect ratio, and more importantly the boundary layers play at very high values of the Rayleigh number. The aspect ratio of Vincent & Yuen (2000) was 3 for their two-dimensional convection study. Despite being half that of this study, it is still greater than many early convection simulations. Kraichnan (1962) states that for very large Ra one might expect that the boundary layers would become unstable to shear instabilities. Indeed Vincent & Yuen (2000) noticed that for $Ra > 10^{12}$ there was severe degradation of the boundary layers.

From a theoretical standpoint Grossman & Lohse (2000) present what they deem a *unifying theory of convection*, that corroborates not only numerical but physical experimental results. Their theory does not offer one such Nusselt number scaling, for all values of the Rayleigh number and the Prandtl number, instead offering different scaling laws in different areas of the (Ra, Pr) parameter space. Moreover, they posit that there could exist hybrid scaling laws that straddle the boundaries between these different regimes, for example the linear combination of $\alpha = \frac{1}{3}$ and $\alpha = \frac{1}{4}$ is conjectured to mimic the behaviour of an $\alpha = \frac{2}{7}$ exponent. These hybrid scaling laws could offer an explanation as to the differing exponents observed in

both numerical and physical experimental results. The different scaling regimes are determined based on the relative thicknesses of the viscous and thermal boundary layers, controlled by the value of the Prandtl number, whose effects had often been neglected in such theory, with all focus being on the Rayleigh number exponent. Furthermore, distinctions must be made between whether dissipation is primarily occurring in the boundary layer, or the core of the convection cell. Again this raises the question of exactly what role the boundary layers play in the limit of very large Ra.

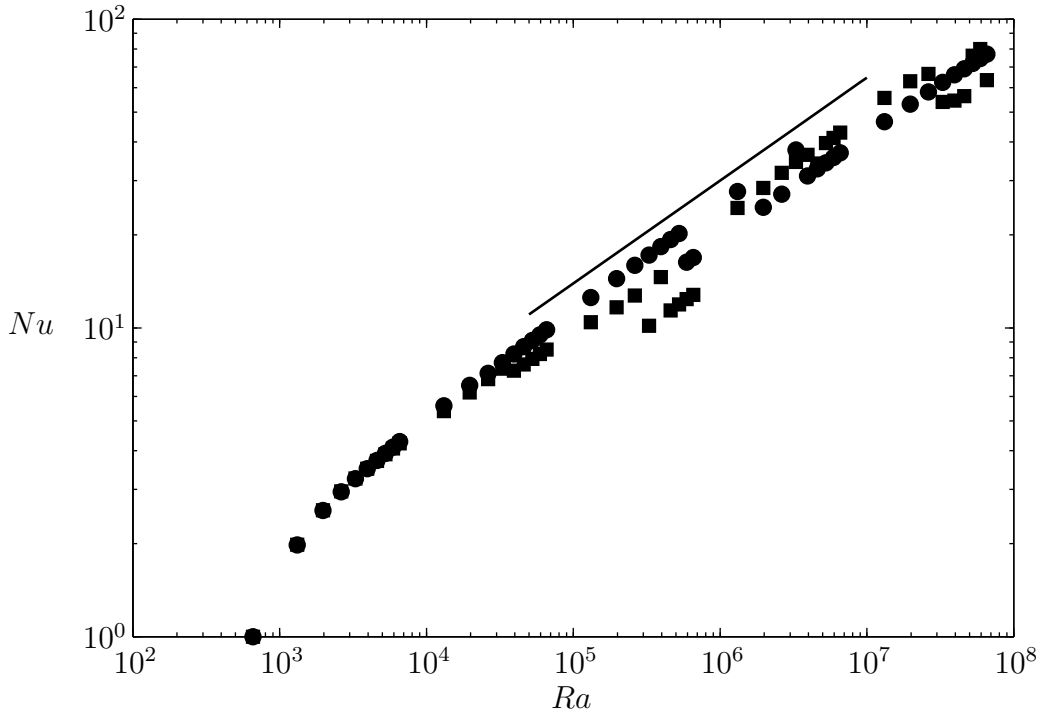

Figure 5.14: Nusselt number scaling for non-rotating convection, with $Pr = 1$ (circles) and $Pr = 10$ (squares). The line has exponent $\frac{1}{3}$.

Although the difference between $\frac{1}{3}$ and $\frac{2}{7}$ may seem negligible, if these scaling laws are to be used in order to extrapolate to parameter regimes realisable in nature, the resultant disagreement in Nusselt number can be several orders of magnitude. It is for this reason that there is such debate as to the precise values of the exponents. In Figure 5.14 we have plotted the Nusselt number from our numerical simulations versus the Rayleigh number. It can be seen that all values scale according to the law

$Nu \sim Ra^{\frac{1}{3}}$. This is to be expected, since the range of Rayleigh numbers that we have studied are all within the soft turbulence regime (see DeLuca *et al.* (1990) and Kerr (1996)). The distinct branches in Figure 5.14 correspond to different wavenumber flow patterns.

5.2.5 Reynolds number scaling

Recall that the average dimensionless kinetic energy dissipation rate is related to the Rayleigh number and Nusselt number via

$$\epsilon_U = Ra(Nu - 1) \equiv Ra_f, \tag{5.64}$$

where we define Ra_f to be the flux Rayleigh number, and recall that the kinetic energy dissipation was given by equation (5.39). Following Schmitz & Tilgner (2009), we approximate the kinetic energy dissipation as

$$\epsilon_U \sim \frac{(RePr)^2}{l_c^2}, \tag{5.65}$$

where l_c is the dimensionless, characteristic length scale over which the kinetic energy is dissipated. We can rearrange this to get an expression for the Reynolds number

$$Re \sim \frac{Ra_f^{\frac{1}{2}} l_c}{Pr}, \tag{5.66}$$

which may be evaluated once we have chosen a suitable length scale. For non-rotating convection we expect convection to develop on the scale of the box, hence we have that the Reynolds number scales as follows

$$Re \sim \frac{Ra_f^{\frac{1}{2}}}{Pr}. \tag{5.67}$$

This scaling can be seen in Figure 5.15, where we note that the agreement is excellent. Furthermore, using $Nu \sim Ra^{\frac{1}{3}}$ within equation (5.67) gives

$$Re \sim \frac{Ra^{\frac{2}{3}}}{Pr}, \tag{5.68}$$

which is in accordance with the numerical results of Moore & Weiss (1973) and the simple boundary layer analysis of Robinson (1967) that was developed to describe steady state convection cells.

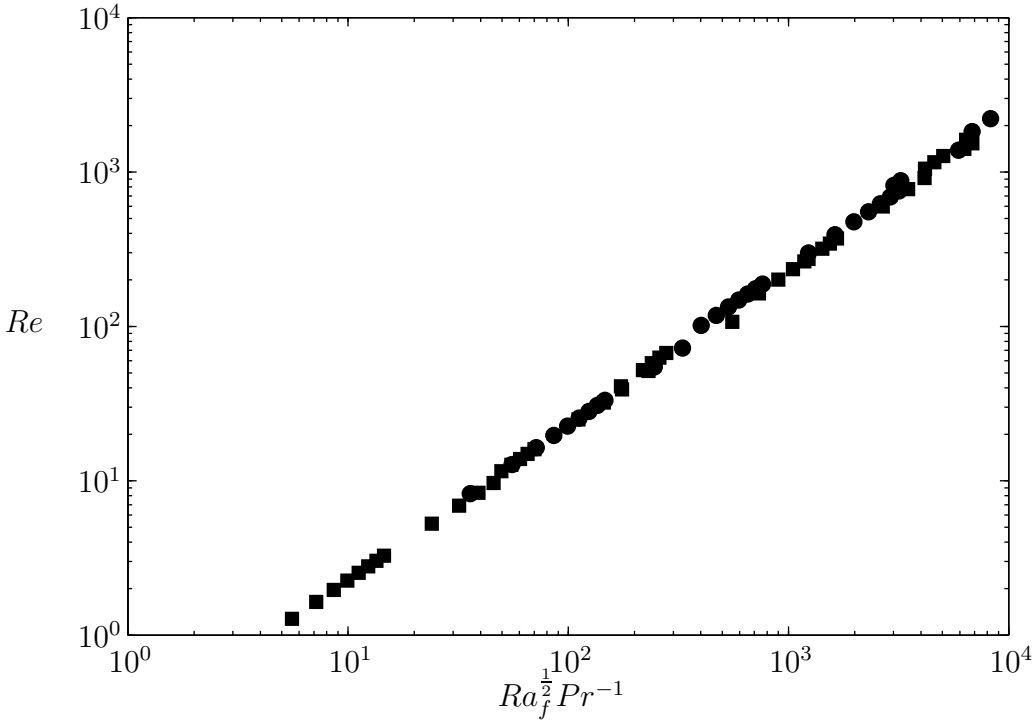

Figure 5.15: Reynolds number scaling for non-rotating convection, with $Pr = 1$ (circles) and $Pr = 10$ (squares).

5.3 The effect of rotation

The earliest notable numerical study of two-dimensional convection was conducted by Veronis (1968), seeking to reproduce the experimental observations made by Rossby (1969) (work conducted for H.T. Rossby's PhD, awarded in 1966, but not published in a journal until 1969). Albeit for low Rayleigh numbers and rotation rates, this work still charted the nonlinear instability mechanism and its saturation. Despite this achievement, there was little subsequent work conducted on rotating, two-dimensional convection, the favour being for three-dimensional

convection instead. Somerville & Lipps (1973) also attempted to reproduce the observations of Rossby (1969), but using a three-dimensional numerical method.

In three space dimensions there are additional processes, such as the Kuppers Lortz instability (see Kuppers & Lortz (1969)), whereby convection rolls become unstable and change their orientation provided the rotation rate is high enough. This has been observed in both numerical (see Clever & Busse (1978)) and physical (see Li & Ecke (1993)) experiments. Further work was devoted to studying rotating convection in geometries more suitably mimicking those found in nature, such as Busse's rotating annulus (see Busse (1978)).

With advances in experimental techniques and computer hardware, the majority of subsequent work on rotating convection has been conducted in three space dimensions. Notable numerical studies include those of Julien *et al.* (1996b)/Julien *et al.* (1996a) and more recently Julien *et al.* (2012). The latter presents a set of *asymptotically reduced equations* that are valid in the limit of small Rossby number (large rotation rates), in order to study the influence of rotation on the system, even for large Rayleigh number. The overwhelming majority of recent numerical and experimental studies of rotating convection have been concerned with deriving scaling laws governing various measures of the dynamics of the system, for example the Nusselt number. This is something we shall address in a subsequent section.

Rotating convection is governed by three dimensionless input parameters: the Rayleigh number, the Prandtl number and the Taylor number. The Rayleigh number controls the thermal driving of the system, whilst the Taylor number controls the rotational driving. The ratio of these two competing effects can be measured by defining what is known as the *convective Rossby number*, Ro_*, which can be thought of as the ratio of a typical convective turnover time, $t_{\text{conv}} = \frac{d}{U_*}$, to a rotation time, $t_{\text{rot}} = \frac{1}{2\Omega}$. Balancing the advection term and the buoyancy term within the momentum equation gives (see Julien *et al.* (1996b))

$$U_*^2 = g\alpha\Delta T d, \tag{5.69}$$

and hence

$$Ro_* = \frac{t_{\rm rot}}{t_{\rm conv}} = \sqrt{\frac{g\alpha\Delta T}{4\Omega^2 d}}. \tag{5.70}$$

Expressed in terms of the dimensionless parameters of the system, we have

$$Ro_* = \sqrt{\frac{Ra}{TaPr}}, \tag{5.71}$$

with $Ro_* \simeq 1$ marking the point at which the relative magnitudes of the buoyancy force and the rotation force are equal. Studying numerical runs with differing values of Ra, Pr, and Ek, but similar values of Ro_* will facilitate comparison of runs where the type of driving—be it rotation or buoyancy—is the same. The parameter regime that we have studied is given by

$$\Big\{Ra \leq 10^8, \quad 10^4 \leq Ta \leq 10^8, \quad Pr = 1 \text{ and } 10\Big\}, \tag{5.72}$$

with the precise simulation values shown in Figure 5.16. The critical Rayleigh numbers and wavenumbers for the onset of convection can be found in Table 3.2 of Chapter 3. As in the non-rotating case we maintain a fixed box length of $L = 2\pi$ for all simulations. Since we expect that as the Taylor number is increased, the preference will be for tall thin columnar convection, this box length should be adequate enough to resolve the flows that arise. Furthermore, it is wider than that used by Moore & Weiss (1973), DeLuca *et al.* (1990) and Vincent & Yuen (1999).

5.3.1 Horizontal length scale

For the non-rotating system it was seen that as the Rayleigh number was increased, the general preference of the system was for a larger horizontal length scale—the largest allowable in the computational box. Furthermore, instability from steady convection was only present for $Pr = 10$. The linear theory of rotating convection told us that as the Taylor number is increased, the critical wave number is also increased. We were able to derive an asymptotic relation to determine the critical wave number in terms of the Taylor number, namely $a_c \sim Ta^{\frac{1}{6}}$.

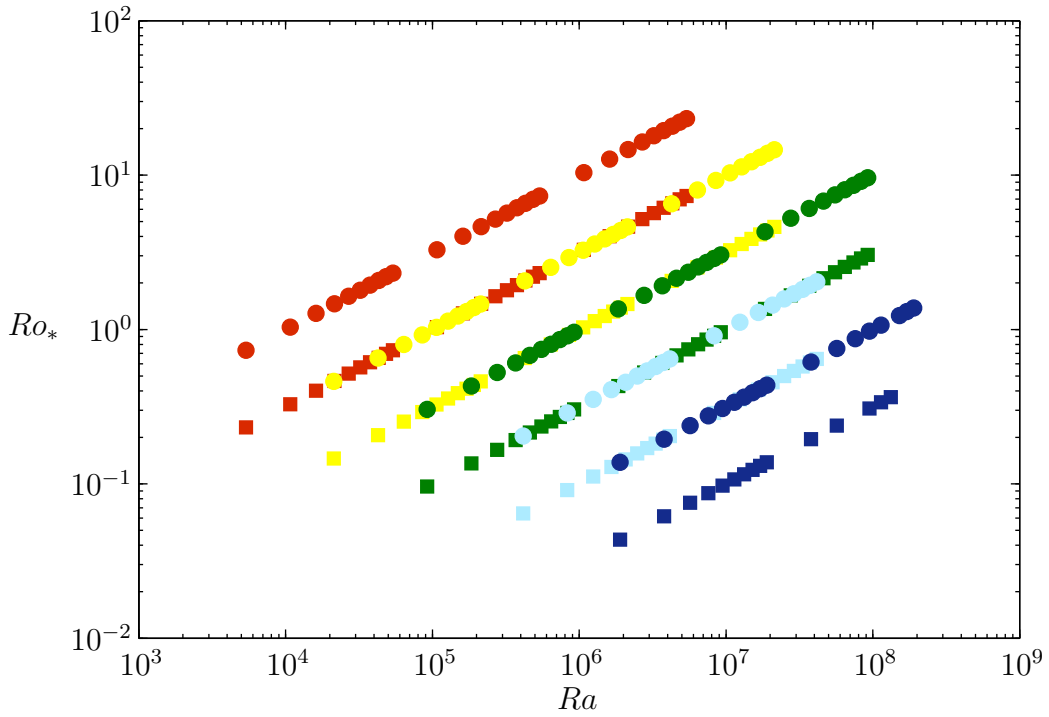

Figure 5.16: Numerical simulations performed: convective Rossby number as a function of Rayleigh number for $Ta = 10^4$ (red), $Ta = 10^5$ (yellow), $Ta = 10^6$ (green), $Ta = 10^7$ (light blue) and $Ta = 10^8$ (dark blue), with $Pr = 1$ (circles) and $Pr = 10$ (squares).

In Figure 5.17 we have plotted the dominant wave number from our nonlinear simulations versus the Taylor number, at the onset of convection. It can be seen quite clearly that this does follow the asymptotic law proposed. The Taylor-Proudman theorem told us that in the limit as $Ta \to \infty$, the flow should become invariant in the vertical direction, leading to tall thin columnar convection—a very short horizontal length scale. Thus we expect competition between the relative effects of buoyancy and rotation, seeking to govern the horizontal length scale of the system, hence the introduction of the convective Rossby number. The form of the convection for large Taylor number, at onset, can be seen in Figure 5.18, whereby the rotational influence over the flow is readily apparent and the columnar structure is quite striking. Of course the linear scaling is only formally valid at onset, and says nothing about the nonlinear development of the flow as the Rayleigh number is increased.

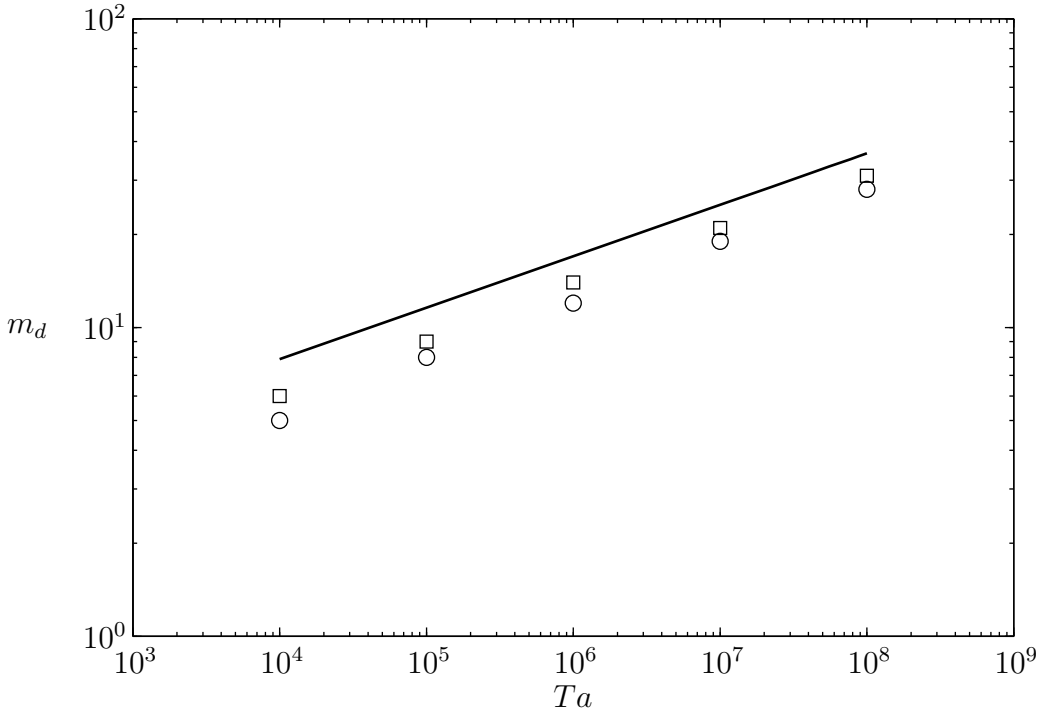

Figure 5.17: Dominant wave number versus Taylor number, at the onset of convection, from numerical simulations, with $Pr = 1$ (circles) and $Pr = 10$ (squares). The solid line represents the asymptotic law from linear theory, given by equation (3.54).

In Figure 5.19 we have plotted the dominant wavenumber from our numerical simulations versus the convective Rossby number. It can be seen that for $Ro_* < 1$, at a given Taylor number and Prandtl number, the system seems to develop according to the wave number chosen at onset, or a larger wave number still. Increasing the Rayleigh number at a fixed Taylor number—increasing the convective Rossby number—eventually causes the effect of buoyancy to dominate over rotation, and so a progression to a smaller dominant wavenumber, and hence larger horizontal length scale, is observed. This seems to occur in a transitional region in the vicinity of $Ro_* = 1$. As Ro_* is increased further still, any notion of rotational influence is lost, with the system returning to a preferred large length scale, as in the non-rotating system.

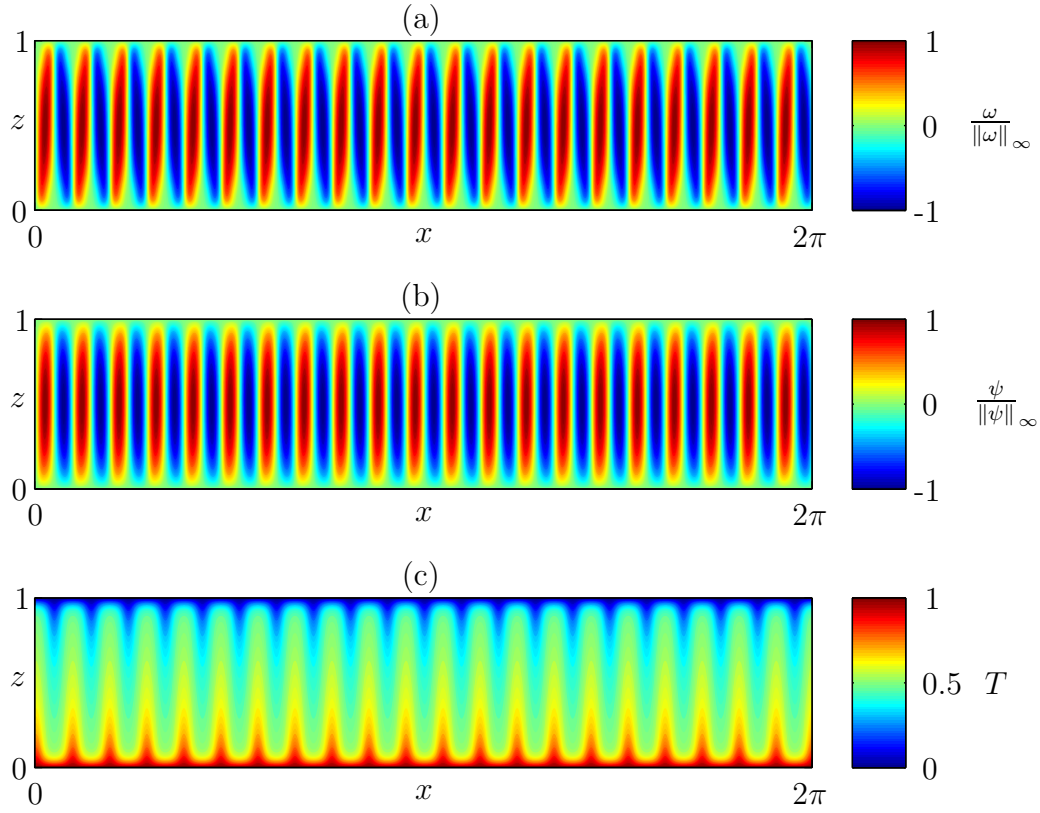

Figure 5.18: Contour plots of (a) the normalised vorticity ($\|\omega\|_\infty = 2958$), (b) the normalised streamfunction ($\|\psi\|_\infty = 7$) and (c) the total temperature, for $Ta = 10^7$, $Pr = 10$, $R = 3$ ($Ra = 1.2441 \times 10^6$), with resolution $[1024 \times 128]$: exhibition of tall thin columnar convection.

In Figure 5.20 we plot the mean temperature profile as a function of height, for various Taylor numbers, at each Prandtl number, for a fixed Rayleigh number. Increasing the Taylor number at fixed Rayleigh number and Prandtl number amounts to decreasing the convective Rossby number. It can be seen in both Prandtl number cases that rotation relaxes the gradient of the mean temperature curve in the middle of the convective layer. As the convective Rossby number is increased the temperature approaches an isothermal profile, as in the non-rotating case, for both values of the Prandtl number. At the lowest rotation rate, the distinguishing feature between $Pr = 1$ and $Pr = 10$ is the magnitude of the overshoot at the transition from the core of the layer to the boundary layer—this being greater in

the $Pr = 1$ case. Note that as in the non-rotating system, the mean temperature plots are taken at a particular moment in time, hence the asymmetry about the line $z = \frac{1}{2}$ in some cases.

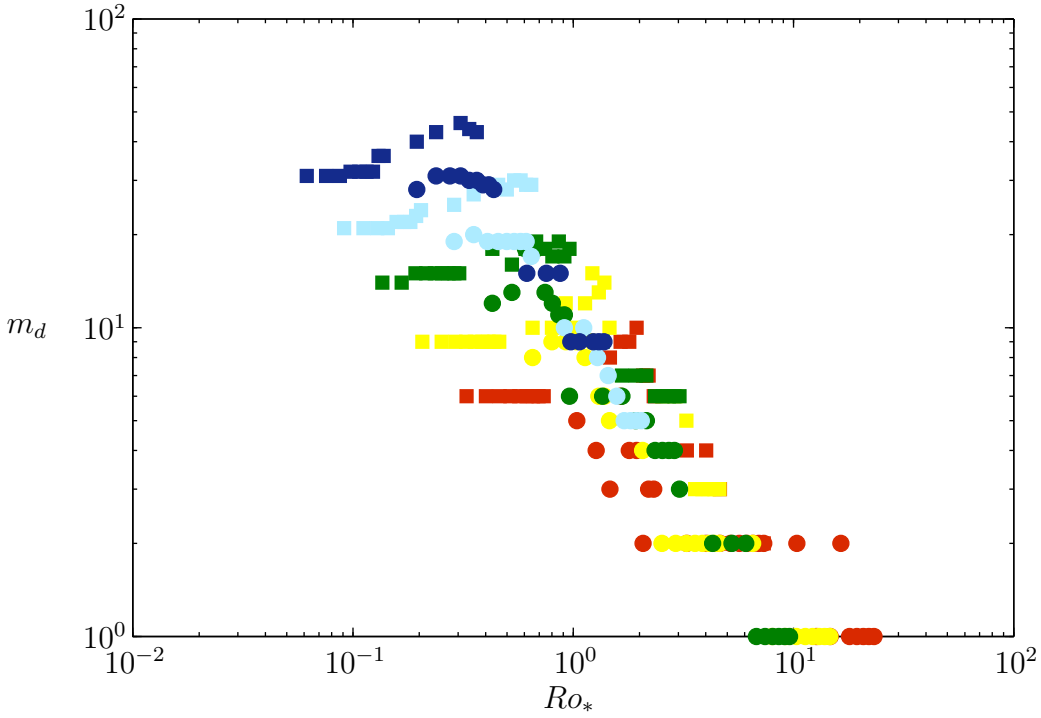

Figure 5.19: Dominant wave number versus convective Rossby number, for $Ta = 10^4$ (red), $Ta = 10^5$ (yellow), $Ta = 10^6$ (green), $Ta = 10^7$ (light blue) and $Ta = 10^8$ (dark blue), with $Pr = 1$ (circles) and $Pr = 10$ (squares).

5.3.2 Flow development

The discussion so far has concerned the development of the horizontal length scale, due to the competing effects of the buoyancy and rotational forces acting on the system, yet we have not mentioned anything about the stability of the system as the Rayleigh number is increased. It does not seem that there is a law governing the values of the input parameters at which the system is expected to become unstable. There are however, a few choice observations to be noted.

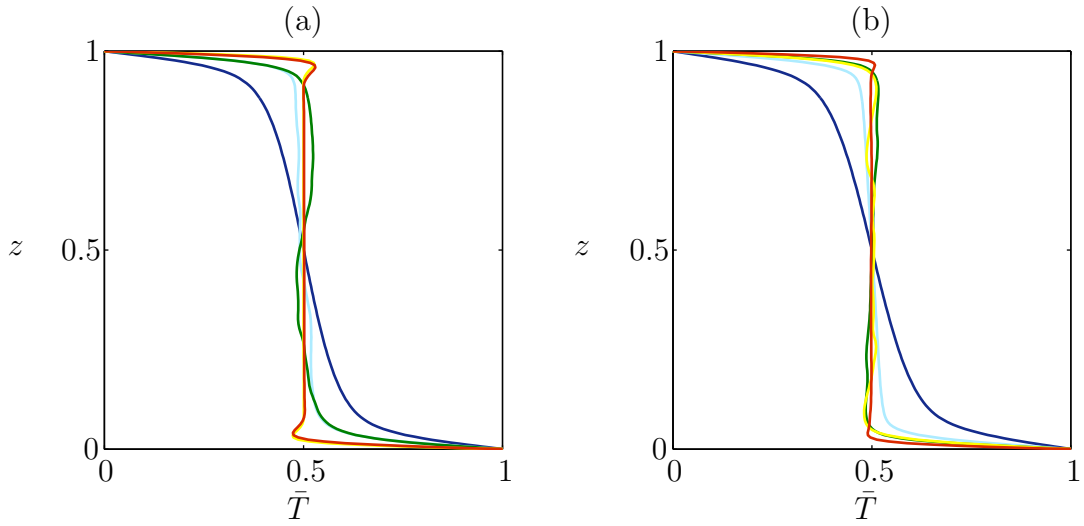

Figure 5.20: Mean temperature profile as a function of z, with $Ra \simeq 5 \times 10^6$ for $Ta = 10^4$ (red), $Ta = 10^5$ (yellow), $Ta = 10^6$ (green), $Ta = 10^7$ (light blue) and $Ta = 10^8$ (dark blue), for (a) $Pr = 1$ and (b) $Pr = 10$.

Beginning with $Ta = 10^4$, the lowest rotation rate implemented, and $Pr = 1$, only steady solutions were found for the range of Rayleigh numbers considered. This is the only such Taylor number where this was the case. Looking at Figure 5.19 it can be seen that in this case (red circles) the convective Rossby number is consistently above unity, hence the system does not feel the effects of rotation, even at onset. The flow develops as if it were non-rotating, eventually evolving on the largest length scale allowable. Furthermore, the structure of the flow is cellular, as in the non-rotating system, hence we have not shown an example here. It can be seen in Figure 5.20(a) that there is a sharp transition in the mean temperature (red curve) near the boundaries, owing to the cellular flow structure.

Increasing the Taylor number to 10^5, but maintaining $Pr = 1$ (yellow circles) means that the convective Rossby number is slightly below unity at onset. Solutions are initially steady but become unsteady for $1.22 \leq Ro_* \leq 1.30$, coinciding with a drop in the dominant horizontal wave number from nine to six. The flow still appeared to have a remnant cellular appearance, with chaotic wavy plumes similar to the instability in the non-rotating system. As the Rayleigh number—and also the

convective Rossby number—is increased the system once again begins to relinquish any appearance of rotational constraint, with the dominant wavenumber decreasing. This has the effect of not only causing the system to evolve on a larger horizontal length scale, but to re-stabilise, with the flow returning to a purely cellular structure. This is the only such case of this behaviour that we have noted.

For all other combinations of Ta and Pr, for the range of Ra studied, it can be seen by looking at Figure 5.19 that the convective Rossby number is always below unity at onset, and in some cases never becomes greater than it. In all these cases, the system was found to be steady for an initial range of Rayleigh numbers but after becoming unsteady they never re-stabilised. This is despite the fact that the convective Rossby number attains similar values to those that re-stabilised for $Ta = 10^5$—for $Ta = 10^6$ at least. For higher Taylor numbers, if the Rayleigh number was increased in order to establish a convective Rossby number greater than unity, we would not expect to see any re-stabilisation. Even if the system can enter a buoyancy-dominated regime, the Rayleigh number will be sufficiently high as to have brought about unsteady behaviour anyway. Instability manifests itself via a similar sequence as presented in the non-rotating system. That is, the emergence of time-periodic flows associated with thermal blob-type instabilities and wavy plumes are the first departure from cellular convection that are realised. In the non-rotating system this instability was caused due to a thermal anomaly in the boundary layer, that in turn induced a build up of vorticity in the rising plume. In the rotating system, this vorticity is enhanced due to the background rotation, leading to a further destabilising effect within the rising plume. This behaviour is consistent with that noted by Julien *et al.* (1996a) in their three-dimensional numerical simulations of rotating convection. A typical visualisation of such an instability can be seen in Figure 5.21. There is a remnant cellular appearance to the flow and the temperature field still consists of plume-like structures. Furthermore, concentrations of intense vorticity can be seen within the rising plumes. After the system has become unsteady, the precise structure of the turbulent flows that are generated differs greatly, dependent on the

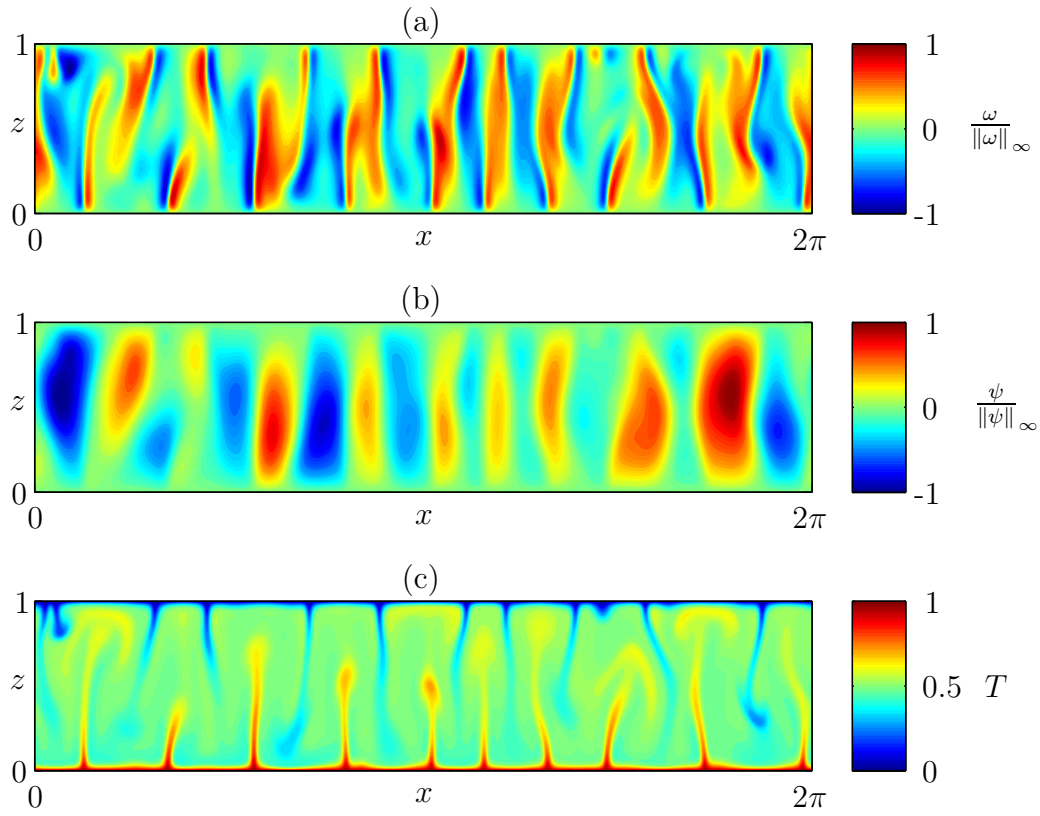

Figure 5.21: Contour plots of (a) the normalised vorticity ($\|\omega\|_\infty = 1.5 \times 10^4$), (b) the normalised streamfunction ($\|\psi\|_\infty = 136$) and (c) the total temperature, for $Ta = 10^5$, $Pr = 10$, $R = 100$ ($Ra = 2.131 \times 10^6$), with resolution $[512 \times 96]$: exhibition of an unstable plume solution.

amount of dominance the rotation has on the system. Thus we can have chaotic large scale flows where the effect of rotation is minimal, as can be seen in Figure 5.22, and chaotic flows that still possess a great amount of rotational constraint, as can be seen in Figure 5.23. Note that these two particular flows are for a similar Rayleigh number, and the same Prandtl number, but with a factor of 10^2 difference in Taylor number. Hence there is roughly a factor 10 difference in the convective Rossby number. In Figure 5.22 it can be seen that there is a strong, large scale flow in the interior of the layer. Weak, coherent vortical structures are present in the interior, corresponding to regions where the temperature is approximately isothermal, whilst intense concentrations of vorticity are located within the rising

and descending plumes. This is in contrast to Figure 5.23 where the vorticity is more evenly distributed throughout the layer, and no large scale flow is present. In both cases, the vorticity attains similar values in the plumes. The defining features of both of these plots are how thin the thermal boundary layers are, and the intense concentrations of vorticity within the rising and descending plumes. Again, this is due to background rotation amplifying the local production of vorticity within the plumes. Based on the schematic in Figure 5.1 it is clear that both of these solutions fall into the turbulent regime, classified by the branching of thermal plumes due to disruptions in the boundary layer. Furthermore, the flows shown in Figures **??** and 5.23 are similar to those of Julien *et al.* (1996b) in their three-dimensional simulations.

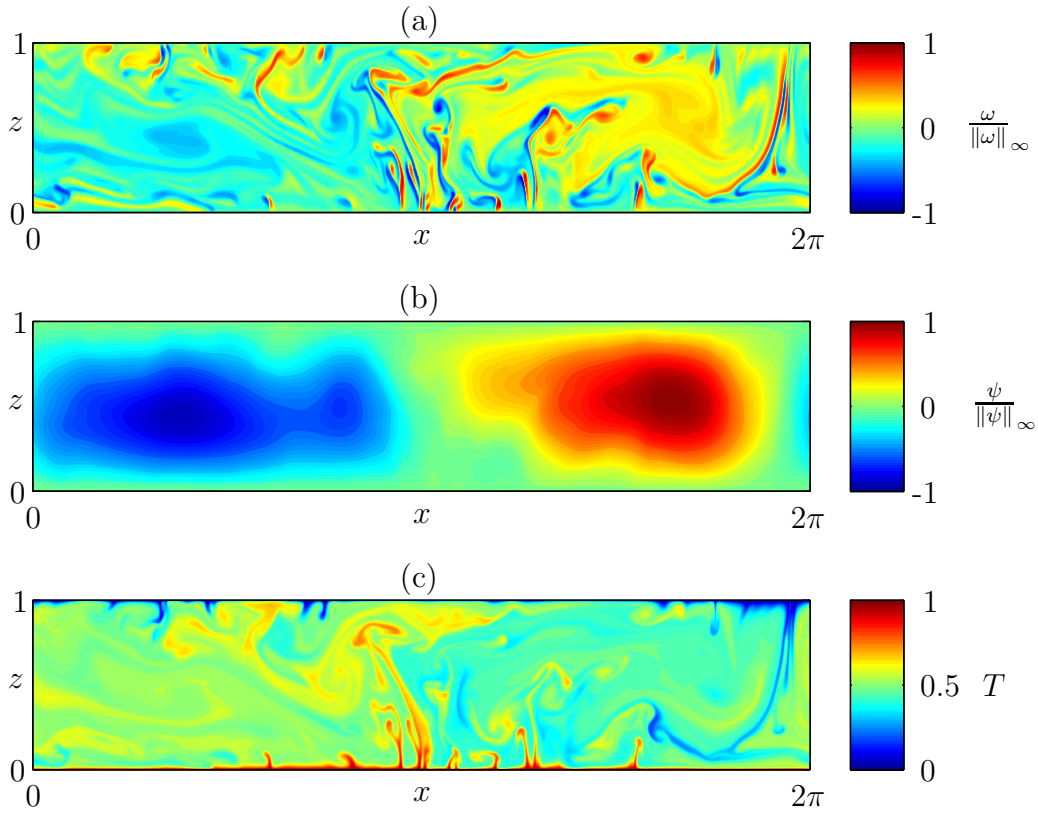

Figure 5.22: Contour plots of (a) the normalised vorticity ($\|\omega\|_\infty = 1.3 \times 10^5$), (b) the normalised streamfunction ($\|\psi\|_\infty = 3107$) and (c) the total temperature, for $Ta = 10^6$, $Pr = 1$, $R = 1000$ ($Ra = 9.222 \times 10^7$), with resolution $[1024 \times 128]$: exhibition of a large-scale chaotic solution.

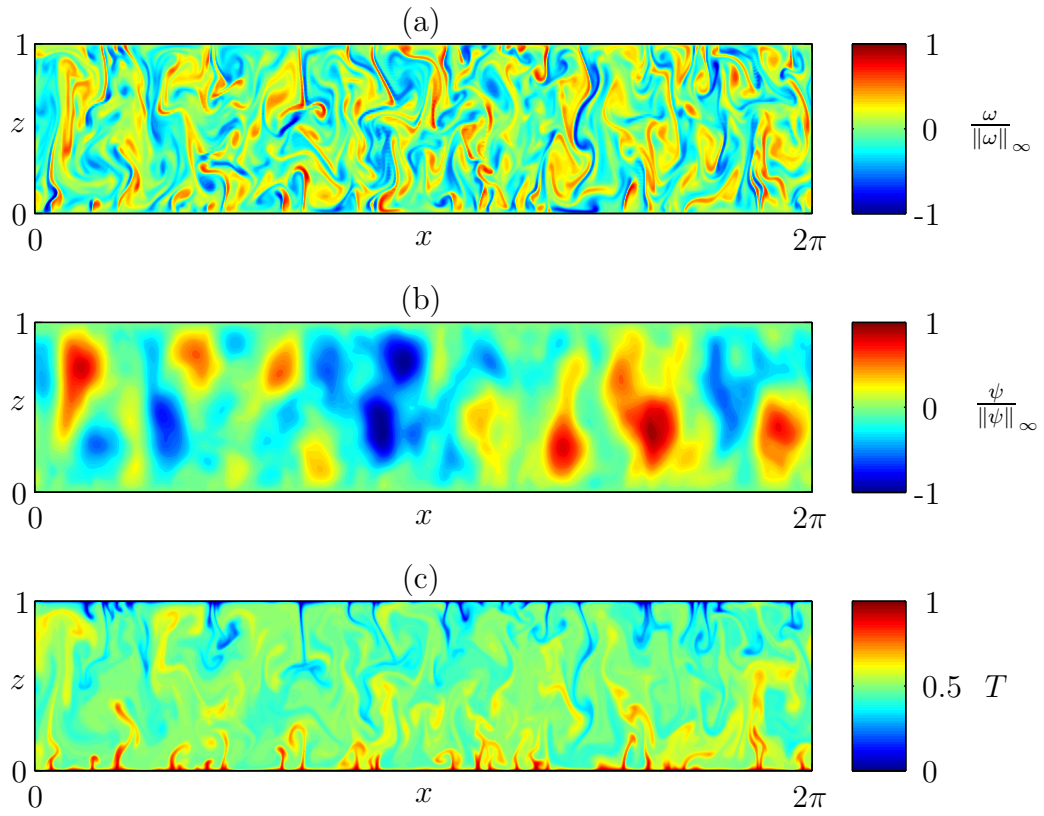

Figure 5.23: Contour plots of (a) the normalised vorticity ($\|\omega\|_\infty = 1.39 \times 10^5$), (b) the normalised streamfunction ($\|\psi\|_\infty = 558$) and (c) the total temperature, for $Ta = 10^8$, $Pr = 1$, $R = 50$ ($Ra = 9.485 \times 10^7$), with resolution $[1024 \times 128]$: exhibition of a rotationally constrained chaotic solution.

5.3.3 Nusselt number scaling

With the addition of rotation, we must also consider the fact that the scaling relationship could be dependent on the Ekman number, hence we have $Nu \sim Ra^\alpha Pr^\beta Ta^\gamma$. Early numerical and experimental studies of rotating convection seemed to favour both $\alpha = \frac{1}{3}$ and $\alpha = \frac{2}{7}$—dependent on the boundary conditions—as in the non-rotating case (see Julien *et al.* (1996b)/Julien *et al.* (1996a) and Liu & Ecke (1997)). Subsequent numerical simulations have almost unanimously reached the conclusion that $\alpha = \frac{2}{7}$ is the preferred Rayleigh number scaling exponent (see

Schmitz & Tilgner (2009), King *et al.* (2009) and King *et al.* (2013)). However, there is not yet a consensus as to the correct values of β and γ, particularly the effect that the rotation has on the system. It is an open problem to determine the values of the governing parameters at which there is a transition from rotationally-dominated to buoyancy-dominated regimes. Once again there is fervent debate as to the role—if any—played by boundary layers. In particular the role of the Ekman layer, for convection with no-slip boundary conditions. As we have seen in the numerical results presented here, increasing the Rayleigh number for a fixed Ekman number results in the loss of all rotational dominance, and the flow mimics that of the non-rotating flow. This has the implication that the Nusselt number scaling relationship should also collapse to that of the non-rotating case for large Ra. We introduced the convective Rossby number, measuring the relative effects of buoyancy and rotation. For a long time it was thought that $Ro_* \simeq 1$ marked the transition between rotationally-dominated and buoyancy-dominated regimes, however this has since come under some scrutiny. In a comprehensive series of numerical experiments, Schmitz & Tilgner (2009) (see also Schmitz & Tilgner (2010) for no-slip boundary conditions, for direct comparison with King *et al.* (2009)) find that a suitable combination of the Reynolds, Ekman and Prandtl numbers can predict when this transition occurs. Their simulations are performed with stress-free boundary conditions, so their theory is not dependent on the existence of an Ekman layer. In contrast to this, via a series of numerical and physical experiments with no-slip boundary conditions, King *et al.* (2009) (see also King *et al.* (2012) and King *et al.* (2013)) argue that it is the boundary layers themselves that dictate the Nusselt number scaling relationship and furthermore the influence of rotation upon the flow. In the asymptotically reduced equations of Julien *et al.* (2012), even for no-slip numerical calculations they assume that the role of the Ekman layer is a passive one, and that it is a global force balance that leads to the transition from rotationally-dominated to buoyancy-dominated regimes. Liu & Ecke (2009) did not come to any definite conclusion as to how the boundary layer affects the Nusselt number scaling in their series of physical experiments, so it remains to be seen if

a consensus can be reached on the matter. Indeed, given the analysis provided by Grossman & Lohse (2000) for the non-rotating system, it is realistic to expect that there is no one-size-fits-all scaling law. In Figure 5.24 we have plotted the Nusselt number from our numerical simulations versus the Rayleigh number, for all Prandtl and Taylor numbers considered, in a similar manner to Schmitz & Tilgner (2009) and King *et al.* (2009). Furthermore, we have included the non-rotating values for comparison.

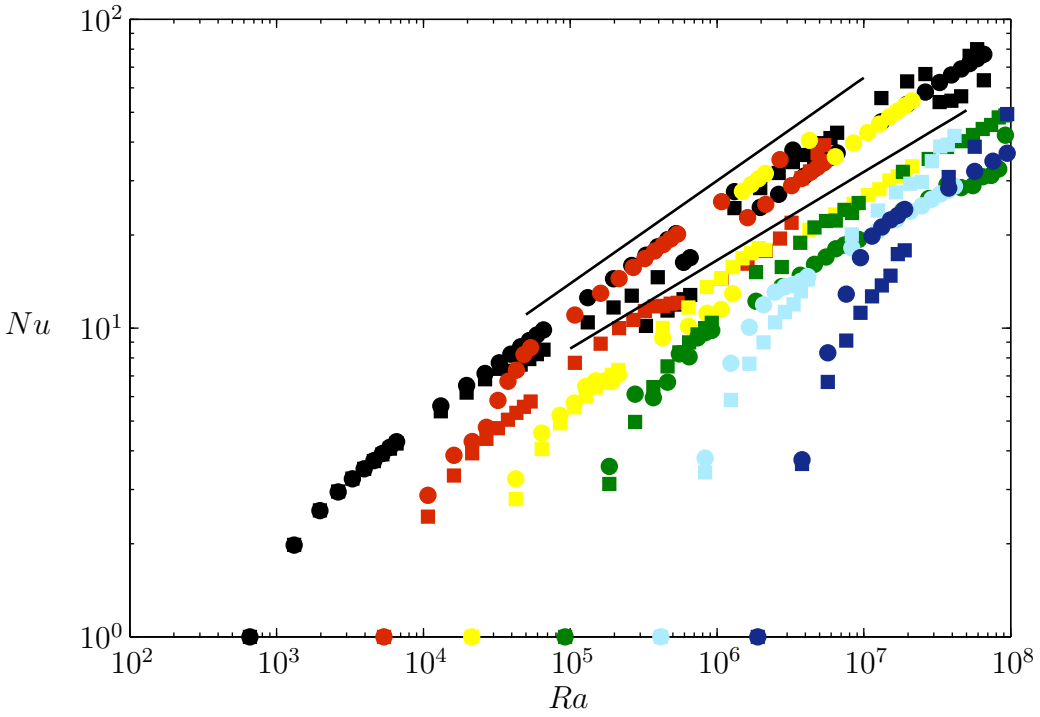

Figure 5.24: Nusselt number versus Rayleigh number for $Ta = 0$ (black), $Ta = 10^4$ (red), $Ta = 10^5$ (yellow), $Ta = 10^6$ (green), $Ta = 10^7$ (light blue), and $Ta = 10^8$ (dark blue), with $Pr = 1$ (circles) and $Pr = 10$ (squares). The upper line has exponent $\frac{1}{3}$ whilst the lower line has exponent $\frac{2}{7}$.

The results that seem to scale with $Ra^{\frac{1}{3}}$ are those with zero rotation, or at lower rotation rates, however even these lower Ta results corresponded to runs where the rotational dominance over the flow was minimal. Recall that in these runs, the onset of convection was characterised by a preferential wavenumber, then as the Rayleigh number was increased we observed a transition to large scale convection. In steady

cases we observed a purely cellular convection pattern but even in time-dependent cases there was an amount of cellular dominance and intermittent periods of steady behaviour. This would seem to suggest that a large scale cellular flow pattern is somehow optimal for the heat transport, at least for the range of parameters considered here.

The results that seem to scale with $Ra^{\frac{2}{7}}$ are those at higher rotation rates. In all these runs, convection was found to be unsteady, whether the flow was rotationally dominated or not. The flow developed in a fully turbulent manner and we witnessed chaotic plumes with no cellular structure at all. This is encouraging to see, as it is conjectured that the transition from the $\frac{1}{3}$ to $\frac{2}{7}$ scaling regime occurs once the flow has become fully turbulent (see Castaing *et al.* (1989) and DeLuca *et al.* (1990)).

Obviously as Ra is increased, one would expect these large scale cellular-type flows to break up and develop in a fully turbulent manner. It would be interesting to see how this affected the Nusselt number scaling. Furthermore, these large scale cellular flows are a definite manifestation of the fact that our system is only two dimensional. In three dimensions, the additional instabilities that we have already mentioned would certainly lead to a break-up of these flows.

5.3.4 Reynolds number scaling

In order to calculate the Reynolds number scaling for the rotating system, we need to choose a suitable length scale to use within equation (5.66). In the limit as $Ta \rightarrow \infty$, at onset, we expect that $l_c \sim Ta^{-\frac{1}{6}}$. Furthermore, King *et al.* (2013) note that this scaling is to be expected in the rotationally-dominated regime, where there is a balance between the Coriolis force and the horizontal diffusion of vorticity within the interior of the domain. In dimensionless variables we have

$$Ta^{\frac{1}{2}} Pr \frac{\partial v}{\partial z} \simeq Pr \nabla^2 \omega. \tag{5.73}$$

It is assumed that the z derivative of the velocity on the left-hand side is proportional to the box height (equal to unity in dimensionless variables), whilst the right-hand

side is dominated by horizontal gradients, therefore we have

$$Ta^{\frac{1}{2}}U_* \simeq \frac{U_*}{l_c^3}. \tag{5.74}$$

Rearranging this gives the required expression $l_c \sim Ta^{-\frac{1}{6}}$. In Figure 5.25 we plotted the dominant horizontal wavenumber—which is inversely proportional to a length scale—in our numerical simulations versus the Taylor number, identifying the scaling $m_d \sim Ta^{\frac{1}{6}}$. For large Taylor numbers it can be seen that the agreement is quite good, regardless of the value of the Rayleigh number. For low Taylor numbers, as the Rayleigh number is increased, the dominant horizontal wavenumber attains an order one value regardless. These were the runs where the rotational dominance over the flow was minimal, hence we might expect some disagreement for lower Taylor numbers at high Rayleigh number.

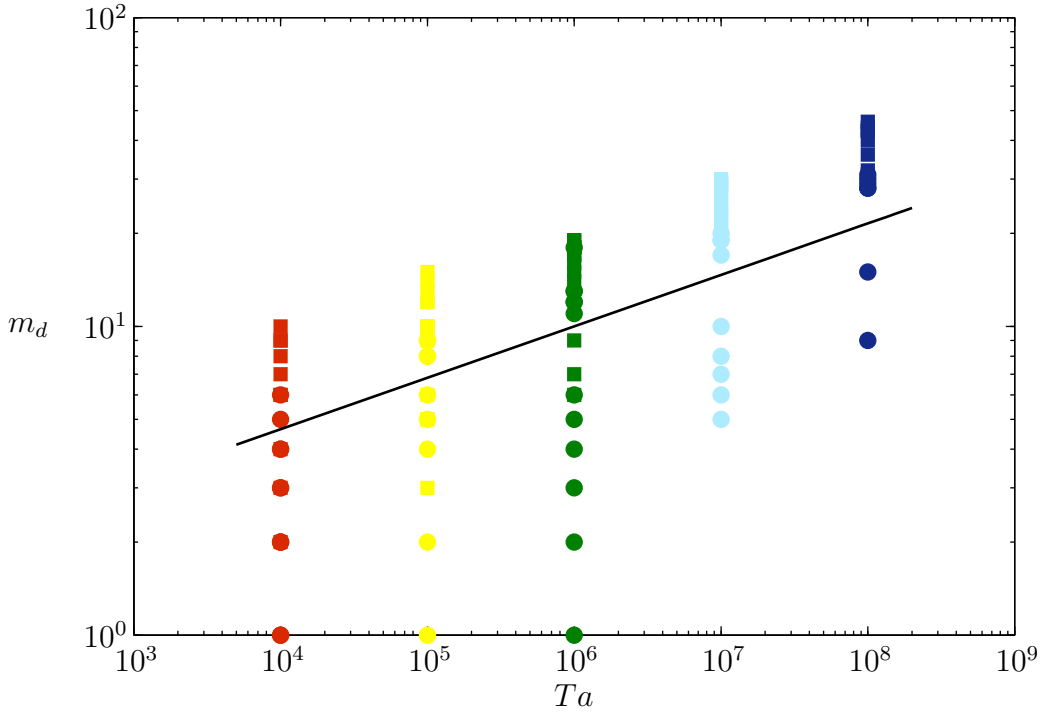

Figure 5.25: Dominant wavenumber versus Taylor number for $Ta = 10^4$ (red), $Ta = 10^5$ (yellow), $Ta = 10^6$ (green), $Ta = 10^7$ (light blue), $Ta = 10^8$ (dark blue), with $Pr = 1$ (circles) and $Pr = 10$ (squares). The solid line is proportional to $Ta^{\frac{1}{6}}$.

Proceeding with this scaling regardless and using equation (5.66), we have that the Reynolds number scales as follows

$$Re \sim \frac{Ra_f^{\frac{1}{2}}}{Ta^{\frac{1}{6}} Pr}. \tag{5.75}$$

Furthermore, this is the same scaling as seen by Schmitz & Tilgner (2009) in their three-dimensional simulations.

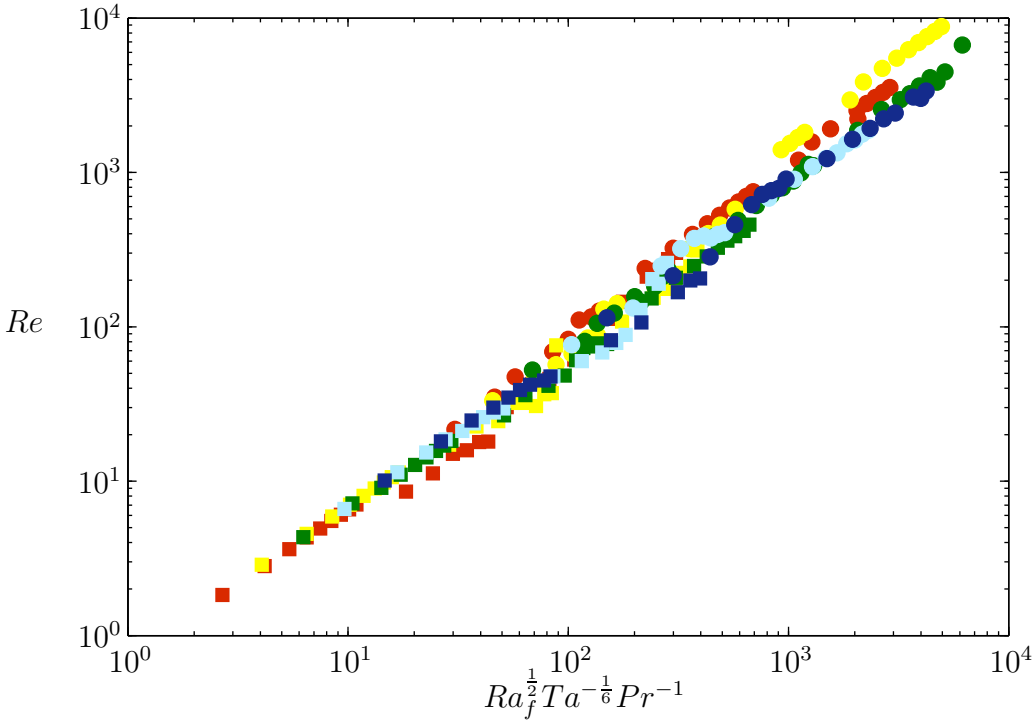

Figure 5.26: Reynolds number scaling for $Ta = 10^4$ (red), $Ta = 10^5$ (yellow), $Ta = 10^6$ (green), $Ta = 10^7$ (light blue), and $Ta = 10^8$ (dark blue), with $Pr = 1$ (circles) and $Pr = 10$ (squares).

This scaling can be seen in Figure 5.26, where we note that the agreement is excellent, even for lower Taylor numbers. For these runs, where the flow was not rotationally dominated, we noted that the Nusselt number versus Rayleigh number scaling was steeper than in the rotationally dominated regime. Within equation (5.75) the relative effect of an increased Nusselt number for lower Taylor numbers compensates for the lack of agreement between the dominant wavenumber

and the Taylor number. This provides an explanation for why equation (5.75) is seemingly still valid even for lower Taylor numbers. To our knowledge, this is the first demonstration that this particular three-dimensional scaling law also holds in the two-dimensional system.

5.4 Summary

In this chapter we presented the results of our numerical simulations, analysing the behaviour of the system as the governing input parameters were altered. A composite approach was taken to this analysis—looking at the physics of the convective flows generated; analysing the nonlinear behaviour of the system, utilising techniques from dynamical systems theory; and attempting to classify the results into different scaling regimes, based on certain output parameters of our simulations. This approach is unique in the sense that previous studies into two-dimensional Rayleigh-Bénard convection have viewed the problem from only one such angle—the current focus being to derive scaling laws (see King *et al.* (2013)). Furthermore, that we have studied the behaviour for two different Prandtl numbers is also somewhat novel: in high Rayleigh number studies (see DeLuca *et al.* (1990) and Vincent & Yuen (1999)) Pr is typically fixed and only unsteady behaviour is found. In being limited to a lower range of Rayleigh numbers, we were able to distinguish between behaviour at different Prandtl numbers, and attempt to explain this behaviour.

For the non-rotating system, at $Pr = 1$, we found only steady solutions for the range of Rayleigh numbers considered. This is consistent with the findings of DeLuca *et al.* (1990) and Vincent & Yuen (1999). For $Pr = 10$, we found time-dependent solutions and described the possible routes to chaos of the system, noting similarities with the findings of Curry (1978). Furthermore, we outlined a physical explanation for the instability that led to this behaviour. In the non-rotating system, independent of the solution—be it steady, periodic or chaotic—there was a general preference for convection to develop on a large length scale as the Rayleigh number was increased.

We found the following scaling laws for the Nusselt and Reynolds numbers

$$Nu \sim Ra^{\frac{1}{3}}, \tag{5.76}$$

$$Re \sim Ra_f^{\frac{1}{2}} Pr^{-1}, \tag{5.77}$$

in accordance with the studies of Moore & Weiss (1973) and DeLuca *et al.* (1990).

In the rotating system we noticed that providing the buoyancy driving was stronger than the rotational driving, as measured by the convective Rossby number, Ro_*, then a large length scale was preferred, as in the non-rotating system. In both regimes we found heavily time-dependent behaviour, with flows varying greatly based on whether they were buoyancy or rotation-dominated. We found the following scaling laws for the Nusselt and Reynolds numbers

$$Nu \sim Ra^{\frac{1}{3}} \quad \text{for buoyancy-dominated flows,} \tag{5.78}$$

$$Nu \sim Ra^{\frac{2}{7}} \quad \text{for rotation-dominated flows,} \tag{5.79}$$

$$Re \sim Ra_f^{\frac{1}{2}} Ta^{-\frac{1}{6}} Pr^{-1}. \tag{5.80}$$

The latter two are consistent with the findings of Schmitz & Tilgner (2009) and King *et al.* (2009), in their three-dimensional studies. That the Rayleigh number exponent is larger in the buoyancy-dominated regime is due to the fact that these solutions were, on the whole, steady. As the Rayleigh number is increased further we would expect these solutions to become time-dependent, and the exponent to resemble that of the rotation-dominated regime.

Chapter 6

Asymptotic theory

Guided by the numerical simulations in Chapter 5, we present an asymptotic theory in order to describe the large Rayleigh number, steady state solutions, observed for $Pr = 1$, in the non-rotating system. We treat separately the different dynamically important regions of the convection cell. With only two term asymptotic expansions in the bottom boundary layer and rising plume we are able to replicate many of the quantitative features of steady state cellular convection. Furthermore these expansions are matched at the corner region. This analysis furnishes us with an asymptotic relation of both the core vorticity value and the Nusselt number, in terms of the Rayleigh number. For large Rayleigh number, we noted that the preference of the system was to develop on a long horizontal length scale. Here the horizontal wave length is the only input parameter needed, for a given Rayleigh number.

6.1 Introduction

6.1.1 Motivation

We wish to derive analytical, mathematical expressions for the steady state solutions that we observed in the large Rayleigh number numerical simulations carried out in Chapter 5, for $Pr = 1$. The solution for the vorticity and temperature was characterised by extremely narrow boundary layer regions around the core of the convection cell, inside which both the vorticity and temperature were approximately constant. Such a solution can be viewed in Figure 6.1, where we have plotted the vorticity, streamfunction and temperature from one of our high Rayleigh number numerical simulations. Note that the numerical simulation was performed in a box of length 2π, yet here we have just shown one of the convection cells. Due to the symmetry of the system in a steady state, it is sufficient to analyse a single convection cell only. Along with this we have plotted the vertical profiles of these three governing variables at a given horizontal location. This makes apparent our statement that the vorticity and temperature were constant in the core of the convection cell. It can be seen that the streamfunction is smooth everywhere, and that in the core of the convection cell the flow is laminar. Furthermore, this has the implication that both the vorticity and the temperature are constant along the core streamlines. Despite this, these laminar solutions are in fact strongly nonlinear, differing greatly from any asymptotic solution coming from weakly nonlinear theory (see Veronis (1966)).

As the Rayleigh number was increased we showed that the thickness of the boundary layer regions decreased, meaning the area we have described as the core of the convection cell increased—a key property that our asymptotic solutions must replicate. Further to arriving at an analytical expression valid in the limit of large Rayleigh number, we would like to use our results in order to derive an asymptotic relation for the Nusselt scaling that we discussed in Chapter 5. For the steady state

simulations at $Pr = 1$ we observed an exponent of $\frac{1}{3}$, in line with the 'classical' prediction. This is a further feature that we would like our asymptotic solutions to impart. As well as the core, we can subdivide the convection cell into different dynamically important regions. We make a distinction between the upper and lower boundary layers and the rising and sinking plumes. These boundary layers and plumes meet at corner regions—areas that will require subtle treatment in order to ensure continuity as we pass from one region to another. We expect there to be different dominant balances within the governing equations in each of these distinct areas, owing to the inherent short length scales, and hence large gradients, involved.

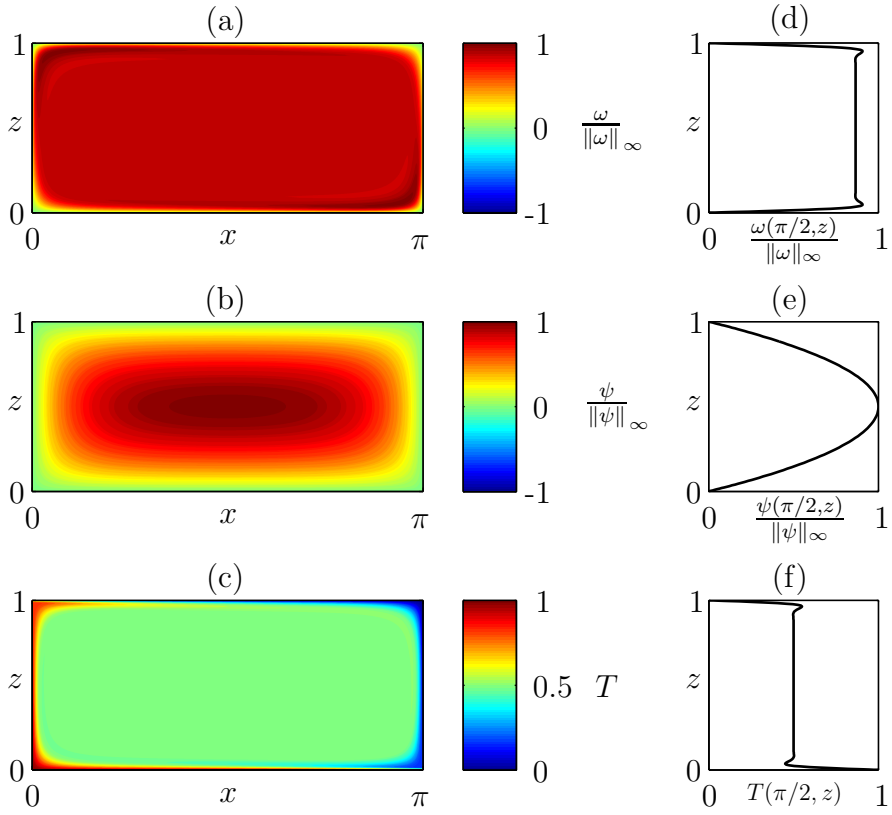

Figure 6.1: Contour plots/vertical profiles at $x = \pi/2$ of (a)/(d) the normalised vorticity ($\|\omega\|_\infty = 18253$), (b)/(e) the normalised streamfunction ($\|\psi\|_\infty = 1944$) and (c)/(f) the total temperature, for $Ta = 0$, $Pr = 1$, $R = 10000$: solutions that were computed numerically in Chapter 5.

One of the first attempts to describe the steady state convection cells that we have witnessed was performed by Robinson (1967). Whilst the treatment of the convection cell core is handled in an identical manner to how we present here, the boundary layer analysis differs somewhat in the approximations made. The treatment of the corner region, and the overall procedure, however, is similar.

A seminal development in the study of strongly nonlinear Rayleigh-Bénard convection was undertaken by Roberts (1979) in the limit of infinite Prandtl number. This followed from his treatment of convection from a heated strip (see Roberts (1977)). In the infinite Prandtl number limit the advective terms in the momentum equation are considered negligible. Asymptotic expressions for the velocity and temperature are derived in the boundary layers and plumes, with the core motion being determined from the streamfunction, as the solution of a biharmonic equation. In the boundary layers and plumes the temperature is the solution of a one-dimensional, parabolic heat diffusion-type equation, when transformed using Von Mises—streamfunction—coordinates. Here the streamfunction is used as the coordinate normal to the boundary and is supplemented by a transverse coordinate that is proportional to the boundary velocity. This heat equation is solved with the periodicity requirement that motion be repeated after one cycle of the convection cell. This solution also provides an asymptotic relation for the Nusselt number dependence on the Rayleigh number and the cell width. Furthermore, an accurate treatment of the corner region is also presented.

Following on from Roberts (1979), Jimenez & Zufiria (1987) perform a semi-analytical treatment of the problem for infinite Prandtl number but with constant heat flux, rather than constant temperature, boundary conditions. Their equations are initially scaled with the Raleigh number, assuming an *a priori* Nusselt number exponent of $\frac{1}{3}$ in the Rayleigh number scaling. They formulate an integral equation for the cell-edge temperature distribution and address the corner region in some detail. Using this they are able to determine, asymptotically, the Nusselt number proportionality constant in the Rayleigh number scaling. Succeeding this Chini

(2008) performed a very similar analysis in the framework of both Langmuir circulation and Rayleigh-Bénard convection but for finite Prandtl number. The methodology is extremely similar to Jimenez & Zufiria (1987) in that an integral equation for the cell-edge temperature distribution is required to be solved. Finally, this work is extended by Chini & Cox (2009) in the framework of constant temperature boundary conditions, in a very similar manner. This work is heavily numerical and does not address the corner region in significant detail. Nonetheless, the solutions determined replicate their own numerical simulations of the nonlinear equations accurately. We wish to follow on from Chini & Cox (2009) but address the problem in a more analytical way, obviating the need for complex numerical procedures.

6.1.2 Mathematical formulation

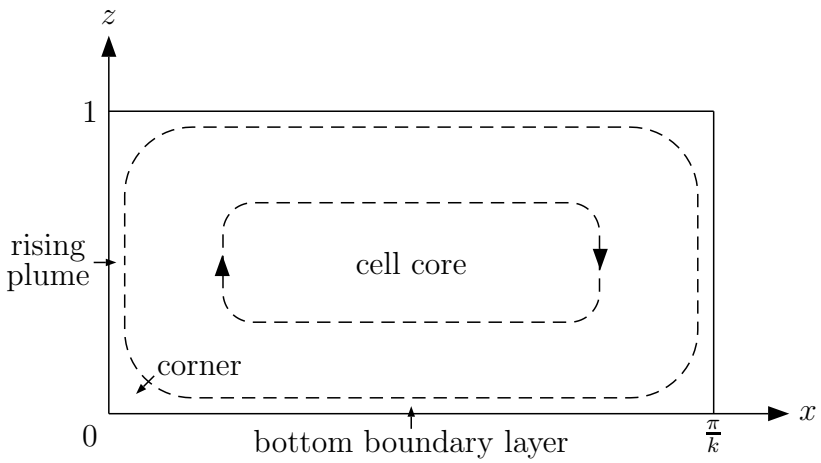

Figure 6.2: Physical setup of the problem: schematic of a convective cell, displaying the convection cell core, bottom boundary layer, rising plume and adjoining corner region.

We wish to describe, mathematically, the type of steady state solutions as seen in Figure 6.1. The required dimensionless equations governing the dynamics of the

system are given by

$$u\frac{\partial \omega}{\partial x} + w\frac{\partial \omega}{\partial z} = -RaPr\frac{\partial T}{\partial x} + Pr\nabla^2\omega, \tag{6.1}$$

$$u\frac{\partial T}{\partial x} + w\frac{\partial T}{\partial z} = \nabla^2 T, \tag{6.2}$$

$$\nabla^2\psi = -\omega, \tag{6.3}$$

where $u = -\frac{\partial \psi}{\partial z}$ and $w = \frac{\partial \psi}{\partial x}$ are the x and z components of the velocity respectively.

It is useful to rescale these equations, to furnish us with a parameter upon which we can base our asymptotic theory. Our numerical simulations of non-rotating convection in Chapter 5 exhibited the following scaling law

$$Re \sim Ra^{\frac{2}{3}}Pr^{-1} \quad \text{providing} \quad Nu \sim Ra^{\frac{1}{3}} \quad \text{as} \quad Ra \to \infty. \tag{6.4}$$

This is equivalent to the dimensionless velocity scaling with $Ra^{\frac{2}{3}}$. Applying this scaling within equations (6.1), (6.2) and (6.3) gives

$$u\frac{\partial \omega}{\partial x} + w\frac{\partial \omega}{\partial z} = -\epsilon Pr\frac{\partial T}{\partial x} + \epsilon^2 Pr\nabla^2\omega, \tag{6.5}$$

$$u\frac{\partial T}{\partial x} + w\frac{\partial T}{\partial z} = \epsilon^2\nabla^2 T, \tag{6.6}$$

$$\nabla^2\psi = -\omega. \tag{6.7}$$

This equation set is valid in the limit as $Ra \to \infty$, or equivalently, $\epsilon \to 0$, where

$$\epsilon \equiv Ra^{-\frac{1}{3}}. \tag{6.8}$$

In Figure 6.1 there is a rising plume located at $x = 0$. This means that the velocity is such that u is negative in the bottom boundary layer and w is positive in the rising plume. The corresponding boundary conditions for equations (6.5), (6.6) and (6.7) are given by

$$\psi = 0, \;\; \omega = 0, \;\; T = 1 \;\; \text{at} \;\; z = 0, \tag{6.9}$$

$$\psi = 0, \;\; \omega = 0, \;\; T = 0 \;\; \text{at} \;\; z = 1. \tag{6.10}$$

The solutions shown in Figure 6.1 possess the following rotational symmetry

$$\omega(x,z,t) = \omega\left(\frac{\pi}{k} - x, 1 - z, t\right), \tag{6.11}$$

$$\psi(x,z,t) = \psi\left(\frac{\pi}{k} - x, 1 - z, t\right), \tag{6.12}$$

$$T(x,z,t) = 1 - T\left(\frac{\pi}{k} - x, 1 - z, t\right), \tag{6.13}$$

where k is a wavenumber defining the aspect ratio of the cell, with $k = 1$ in Figure 6.1. Due to this symmetry, the top and bottom boundary layers are mathematically equivalent, as are the rising and sinking plumes. Hence we only need to address the dynamics in—arbitrarily—the bottom boundary layer and rising plume, as well as the adjoining corner region. The geometry of the problem is described in Figure 6.2, where we have labelled the dynamically important regions that we shall study. Furthermore, this symmetry gives us the following conditions on the lateral boundaries

$$\psi = 0, \;\; \omega = 0, \;\; \frac{\partial T}{\partial x} = 0 \;\; \text{at} \;\; x = 0, \tag{6.14}$$

$$\psi = 0, \;\; \omega = 0, \;\; \frac{\partial T}{\partial x} = 0 \;\; \text{at} \;\; x = \frac{\pi}{k}. \tag{6.15}$$

6.2 Convection cell core

Following the work of Chini & Cox (2009), first we address the behaviour within the core of the convection cell.

6.2.1 Temperature

Written in terms of the streamfunction, the temperature equation (cf. equation (6.6) is given by

$$\frac{\partial \psi}{\partial x}\frac{\partial T}{\partial z} - \frac{\partial \psi}{\partial z}\frac{\partial T}{\partial x} = \epsilon^2 \nabla^2 T. \tag{6.16}$$

We begin by integrating this equation over the area enclosed by a core streamline

$$\int_{A_\psi} \left(\frac{\partial \psi}{\partial x}\frac{\partial T}{\partial z} - \frac{\partial \psi}{\partial z}\frac{\partial T}{\partial x}\right) \mathrm{d}A_\psi = \epsilon^2 \int_{A_\psi} \nabla^2 T \, \mathrm{d}A_\psi. \tag{6.17}$$

In the core of the convection cell, away from the boundary layers and plumes, we assume that the temperature depends smoothly upon the streamfunction, i.e. $T \equiv T(\psi)$. With this in mind we have

$$\frac{\partial\psi}{\partial x}\frac{\partial T}{\partial z} - \frac{\partial\psi}{\partial z}\frac{\partial T}{\partial x} = \frac{\partial\psi}{\partial x}\frac{\partial T}{\partial\psi}\frac{\partial\psi}{\partial z} - \frac{\partial\psi}{\partial z}\frac{\partial T}{\partial\psi}\frac{\partial\psi}{\partial x} = 0, \tag{6.18}$$

hence we have

$$\epsilon^2 \int_{A_\psi} \nabla^2 T \mathrm{d}A_\psi = 0. \tag{6.19}$$

Using the fact that $\nabla^2 T = \nabla \cdot (\nabla T)$ and applying the divergence theorem to transform this equation gives

$$\epsilon^2 \oint_{C_\psi} \nabla T \cdot \hat{\mathbf{n}} \mathrm{d}l = 0, \tag{6.20}$$

where $\hat{\mathbf{n}}$ is a outward-pointing unit normal vector to the closed streamline C_ψ and $\mathrm{d}l$ is an infinitesimal line element. Using the fact that $T \equiv T(\psi)$ this means

$$\epsilon^2 \oint_{C_\psi} \frac{\partial T}{\partial\psi}\frac{\partial\psi}{\partial n}\mathrm{d}l = 0, \tag{6.21}$$

which can be written as

$$\epsilon^2 T'(\psi)\Gamma_{C_\psi} = 0, \tag{6.22}$$

where Γ_{C_ψ} is the non-zero circulation around the closed streamline C_ψ. This last equation tells us that the temperature is constant everywhere in the core of the convection cell. Due to the boundary conditions on the temperature, by symmetry, we must have $T \sim T_c = \frac{1}{2}$ in the core of the convection cell.

6.2.2 Vorticity

Written in terms of the streamfunction, the vorticity equation (cf. equation (6.5)) is given by

$$\frac{\partial\psi}{\partial x}\frac{\partial\omega}{\partial z} - \frac{\partial\psi}{\partial z}\frac{\partial\omega}{\partial x} = -\epsilon Pr\frac{\partial T}{\partial x} + \epsilon^2 Pr\nabla^2\omega. \tag{6.23}$$

Once again we integrate this over the area enclosed by a core streamline

$$\int_{A_\psi}\left(\frac{\partial\psi}{\partial x}\frac{\partial\omega}{\partial z} - \frac{\partial\psi}{\partial z}\frac{\partial\omega}{\partial x}\right)\mathrm{d}A_\psi = \epsilon Pr\int_{A_\psi}\left(-\frac{\partial T}{\partial x} + \epsilon\nabla^2\omega\right)\mathrm{d}A_\psi. \tag{6.24}$$

In the core of the convection cell, away from the boundary layers and plumes, we know that the temperature is given by $T \sim T_c$ and hence the first term on the right-hand side vanishes. Furthermore, we assume that the vorticity depends smoothly upon the streamfunction, i.e. $\omega \equiv \omega(\psi)$. With this in mind we have

$$\frac{\partial \psi}{\partial x}\frac{\partial \omega}{\partial z} - \frac{\partial \psi}{\partial z}\frac{\partial \omega}{\partial x} = \frac{\partial \psi}{\partial x}\frac{\partial \omega}{\partial \psi}\frac{\partial \psi}{\partial z} - \frac{\partial \psi}{\partial z}\frac{\partial \omega}{\partial \psi}\frac{\partial \psi}{\partial x} = 0, \tag{6.25}$$

hence we have

$$\epsilon \int_{A_\psi} \nabla^2 \omega \mathrm{d}A_\psi = o(\epsilon^m), \tag{6.26}$$

for any positive integer m. In an identical matter to how we proceeded for the core temperature, we derive the following equation

$$\epsilon \omega'(\psi) \Gamma_{C_\psi} = o(\epsilon^m). \tag{6.27}$$

This last equation tells us that, to within exponentially small corrections in ϵ, the vorticity is constant everywhere in the core of the convection cell, given by $\omega \sim \omega_c$. Unlike for the temperature, there is no *a priori* method for ascertaining the value ω_c, it must be determined as part of the —asymptotic—solution to the problem.

6.2.3 Streamfunction

Since the vorticity is approximately constant in the core of the convection cell, taking the value ω_c, the streamfunction in the core of the convection cell satisfies the following

$$\nabla^2 \psi_c = -\omega_c. \tag{6.28}$$

We are able to solve this Poisson equation analytically for the core streamfunction ψ_c subject to the boundary conditions $\psi_c(0, x) = \psi_c\left(\frac{\pi}{k}, z\right) = \psi_c(x, 0) = \psi_c(x, 1) = 0$. Due to the boundary conditions at $x = 0$ and $x = \frac{\pi}{k}$ it is clear that a Fourier-Sine series in x is necessary, hence we postulate that the solution be of the form

$$\psi_c(x, z) = \sum_{n=1}^{\infty} \psi_n(z) \sin nkx. \tag{6.29}$$

Inserting this into equation (6.28) gives

$$\sum_{n=1}^{\infty} \left(\psi_n'' - n^2k^2\psi_n\right) \sin nkx = -\omega_c. \tag{6.30}$$

In order to calculate the coefficients ψ_n we multiply this equation by $\sin mkx$ and integrate from $x = 0$ to $x = \frac{\pi}{k}$, hence we have

$$\int_0^{\frac{\pi}{k}} \sum_{n=1}^{\infty} \left(\psi_n'' - n^2k^2\psi_n\right) \sin mkx \sin nkx \mathrm{d}x = -\int_0^{\frac{\pi}{k}} \omega_c \sin mkx \mathrm{d}x. \tag{6.31}$$

For non-trivial solutions we require that $n = m$ and furthermore that m be odd. In this case we have

$$\psi_m'' - m^2k^2\psi_m = -\frac{4\omega_c}{\pi m}. \tag{6.32}$$

The solution to this equation is given by

$$\psi_m = A_m \cosh mkz + B_m \sinh mkz + \frac{4\omega_c}{\pi m^3 k^2}. \tag{6.33}$$

Applying the boundary conditions $\psi_m(x, 0) = \psi_m(x, 1) = 0$ gives

$$\begin{aligned} \psi_m &= \frac{4\omega_c}{\pi m^3 k^2} \left(1 - \cosh mkz + \frac{(\cosh mk - 1)\sinh mkz}{\sinh mk}\right), \\ &= \frac{4\omega_c}{\pi m^3 k^2} \left(1 - \frac{\cosh mk\left(z - \frac{1}{2}\right)}{\cosh \frac{mk}{2}}\right), \end{aligned} \tag{6.34}$$

where in order to derive the final equation we have made use of the identity $\tanh \frac{mk}{2} = \frac{\cosh mk - 1}{\sinh mk}$. Hence the solution for the interior streamfunction is given by

$$\psi_c = \sum_{n=1}^{\infty} \frac{4\omega_c}{\pi n^3 k^2} \sin nkx \left(1 - \frac{\cosh nk\left(z - \frac{1}{2}\right)}{\cosh \frac{nk}{2}}\right), \tag{6.35}$$

for n odd. Following Chini & Cox (2009), to allow us to match the core streamfunction onto its counterpart within the bottom boundary layer and rising plume, we perform Taylor expansions of the core streamfunction at the perimeter of the cell core. Hence, to match with the streamfunction in the bottom boundary layer we have

$$\psi_c(x, z) \sim z \sum_{n=1}^{\infty} \frac{4\omega_c}{\pi n^2 k} \tanh \frac{nk}{2} \sin nkx \tag{6.36}$$

as $z \to 0^+$ and to match with the streamfunction in the rising plume we have

$$\psi_c(x,z) \sim x \sum_{n=1}^{\infty} \frac{4\omega_c}{\pi n^2 k} \left(1 - \frac{\cosh nk\left(z - \frac{1}{2}\right)}{\cosh \frac{nk}{2}}\right), \tag{6.37}$$

as $x \to 0^+$.

6.3 Bottom boundary layer

In the bottom boundary layer, since there is a sharp transition in the temperature, as we go from the boundary into the core of the convection cell, gradients in the vertical direction are much larger than in the horizontal direction. With this, we rescale the vertical coordinate in terms of the small parameter ϵ, giving

$$z_{bl} = \frac{z}{\epsilon}. \tag{6.38}$$

The asymptotic expansion of the governing hydrodynamical variables, that is valid within the bottom boundary layer, and matches with the core values, is then given by

$$T(x,z) \sim T_c + T_{bl}(x, z_{bl}) + O(\epsilon), \tag{6.39}$$

$$\omega(x,z) \sim \omega_c + \omega_{bl}(x, z_{bl}) + O(\epsilon), \tag{6.40}$$

$$\psi(x,z) \sim \epsilon\psi_{bl}(x, z_{bl}) + O(\epsilon^2). \tag{6.41}$$

In the bottom boundary layer, by definition of the streamfunction, we have that the horizontal velocity must satisfy $u = -\frac{\partial \psi_{bl}}{\partial z_{bl}}$. In order to match with the core streamfunction expression given by equation (6.36), we have

$$\psi_{bl}(x, z_{bl}) = z_{bl} u(x), \tag{6.42}$$

where, by comparison with equation (6.36), we have

$$u(x) = -\sum_{n=1}^{\infty} \frac{4\omega_c}{\pi n^2 k} \tanh \frac{nk}{2} \sin nkx. \tag{6.43}$$

This expression is dominated by the $n = 1$ mode, and it is instructive to take only this component, although in principle we could proceed with any number of modes. Hence the tangential velocity in the bottom boundary layer is given by

$$U(x) = -\lambda \sin kx, \tag{6.44}$$

with

$$\lambda = \frac{4\omega_c}{\pi k} \tanh \frac{k}{2}. \tag{6.45}$$

The continuity equation then tells us that in the boundary layer

$$\frac{\partial U}{\partial x} + \frac{\partial w}{\partial z_{bl}} = 0 \Rightarrow w = -z_{bl}\frac{\partial U}{\partial x} = \lambda k z_{bl} \cos kx. \tag{6.46}$$

Hence in the bottom boundary layer, using asymptotic expansions (6.39), (6.40) and (6.41) within the rescaled temperature equation (cf. equation (6.6)), gives, to leading order

$$U\frac{\partial T_{bl}}{\partial x} - z_{bl}\frac{\partial U}{\partial x}\frac{\partial T_{bl}}{\partial z_{bl}} = \frac{\partial^2 T_{bl}}{\partial z_{bl}^2}. \tag{6.47}$$

This must be solved for T_{bl} subject to the following boundary and infinity conditions

$$T_{bl} = \frac{1}{2} \quad \text{at} \quad z_{bl} = 0, \tag{6.48}$$

$$T_{bl} \to 0 \quad \text{as} \quad z_{bl} \to \infty. \tag{6.49}$$

Note that any expression for T_{bl} must be an odd function, since we require it to be symmetric with respect to rotations of π. A solution possessing these properties is

$$T_{bl} = \frac{1}{2}\text{erfc}(s) + \sum_{n=1}^{\infty} \alpha_n(x) s^n e^{-s^2}, \tag{6.50}$$

$$\equiv \frac{1}{\pi^{\frac{1}{2}}} \int_s^{\infty} e^{-\hat{s}^2} \mathrm{d}\hat{s} + \sum_{n=1}^{\infty} \alpha_n(x) s^n e^{-s^2}, \tag{6.51}$$

for n odd, where s is given by

$$s = z_{bl} g_{bl}^{-\frac{1}{2}}(x). \tag{6.52}$$

The function g_{bl} modulates the thickness of the bottom boundary layer and must be determined as part of the solution to the problem, along with the functions $\alpha_n(x)$. In principle we will truncate the above expansion after a finite number of

terms. Indeed, with just two terms it will be shown that the resulting solution is remarkably accurate. For such an expansion we have

$$\frac{\partial s}{\partial x} = -\frac{1}{2} z_{bl} g_{bl}^{-\frac{3}{2}} \frac{\mathrm{d}g_{bl}}{\mathrm{d}x} = -\frac{1}{2} s g_{bl}^{-1} \frac{\mathrm{d}g_{bl}}{\mathrm{d}x}, \tag{6.53}$$

$$\frac{\partial s}{\partial z_{bl}} = g_{bl}^{-\frac{1}{2}}. \tag{6.54}$$

Hence the required partial derivatives are given by

$$\frac{\partial T_{bl}}{\partial x} = \frac{1}{2\pi^{\frac{1}{2}}} s g_{bl}^{-1} \frac{\mathrm{d}g_{bl}}{\mathrm{d}x} e^{-s^2} + \sum_{n=1}^{\infty} \left\{ \frac{\mathrm{d}\alpha_n}{\mathrm{d}x} s^n + \frac{1}{2} \left(2s^{n+2} - n s^n \right) \alpha_n g_{bl}^{-1} \frac{\mathrm{d}g_{bl}}{\mathrm{d}x} \right\} e^{-s^2}, \tag{6.55}$$

$$\frac{\partial T_{bl}}{\partial z_{bl}} = -\frac{g_{bl}^{-\frac{1}{2}}}{\pi^{\frac{1}{2}}} e^{-s^2} + \sum_{n=1}^{\infty} \left(n s^{n-1} - 2s^{n+1} \right) \alpha_n g_{bl}^{-\frac{1}{2}} e^{-s^2}, \tag{6.56}$$

$$\frac{\partial^2 T_{bl}}{\partial z_{bl}^2} = \frac{2 g_{bl}^{-1}}{\pi^{\frac{1}{2}}} s e^{-s^2} + \sum_{n=1}^{\infty} \left(4s^{n+2} - (4n+2) s^n + n(n-1) s^{n-2} \right) \alpha_n g_{bl}^{-1} e^{-s^2} \quad . \tag{6.57}$$

Using the fact that $z_{bl} = s g_{bl}^{\frac{1}{2}}$, we use these expressions within the following equation

$$U \frac{\partial T_{bl}}{\partial x} - s g_{bl}^{\frac{1}{2}} \frac{\partial U}{\partial x} \frac{\partial T_{bl}}{\partial z_{bl}} = \frac{\partial^2 T_{bl}}{\partial z_{bl}^2}. \tag{6.58}$$

Truncating our series expansion at $n = M$ allows us to equate coefficients at different orders of $s^n e^{-s^2}$. Equating terms proportional to $s^{M+2} e^{-s^2}$ gives

$$\frac{\mathrm{d}g_{bl}}{\mathrm{d}x} + \frac{2}{U} \frac{\partial U}{\partial x} g_{bl} = \frac{4}{U}. \tag{6.59}$$

An integrating factor for this equation is given by U^2, hence we have

$$\frac{\mathrm{d}}{\mathrm{d}x} \left[U^2 g_{bl} \right] = 4U. \tag{6.60}$$

Using the approximation $U = -\lambda \sin kx$, we gain the following expression for g_{bl}

$$g_{bl} = \frac{4}{k\lambda} \left(\frac{A_1 + \cos kx}{\sin^2 kx} \right), \tag{6.61}$$

where A_1 is a constant of integration to be determined. Looking at the terms arising from expressions (6.55), (6.56) and (6.57) when inserted into equation (6.58) that

are proportional to se^{-s^2} but independent of n, we see that they too satisfy equation (6.59) and hence may be cancelled. It is key that they do in fact satisfy this equation, or we would have a contradictory expression for the function g_{bl}. Finally, equating terms that are proportional to $s^n e^{-s^2}$ gives

$$U\frac{\mathrm{d}\alpha_n}{\mathrm{d}x} + \left(\alpha_{n-2} - \frac{n}{2}\alpha_n\right) g_{bl}^{-1} U \frac{\mathrm{d}g_{bl}}{\mathrm{d}x} + (2\alpha_{n-2} - n\alpha_n)\frac{\partial U}{\partial x} = (4\alpha_{n-2} - (4n+2)\alpha_n + (n+2)(n+1)\alpha_{n+2})\, g_{bl}^{-1}. \tag{6.62}$$

We may once again use equation (6.59) to cancel various terms, leaving us with

$$\frac{\mathrm{d}\alpha_n}{\mathrm{d}x} + \frac{2(n+1)}{U g_{bl}}\alpha_n = \frac{(n+2)(n+1)}{U g_{bl}}\alpha_{n+2}. \tag{6.63}$$

For $U = -\lambda \sin kx$ and g_{bl} given by equation (6.61), an integrating factor for this equation is given by $(A_1 + \cos kx)^{\frac{n+1}{2}}$, hence we have

$$\frac{\mathrm{d}}{\mathrm{d}x}\left[(A_1 + \cos kx)^{\frac{n+1}{2}}\,\alpha_n\right] = -\frac{k(n+2)(n+1)}{4}(A_1 + \cos kx)^{\frac{n-1}{2}} \sin kx \alpha_{n+2}. \tag{6.64}$$

This differential equation for α_n cannot be solved unless we first know α_{n+2}. For $n = M$, $\alpha_n = 0$ for $n > M$, hence we have

$$\frac{\mathrm{d}}{\mathrm{d}x}\left[(A_1 + \cos kx)^{\frac{M+1}{2}}\,\alpha_M\right] = 0. \tag{6.65}$$

Thus we may solve this equation, arriving at the following solution for α_M

$$\alpha_M = \frac{k_M}{(A_1 + \cos kx)^{\frac{M+1}{2}}}, \tag{6.66}$$

where k_M is a constant of integration to be determined. Now, letting $n = M - 2$ in equation (6.64) gives

$$\frac{\mathrm{d}}{\mathrm{d}x}\left[(A_1 + \cos kx)^{\frac{M-1}{2}}\,\alpha_{M-2}\right] = -\frac{kM(M-1)}{4}(A_1 + \cos kx)^{\frac{M-3}{2}} \sin kx\, \alpha_M, \tag{6.67}$$

but we have an expression for α_M, hence

$$\frac{\mathrm{d}}{\mathrm{d}x}\left[(A_1 + \cos kx)^{\frac{M-1}{2}}\,\alpha_{M-2}\right] = -\frac{kM(M-1)k_M \sin kx}{4\,(A_1 + \cos kx)^2}. \tag{6.68}$$

We are able to solve this equation, giving the following expression for α_{M-2}

$$\alpha_{M-2} = -\frac{M(M-1)k_M}{4\,(A_1 + \cos kx)^{\frac{M+1}{2}}} + \frac{k_{M-2}}{(A_1 + \cos kx)^{\frac{M-1}{2}}}, \tag{6.69}$$

where k_{M-2} is a constant of integration to be determined. Thus in knowing the expression for α_M, we are able to find the solutions to equation (6.64) recursively. The $M-n$'th term is given by

$$\alpha_{M-n} = \sum_{m=0}^{n} \frac{(-4)^{\frac{m-n}{2}}(M-m)!\,k_{M-m}}{\left(\frac{n-m}{2}\right)!(M-n)!\,(A_1+\cos kx)^{\frac{M+1-m}{2}}}, \tag{6.70}$$

where m and n are even and N is odd. Hence the solution in the bottom boundary layer is given by

$$T_{bl} = \frac{1}{2}\left(1+\mathrm{erfc}(s)\right) + \sum_{n=0}^{N-1}\sum_{m=0}^{n} \frac{(-4)^{\frac{m-n}{2}}(N-1-m)!\,k_{N-1-m}s^{N-1-n}e^{-s^2}}{\left(\frac{n-m}{2}\right)!(N-1-n)!\,(A_1+\cos kx)^{\frac{N-m}{2}}}, \tag{6.71}$$

where m and n are even and we have redefined $M \equiv N-1$ so that N is even, and s is given by

$$s = z_{bl}g_{bl}^{-\frac{1}{2}}(x) \equiv \frac{k^{\frac{1}{2}}\lambda^{\frac{1}{2}}z_{bl}\sin kx}{2\,(A_1+\cos kx)^{\frac{1}{2}}}. \tag{6.72}$$

With $N=2$ the solution is given by

$$T_{bl} = \frac{1}{\pi^{\frac{1}{2}}}\int_s^\infty e^{-\hat{s}^2}\mathrm{d}\hat{s} + \frac{k_1 s e^{-s^2}}{(A_1+\cos kx)}. \tag{6.73}$$

6.4 Rising plume

In the rising plume, since there is a sharp transition in the temperature, as we go from the plume into the core of the convection cell, gradients in the horizontal direction are much larger than in the vertical direction. With this, we rescale the horizontal coordinate in terms of the small parameter ϵ, giving

$$x_{pl} = \frac{x}{\epsilon}. \tag{6.74}$$

The asymptotic expansion of the governing hydrodynamical variables, that is valid within the rising plume, and matches with the core values, is then given by

$$T(x,z) \sim T_c + T_{pl}(x_{pl},z) + O(\epsilon), \tag{6.75}$$

$$\omega(x,z) \sim \omega_c + \omega_{pl}(x_{pl},z) + O(\epsilon), \tag{6.76}$$

$$\psi(x,z) \sim \epsilon\psi_{pl}(x_{pl},z) + O(\epsilon^2). \tag{6.77}$$

In the rising plume, by definition of the streamfunction, we have that the vertical velocity must satisfy $w = \frac{\partial \psi_{pl}}{\partial x_{bl}}$. In order to match with the core streamfunction expression given by equation (6.37), we have

$$\psi_{pl}(x_{pl}, z) = x_{pl} w(z), \tag{6.78}$$

where, by comparison with equation (6.37), we have

$$w(z) = \sum_{n=1}^{\infty} \frac{4\omega_c}{\pi n^2 k} \left(1 - \frac{\cosh nk \left(z - \frac{1}{2} \right)}{\cosh \frac{nk}{2}} \right). \tag{6.79}$$

This expression is dominated by the $n = 1$ mode, and it is instructive to take only this component, although in principle we could proceed with any number of modes. Furthermore, we choose to express the velocity in a simpler trigonometric form, to simplify the forthcoming analysis. Hence the tangential velocity in the bottom boundary layer is given by

$$W(z) = \lambda \sin \pi z, \tag{6.80}$$

with λ given by equation (6.45). The continuity equation then tells us that in the rising plume

$$\frac{\partial u}{\partial x_{pl}} + \frac{\partial W}{\partial z} = 0 \Rightarrow u = -x_{pl} \frac{\partial W}{\partial z} = -\lambda \pi x_{pl} \cos \pi z. \tag{6.81}$$

Hence in the rising plume, using asymptotic expansions (6.75), (6.76) and (6.77) within the rescaled temperature equation (cf. equation (6.6)), gives, to leading order

$$-x_{pl} \frac{\partial W}{\partial z} \frac{\partial T_{pl}}{\partial x_{pl}} + W \frac{\partial T_{pl}}{\partial z} = \frac{\partial^2 T_{pl}}{\partial x_{pl}^2}. \tag{6.82}$$

This must be solved for T_{pl} subject to the following boundary and infinity conditions

$$\frac{\partial T_{pl}}{\partial x_{pl}} = 0 \quad \text{at} \quad x_{pl} = 0, \tag{6.83}$$

$$T_{pl} \to 0 \quad \text{as} \quad x_{pl} \to \infty, \tag{6.84}$$

Note that any expression for T_{pl} must be an even function, since we require it to be symmetric about the plume centreline at $x_{pl} = 0$. A solution possessing these properties is

$$T_{pl} = \sum_{n=0}^{\infty} \beta_n(z) s^n e^{-s^2}, \tag{6.85}$$

for n even, where s is given by

$$s = x_{pl} g_{pl}^{-\frac{1}{2}}(z). \tag{6.86}$$

The function g_{pl} modulates the thickness of the rising plume and must be determined as part of the solution to the problem, along with the functions $\beta_n(z)$. In principle we will once again truncate the above expansion at a finite value $n = N$, say. With just $N = 2$ it will be shown that the resulting solution is remarkably accurate. For such an expansion we have

$$\frac{\partial s}{\partial x_{pl}} = g_{pl}^{-\frac{1}{2}}. \tag{6.87}$$

$$\frac{\partial s}{\partial z} = -\frac{1}{2} z g_{pl}^{-\frac{3}{2}} \frac{\mathrm{d}g_{pl}}{\mathrm{d}z} = -\frac{1}{2} s g_{pl}^{-1} \frac{\mathrm{d}g_{pl}}{\mathrm{d}z}, \tag{6.88}$$

Hence the required partial derivatives are given by

$$\frac{\partial T_{pl}}{\partial x_{pl}} = \sum_{n=0}^{\infty} \left(n s^{n-1} - 2 s^{n+1} \right) \beta_n g_{pl}^{-\frac{1}{2}} e^{-s^2}, \tag{6.89}$$

$$\frac{\partial^2 T_{pl}}{\partial x_{pl}^2} = \sum_{n=0}^{\infty} \left(4 s^{n+2} - (4n+2) s^n + n(n-1) s^{n-2} \right) \beta_n g_{pl}^{-1} e^{-s^2}, \tag{6.90}$$

$$\frac{\partial T_{pl}}{\partial z} = \sum_{n=0}^{\infty} \left\{ \frac{\mathrm{d}\beta_n}{\mathrm{d}z} s^n + \frac{1}{2} \left(2 s^{n+2} - n s^n \right) \beta_n g_{pl}^{-1} \frac{\mathrm{d}g_{pl}}{\mathrm{d}z} \right\} e^{-s^2}, \tag{6.91}$$

Using the fact that $x_{pl} = s g_{pl}^{\frac{1}{2}}$, we use these expressions within the following equation

$$-s g_{pl}^{\frac{1}{2}} \frac{\partial W}{\partial z} \frac{\partial T_{pl}}{\partial x_{pl}} + W \frac{\partial T_{pl}}{\partial z} = \frac{\partial^2 T_{pl}}{\partial x_{pl}^2}. \tag{6.92}$$

Truncating our series expansion at $n = N$ allows us to equate coefficients at different orders of $s^n e^{-s^2}$. Equating terms proportional to $s^{N+2} e^{-s^2}$ gives

$$\frac{\mathrm{d}g_{pl}}{\mathrm{d}z} + \frac{2}{W} \frac{\partial W}{\partial z} g_{pl} = \frac{4}{W}. \tag{6.93}$$

An integrating factor for this equation is given by W^2, hence we have

$$\frac{\mathrm{d}}{\mathrm{d}z} \left[W^2 g_{pl} \right] = 4W. \tag{6.94}$$

Using the fact that $W = \lambda \sin \pi z$, we gain the following expression for g_{pl}

$$g_{pl} = \frac{4}{\pi \lambda} \left(\frac{A_2 - \cos \pi z}{\sin^2 \pi z} \right), \tag{6.95}$$

where A_2 is a constant of integration to be determined. Equating terms that are proportional to $s^n e^{-s^2}$ gives

$$\begin{aligned}(2\beta_{n-2} - n\beta_n)\frac{\partial W}{\partial z} + W\frac{\mathrm{d}\beta_n}{\mathrm{d}z} + \left(\beta_{n-2} + \frac{n}{2}\beta_n\right) g_{pl}^{-1} W \frac{\mathrm{d}g_{pl}}{\mathrm{d}z} \\ = \left(4\beta_{n-2} - (4n+2)\beta_n + (n+2)(n+1)\beta_{n+2}\right) g_{pl}^{-1}\end{aligned} \tag{6.96}$$

We may use equation (6.93) to cancel various terms, leaving us with

$$\frac{\mathrm{d}\beta_n}{\mathrm{d}z} + \frac{2(n+1)}{W g_{pl}}\beta_n = \frac{(n+2)(n+1)}{W g_{pl}}\beta_{n+2}. \tag{6.97}$$

For $W = \lambda \sin \pi z$ and g_{pl} given by equation (6.95), an integrating factor for this equation is given by $(A_2 - \cos \pi z)^{\frac{n+1}{2}}$, hence we have

$$\frac{\mathrm{d}}{\mathrm{d}z}\left[(A_2 - \cos \pi z)^{\frac{n+1}{2}} \beta_n\right] = \frac{\pi(n+2)(n+1)}{4} (A_2 - \cos \pi z)^{\frac{n-1}{2}} \sin \pi z \beta_{n+2}. \tag{6.98}$$

This differential equation for β_n cannot be solved unless we first know β_{n+2}. For $n = N$, $\beta_n = 0$ for $n > N$, hence we have

$$\frac{\mathrm{d}}{\mathrm{d}z}\left[(A_2 - \cos \pi z)^{\frac{n+1}{2}} \beta_n\right] = 0. \tag{6.99}$$

Thus we may solve this equation, arriving at the following solution for β_N

$$\beta_N = \frac{l_N}{(A_2 - \cos \pi z)^{\frac{N+1}{2}}}, \tag{6.100}$$

where l_N is a constant of integration to be determined. Now, letting $n = N - 2$ in equation (6.98)

$$\frac{\mathrm{d}}{\mathrm{d}z}\left[(A_2 - \cos \pi z)^{\frac{N-1}{2}} \beta_{N-2}\right] = \frac{\pi N(N-1)}{4} (A_2 - \cos \pi z)^{\frac{N-3}{2}} \sin \pi z \, \beta_N, \tag{6.101}$$

but we have an expression for β_N, hence

$$\frac{\mathrm{d}}{\mathrm{d}z}\left[(A_2 - \cos \pi z)^{\frac{N-1}{2}} \beta_{N-2}\right] = -\frac{\pi N(N-1) l_N \sin \pi z}{4 (A_2 - \cos \pi z)^2}. \tag{6.102}$$

We are able to solve this equation, giving the following expression for β_{N-2}

$$\beta_{N-2} = -\frac{N(N-1) l_N}{4 (A_2 - \cos \pi z)^{\frac{N+1}{2}}} + \frac{l_{N-2}}{(A_2 - \cos \pi z)^{\frac{N-1}{2}}}, \tag{6.103}$$

where l_{N-2} is a constant of integration to be determined. Thus in knowing the expression for β_N, we are able to find the solutions to equation (6.98) recursively. Hence the $N-n$'th term is given by

$$\beta_{N-n} = \sum_{m=0}^{n} \frac{(-4)^{\frac{m-n}{2}}(N-m)!\, l_{N-m}}{\left(\frac{n-m}{2}\right)!(N-n)!\,(A_2-\cos\pi z)^{\frac{N+1-m}{2}}}, \tag{6.104}$$

where m, n are N are all even. Hence the solution in the bottom boundary layer is given by

$$T_{pl} = \sum_{n=0}^{N}\sum_{m=0}^{n} \frac{(-4)^{\frac{m-n}{2}}(N-m)!\, l_{N-m} s^{N-n} e^{-s^2}}{\left(\frac{n-m}{2}\right)!(N-n)!\,(A_2-\cos\pi z)^{\frac{N+1-m}{2}}}, \tag{6.105}$$

where m, n are N are all even, and s is given by

$$s = x_{pl} g_{pl}^{-\frac{1}{2}}(z) \equiv \frac{\pi^{\frac{1}{2}}\lambda^{\frac{1}{2}} x_{pl}\sin\pi z}{2\,(A_2-\cos\pi z)^{\frac{1}{2}}}. \tag{6.106}$$

With $N=2$ the solution is given by

$$T_{pl} = \left(\frac{l_0}{(A_2-\cos\pi z)^{\frac{1}{2}}} - \frac{l_2}{2\,(A_2-\cos\pi z)^{\frac{3}{2}}}\right) e^{-s^2} + \frac{l_2 s^2 e^{-s^2}}{(A_2-\cos\pi z)^{\frac{3}{2}}}. \tag{6.107}$$

6.5 Corner region

Close to the corner at $(0,0)$, the boundary layer and plume thicknesses are $O(\epsilon^{\frac{1}{2}})$, and we may write the streamfunction as

$$\psi \sim \epsilon x z, \tag{6.108}$$

in accordance with Jimenez & Zufiria (1987). This means that the velocity components close to the corner are given by

$$u = -\epsilon x, \quad w = \epsilon z. \tag{6.109}$$

The temperature equation therefore reads

$$-\epsilon x \frac{\partial T}{\partial x} + \epsilon z \frac{\partial T}{\partial z} = \epsilon^2 \nabla^2 T. \tag{6.110}$$

We shall introduce a new streamline coordinate system (ψ, ζ) with

$$\psi = \epsilon x z, \quad \zeta = \frac{\epsilon}{2}\left(z^2 - x^2\right). \tag{6.111}$$

In this coordinate system ψ picks out a particular streamline and ζ gives the corresponding location along that streamline. Hence given this coordinate transformation we have

$$\frac{\partial}{\partial x} = \epsilon z \frac{\partial}{\partial \psi} - \epsilon x \frac{\partial}{\partial \zeta} \tag{6.112}$$

$$\frac{\partial}{\partial z} = \epsilon x \frac{\partial}{\partial \psi} + \epsilon z \frac{\partial}{\partial \zeta}. \tag{6.113}$$

Using this within equation (6.110) gives

$$\frac{\partial T}{\partial \zeta} = \epsilon \left(\frac{\partial^2 T}{\partial \zeta^2} + \frac{\partial^2 T}{\partial \psi^2} \right). \tag{6.114}$$

Hence, to leading order we have

$$\frac{\partial T}{\partial \zeta} = 0. \tag{6.115}$$

This means that within the corner region diffusion is negligible, implying that the temperature is constant on the streamlines of the flow as we go round the corner. This has important consequences for the matching that we shall perform in the following section in order to determine the—currently unknown—constants of integration.

6.6 Matching conditions

6.6.1 The general case

In general we are furnished with $N + 3$ constants of integration that we are to determine. For any value of N, we always have A_1 and A_2 that are located in the expressions for g_{bl} and g_{pl} given by equations (6.61) and (6.95) respectively. Furthermore there are $\frac{N}{2}$ values of k_n arising in equation (6.71) and $\frac{N}{2} + 1$ values of

l_n arising in equation (6.105) that are unknown. Hence we require $N+3$ equations relating these constants in order to determine them. The first equation is obtained by specifying $T_{pl} = \frac{1}{2}$ at $z = 0$. Looking at equation (6.105) it is clear that the only non-zero contribution occurs when $n = N$, hence we require

$$\beta_0(0) = \frac{1}{2}. \tag{6.116}$$

Using the expression for β_0 given by equation (6.104) with $n = N$, this amounts to satisfying

$$\sum_{m=0}^{N} \frac{(-4)^{\frac{m-N}{2}}(N-m)!\, l_{N-m}}{\left(\frac{N-m}{2}\right)!\,(A_2-1)^{\frac{N+1-m}{2}}} = \frac{1}{2}. \tag{6.117}$$

Equation (6.115) told us that to leading order, within the corner region, diffusion was negligible. This means that the solution in the boundary layer matches onto the solution in the plume as we pass through the corner region. Furthermore, this has the implication that each moment of the temperature can be matched as we go from the bottom boundary layer to the plume. Since we are able to write the velocity in terms of a streamfunction: $u = -\frac{\partial \psi}{\partial z}$ or $w = \frac{\partial \psi}{\partial x}$, in either the bottom boundary layer or the rising plume, we define the p-th moment of temperature as

$$M^{(p)} = \int_0^\infty \psi^p \,(T - T_c)\,\mathrm{d}\psi, \tag{6.118}$$

for $p = 0, 1, \ldots, \frac{N}{2}$. The remaining $N+2$ conditions are obtained by specifying that the first $\frac{N}{2}+1$ moments match as we go from the bottom boundary layer into the rising plume, and from the rising plume into the top boundary layer. All the required integrals are able to be computed analytically.

In the bottom boundary layer we have

$$M_{bl}^{(p)} = \int_0^\infty \psi_{bl}^p T_{bl} \mathrm{d}\psi_{bl}, \tag{6.119}$$

for $p = 0, 1, \ldots, \frac{N}{2}$. Using $U = -\frac{\partial \psi_{bl}}{\partial z_{bl}}$ and $z_{bl} = s g_{bl}^{\frac{1}{2}}$ we are able to rewrite this as

$$M_{bl}^{(p)}(x) = \int_0^\infty \left(-U g_{bl}^{\frac{1}{2}}\right)^{p+1} T_{bl} s^p \mathrm{d}s, \tag{6.120}$$

for $p = 0, 1, \ldots, \frac{N}{2}$. Noting that U and g_{bl} are functions of x only, and using the expression for T_{bl} from equation (6.71) we have

$$M_{bl}^{(p)}(x) = \left(-U g_{bl}^{\frac{1}{2}}\right)^{p+1} \int_0^\infty \left(\frac{1}{2}\mathrm{erfc}(s) + \sum_{n=0}^{N-1} \alpha_{N-1-n}(x) s^{N-1-n} e^{-s^2}\right) s^p \mathrm{d}s, \quad (6.121)$$

for $p = 0, 1, \ldots, \frac{N}{2}$, and N and n both even. This can be written

$$M_{bl}^{(p)}(x) = \left(\frac{4\lambda\left(A_1 + \cos kx\right)}{k}\right)^{\frac{p+1}{2}} \left(\frac{J_p}{\pi^{\frac{1}{2}}} + \sum_{n=0}^{N-1} \alpha_{N-1-n}(x) I_{N-1-n+p}\right), \quad (6.122)$$

for $p = 0, 1, \ldots, \frac{N}{2}$, and N and n both even, where the values of the integrals I_n and J_n are given by equations (B.10) and (B.15) respectively, in Appendix B. Due to the symmetry of the system, the p-th moment in the top boundary layer is given by

$$M_{tbl}^{(p)}(x) = -M_{bl}^{(p)}\left(\frac{\pi}{k} - x\right). \quad (6.123)$$

In a similar manner we are able to derive an expression for the p-th moment in the rising plume. This is given by

$$M_{pl}^{(p)}(z) = \left(\frac{4\lambda\left(A_2 - \cos \pi z\right)}{\pi}\right)^{\frac{p+1}{2}} \sum_{n=0}^{N} \beta_{N-n}(z) I_{N-n+p}, \quad (6.124)$$

for $p = 0, 1, \ldots, \frac{N}{2}$. Hence the remaining $N + 2$ matching conditions come from satisfying

$$M_{bl}^{(p)}(0) = M_{pl}^{(p)}(0), \quad (6.125)$$

$$-M_{bl}^{(p)}\left(\frac{\pi}{k}\right) = M_{pl}^{(p)}(1), \quad (6.126)$$

for $p = 0, 1, \ldots, \frac{N}{2}$, and N and n both even. Using equations (6.122) and (6.124), along with the expressions for α_n and β_n from equations (6.70) and (6.104)

respectively, these conditions are given by

$$\frac{J_p}{\pi^{\frac{1}{2}}k^{\frac{p+1}{2}}}(A_1+1)^{\frac{p+1}{2}}+\frac{1}{k^{\frac{p+1}{2}}}\sum_{n=0}^{N-1}\sum_{m=0}^{n}\frac{(-4)^{\frac{m-n}{2}}(N-1-m)!\,I_{N-1-n+p}\,k_{N-1-m}}{\left(\frac{n-m}{2}\right)!(N-1-n)!\,(A_1+1)^{\frac{N-1-m-p}{2}}}$$
$$=\frac{1}{\pi^{\frac{p+1}{2}}}\sum_{n=0}^{N}\sum_{m=0}^{n}\frac{(-4)^{\frac{m-n}{2}}(N-m)!\,I_{N-n+p}\,l_{N-m}}{\left(\frac{n-m}{2}\right)!(N-n)!\,(A_2-1)^{\frac{N-m-p}{2}}}, \tag{6.127}$$

$$-\frac{J_p}{\pi^{\frac{1}{2}}k^{\frac{p+1}{2}}}(A_1-1)^{\frac{p+1}{2}}-\frac{1}{k^{\frac{p+1}{2}}}\sum_{n=0}^{N-1}\sum_{m=0}^{n}\frac{(-4)^{\frac{m-n}{2}}(N-1-m)!\,I_{N-1-n+p}\,k_{N-1-m}}{\left(\frac{n-m}{2}\right)!(N-1-n)!\,(A_1-1)^{\frac{N-1-m-p}{2}}}$$
$$=\frac{1}{\pi^{\frac{p+1}{2}}}\sum_{n=0}^{N}\sum_{m=0}^{n}\frac{(-4)^{\frac{m-n}{2}}(N-m)!\,I_{N-n+p}\,l_{N-m}}{\left(\frac{n-m}{2}\right)!(N-n)!\,(A_2+1)^{\frac{N-m-p}{2}}} \tag{6.128}$$

for $p=0,1,\ldots,\frac{N}{2}$, and N, n and m all even.

6.6.2 The case $N=2$

With $N=2$ we have five constants of integration that we are to determine: A_1, A_2, k_1, l_0 and l_2. To do this we must obtain five equations governing these coefficients. The first equation is obtained by specifying $T_{pl}=\frac{1}{2}$ at $z=0$, hence by equation (6.116) we have

$$\frac{l_0}{(A_2-1)^{\frac{1}{2}}}-\frac{l_2}{2\,(A_2-1)^{\frac{3}{2}}}=\frac{1}{2}. \tag{6.129}$$

Using equations (6.127) and (6.128) we are able to derive expressions for the zero-th order and first order moments in the bottom boundary layer and the rising plume. Matching these moments gives the following set of equations

$$(A_1+1)^{\frac{1}{2}}+\frac{\pi^{\frac{1}{2}}k_1}{(A_1+1)^{\frac{1}{2}}}=\pi^{\frac{1}{2}}k^{\frac{1}{2}}l_0, \tag{6.130}$$

$$-(A_1-1)^{\frac{1}{2}}-\frac{\pi^{\frac{1}{2}}k_1}{(A_1-1)^{\frac{1}{2}}}=\pi^{\frac{1}{2}}k^{\frac{1}{2}}l_0, \tag{6.131}$$

$$\frac{(A_1+1)}{2}+\pi^{\frac{1}{2}}k_1=\frac{2l_0k}{\pi}(A_2-1)^{\frac{1}{2}}+\frac{l_2k}{\pi(A_2-1)^{\frac{1}{2}}}, \tag{6.132}$$

$$-\frac{(A_1-1)}{2}-\pi^{\frac{1}{2}}k_1=\frac{2l_0k}{\pi}(A_2+1)^{\frac{1}{2}}+\frac{l_2k}{\pi(A_2+1)^{\frac{1}{2}}}. \tag{6.133}$$

Once we have determined these five constants, we will possess two-term asymptotic series for the temperature in the bottom boundary layer and rising plume. It is possible to combine these equations, eliminating three of the variables, leaving two equations for—arbitrarily—A_1 and A_2. These are given by

$$\frac{(A_1+1)}{2} - \left(A_1^2-1\right)^{\frac{1}{2}} + \frac{k}{\pi}(A_2-1) = \frac{4k^{\frac{1}{2}}}{\pi^{\frac{3}{2}}}(A_2-1)^{\frac{1}{2}}\left((A_1+1)^{\frac{1}{2}} - (A_1-1)^{\frac{1}{2}}\right), \tag{6.134}$$

$$-\frac{(A_1-1)}{2} + \left(A_1^2-1\right)^{\frac{1}{2}} + \frac{k}{\pi}\frac{(A_2-1)^{\frac{3}{2}}}{(A_2+1)^{\frac{1}{2}}} = \frac{4k^{\frac{1}{2}}}{\pi^{\frac{3}{2}}}\frac{A_2}{(A_2+1)^{\frac{1}{2}}}\left((A_1+1)^{\frac{1}{2}} - (A_1-1)^{\frac{1}{2}}\right). \tag{6.135}$$

It is possible to combine these final two equations, giving an expression for—arbitrarily—A_1 in terms of A_2

$$A_1 = \left(\frac{32\left(A_2 + (A_2^2-1)^{\frac{1}{2}}\right) - k\pi(A_2-1)^2}{16\left(A_2 + (A_2^2-1)^{\frac{1}{2}}\right)}\right)^{\frac{1}{2}}, \tag{6.136}$$

however we have been unsuccessful in using this to yield a usable equation to determine A_2; we must solve the system numerically. For the solution shown in Figure 6.1 the wavenumber is given by $k = 1$. Solving the system in this case gives the following values of the coefficients

$$\left\{A_1 = 1.4133,\ A_2 = 1.1546,\ k_1 = -0.56342,\ l_0 = 0.51376,\ l_2 = 0.098059\right\}. \tag{6.137}$$

The computed solution with these coefficient values can be seen in Figure **??**.

6.7 Energy balances

6.7.1 Determining ω_c asymptotically

In the asymptotic expansions for the temperature in the bottom boundary layer and the rising plume, occurring within the scaled boundary layer coordinate, s, is the

parameter ω_c: the core value of the vorticity. In order to specify the temperature solution fully, we must determine its value.

The momentum equation, written in terms of the vorticity and streamfunction is given by

$$\frac{\partial \psi}{\partial x}\frac{\partial \omega}{\partial z} - \frac{\partial \psi}{\partial z}\frac{\partial \omega}{\partial x} = -\epsilon Pr\frac{\partial T}{\partial x} + \epsilon^2 Pr\nabla^2\omega. \tag{6.138}$$

It is possible to estimate the core vorticity asymptotically by considering the global energy balance. We multiply the above equation by ψ and integrate over the whole domain

$$\int_0^1\int_0^{\frac{\pi}{k}}\left(\frac{\partial \psi}{\partial x}\frac{\partial \omega}{\partial z} - \frac{\partial \psi}{\partial z}\frac{\partial \omega}{\partial x}\right)\psi \mathrm{d}x\mathrm{d}z = \int_0^1\int_0^{\frac{\pi}{k}}\left(-\epsilon Pr\frac{\partial T}{\partial x} + \epsilon^2 Pr\nabla^2\omega\right)\psi \mathrm{d}x\mathrm{d}z. \tag{6.139}$$

Considering the left hand side of the above equation, we integrate the terms by parts, the first with respect to z and the second with respect to x, giving

$$\begin{aligned}\int_0^1\int_0^{\frac{\pi}{k}}\frac{\partial \psi}{\partial x}\frac{\partial \omega}{\partial z}\psi \mathrm{d}x\mathrm{d}z &= \int_0^{\frac{\pi}{k}}\left\{\left[\frac{\partial \psi}{\partial x}\psi\omega\right]_0^1 - \int_0^1\left(\frac{\partial \psi}{\partial x}\frac{\partial \psi}{\partial z} + \frac{\partial^2\psi}{\partial x\partial z}\psi\right)\omega \mathrm{d}z\right\}\mathrm{d}x\\ \int_0^1\int_0^{\frac{\pi}{k}}\frac{\partial \psi}{\partial z}\frac{\partial \omega}{\partial x}\psi \mathrm{d}x\mathrm{d}z &= \int_0^1\left\{\left[\frac{\partial \psi}{\partial z}\psi\omega\right]_0^{\frac{\pi}{k}} - \int_0^{\frac{\pi}{k}}\left(\frac{\partial \psi}{\partial x}\frac{\partial \psi}{\partial z} + \frac{\partial^2\psi}{\partial x\partial z}\psi\right)\omega \mathrm{d}x\right\}\mathrm{d}z.\end{aligned} \tag{6.140}$$

The boundary terms vanish due to the boundary conditions at the cell edge and the remaining terms cancel if we rearrange the order of integration in one of the terms, hence, after rearranging, we have

$$\int_0^1\int_0^{\frac{\pi}{k}}\frac{\partial T}{\partial x}\psi \mathrm{d}x\mathrm{d}z = \epsilon\int_0^1\int_0^{\frac{\pi}{k}}\psi\nabla^2\omega \mathrm{d}x\mathrm{d}z. \tag{6.141}$$

On the right hand side we integrate the terms by parts; the x derivative with respect to x and the z derivative with respect to z, giving

$$\int_0^1\int_0^{\frac{\pi}{k}}\psi\nabla^2\omega \mathrm{d}x\mathrm{d}z = \int_0^1\left\{\left[\psi\frac{\partial \omega}{\partial x}\right]_0^{\frac{\pi}{k}} - \int_0^{\frac{\pi}{k}}\frac{\partial \psi}{\partial x}\frac{\partial \omega}{\partial x}\mathrm{d}x\right\}\mathrm{d}z \tag{6.142}$$

$$+\int_0^{\frac{\pi}{k}}\left\{\left[\psi\frac{\partial \omega}{\partial z}\right]_0^1 - \int_0^1\frac{\partial \psi}{\partial z}\frac{\partial \omega}{\partial z}\mathrm{d}z\right\}\mathrm{d}x. \tag{6.143}$$

Once again the boundary terms vanish due to the boundary conditions and we are left with

$$\int_0^1 \int_0^{\frac{\pi}{k}} \psi \nabla^2 \omega \mathrm{d}x\mathrm{d}z = -\int_0^1 \int_0^{\frac{\pi}{k}} \frac{\partial \psi}{\partial x}\frac{\partial \omega}{\partial x}\mathrm{d}x\mathrm{d}z - \int_0^{\frac{\pi}{k}} \int_0^1 \frac{\partial \psi}{\partial z}\frac{\partial \omega}{\partial z}\mathrm{d}z\mathrm{d}x. \tag{6.144}$$

Integrating by parts again, the first term with respect to x and the second term with respect to z yields

$$\int_0^1 \int_0^{\frac{\pi}{k}} \psi \nabla^2 \omega \mathrm{d}x\mathrm{d}z = -\int_0^1 \left\{ \left[\frac{\partial \psi}{\partial x}\omega\right]_0^{\frac{\pi}{k}} - \int_0^{\frac{\pi}{k}} \frac{\partial^2 \psi}{\partial x^2}\omega \mathrm{d}x \right\} \mathrm{d}z \tag{6.145}$$

$$-\int_0^{\frac{\pi}{k}} \left\{ \left[\frac{\partial \psi}{\partial z}\omega\right]_0^1 - \int_0^1 \frac{\partial^2 \psi}{\partial z^2}\omega \mathrm{d}z \right\} \mathrm{d}x. \tag{6.146}$$

Once again the boundary terms vanish due to the boundary conditions. Reversing the order of integration in one term and combining the integrals gives

$$\int_0^1 \int_0^{\frac{\pi}{k}} \psi \nabla^2 \omega \mathrm{d}x\mathrm{d}z = -\int_0^1 \int_0^{\frac{\pi}{k}} - \left\{ \frac{\partial^2 \psi}{\partial x^2} + \frac{\partial^2 \psi}{\partial z^2} \right\} \omega \mathrm{d}x\mathrm{d}z \tag{6.147}$$

$$= -\int_0^1 \int_0^{\frac{\pi}{k}} \omega^2 \mathrm{d}x\mathrm{d}z. \tag{6.148}$$

Hence we have

$$-\int_0^1 \int_0^{\frac{\pi}{k}} \frac{\partial T}{\partial x}\psi \mathrm{d}x\mathrm{d}z = \epsilon \int_0^1 \int_0^{\frac{\pi}{k}} \omega^2 \mathrm{d}x\mathrm{d}z. \tag{6.149}$$

The left hand side expresses the rate at which buoyancy torque does work on the cellular flow in a steady state and it is balanced, on the right hand side, by the rate at which kinetic energy is dissipated by viscous forces, that is, the enstrophy. The leading order contribution to the enstrophy comes from the vortex core, where we have $\omega \sim \omega_c$. The leading order contribution to the energy production on the left hand side occurs within the vertical plume. This is because gradients in x are largest within this region. Hence we have

$$-2\epsilon \int_0^1 \int_0^{\infty} \frac{\partial T_{pl}}{\partial x_{pl}} \psi_{pl} \, \mathrm{d}x_{pl}\mathrm{d}z \sim \frac{\pi \epsilon}{k}\omega_c^2. \tag{6.150}$$

We shall re-write this equation in terms of the plume coordinate $s = x_{pl} g_{pl}^{-\frac{1}{2}}$. In the rising plume we have $\psi = \lambda s g_{pl}^{\frac{1}{2}} \sin \pi z$ and T_{pl} is given by equation (6.107), hence

we have

$$-2\epsilon\int_0^1\int_0^\infty \frac{\partial T_{pl}}{\partial x_{pl}}\psi_{pl}\mathrm{d}x_{pl}\mathrm{d}z = -2\epsilon\int_0^1\int_0^\infty \lambda s g_{pl}^{\frac{1}{2}}\sin\pi z\left(\frac{-2l_0 s}{(A_2-\cos\pi z)^{\frac{1}{2}}} + \frac{3l_2 s}{(A_2-\cos\pi z)^{\frac{3}{2}}} - \frac{2l_2 s^3}{(A_2-\cos\pi z)^{\frac{3}{2}}}\right)e^{-s^2}\mathrm{d}s\mathrm{d}z. \tag{6.151}$$

The first and second terms are proportional to I_2 and the third term is proportional to I_4. The values of I_2 and I_4 are given by equation (B.11) in Appendix B, as $\frac{\pi^{\frac{1}{2}}}{4}$ and $\frac{3\pi^{\frac{1}{2}}}{8}$ respectively, hence the second and third terms cancel, leaving

$$-2\epsilon\int_0^1\int_0^\infty \frac{\partial T_{pl}}{\partial x_{pl}}\psi_{pl}\mathrm{d}x_{pl}\mathrm{d}z = 2\epsilon\int_0^1 \lambda g_{pl}^{\frac{1}{2}}\sin\pi z\left(\frac{\pi^{\frac{1}{2}}l_0}{2\left(A_2-\cos\pi z\right)^{\frac{1}{2}}}\right)\mathrm{d}z. \tag{6.152}$$

With g_{pl} given by equation (6.95) this gives

$$-2\epsilon\int_0^1\int_0^\infty \frac{\partial T_{pl}}{\partial x_{pl}}\psi_{pl}\mathrm{d}x_{pl}\mathrm{d}z = 2\epsilon\lambda^{\frac{1}{2}}l_0. \tag{6.153}$$

Recall that λ was a coefficient that we put in our definition of the tangential velocity components and the corresponding streamfunction. Using the expression for λ given by equation (6.45), equations (6.150) and (6.153) give

$$\omega_c \sim \left(\frac{16l_0^2 k}{\pi^3}\tanh\frac{k}{2}\right)^{\frac{1}{3}}. \tag{6.154}$$

Note that this relation is independent of ϵ—as it should be—since we have been working with a rescaled set of equations. With the Rayleigh number specified, the only free parameter we have is the wavenumber k, hence it is natural that ω_c in equation (6.154) is a function of k. For direct comparison with our numerical results in Chapter 5, we must multiply equation (6.154) by a factor of ϵ^{-2}, or, $Ra^{\frac{2}{3}}$. In Figure 6.3 we have plotted the asymptotically computed values of ω_c versus the corresponding values from our steady state, nonlinear numerical simulations at $Pr = 1$, for all the Rayleigh numbers we studied. As can be seen, the agreement is excellent.

With ω_c now given by equation (6.154), we are able to work out a precise expression

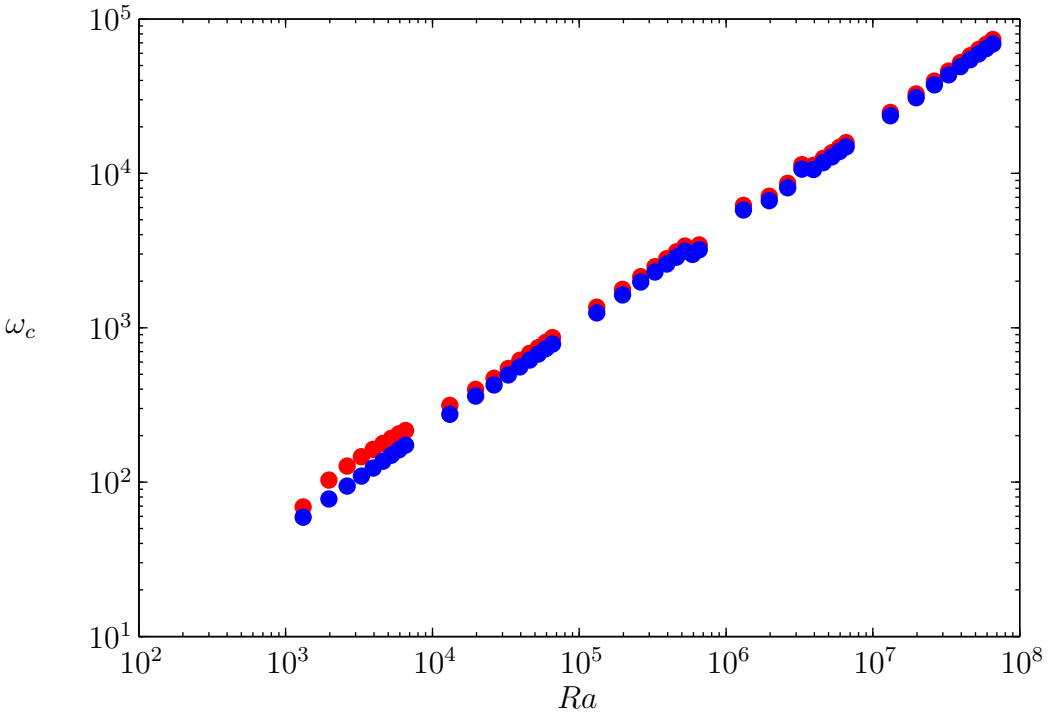

Figure 6.3: Core vorticity versus Rayleigh number comparison. The red circles are taken from steady state numerical simulations at $Pr = 1$ and the blue circles are taken from the asymptotic theory.

for λ, originally given by equation (6.45), as

$$\lambda = \frac{4\omega_c}{\pi k}\tanh\frac{k}{2} \sim \left(\frac{1024 l_0^2}{\pi^6 k^2}\tanh^4\frac{k}{2}\right)^{\frac{1}{3}}. \tag{6.155}$$

It is this expression that we use in the solutions for T_{bl} and T_{pl} given by equations (6.73) and (6.107) respectively.

6.7.2 Nusselt number

The expression for the Nusselt number that we derived in Chapter 5 is given by equation (5.11)

$$Nu = \frac{k}{\pi}\int_0^{\frac{\pi}{k}} -\left.\frac{\partial T}{\partial z}\right|_{z=0} \mathrm{d}x. \tag{6.156}$$

Since the above expression evaluates the temperature derivative on the bottom boundary, we use our expression for the temperature in the bottom boundary layer,

given by equation (6.73). Hence we have

$$Nu = -\frac{k}{\pi}\int_0^{\frac{\pi}{k}} \left(\frac{1}{\pi^{\frac{1}{2}}} + \frac{k_1}{(A_1+\cos kx)^{\frac{1}{2}}} \right) g_{bl}^{-\frac{1}{2}} \mathrm{d}x. \tag{6.157}$$

Using the expression for g_{bl} from equation (6.61) we have

$$Nu = \frac{k^{\frac{3}{2}}\lambda^{\frac{1}{2}}}{2\pi}\int_0^{\frac{\pi}{k}} \left(\frac{\sin kx}{\pi^{\frac{1}{2}}\,(A_1+\cos kx)^{\frac{1}{2}}} - \frac{k_1 \sin kx}{(A_1+\cos kx)^{\frac{3}{2}}} \right) \mathrm{d}x. \tag{6.158}$$

Finally, evaluating this integral gives

$$Nu = -\frac{k^{\frac{1}{2}}\lambda^{\frac{1}{2}}}{\pi}\left[\frac{(A_1+\cos kx)^{\frac{1}{2}}}{\pi^{\frac{1}{2}}} + \frac{k_1}{(A_1+\cos kx)^{\frac{1}{2}}} \right]_0^{\frac{\pi}{k}}, \tag{6.159}$$

$$= \frac{k^{\frac{1}{2}}\lambda^{\frac{1}{2}}}{\pi}\left(\frac{(A_1+1)^{\frac{1}{2}} - (A_1-1)^{\frac{1}{2}}}{\pi^{\frac{1}{2}}} + k_1 \frac{(A_1-1)^{\frac{1}{2}} - (A_1+1)^{\frac{1}{2}}}{(A_1-1)^{\frac{1}{2}}(A_1+1)^{\frac{1}{2}}} \right). \tag{6.160}$$

Using the expression for λ given by equation (6.155) we have

$$Nu \sim \left(\frac{1024 l_0^2 k}{\pi^{12}} \tanh^4 \frac{k}{2} \right)^{\frac{1}{6}} \left(\frac{(A_1+1)^{\frac{1}{2}} - (A_1-1)^{\frac{1}{2}}}{\pi^{\frac{1}{2}}} + k_1 \frac{(A_1-1)^{\frac{1}{2}} - (A_1+1)^{\frac{1}{2}}}{(A_1-1)^{\frac{1}{2}}(A_1+1)^{\frac{1}{2}}} \right). \tag{6.161}$$

Note that like ω_c, this relation is also independent of ϵ, since we rescaled the original equations. We stated that the asymptotic theory was valid providing $Nu \sim Ra^{\frac{1}{3}}$, in accordance with the 'classical' scaling law that we presented in Chapter 5. For direct comparison with our numerical results in Chapter 5, we must multiply equation (6.161) by a factor of ϵ^{-1}, or, $Ra^{\frac{1}{3}}$. In Figure 6.4 we have plotted the asymptotically computed values of Nu versus the corresponding values from our steady state, nonlinear numerical simulations at $Pr = 1$, for all the Rayleigh numbers we studied. As can be seen, the agreement is excellent, with the asymptotic prediction capturing the different scaling branches corresponding to different wavenumber patterns.

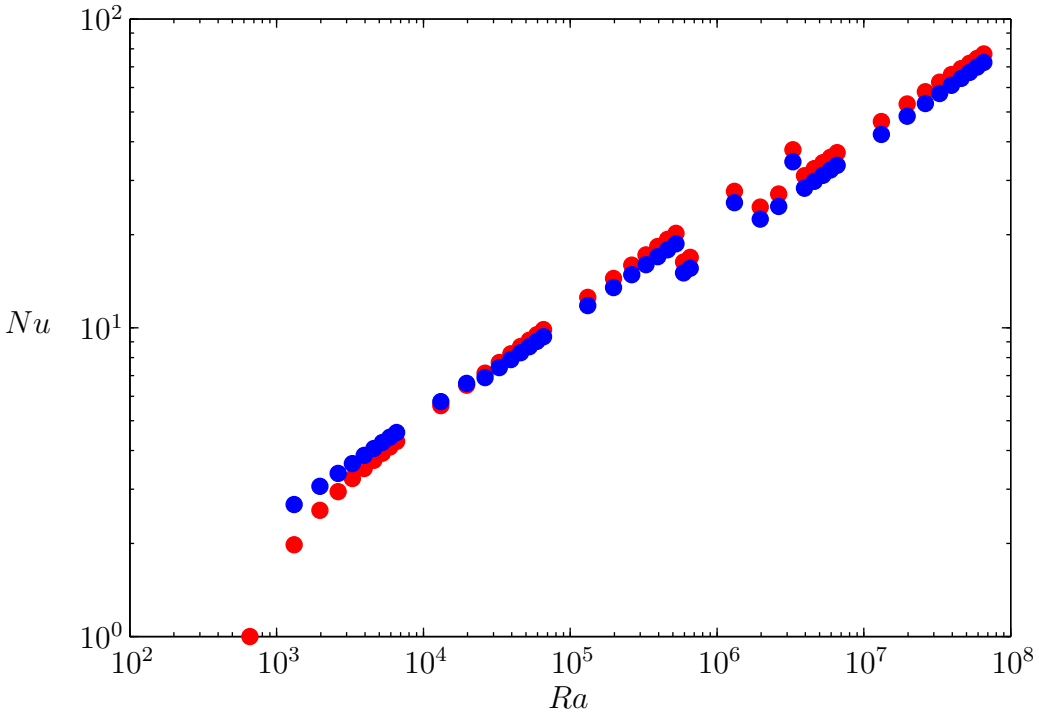

Figure 6.4: Nusselt number versus Rayleigh number comparison. The red circles are taken from steady state numerical simulations at $Pr = 1$ and the blue circles are taken from the asymptotic theory.

6.8 Solutions

It remains to plot the solutions for the temperature in the bottom boundary layer and the rising plume, as given by equations (6.73) and (6.107) respectively. This is done in Figure 6.5 and should be compared with the corresponding plots in Figure 6.1. It can be seen that both the asymptotic bottom boundary layer and rising plume temperature solutions agree qualitatively with the numerically computed temperature in both of those regions. Further to this, in Figure 6.6, we have plotted the vertical profile of the temperature, from both the numerical simulations and the asymptotic theory. The asymptotic expansion adequately captures the overshoot as we transition from the bottom boundary layer into the core of the convection cell. It is to be noted that these solutions took a matter of seconds to compute, whereas solving the fully nonlinear equations took several hours.

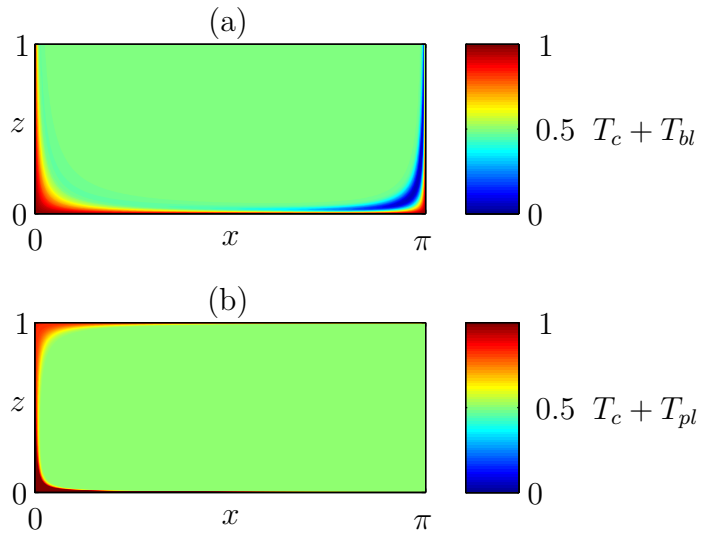

Figure 6.5: Contour plots of (a) the total boundary layer temperature and (b) the total plume temperature, computed using the asymptotic theory, for $Ta = 0$, $Pr = 1$, $R = 10000$.

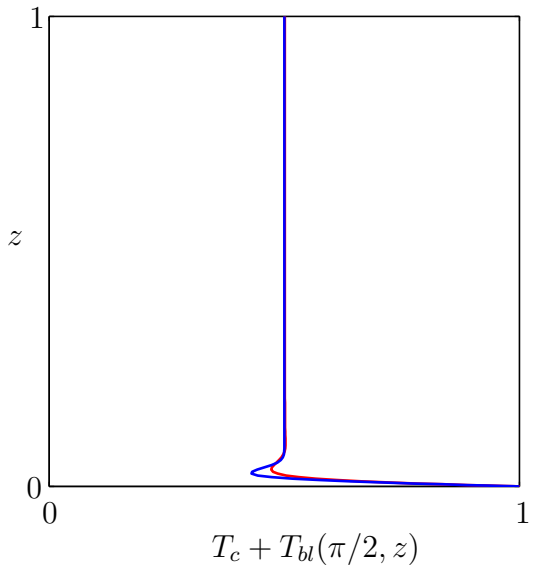

Figure 6.6: Vertical profile at $x = \frac{\pi}{2}$ of the total boundary layer temperature; the blue line is taken from the asymptotic theory and the red line is taken from the numerical simulations, for $Ta = 0$, $Pr = 1$, $R = 10000$.

6.9 Summary

In this chapter we presented an asymptotic theory capable of describing the steady state solutions of Chapter 5, for non-rotating convection. The foundations of this theory were built upon the work of Jimenez & Zufiria (1987) and Chini & Cox (2009), however our technique relies less on complex numerical procedures. The novelty of this asymptotic theory is in its relative simplicity over its predecessors. Furthermore, it is hoped that it can provide a natural starting point for addressing the time-dependent behaviour exhibited in Chapter 5, with a view to describing this mathematically.

First, we rescaled the system of equations in terms of the small parameter ϵ, related to the Rayleigh number via $\epsilon = Ra^{-\frac{1}{3}}$. We used ϵ as the basis for our asymptotic theory, equating terms at the same order. We performed asymptotic expansions of the governing hydrodynamical variables in both the bottom boundary layer and the rising plume. With only two terms in these expansions we were able to accurately predict the value of the core vorticity, ω_c, and Nusselt number, Nu, finding excellent agreement with the numerical results of Chapter 5. Furthermore, the vertical temperature profile predicted by our asymptotic theory was in excellent quantitative agreement with that of the numerical simulations.

Building on this, we attempted to perform the same analysis but with three terms in our expansions. In principle, this is possible, although we encountered some issues in solving the required set of seven simultaneous equations.

Chapter 7

Conclusions

7.1 Discussion

In this thesis we have studied nonlinear Rayleigh-Bénard convection, in two dimensional geometry, with and without rotation about the vertical axis, subject to stress free boundary conditions.

We began by presenting the equations governing the dynamics of the system and posing them in a dimensionless form. This furnished us with three dimensionless parameters: the Rayleigh number, Ra, the Prandtl number, Pr, and the Taylor number, Ta. Before studying the nonlinear equations in full, we first looked at their linear counterparts. Using normal mode analysis we were able to solve the equations analytically, in a plane layer of unbounded horizontal extent. The resulting linear theory allowed us to work out the critical Rayleigh number at which the onset of convection would take place, for a given horizontal wavenumber and Taylor number. The effect of rotation was to increase this critical Rayleigh number, therefore delaying the onset of convection. The distinguishing flow feature of rotating convection, that linear theory told us, was the preference for tall thin columns, with the horizontal length scale decreasing with increasing Taylor number. For rotating convection only, the stability of the system could change via a direct bifurcation

or a Hopf bifurcation. We analysed both cases and, furthermore, derived stability boundaries in (Ta, Pr) space outlining when convection will onset at either type of bifurcation. This is all work that has been previously undertaken by Chandrasekhar (1961).

Subsequent investigation was devoted to changing the values of the dimensionless parameters and seeing how this shaped the nonlinear evolution of the system. It was necessary to solve the governing equations numerically, so a suitable algorithm was devised in order to do this. We made the assumption of periodicity in the horizontal direction, allowing us to express the hydrodynamic variables in terms of Fourier series. We coupled this with a Chebyshev expansion in the vertical coordinate, giving a spectral representation of the variables (see Peyret (2002)). Sampling the equations on a discrete grid and calculating nonlinear terms in a pseudospectral manner allowed us to pose the solution to the system in terms of a set of matrix-vector problems. The numerical algorithm was devised so as to take particular advantage of the structure of these matrices, allowing them to be solved in an efficient manner. We made use of the FFTW (see Frigo & Johnson (2012)) and MKL (see Intel® (2012)) software libraries in order compute spectral transforms and matrix inversions respectively.

The nonlinear algorithm that was developed allowed us to conduct a comprehensive survey of the $\{Ra, Pr, Ta\}$ parameter space. Our interest was focused on what the effects were on the resultant nonlinear flows, in particular their form and structure, how these were affected by the temporal stability of the system and what implications these held for global properties of the system such as the Nusselt number and Reynolds number scaling. It was found that for the non-rotating system, for $Pr = 1$, the system was steady for all values of the Rayleigh number considered: here $Ra \leq 10^8$. This was consistent with the observations of DeLuca *et al.* (1990) and Vincent & Yuen (1999). Furthermore, as the Rayleigh number was increased, the horizontal length scale that dominated was the largest allowable in the computational box. These solutions were characterised by their robust cellular

structure and strikingly thin thermal boundary layers and plumes.

For $Pr = 10$ the system became time-dependent—specifically periodic in time—due to an instability whose origins were thermal. We addressed the nature of this instability from the point of view of nonlinear dynamical systems theory. We charted the phase space evolution of the system, finding subsequent bifurcations at similar parameter values to Curry (1978). After an initial Hopf bifurcation, there was a period doubling bifurcation, followed by a transition to motion on a two-torus in phase space. The breakdown of this torus led to quasi-periodicity and eventually chaos. Whilst we noted that, like Curry (1978), this behaviour was symptomatic of a Ruelle-Takens-Newhouse route to chaos (Newhouse *et al.* (1978)), we observed intermittent windows of steady behaviour. This led to the belief that route to chaos was more in line with the theory of Pomeau & Manneville (1980). Indeed, concluding the precise manner in which a nonlinear system evolves to chaos is particularly difficult, as noted by Glendinning (2005). This is especially so when numerically solving a system of PDEs rather than ODEs. The actual physical effect of the instability, on the solutions of the system, was to cause lateral motion of the upward and downward welling plumes. This was also noticed by Moore & Weiss (1973) in their numerical simulations and Krishnamurti (1970a)/Krishnamurti (1970b) in physical experiments. The basic dynamics of the instability can be explained by a much simpler model of convection within a closed loop, due to Welander (1967).

It was found that the Nusselt number scaled with the Rayleigh number with an exponent of $\frac{1}{3}$, independent of the value of Pr. This is consistent with the numerical simulations of Moore & Weiss (1973) and the classical theory summarised by Kraichnan (1962). Whilst we did not witness a scaling with an exponent of $\frac{2}{7}$, this is due to the fact that the Rayleigh number was consistently below the required value in the hard turbulence regime (see DeLuca *et al.* (1990)), where the $\frac{2}{7}$ scaling is conjectured to appear.

For the rotating system it was found that, after the initial convective instability predicted by linear theory, increasing the rotation rate had a destabilising effect on

the system. We charted the parameter space dynamics by considering the value of the convective Rossby number, Ro_*. Some steady solutions were found for lower rotation rates, with $Ro_* > 1$, though generally instability prevailed. As predicted by linear theory, for large values of Ta, at the onset of convection, the horizontal length scale was very short. As the Rayleigh number, and hence the convective Rossby number was increased, we noticed that the preference was for the length scale to increase. Furthermore, the form of the solutions for large Rayleigh number was consistent with the hard turbulence solutions of Vincent & Yuen (2000). Due to the number of simulations performed, to facilitate comparison of all runs, we concentrated on the global properties of the system. For simulations at lower rotation rates, where we found steady solutions, the Nusselt number scaled with the Rayleigh number with an exponent of $\frac{1}{3}$, as in the non-rotating case. All other—unsteady—solutions were found to scale with the Rayleigh number with an exponent of $\frac{2}{7}$, as noted by Julien *et al.* (1996b). This transition in scaling is undoubtedly due to the transition from the soft to hard turbulent regime, with the rotation acting as a catalyst for physical instability in two dimensions. For both the rotating and non-rotating systems, the Reynolds number was found to scale with flux Rayleigh number and the Prandtl number, in a like manner to that put forward by King *et al.* (2013). The length scale differed between the two cases, with non-rotating convection evolving on the scale of the box, and the length scale of rotating convection being governed by the value of the Taylor number.

Motivated by the remarkably steady nature of the nonlinear solutions found, even for large values of the Rayleigh number, at $Pr = 1$, we sought to develop an asymptotic theory capable of reproducing such solutions. Furthermore, it was hoped that this would offer a natural extension in order to explain the instability mechanism at $Pr = 10$. We were motivated by similar work on the structure of cellular convection by Roberts (1979), Jimenez & Zufiria (1987) and Chini & Cox (2009) but wanted to rely less on complicated numerical techniques, instead hoping for an analytical, asymptotic expansion.

We treated the temperature and vorticity as constant in the core of the convection cell, allowing us to solve for the core streamfunction analytically. By symmetry, and due to the boundary conditions, the core value of the temperature was discernible, taking the value $\frac{1}{2}$. The core value of the vorticity, however, was *a priori* unknown and played a role in all subsequent asymptotic solutions. From the analytically known core streamfunction we were able to derive expressions for the velocities in the bottom boundary layer and rising plume. This allowed us to solve the steady state temperature equation in these dynamically important regions, yielding a solution valid in the asymptotic limit of large Rayleigh number. We studied the behaviour of the system in the corner region, justifying that the role of the corner, to leading order, was passive. Both Jimenez & Zufiria (1987) and Chini (2008) came to the same conclusion about the corner region in similar studies. This had the implication that solutions should match as we transition from the bottom boundary layer to the rising plume, through the corner region, and likewise from the rising plume to the upper boundary layer. Moreover, this analysis furnished us with a natural set of constraints to place upon our solutions, demanding that moments of the temperature were continuous as we transition through the corner region. With this closure in place we were able to determine the various constants of integration that had arisen through solution to the governing equations.

The agreement between our asymptotic expansions with only two terms, and our fully nonlinear solutions from numerical simulations was excellent. Even with the inclusion of more terms in the asymptotic expansions, we showed that the system is always closed, and consistent, for any finite truncation value. The inclusion of more terms does not make the problem conceptually harder, it just requires the matching of higher order moments in the corner region, leading to more equations for more constants of integration. Solving these algebraic equations will always be faster than performing nonlinear numerical simulations, by many orders of magnitude. The required inputs of the asymptotic theory are the Rayleigh number, and a particular wavenumber governing the horizontal wavelength of the desired solution.

Using our asymptotic expansion for the temperature allowed us to calculate the value of the core vorticity by considering the global energy balance in the momentum equation: the production of vorticity due to buoyancy in the plumes, in equilibrium with the dissipation of vorticity, or enstrophy. This was shown to scale with the Rayleigh number with an exponent of $\frac{2}{3}$, and we were also able to determine the scaling pre-factor. This relation was shown to be in excellent agreement with the values coming from numerical simulations. Furthermore, the asymptotic theory gave rise to the Nusselt number scaling with the Rayleigh number with an exponent of $\frac{1}{3}$, and once more we were able to determine the scaling pre-factor; again this was shown to be in excellent agreement with the numerical simulations.

Two-dimensional Rayleigh-Bénard convection is limited in the sense that in a geophysical or astrophysical setting, there are three spatial dimensions. Nevertheless, the work presented here can still provide an insight into processes occurring in the natural world. In particular, the asymptotic theory of Chapter 6 is applicable to coherent structures found in convecting bodies such as the Earth and Sun, as well as those found in physical convection experiments—plumes are ubiquitous in such systems. In understanding the coupling between the boundary layers, plumes and the core of a convection cell, predictions can be made about thermal properties such as the Nusselt number. Within the context of the Earth, for example, it is believed that convection is responsible for transporting a significant proportion of heat from the ICB to the CMB (see Jones (2007)). Understanding this process is key to explaining the persistence of the Earth's magnetic field.

7.2 Development and further work

As with any body of work, it is natural to elucidate the extensions that could improve and advance the ideas put forward.

The $\{Ra, Pr, Ta\}$ parameter regime studied here was limited by the achievable

resolution of the numerical algorithm presented in Chapter 4. By achievable, we mean the highest resolution possible that allowed a typical well-resolved numerical simulation to be executed in a realistic amount of time. For non-rotating convection at $Pr = 1$, even our highest Rayleigh number simulation did not exhibit time dependent behaviour. In order to reach higher Rayleigh numbers, and witness the breakdown of cellular convection, we would need to increase the numerical resolution. Furthermore, for our rotating convection studies, the highest Taylor number that we reached was modest in terms of what is currently achievable in numerical simulations and physical experiments (see King *et al.* (2013)). Again, this would require an increased resolution in order to reach higher Taylor numbers. Thus to open up more extreme parameter regimes, some modifications to the numerical algorithm would have to be implemented.

Most importantly, by parallelising the numerical algorithm, we would be able to take advantage of computer architectures with a large number of cores. Within the framework of the numerical algorithm presented here, this would be easily accomplished. Since we expanded the horizontal dependence in terms of Fourier series, we were required to repeat the same actions for every wavenumber in our expansion, at every timestep. This provides a natural partition, whereby if we were to modify the algorithm, we would perform these actions simultaneously, clustering a set of wavenumbers on each core available. The only inter-dependence of these wavenumbers arises when computing nonlinear terms, pseudospectrally, in physical space. Here we would still have to utilise only one core. Nonetheless, the partitioning mentioned would speed the code up, proportional to the number of cores used.

Another natural extension would be to study the same system but in three space dimensions. This would be more realistic, and facilitate not only comparison with other three-dimensional numerical studies, but physical experiments. The robust nature of the steady, cellular solutions found in non-rotating convection at $Pr = 1$ is an inherent two-dimensional effect. In three dimensions a transition to an unsteady flow pattern would take place at a much lower value of Ra (see Kerr

(1996)). Furthermore, investigations into the dependence of the Nusselt number on the Rayleigh number could be more transparently compared with the existing theory of Grossman & Lohse (2000). In order to do this, the numerical algorithm would have to be modified to account for a third spatial dimension. The easiest way to implement this would be to assume periodicity in the third—horizontal—direction; applying a Fourier expansion in that variable. This would furnish us with another set of wavenumbers, requiring the solution of a matrix-vector problem for each, at each timestep. Furthermore, this could also be combined with the parallelisation procedure described above, in order to accelerate the algorithm when implemented on multi-core computer architectures.

The asymptotic theory that we have presented has only been used to describe the steady state solutions at $Pr = 1$. Due to time constraints we were not able to pursue other avenues of study, using this theory as a platform. It is hoped, however, that without much conceptual change, the theory could easily be extended to facilitate the study of further interesting problems. We would like to try and describe, mathematically, the time-dependent solutions that we witnessed for non-rotating convection at $Pr = 10$. However these solutions occurred for $R = 50$, which is not particularly high, meaning that the validity of our asymptotic theory is limited. For example, the boundary layer structure was not strikingly narrow, and the solution was not dominated by its core contribution. A more relevant study would be to find an example of the same time-dependent behaviour, but at a lower Prandtl number. The hope is that this would require a higher Rayleigh number before the presence of instability, meaning that solutions would be in the asymptotic regime. For example, having modified the numerical algorithm in the manner described above, this could be achieved for $Pr = 1$. It is expected that the physical instability mechanism that we presented in Chapter 4 would remain the same. Armed with this understanding of the instability would allow us to equilibrate the correct terms within the governing equations. Although the instability is thermal in origin, it induces a vorticity anomaly in the rising plume that needs to be addressed mathematically. This

requires extending the theory to incorporate kinematic effects coming from the momentum equation. We believe that the vorticity can be expanded in a like manner to the temperature, and the momentum equation can be addressed similarly.

What is clear is that there is still much work to be done in order to fully understand the dynamics of two-dimensional Rayleigh-Bénard convection. As with any investigative study, answering one question leads to the posing of another—if not more.

Appendices

A Vector identities

For any vector fields $\mathbf{a}$ and $\mathbf{b}$, and any scalar functions f and g, we have the following

$$\frac{1}{2}\nabla\left(\mathbf{a}\cdot\mathbf{a}\right) \equiv \nabla\left(\frac{1}{2}\left|\mathbf{a}\right|^2\right) = \mathbf{a}\times\left(\nabla\times\mathbf{a}\right) + \left(\mathbf{a}\cdot\nabla\right)\mathbf{a}, \tag{A.1}$$

$$\nabla\times\left(\mathbf{a}\times\mathbf{b}\right) = \mathbf{a}(\nabla\cdot\mathbf{b}) - \mathbf{b}(\nabla\cdot\mathbf{a}) + (\mathbf{b}\cdot\nabla)\mathbf{a} - (\mathbf{a}\cdot\nabla)\mathbf{b}, \tag{A.2}$$

$$\nabla\times\left(\nabla\times\mathbf{a}\right) = \nabla\left(\nabla\cdot\mathbf{a}\right) - \nabla^2\mathbf{a}, \tag{A.3}$$

$$\nabla\cdot\left(\mathbf{a}f\right) = f\left(\nabla\cdot\mathbf{a}\right) + \left(\mathbf{a}\cdot\nabla\right)f, \tag{A.4}$$

$$\nabla^2 f = \nabla\cdot\left(\nabla f\right), \tag{A.5}$$

$$\nabla\cdot\left(\mathbf{a}\times\mathbf{b}\right) = \mathbf{b}\cdot\left(\nabla\times\mathbf{a}\right) - \mathbf{a}\cdot\left(\nabla\times\mathbf{b}\right). \tag{A.6}$$

B Integral relations

A frequently occurring integral in Chapter 6 is given by

$$I_n = \int_0^\infty s^n e^{-s^2} \mathrm{d}s. \tag{B.7}$$

Using integration by parts we have

$$I_n = \left[-\frac{1}{2} s^{n-1} e^{-s^2} \right]_0^\infty + \frac{n-1}{2} \int_0^\infty s^{n-2} e^{-s^2} \mathrm{d}s, \tag{B.8}$$

where the boundary term is zero, hence

$$I_n = \frac{n-1}{2} I_{n-2}, \quad \text{for } \; n \geq 2. \tag{B.9}$$

It is possible to use this recursion relation to calculate the value for any n. Hence we have

$$I_n = \begin{cases} 2^{-\left(\frac{n+2}{2}\right)} (n-1)!! \, \pi^{\frac{1}{2}} & \text{for } n \text{ even}, \\ 2^{-\left(\frac{n+1}{2}\right)} (n-1)!! & \text{for } n \text{ odd}. \end{cases} \tag{B.10}$$

This is also given by Abramowitz & Stegun (1965) in §7.4.4 and §7.5.5. Some values that we will require are given by

$$I_0 = \frac{\pi^{\frac{1}{2}}}{2}, \; I_1 = \frac{1}{2}, \; I_2 = \frac{\pi^{\frac{1}{2}}}{4}, \; I_3 = \frac{1}{2}, \; I_4 = \frac{3\pi^{\frac{1}{2}}}{8}. \tag{B.11}$$

A second integral that we are required to evaluate is given by

$$J_n = \frac{\pi^{\frac{1}{2}}}{2} \int_0^\infty s^n \mathrm{erfc}\,(s) \mathrm{d}s = \int_0^\infty s^n \left(\int_s^\infty e^{-\hat{s}^2} \mathrm{d}\hat{s} \right) \mathrm{d}s. \tag{B.12}$$

Using integration by parts we have

$$J_n = \left[\frac{s^{n+1}}{n+1} \int_s^\infty e^{-\hat{s}^2} \mathrm{d}\hat{s} \right]_0^\infty + \frac{1}{n+1} \int_0^\infty s^{n+1} e^{-s^2} \mathrm{d}s \tag{B.13}$$

where the boundary terms is zero and by comparison with equation (B.9) we note that the remaining term is equivalent to I_{n+1}, hence we have

$$J_n = \frac{1}{n+1} I_{n+1} \quad \text{for } \; n \geq 0. \tag{B.14}$$

Using equation (B.10) we are able to write this as

$$J_n = \begin{cases} 2^{-\left(\frac{n+2}{2}\right)}(n-1)^{-1}\, n!! & \text{for } n \text{ even}, \\ 2^{-\left(\frac{n+1}{2}\right)}(n-1)^{-1}\, n!!\, \pi^{\frac{1}{2}} & \text{for } n \text{ odd}. \end{cases} \tag{B.15}$$

Some values that we will require are given by

$$J_0 = \frac{1}{2},\ J_1 = \frac{\pi^{\frac{1}{2}}}{8}. \tag{B.16}$$

Bibliography

Abramowitz, M., & Stegun, I.A. 1965. *Handbook of Mathematical Functions*. Dover.

Acheson, D.J. 1990. *Elementary Fluid Dynamics*. Clarendon Press.

Anderson, E., Bai, Z., Bischof, C., Blackford, S., Demmel, J., J., Dongarra, Du Croz, J., Greenbaum, A., Hammarling, S., McKenny, A., & Sorensen, D. 1999. *LAPACK Users' Guide*. third edn. SIAM.

Batchelor, G.K. 1967. *An introduction to fluid dynamics*. Cambridge University Press.

Bénard, H. 1900. Les Tourbillons cellulaires dans une nappe liquide. *Revue générale des Sciences pures et appliquées.*, **11**, 1261–1271.

Bénard, H. 1901. Les Tourbillons cellulaires dans une nappe liquide transportant de la chaleur par convection en régime permanent. *Annales de Chimie de Physique*, **23**, 62–144.

Boussinesq, J. 1903. Théorie Analytique de la Chaleur. *Paris: Gauthier-Villars*, **2**, 172.

Boyd, J.P. 2001. *Chebyshev and Fourier spectral methods*. Dover.

Brummell, N.H., Hurlburt, N.E., & Toomre, J. 1996. Turbulent Compressible Convection with Rotation. I. Flow Structure and Evolution. *The Astrophysical Journal*, **473**, 494–513.

Brummell, N.H., Hurlburt, N.E., & Toomre, J. 1998. Turbulent Compressible Convection with Rotation. II. Mean Flows and Differential Rotation. *The Astrophysical Journal*, **493**, 955–969.

Busse, F. H. 1978. Non-linear properties of thermal convection. *Reports on Progress in Physics*, **41**, 1929–1967.

Busse, F. H., & Cuong, P.G. 1977. Convection in Rapidly Rotating Spherical Fluid Shells. *Geophysical and Astrophysical Fluid Dynamics*, **8**, 17–44.

Canuto, C., Hussaini, M.Y., Quarteroni, A., & Zang, T.A. 1988. *Spectral Methods in Fluid Dynamics*. Springer Verlag.

Canuto, C., Hussaini, M.Y., Quarteroni, A., & Zang, T.A. 2006. *Spectral Methods: Fundamentals in Single Domains*. Springer.

Castaing, B., Gunaratne, G., Heslot, F., Kadanoff, L., Libchaber, A., Thomae, S., Wu, X.Z., Zaleski, S., & Zanetti, G. 1989. Scaling of hard thermal turbulence in Rayleigh-Bénard convection. *Journal of Fluid Mechanics*, **204**, 1–30.

Chandrasekhar, S. 1961. *Hydrodynamic and Hydromagnetic Stability*. Dover.

Chini, G.P. 2008. Strongly nonlinear Langmuir circulation and Rayleigh-Bénard convection. *Journal of Fluid Mechanics*, **614**, 39–65.

Chini, G.P., & Cox, S.M. 2009. Large Rayleigh number thermal convection: Heat flux predictions and strongly nonlinear solutions. *Physics of Fluids*, **21**, 083603.

Christensen, U.R. 2002. Zonal flow driven by strongly supercritical convection in rotating spherical shells. *Journal of Fluid Mechanics*, **470**, 115–133.

Christensen-Dalsgaard, J. 1988. Study of the solar structure based on p-mode. *Pages 431–450 of:* Rolfe, E.J. (ed), *Seismology of the Sun and Sun-Like Stars*. ESA Special Publications.

Clever, R.M., & Busse, F.H. 1978. Nonlinear properties of convection rolls in a horizontal layer rotating about a vertical axis. *Journal of Fluid Mechanics*, **94**, 609–627.

Cooley, J.W., & Tukey, J.W. 1965. An algorithm for the machine calculation of complex Fourier series. *Mathematics of Computation*, **19**, 297–301.

Cox, S.M., & Matthews, P.C. 1997. A pseudospectral code for convection with analytical/numerical implementation of horizontal boundary conditions. *International Journal for Numerical Methods in Fluids*, **25**, 151–166.

Curry, J.H. 1978. A Generalized Lorenz System. *Communications in Mathematical Physics*, **60**, 193–204.

Curry, J.H., Herring, J.R., Loncaric, J., & Orszag, S.A. 1984. Order and disorder in two- and three-dimensional Bénard convection. *Journal of Fluid Mechanics*, **147**, 1–38.

Deardorff, J.W. 1970. Convective Velocity and Temperature Scales for the Unstable Planetary Boundary Layer and for Rayleigh Convection. *Journal of the Atmospheric Sciences*, **27**, 1211–1213.

DeLuca, E.E., Werne, J., Rosner, R., & Cattaneo, F. 1990. Numerical Simulations of Soft and Hard Turbulence: Preliminary Results for Two-Dimensional Convection. *Physical Review Letters*, **64**, 2370–2373.

Doering, C.R., & Constantin, P. 1996. Variational bounds on energy dissipation in incompressible flows. III. Convection. *Physical Review E*, **53**, 5957–5981.

Doering, C.R., Otto, F., & Reznikoff, M.G. 2006. Bounds on vertical heat transport for infinite-Prandtl-number Rayleigh-Bénard convection. *Journal of Fluid Mechanics*, **560**, 229–241.

Dormy, E. 1997. *Modélisation Numérique de la Dynamo Terrestre*. Ph.D. thesis, Institut de Physique du Globe de Paris.

Dormy, E., & Soward, A.M. 2007. *Mathematical Aspects of Natural Dynamos*. Chapman and Hall.

Dormy, E., Soward, A.M., Jones, C.A., Jault, D., & Cardin, P. 2004. The onset of thermal convection in rotating spherical shells. *Journal of Fluid Mechanics*, **501**, 43–70.

Drazin, P.G., & Reid, W.H. 1981. *Hydrodynamic stability*. Cambridge University Press.

Fearn, D.R. 2007. The geodynamo. *In:* Dormy, E., & Soward, A.M. (eds), *Mathematical Aspects of Natural Dynamos*. Chapman and Hall.

Frigo, M., & Johnson, S.G. 2005. The Design and Implementation of FFTW3. *Proceedings of the IEEE*, **93**, 216–231. Special issue on "Program Generation, Optimization, and Platform Adaptation".

Frigo, M., & Johnson, S.G. 2012. *FFTW3.3.3 Users' Manual*. Massachusetts Institute of Technology.

Gauss, C.F. 1866. Theoria interpolationis methodo nova tractata. *Carl Friedrich Gauss Werke*, **3**, 265–303.

Gilbert, W. 1600. *De Magnete, Magneticisque Corporibus, et de Magno Magnete Tellure*. Peter Short.

Gillet, N., & Jones, C.A. 2006. The quasi-geostrophic model for rapidly rotating spherical convection outside the tangent cylinder. *Journal of Fluid Mechanics*, **554**, 343–369.

Gilman, P.A. 1977. Nonlinear Dynamics of Boussinesq Convection in a Deep Rotating Spherical Shell I. *Geophysical and Astrophysical Fluid Dynamics*, **8**, 93–135.

Gilman, P.A. 1978a. Nonlinear Dynamics of Boussinesq Convection in a Deep Rotating Spherical Shell II: Effects of Temperature Boundary Conditions. *Geophysical and Astrophysical Fluid Dynamics*, **11**, 157–179.

Gilman, P.A. 1978b. Nonlinear Dynamics of Boussinesq Convection in a Deep Rotating Spherical Shell III: Effects of Velocity Boundary Conditions. *Geophysical and Astrophysical Fluid Dynamics*, **11**, 181–208.

Glatzmaier, G.A. 2013. *Introduction to Modeling Convection in Planets and Stars: Magnetic Field, Density Stratification, Rotation.* Princeton University Press.

Glatzmaier, G.A., & Roberts, P.H. 1995. A three-dimensional self-consistent computer simulation of a geomagnetic field reversal. *Nature*, **377**, 203–209.

Glendinning, P. 2005. Routes to Chaos. *Pages 815–817 of:* Scott, A. (ed), *Encyclopedia of Nonlinear Science.* Routledge.

Gough, D.O. 1969. The anelastic approximation for thermal convection. *Journal of the Atmospheric Sciences*, **26**, 448–456.

Greenspan, H.P. 1968. *The theory of rotating fluids.* Cambridge University Press.

Grossman, S., & Lohse, D. 2000. Scaling in thermal convection: a unifying theory. *Journal of Fluid Mechanics*, **407**, 27–56.

Gubbins, D., & Herrero-Bervera, E. (eds). 2007. *Encyclopedia of Geomagnetism and Paleomagnetism.* Springer-Verlag.

Guckenheimer, G., & Holmes, P. 1997. *Nonlinear Oscillations, Dynamical Systems, and Bifurcations of Vector Fields.* Springer.

Hollerbach, R. 2000. A spectral solution of the magneto-convection equations in spherical geometry. *International Journal for Numerical Methods in Fluids*, **32**, 773–797.

Hollerbach, R., & Jones, C.A. 1993a. A geodynamo model incorporating a finitely conducting inner core. *Physics of the Earth and Planetary Interiors*, **75**, 317–327.

Hollerbach, R., & Jones, C.A. 1993b. Influence of the Earth's inner core on geomagnetic fluctuations and reversals. *Nature*, **365**, 541–543.

Hoyle, R. 2006. *Pattern Formation: An Introduction to Methods*. Cambridge University Press.

Hughes, D.W., Rosner, R., & Weiss, N.O. 2007. *The Solar Tachocline*. Cambridge University Press.

Intel®. 2012. *Intel® Math Kernel Library Reference Manual 11.0 Update 3*.

Jacobs, J.A. 1987. *The Earth's Core*. Academic Press.

Jeffreys, H. 1926. The stability of a layer of fluid heated below. *Philosophical Magazine*, **2**, 833–844.

Jeffreys, H. 1928. Som cases of instability in fluid motion. *Proceedings of the Royal Society A*, **118**, 195–208.

Jimenez, J., & Zufiria, J.A. 1987. A boundary-layer analysis of Rayleigh-Bénard convection at large Rayleigh number. *Journal of Fluid Mechanics*, **178**, 53–71.

Jones, C.A. 2007. Thermal and Compositional Convection in the Outer Core. *Pages 131–185 of:* Olson, P. (ed), *Core Dynamics: Treatise on Geophysics*. Elsevier.

Jones, C.A., Soward, A.M., & Mussa, A.I. 2000. The onset of thermal convection in a rapidly rotating sphere. *Journal of Fluid Mechanics*, **405**, 157–179.

Julien, K., Legg, S., McWilliams, J., & Werne, J. 1996a. Hard turbulence in rotating Rayleigh-Bénard convection. *Physical Review E*, **53**, R5557–R5560.

Julien, K., Legg, S., McWilliams, J., & Werne, J. 1996b. Rapidly rotating turbulent Rayleigh-Bénard convection. *Journal of Fluid Mechanics*, **322**, 243–273.

Julien, K., Rubio, A.M., Grooms, E., & Knobloch, E. 2012. Statistical and physical balances in low Rossby number Rayleigh-Bénard convection. *Geophysical and Astrophysical Fluid Dynamics*, **106**, 392–428.

Kerr, R.M. 1996. Rayleigh number scaling in numerical convection. *Journal of Fluid Mechanics*, **310**, 139–179.

Kerswell, R.R. 2000. New results in the variational approach to turbulent Boussinesq convection. *Physics of Fluids*, **13**, 192–209.

King, E.M., Stellmach, S., Noir, J., Hansen, U., & Aurnou, J.M. 2009. Boundary layer control of rotating convection systems. *Nature*, **457**, 301–304.

King, E.M., Stellmach, S., & Aurnou, J.M. 2012. Heat transfer by rapidly rotating Rayleigh-Bénard convection. *Journal of Fluid Mechanics*, **691**, 568–582.

King, E.M., Stellmach, S., & Buffett, B. 2013. Scaling behaviour in Rayleigh-Bénard convection with and without rotation. *Journal of Fluid Mechanics*, **717**, 449–471.

Kloosterziel, R.C., & Carnevale, G.F. 2003. Closed-form linear stability conditions for rotating Rayleigh-Bénard convection with rigid stress-free upper and lower boundaries. *Journal of Fluid Mechanics*, **480**, 25–42.

Kraichnan, R. 1962. Turbulent Thermal Convection at Arbitrary Prandtl Number. *Physics of Fluids*, **5**, 1374–1389.

Krishnamurti, R. 1970a. On the transition to turbulent convection. Part 1. The transition from two- to three-dimensional flow. *Journal of Fluid Mechanics*, **42**, 299–307.

Krishnamurti, R. 1970b. On the transition to turbulent convection. Part 2. The transition to time-dependent flow. *Journal of Fluid Mechanics*, **42**, 309–320.

Kuppers, G, & Lortz, D. 1969. Transition from laminar convection to thermal turbulence in a rotating fluid layer. *Journal of Fluid Mechanics*, **35**, 609–620.

Larmor, J. 1919. How could a rotating body such as the Sun become a magnet? *Reports of the British Association for the Advancement of Science*, **14**, 87–115.

Lehmann, I. 1936. P'. *Publications du Bureau Central Séismologique International*, **87**, 159–160.

Lennie, T.B., McKenzie, D.P., Moore, D.R., & Weiss, N.O. 1988. The breakdown of steady convection. *Journal of Fluid Mechanics*, **188**, 47–85.

Li, N., & Ecke, R.E. 1993. Kuppers-Lortz transition at high dimensionless rotation rates in rotating Rayleigh-Bénard convection. *Physical Review E*, **47**, R2991.

Liu, Y., & Ecke, R.E. 1997. Heat Transport Scaling in Turbulent Rayleigh-Bénard Convection: Effects of Rotation and Prandtl Number. *Physical Review Letters*, **79**, 2257–2260.

Liu, Y., & Ecke, R.E. 2009. Heat transport measurements in turbulent rotating Rayleigh-Bénard convection. *Physical Review E*, **80**, 036314.

Lorenz, E.N. 1963. Deterministic Nonperiodic Flow. *Journal of the Atmospheric Sciences*, **120**, 130–141.

Malkus, W.V.R. 1954a. Discrete Transitions in Turbulent Convection. *Proceedings of the Royal Society A*, **225**, 185–195.

Malkus, W.V.R. 1954b. The Heat Transport and Spectrum of Thermal Turbulence. *Proceedings of the Royal Society A*, **225**, 196–212.

Malkus, W.V.R., & Veronis, G. 1958. Finite amplitude cellular convection. *Journal of Fluid Mechanics*, **4**, 225–260.

Moffatt, H.K. 1978. *Magnetic field generation in electrically conducting fluids.* Cambridge University Press.

Moore, D.R., & Weiss, N.O. 1973. Two-dimensional Rayleigh-Bénard convection. *Journal of Fluid Mechanics*, **58**, 289–312.

Newhouse, S., Reulle, D., & Takens, F. 1978. Occurrence of Strange Axiom A Attractors Near Quasi Periodic Flows on $T^m, m \geq 3$. *Communications in Mathematical Physics*, **64**, 35–40.

Ogura, Y. 1971. A Numerical Study of Wavenumber Selection in Finite-Amplitude Rayleigh Convection. *Journal of the Atmospheric Sciences*, **28**, 709–717.

Orszag, S.M. 1971. On the Elimination of Aliasing in Finite-Difference Schemes by Filtering High-Wavenumber Components. *Journal of the Atmospheric Sciences*, **28**, 1074.

Pellow, A., & Southwell, R.V. 1940. On maintained convective motion in a fluid heated from below. *Proceedings of the Royal Society A*, **176**, 312–343.

Peyret, R. 2002. *Spectral Methods for Incompressible Viscous Flow.* Springer.

Pomeau, Y., & Manneville, P. 1980. Intermittent Transition to Turbulence in Dissipative Dynamical Systems. *Communications in Mathematical Physics*, **74**, 189–197.

Proudman, J. 1916. On the Motion of Solids in a Liquid Possessing Vorticity. *Proceedings of the Royal Society A*, **92**, 408–424.

Rayleigh, Lord. 1916. On convection currents in a horizontal layer of fluid, when the higher temperature is on the under side. *Philosophical Magazine*, **32**, 529–546.

Roberts, G.O. 1977. Fast viscous convection. *Geophysical and Astrophysical Fluid Dynamics*, **8**, 197–233.

ROBERTS, G.O. 1979. Fast viscous Bénard convection. *Geophysical and Astrophysical Fluid Dynamics*, **12**, 235–272.

ROBERTS, P.H. 1968. On the Thermal Instability of a Rotating-Fluid Sphere Containing Heat Sources. *Philosophical Transactions of the Royal Society A*, **263**, 93–117.

ROBINSON, J.L. 1967. Finite amplitude convection cells. *Journal of Fluid Mechanics*, **30**, 577–600.

ROSSBY, H.T. 1969. A study of Bénard convection with and without rotation. *Journal of Fluid Mechanics*, **36**, 309–335.

ROTVIG, J., & JONES, C.A. 2002. Rotating convection-driven dynamos at low Ekman number. *Physical Review E*, **66**, 056308.

SCHMIDT, R.J., & MILVERTON, S.W. 1935. On the instability of a fluid when heated from below. *Proceedings of the Royal Society A*, **152**, 586–594.

SCHMITZ, S., & TILGNER, A. 2009. Heat transport in rotating convection without Ekman layers. *Physical Review E*, **80**, 015305(R).

SCHMITZ, S., & TILGNER, A. 2010. Transitions in turbulent rotating Rayleigh-Bénard convection. *Geophysical and Astrophysical Fluid Dynamics*, **104**, 481–489.

SHRAIMAN, B.I., & SIGGIA, S.D. 1990. Heat transport in high-Rayleigh-number convection. *Physical Review A*, **42**, 3650–3653.

SIGGIA, S.D. 1994. High Rayleigh number convection. *Annual Review of Fluid Mechanics*, **26**, 137–168.

SOMERVILLE, R.C.J., & LIPPS, F.B. 1973. A Numerical Study in Three Space Dimensions of Bénard Convection in a Rotating Fluid. *Journal of the Atmospheric Sciences*, **30**, 590–596.

Soward, A.M. 1977. On the Finite amplitude thermal instability of a rapidly rotating fluid sphere. *Geophysical and Astrophysical Fluid Dynamics*, **9**, 19–74.

Sparrow, C. 1982. *The Lorenz Equations: Bifurcations, Chaos, and Strange Attractors*. Springer Verlag.

Spiegel, E.A., & Veronis, G. 1960. On the Boussinesq approximation for a compressible fluid. *Astrophysical Journal*, **131**, 442–447.

Strogatz, S.H. 2000. *Nonlinear Dynamics and Chaos*. Perseus Books.

Swift, J., & Hohenberg, P.C. 1977. Hydrodynamic fluctuations at the convective instability. *Physical Review A*, **15**, 319–328.

Taylor, G.I. 1917. Motion of Solids in Fluids When the Flow is Not Irrotational. *Proceedings of the Royal Society A*, **93**, 99–113.

Taylor, G.I. 1922. The Motion of a Sphere in a Rotating Liquid. *Proceedings of the Royal Society A*, **102**, 180–189.

Tilgner, A., & Busse, F.H. 1997. Finite-amplitude convection in rotating spherical fluid shells. *Journal of Fluid Mechanics*, **332**, 359–376.

Tobias, S.M., Brummell, N.H., Clune, T.L., & Toomre, J. 2001. Transport and Storage of Magnetic Fields by Overshooting Turbulent Compressible Convection. *The Astrophysical Journal*, **549**, 1183–1203.

Trefethen, L.N. 2000. *Spectral Methods in MATLAB*. SIAM.

Veronis, G. 1959. Cellular convection with finite amplitude in a rotating fluid. *Journal of Fluid Mechanics*, **5**, 401–435.

Veronis, G. 1966. Large-amplitude Bénard convection. *Journal of Fluid Mechanics*, **26**, 49–68.

Veronis, G. 1968. Large-amplitude Bénard convection in a rotating fluid. *Journal of Fluid Mechanics*, **31**, 113–139.

Vincent, A.P., & Yuen, D.A. 1999. Plumes and waves in two-dimensional turbulent thermal convection. *Physical Review E*, **60**, 2957–2963.

Vincent, A.P., & Yuen, D.A. 2000. Transition to turbulent thermal convection beyond $Ra = 10^{10}$ detected in numerical simulations. *Physical Review E*, **61**, 5241–5246.

Welander, P. 1967. On the oscillatory instability of a differentially heated fluid loop. *Journal of Fluid Mechanics*, **29**, 17–30.

Whitehead, J.P., & Doering, C.R. 2011. Ultimate State of Two-Dimensional Rayleigh-Bénard Convection between Free-Slip Fixed-Temperature Boundaries. *Physical Review Letters*, **106**, 244501.

Zhang, K. 1992. Spiralling columnar convection in rapidly rotating spherical fluid shells. *Journal of Fluid Mechanics*, **236**, 535–556.

Zocchi, G., Moses, E., & Libchaber, A. 1990. Coherent structures in turbulent convection, and experimental study. *Physica A*, **166**, 387–407.